Western Graduate&PostdoctoralStudies

Western University
Scholarship@Western

Electronic Thesis and Dissertation Repository

3-30-2023 10:30 AM

Novel 129Xe Magnetic Resonance Imaging and Spectroscopy Measurements of Pulmonary Gas-Exchange

Alexander M. Matheson, *The University of Western Ontario*

Supervisor: Parraga, Grace E., *The University of Western Ontario*

A thesis submitted in partial fulfillment of the requirements for the Doctor of Philosophy degree in Medical Biophysics

© Alexander M. Matheson 2023

Follow this and additional works at: https://ir.lib.uwo.ca/etd

Part of the Biophysics Commons, Medical Biophysics Commons, and the Respiratory System Commons

Recommended Citation

Matheson, Alexander M., "Novel 129Xe Magnetic Resonance Imaging and Spectroscopy Measurements of Pulmonary Gas-Exchange" (2023). *Electronic Thesis and Dissertation Repository*. 9179.
https://ir.lib.uwo.ca/etd/9179

This Dissertation/Thesis is brought to you for free and open access by Scholarship@Western. It has been accepted for inclusion in Electronic Thesis and Dissertation Repository by an authorized administrator of Scholarship@Western. For more information, please contact wlswadmin@uwo.ca.

Abstract

Gas-exchange is the primary function of the lungs and involves removing carbon dioxide from the body and exchanging it within the alveoli for inhaled oxygen. Several different pulmonary and cardiovascular abnormalities have negative effects on pulmonary gas-exchange. Unfortunately, clinical tests do not always pinpoint the problem; sensitive and specific measurements are needed to probe the individual components participating in gas-exchange for a better understanding of pathophysiology, disease progression and response to therapy.

In vivo Xenon-129 gas-exchange magnetic resonance imaging (^{129}Xe gas-exchange MRI) has the potential to overcome these challenges. When participants inhale hyperpolarized ^{129}Xe gas, it has different MR spectral properties as a gas, as it diffuses through the alveolar membrane and as it binds to red-blood-cells. ^{129}Xe MR spectroscopy and imaging provides a way to tease out the different anatomic components of gas-exchange simultaneously and provides spatial information about where abnormalities may occur.

In this thesis, I developed and applied ^{129}Xe MR spectroscopy and imaging to measure gas-exchange in the lungs alongside other clinical and imaging measurements. I measured ^{129}Xe gas-exchange in asymptomatic congenital heart disease and in prospective, controlled studies of long-COVID. I also developed mathematical tools to model ^{129}Xe MR signals during acquisition and reconstruction. The insights gained from my work underscore the potential for ^{129}Xe gas-exchange MRI biomarkers towards a better understanding of cardiopulmonary disease. My work also provides a way to generate a deeper imaging and physiologic understanding of gas-exchange *in vivo* in healthy participants and patients with chronic lung and heart disease.

Keywords

Magnetic Resonance Imaging, Magnetic Resonance Spectroscopy, ^{129}Xe MRI, Hyperpolarized Gas, Gas-Exchange, COVID-19, Long-COVID, Atrial Septal Defect, Pulmonary Vasculature, Linear Systems Theory, Pulmonary Imaging

Summary for Lay Audience

Gas-exchange is the primary function of the lung, where breath moves down the airways, into sacs called alveoli, through the surrounding tissue membrane and into the tiniest blood vessels, called capillaries, where oxygen binds to red-blood-cells (RBC). Diseases can affect each of these steps but most techniques to detect gas-exchange only look at the whole process. Therefore, the development of new imaging tools may help to probe the individual steps in gas exchange to study disease and treat patients. Current tools for imaging the lung only look at ventilation or cannot measure all the way to the alveoli, the air sacs at the end of airways. A new way to probe the alveoli is by using a magnetized gas called xenon-129, which can act like oxygen and undergo gas-exchange. Since xenon also passes into the bloodstream and attaches to RBC, this technique also allows us to learn about each individual step of gas-exchange. Magnetic resonance imaging (MRI) can be used to measure xenon in each compartment to determine the effectiveness of gas exchange, as well as providing maps of lung function to locate diseased regions of the lung. In this thesis, I used xenon MRI to measure gas-exchange and compare results with current imaging and breath-analysis tools. Specifically, I built mathematical tools to model how gas-exchange measurements are detected by xenon MRI. I then applied this technique in people with long-COVID and in a case of a congenital heart defect. Together, this work demonstrates the potential of xenon MRI for understanding gas-exchange in pulmonary and heart disease.

Co-Authorship Statement

The following thesis contains five manuscripts that have been published. As first author of these manuscripts, I was a significant contributor to all aspects of the studies as well as manuscript preparation and submission. I was responsible for conceiving study design, performing study visits, data analysis, image processing, statistical analysis, manuscript and revision writing. I was also responsible for implementation of CT pulmonary vascular analysis software and development/implementation of ^{129}Xe gas-exchange MRI acquisition and reconstruction software. Grace Parraga, as the Principal Investigator and thesis Supervisor, provided continued guidance and was responsible for the conception of the study, experimental design, data interpretation and drafting and approval of the manuscript. She was also the guarantor of data integrity and responsible for Good Clinical Practice. Study visits and acquisition of pulmonary function data were performed under the supervision of Danielle Knipping and Angela Wilson. Polarization of hyperpolarized gas was performed by myself, Andrew Westcott, Jonathan MacNeil, Maksym Sharma, Ivailo Petrov and Alexander Biancanello. MRI acquisition was performed by David Reese. I outline the specific contributions for all co-authors for the manuscripts contained in this thesis as follows:

Chapter 2 is an original conference research manuscript entitled "*A Linear Systems Description of Multi-Compartment Pulmonary ^{129}Xe Magnetic Resonance Imaging Methods"* and was published in the Proceedings of SPIE: Medical Imaging 2021. This manuscript was co-authored by Alexander M Matheson, Grace Parraga and Ian Cunningham. Grace Parraga and Ian Cunningham assisted with drafting and approval of the manuscript.

Chapter 3 is an original research article entitled "*Persistent ^{129}Xe MRI Pulmonary and CT Vascular Abnormalities in Symptomatic Individuals with Post-Acute COVID-19 Syndrome"* and was published in Radiology in 2022. This manuscript was co-authored by Alexander M Matheson, Marrissa J McIntosh, Harkiran K Kooner, Justin Lee, Vedanth Desaigoudar, Elianna Bier, Bastiaan Driehuys, Sarah Svenningsen, Giles E Santyr, Miranda Kirby, Mitchell S Albert, Yurii Shepelytskyi, Vira Grynko, Alexei Ouriadov, Mohamed Abdelrazek, Inderdeep Dhaliwal, J Michael Nicholson, and Grace Parraga. Marrissa McIntosh and Harkiran Kooner assisted with data acquisition. Marrissa McIntosh, Harkiran Kooner, Justin Lee, Vedanth Desaigoudar, Bastiaan Driehuys, Sarah Svenningsen, Mitchell Albert and Grace Parraga assisted with literature research. Elianna Bier, Giles E Santyr, Mitchell Albert, Mohamed Abdelrazek, Inderdeep Dhaliwal, Michael Nicholson and Grace Parraga assisted with clinical interpretation of the data. Justin Lee, Bastiaan Driehuys, Mitchell Albert and Grace Parraga assisted with statistical analysis and Marrissa McIntosh, Harkiran Kooner, Vedanth Desaigoudar, Bastiaan Driehuys, Sarah Svenningsen, Giles Santyr, Miranda Kirby, Mitchell Albert, Yurii Shepelytskyi, Vira Grynko, Alexei Ouriadov, Mohamed Abdelrazek, Inderdeep Dhaliwal, Michael Nicholson and Grace Parraga assisted with manuscript editing. Sarah Svenningsen, Giles Santyr, Miranda Kirby, Mitchell Albert, Alexei Ouriadov, Inderdeep Dhaliwal and Michael Nicholson were responsible for study conception and design of the LIVECOVIDFREE protocol.

Chapter 4 is an original research article entitled "*Longitudinal Follow-up of Post-Acute COVID-19 Syndrome: $DL_{CO,}$ Quality-of-Life and MRI Pulmonary Gas-Exchange Abnormalities"* and was published in Thorax in 2023. This manuscript was co-authored by Marrissa J McIntosh, Harkiran K Kooner, Mohamed Abdelrazek, Mitchell S Albert, Inderdeep

Dhaliwal, J Michael Nicholson, Alexei Ouriadov, Sarah Svenningsen and Grace Parraga. Marrissa McIntosh and Harkiran Kooner assisted with data acquisition and analysis. Inderdeep Dhaliwal and Michael Nicholson were responsible for recruiting study participants and providing clinical input and interpretation of the data. Mohamed Abdelrazek, Mitchell Albert, Alexei Ouriadov and Sarah Svenningsen supported the study design development and interpretation of the data. Grace Parraga was responsible for study design, data analysis and interpretation. All authors were responsible for manuscript editing. Alexander Matheson contributed 70% of the work presented.

Chapter 5 contains an original case report entitled "*Hyperpolarized ^{129}Xe Pulmonary MRI and Asymptomatic Septal Defect"* and was published in CHEST journal in 2022. This case report was co-authored by Alexander M Matheson, Robin SP Cunningham, Elianna Bier, Junlan Lu, Bastiaan Driehuys, J Geoffrey Pickering, Pantelis Diamantouros, Ali Islam, J Michael Nicholson, Grace Parraga and Sarah Blissett. Robin Cunningham, Elianna Bier and Junlan Lu assisted with data analysis. Elianna Bier, Junlan Lu and Bastiaan Driehuys assisted with MRI interpretation. Ali Islam and Sarah Blissett were responsible for clinical data acquisition. Geoffrey Pickering, Pantelis Diamantouros, Ali Islam, Michael Nicholson and Sarah Blissett assisted in clinical analysis. All authors were responsible for manuscript editing. **Chapter 5** also included content from a follow-up letter to the editor entitled "*Cardiac Surgery for Atrial Septal Defect Repair: Normalization of Hyperpolarized Xenon-129 MRI RBC-to-Barrier Ratio"* and was published in CHEST journal in 2022. This letter was co-authored by Alexander M Matheson, Robin SP Cunningham, Grace Parraga, Michael WA Chu and Sarah Blissett. Robin Cunningham assisted with data analysis. Michael Chu and Sarah Blissett were

responsible for clinical data acquisition and care. Grace Parraga assisted with data analysis and interpretation. All authors were responsible for manuscript editing.

Appendix A contains an additional unpublished manuscript that is complementary to the objective and hypothesis of this thesis. The manuscript is entitled "*Pulmonary Fourier-Decomposition Magnetic Resonance Imaging and X-Ray Computed Tomography of Lung Perfusion and Pulmonary Vascular Density*" and is co-authored by Alexander M Matheson, Rachel L Eddy, David G McCormack and Grace Parraga. Rachel Eddy assisted with data analysis. David McCormack assisted with clinical interpretation of data.

Appendix B contains an additional unpublished manuscript that is in preparation for submission to the Journal of Magnetic Resonance Imaging and is complementary to the objective and hypothesis of this thesis. The manuscript is entitled "*Fully-automated Hyperpolarized Gas Magnetic Resonance Ventilation Imaging Segmentation and Registration Using Convolutional Neural Networks*" and co-authored by Alexander M Matheson, Marrissa J McIntosh, Harkiran K Kooner, Sarah Svenningsen, Rachel L Eddy, Jonathan Rayment, Aaron Fenster and Grace Parraga. Marrissa McIntosh, Harkiran Kooner and Rachel Eddy assisted in data analysis and providing training segmentations. Rachel Eddy, Jonathan Rayment, and Sarah Svenningsen provided external datasets for validation. Aaron Fenster aided study design, data analysis and technical evaluation. In future, all authors will be involved with manuscript editing and revision.

Acknowledgments

First, I want to express my thanks to the people and organizations who have contributed funding to my research during my PhD. I have received generous support from the Schulich School of Medicine and Dentistry, the Province of Ontario, the Natural Sciences and Engineering Council of Canada (NSERC) and travel funding from the Canadian Institutes of Health Research. I would also like to express my deep appreciation for the dozens of participants I have had the pleasure to meet during study visits. While the data obtained during visits was what made this PhD, the stories and insight I gained from speaking to people during visits was equally important.

I would like to thank my supervisor, Dr. Grace Parraga for her supervision and mentorship over the last five years. While I don't have the space to mention all the lessons I have learned, thank you for teaching me to always say yes to opportunities, to set my goals high and to fight for what I've earned. Thank you for pushing me to achieve when I needed it and reminding me of my success when I needed it too.

To the members of my advisory committee, Drs. Tim Scholl, Aaron Fenster, David McCormack and Alexei Ouriadov, thank you all for your wisdom and your advocacy for me both inside and outside of committee meetings. To Dr. Scholl, thank you for your support since I first applied to Western, and for providing me with teaching opportunities early in my degree. To Dr. Fenster, thank you for encouraging constant curiosity and advocating the importance of my work. To Dr. McCormack, thank you for helping me to foster clinical connections with the division of respirology and for encouraging me to take firm positions on research. To Dr. Ouriadov, thank you for your invaluable technical assistance without which this thesis wouldn't have been possible. I was also fortunate for wonderful external collaborators that

helped make this thesis possible including Dr. Sean Fain, Dr. Andrew Hahn, and Dr. Bastiaan Driehuys.

The members of the Parraga lab and Robarts Research Institute were instrumental in my graduate education. To Dave, thank you for your friendly ribbing and for helping make patient visits both fun and professional. To Danielle, thank you for advocating for patients and our laughter-filled lunch meetings. To Angela, thank you for the care you demonstrate to everyone around you, and for indulging my prolific sweet tooth. To Tamas, thank you for making my life easier through your organized ways. To Ivailo, thank you for always being cheerful and a source of great conversation. To Rachel, thank you for being a phenomenal senior student with all your mentorship and encouragement in reclassifying to a PhD. Thank you for being a great conference travel buddy and for all the cackles over my terrible jokes. To Andrew, thank you for your guidance in my first year and fostering a sense of calm in the lab. To Cathy, Andrea and Jonathan, who started alongside me from the beginning of the lab – thank you for making my start in research memorable and collaborative. To the other lab members who made it through the pandemic with me, thanks for our outdoor distanced snack breaks and keeping each other sane. To Marrissa, thank you for being a helpful critic and a steadfast friend. To Maks, thank you for being a great person to work alongside and for entertaining my long-winded end-of-day discussions. To Kiran, thank you for keeping the lab lively and full of laughs, even if my accents don't entertain you. To Paulina, thank you for your infectious encouragement and for your hard work in lab outreach. To Alexander, thank you for helping craft a legacy of Alex-cellence in research in the lab, and pickup up where I've left off. To Hana, thank you for being an invaluable portal to the world of medicine and for teaching me Persian words. And to all the undergraduate students I worked with during my time in the lab,

thank you for putting up with my jokes and keeping me up to date on the latest slang. And thank you to the students and staff I met at Robarts who made my education comprehensive: Nathan, Claire, Tiana, Miriam, Olivia, Trevor, Lindsey and Paco.

This thesis would not have been possible without the support of my friends and family, throughout the pandemic. To my former UofC residence friends, especially team Cascade, I have been so fortunate to have friendships that have lasted a decade. Thank you for setting a foundation for me that I am still using today. To Mike and Syler, thank you for not taking me seriously and for being the break I needed over this degree. To Sepideh thank you for your care, your thoughtfulness, your intellect and for making my days brighter. And to my family, thank you for your constant support after these many, many years of school. To my grandmother, thank you for your never-flinching belief in me. To my father, thank you for being steady and level-headed throughout my life, and for always being there when I need a call. Finally, to my mother, who taught me physics all those years ago, thank you for making me who I am today.

Table of Contents

Abstract ... **ii**

Summary for Lay Audience ... **iv**

Co-Authorship Statement ... **v**

Acknowledgments ... **ix**

List of Tables ... **xviii**

List of Figures ... **xix**

List of Appendices ... **xxii**

List of Abbreviations ... **xxiii**

CHAPTER 1 ... **1**

1 INTRODUCTION ... **1**

1.1 Motivation and Rationale ... **1**

1.2 Structure and Function of the Lung ... **4**

1.2.1 Airways ... 5

1.2.2 Alveoli ... 7

1.2.3 Vasculature ... 7

1.2.4 The Cardiopulmonary Circuit ... 8

1.2.5 Ventilation ... 9

1.2.6 Perfusion ... 9

1.2.7 Gas Diffusion ... 10

1.3 Pathophysiology ... **11**

1.3.1 Long-COVID ... 11

1.3.2 Atrial Septal Defects ... 12

1.3.3 Pulmonary Vascular Pruning ... 13

1.4 Clinical Measures of Lung Disease ... **15**

1.4.1 Spirometry ... 15

1.4.2 Plethysmography ... 16

1.4.3 Diffusing Capacity of the Lung for Carbon Monoxide 17
1.4.4 Complete Blood Count 19
1.4.5 Oxygen Saturation 19
1.4.6 Six Minute Walk Test 20
1.4.7 Patient Questionnaires 21

1.5 Imaging Pulmonary Structure and Function 21
1.5.1 Planar Chest X-ray 22
1.5.2 X-ray Computed Tomography 24
1.5.3 Proton Magnetic Resonance Imaging 28
1.5.4 Echocardiography 30
1.5.5 CT Pulmonary Angiogram and CT Perfusion 32
1.5.6 Ventilation Perfusion SPECT 34

1.6 ^{129}Xe Magnetic Resonance Imaging 35
1.6.1 Hyperpolarization 36
1.6.2 ^{129}Xe Magnetic Resonance Spectroscopy 37
1.6.3 ^{129}Xe Ventilation Imaging 40
1.6.4 ^{129}Xe Gas-Exchange Imaging 42

1.7 Thesis Hypotheses and Objectives 45

1.8 References 48

CHAPTER 2 62

2 A LINEAR SYSTEMS DESCRIPTION OF MULTI-COMPARTMENT PULMONARY ^{129}XE MAGNETIC RESONANCE IMAGING METHODS 62

2.1 Introduction 62

2.2 Methods 63
2.2.1 Image Acquisition 63
2.2.2 Linear Systems Analysis 64

2.3 Results 66
2.3.1 RF Excitation 66
2.3.2 Line Broadening 67
2.3.3 Gradient Encoding 69

2.3.4 Free-induction Decay Acquisition and Demodulation 69
2.3.5 Non-uniform Fast Fourier Transform 73
2.3.6 Post-processing Corrections 74
2.4 New or Breakthrough Work 75
2.5 Discussion and Conclusion 75
2.6 References 77
CHAPTER 3 79
3 PERSISTENT ^{129}XE MRI PULMONARY AND CT VASCULAR ABNORMALITIES IN SYMPTOMATIC INDIVIDUALS WITH POST-ACUTE COVID-19 SYNDROME 79
3.1 Introduction 79
3.2 Materials and Methods 81
3.2.1 Study Participants 81
3.2.2 Study Design 82
3.2.3 Pulmonary Function Tests 82
3.2.4 ^{129}Xe MRI 83
3.2.5 Thoracic CT 83
3.2.6 Statistical Analysis 84
3.3 Results 84
3.3.1 Participant Characteristics 84
3.3.2 Qualitative MRI and CT Findings 87
3.3.3 Differences Between Never- and Ever-hospitalized Participants 88
3.3.4 Relationships between Imaging Measurements, Symptoms, and Exercise Limitation 90
3.4 Discussion 91
3.5 References 99
3.6 Supplemental Material 103
3.6.1 Methods 103
3.6.2 REFERENCES 105
CHAPTER 4 110

4 LONGITUDINAL FOLLOW-UP OF POST-ACUTE COVID-19 SYNDROME: DL_{CO}, QUALITY-OF-LIFE AND MRI PULMONARY GAS-EXCHANGE ABNORMALITIES 110

4.1 Introduction 110

4.2 Methods 111

4.3 Results 112

4.4 Discussion 117

4.5 References 119

4.6 Supplemental Material 120

4.6.1 Material and Methods 120

4.6.2 Supplementary Tables 123

4.6.3 Supplemental Figures 125

4.6.4 References 126

CHAPTER 5 128

5 HYPERPOLARIZED ^{129}XE PULMONARY MRI AND ASYMPTOMATIC ATRIAL SEPTAL DEFECT 128

5.1 Introduction 128

5.2 Case Report 128

5.3 Discussion 132

5.4 Follow-up: POST-CARDIAC SURGERY ATRIAL SEPTAL DEFECT REPAIR: NORMALIZATION OF HYPERPOLARIZED ^{129}XE MRI RBC-TO-BARRIER RATIO 133

5.5 References 136

CHAPTER 6 138

6 CONCLUSIONS AND FUTURE DIRECTIONS 138

6.1 Overview and Research Questions 138

6.2 Summary and Conclusions 140

6.3 Limitations 143

6.3.1 Study Specific Limitations 143

6.3.2 General Limitations 146

6.4 Future Directions 148

6.4.1 Physiologic Variatiability of ^{129}Xe MRI Gas-Exchange Measurements 148

6.4.2 Gas-exchange in diverse pulmonary diseases 150

6.4.3 Biomechanical Modelling of Cardiogenic Oscillations 152

6.5 Significance and Impact 155

6.6 References 157

A PULMONARY FOURIER-DECOMPOSITION MAGNETIC RESONANCE IMAGING AND X-RAY COMPUTED TOMOGRAPHY OF LUNG PERFUSION AND PULMONARY VASCULAR DENSITY 162

A.1 Introduction 162

A.2 Materials and Methods 164

A.2.1 Study Participants 164

A.2.2 Pulmonary Function Tests 164

A.2.3 ^{1}H MRI 165

A.2.4 Hyperpolarized Gas MRI 166

A.2.5 CT 166

A.2.6 Image Analysis 167

A.2.7 Statistics 168

A.3 Results 169

A.4 Discussion 176

A.5 References 182

B FULLY-AUTOMATED HYPERPOLARIZED GAS MAGNETIC RESONANCE VENTILATION IMAGING SEGMENTATION AND REGISTRATION USING CONVOLUTIONAL NEURAL NETWORKS 186

B.1 Introduction 186

B.2 Materials and Methods 188

B.2.1 Study Participants 188

B.2.2 Pulmonary Function Tests 189

B.2.3 MRI 190
B.2.4 Data Processing, Annotation and Generation 190
B.2.5 Pipeline and Network Design 191
B.2.6 Training, Validation and Testing 196
B.2.7 External Validation 196
B.2.8 Statistical Analysis 197

B.3 Results 198
B.3.1 Participant Demographics 198
B.3.2 Model Training and Network Parameters 198
B.3.3 Deep Learning Registration 199
B.3.4 Deep Learning Segmentation 202
B.3.5 Inter-method Correlation and Agreement 204
B.3.6 External Validation 205

B.4 Discussion 206

B.5 Conclusions 210

B.6 References 212

List of Tables

Table 3-1 Participant demographics 85
Table 3-2 Imaging measurements 88
Table 3-3 Participant symptoms 103
Table 3-4 Medications at research visit summary 108
Table 3-5 CT findings 108
Table 3-6 Relationships between pulmonary function tests, imaging and quality of life measurements 109
Table 4-1 Participant demographics 123
Table 4-2 Participant medications 124
Table 6-1 Multivariable model for RBC:membrane in healthy participants 150
Table A-1 Participant demographics and pulmonary function measurements. 171
Table A-2 CT and MR Imaging measurements 171
Table B-1 Participant demographics, pulmonary function tests and imaging measurements. 198
Table B-2 Performance of segmentation and registration neural networks on testing data 201

List of Figures

Figure 1-1 Self-reported long-COVID cases in the United Kingdom. 2
Figure 1-2 Diagram of the airway tree and alveolus..... 6
Figure 1-3 The cardiopulmonary circuit 8
Figure 1-4 Blood flow in the heart in the presence of an atrial septal defect. 12
Figure 1-5 pulmonary vascular pruning observed in the vessel tree..... 14
Figure 1-6 Spirometry curves as measured by spirometer..... 15
Figure 1-7 predicted DL_{CO} values for a single healthy male 18
Figure 1-8 Chest radiographs of a healthy individual and an individual with COVID-19 pneumonia..... 24
Figure 1-9 CT images in healthy and diseased lungs..... 28
Figure 1-10 Ultra-short echo-time MRI in a person with COVID-19 pneumonia, compared to CT 30
Figure 1-11 Echocardiogram in the four-chamber plane acquired near the apex..... 31
Figure 1-12 CT pulmonary angiogram in a patient with COVID-19 pneumonia..... 33
Figure 1-13 SPECT tomographic coronal, sagittal and axial images of participants with COVID-19 infection. 35
Figure 1-14 Schematic diagram of polarizer apparatus 37
Figure 1-15 ^{129}Xe magnetic resonance spectrum in a healthy individual 38
Figure 1-16 ^{129}Xe dynamic spectroscopy acquired in a healthy participant 40
Figure 1-17 ^{129}Xe MRI static ventilation images..... 42
Figure 1-18 Multi-compartment ^{129}Xe MR images 44
Figure 2-1 Pulse sequence diagram of MR imaging sequence (not to scale). 64
Figure 2-2 The effect of selective RF pulses on three compartments of xenon in vivo. 66
Figure 2-3 Signal decay over time due to magnetic relaxation..... 70
Figure 2-4 Sampling of the FID performed by analog-to-digital converter (ADC). 71
Figure 2-5 Discrete Fourier transformation (DFT) 72
Figure 2-6 Spatial resampling from a radial to a Cartesian coordinate system performed during non-uniform fast Fourier transform (NUFFT).. 74

Figure 3-1 CONSORT Flow Diagram. 84
Figure 3-2 ^{129}Xe gas-transfer MRI and CT pulmonary vascular trees in never-COVID and ever-COVID participants. 87
Figure 3-3 ^{129}Xe spectroscopy measurements for controls, never-hospitalized and ever-hospitalized participants with PACS. 89
Figure 3-4 ^{129}Xe MR Spectroscopy measurement relationships with pulmonary function and exercise measurements in participants with PACS 90
Figure 3-5 Proposed Mechanisms explaining relationships for ^{129}Xe MRI RBC AUC 95
Figure 3-6 Gas-exchange measurements in never-COVID and PACS participants at varying imaging dates post-infection. 106
Figure 3-7 Evidence of pulmonary vascular abnormalities in participants with PACS. 107
Figure 4-1 Clinical, quality-of-life and imaging measurements at baseline (7±4 months since PCR test) and follow-up (14±4 months since PCR test). 113
Figure 4-2 ^{129}Xe MRI and co-registered pulmonary vascular tree CT at baseline and follow-up. 114
Figure 4-3 Correlations between DL_{CO} and ^{129}Xe MRI measurements. 116
Figure 4-4 ^{129}Xe gas-exchange and ventilation MRI in two participants with PACS 125
Figure 4-5 Correlations between changes in SGRQ score and clinical measurements. 125
Figure 5-1 Initial findings using MRI and pulmonary function fests. 129
Figure 5-2 Cardiac imaging and proposed models explaining MRI result. 130
Figure 5-3 Pre- (blue) and Post- (red) surgery ^{129}Xe MRI Spectroscopy. 135
Figure 6-1 Gas-exchange measurements in healthy participants 150
Figure 6-2 Cardiogenic oscillations in three compartments 154
Figure A-1 Consort diagram for the participants analyzed using FDMRI. 169
Figure A-2 Pulsatile blood flow artifact present in ^{1}H MRI. 170
Figure A-3 FDMRI ventilation (blue) and perfusion (magenta) maps, CT attenuation<-950HU (yellow) and CT-segmented vessel trees for representative participants with COPD. 173
Figure A-4 Relationship of FDMRI QDP with pulmonary imaging measurements. 174

Figure A-5 FDMRI QDP relationships with pulmonary function, SGRQ and 6MWT measurements. 175
Figure A-6 Comparison of FDMR and ^{129}Xe MR images 179
Figure B-1 Ventilation defect percent semi-automated and fully-automated CNN methods. 192
Figure B-2 Demonstration of neural-net registration compared to ground truth registration. 199
Figure B-3 Performance of registration neural network on affine degrees of freedom. 200
Figure B-4 Segmentation CNN output. 202
Figure B-5 Comparison between semi-automated ventilation measurements and fully-automated CNN ventilation measurements. 204
Figure B-6 Performance of neural networks in external data sets. 205

List of Appendices

Appendix A – FDMRI Unpublished Work 162
Appendix B – Neural Networks Unpublished Work 186
Appendix C – Permission for Reproduction of Scientific Articles 217
Appendix D – Health Science Research Ethics Board Approval Notices 227
Appendix E - Curriculum Vitae 238

List of Abbreviations

^{129}Xe	Xenon-129
^{3}He	Helium-3
6MWD	Six Minute Walk Distance
6MWT	Six Minute Walk Test
ACE	Angiotensin-converting Enzyme
ADC	Analog to Digital Converter
ANOVA	Analysis of Variance
ASD	Atrial Septal Defect
a.u.	Arbitrary Unit
AUC	Area Under the Curve
BD	Bronchodilator
bSSFP	Balanced Steady State Free Precession
BMI	Body Mass Index
BPD	Bronchopulmonary Dysplasia
BV_5	Blood Volume in Vessels with Cross-sectional Area < $5mm^2$
$BV_{5\text{-}10}$	Blood Volume in Vessels with Cross-sectional Area ≥ $5mm^2$ and < $10mm^2$
BV_{10}	Blood Volume in Vessels with Cross-sectional Area ≥ $10mm^2$
BW	Bandwidth
C_A	Arterial oxygen concentration
CAT	COPD Assessment Test
CBC	Complete Blood Count
CCE	Categorical Cross-Entropy
CDC	Centers for Disease Control and Prevention
CI	Confidence Interval
CNN	Convolutional Neural Network
COPD	Chronic Obstructive Pulmonary Disease
COPDGene	Genetic Study of COPD Epidemiology
COVID-19	Coronavirus Disease 2019
CT	X-ray Computed Tomography
CTPA	Computed Tomography Pulmonary Angiography
C_V	Venous Oxygen Concentration
DFT	Discrete Fourier Transform
DL_{CO}	Diffusing Capacity of the Lung for Carbon Monoxide
DSC	Dice Similarity Coefficient
ERC	Erythrocyte Count
FDMRI	Fourier Decomposition Magnetic Resonance Imaging
FeNO	Fractional Exhaled Nitric Oxide
FEV_1	Forced Expiratory Volume in 1 Second
FFT	Fast Fourier Transform
FGRE	Fast Gradient Recalled Echo
FID	Free Induction Decay
FOV	Field of View
FRC	Functional Residual Capacity
FVC	Forced Vital Capacity
gDSC	Generalized Dice Similarity Coefficient
GOLD	Global Initiative for Chronic Lung Disease
GRE	Gradient Recalled Echo
Hb	Hemoglobin

HCT	Hematocrit
HU	Hounsfield Units
ICS	Inhaled Corticosteroids
ICU	Intensive Care Unit
IDEAL	Iterative Decomposition of Water and Fat with Echo Asymmetry and Least-squares Estimation
IPAQ	International Physical Activity Questionnaire
IVC	Inferior Vena Cava
LABA	Long-acting Beta-agonist
LLN	Lower Limit of Normal
MAE	Mean Absolute Error
mBDS	Modified Borg Dyspnea Scale
MCHC	Mean Corpuscular Hemoglobin Concentration
MCID	Minimum Clinically Important Difference
MCV	Mean Corpuscular Volume
MET	Metabolic Equivalent of Task
mMRC	Modified Medical Research Council Dyspnea Scale
MRI	Magnetic Resonance Imaging
MRS	Magnetic Resonance Spectroscopy
NUFFT	Non-uniform Fast Fourier Transform
PA:A	Pulmonary Artery to Aorta Ratio
PACS	Post-acute COVID-19 Syndrome
PCFS	Post-COVID Functional Scale
PCR	Polymerase Chain Reaction
PFT	Pulmonary Function Test
PREFUL	Phase Resolved Functional Lung Imaging
PV_1	Volume of Vessels < 1 Voxel-radius
QDP	Perfusion Defect Percent
QoL	Quality-of-Life
RA_{950}	Relative Lung Area with CT Attenuation <-950HU
RBC	Red-blood-cell
ReLU	Rectified Linear Unit
RF	Radio Frequency
RT-PCR	Reverse Transcription Polymerase Chain Reaction
RV	Residual Volume
SABA	Short-acting Beta-agonists
SaO_2	Oxygen Saturation of Arterial Blood
SARS-CoV-2	Severe Acute Respiratory Syndrome Coronavirus 2
SEOP	Spin Exchange Optical Pumping
SGRQ	St. George's Respiratory Questionnaire
SPECT	Single Photon Emission Computed Tomography
SpO_2	Oxygen Saturation of Peripheral Blood
SSIM	Structural Similarity Index
TBV	Total Blood Volume
TE	Echo Time
TE_{90}	Echo Time Needed for a 90° Phase Difference
TINCan	Thoracic Imaging Nework of Canada Study
TLC	Total Lung Capacity
TLV	Total Lung Volume
TP	Tissue/Plasma
TR	Repetition Time

UTE	Ultra-short Echo Time
VDP	Ventilation Defect Percent
VDV	Ventilation Defect Volume
VO_2	Oxygen consumption
VQ	Ventilation-Perfusion
VT	Tidal Volume
WHO	World Health Organization

CHAPTER 1

1 INTRODUCTION

The lung is responsible for exchanging gases in the bloodstream to supply the body with oxygen, however disease can alter the alveolar membrane and capillary networks central to gas-exchange. In this thesis, novel magnetic resonance imaging (MRI) measurements of gas-exchange were performed to investigate mechanisms driving abnormal gas-exchange in long-COVID, a case of atrial septal defect and in preliminary investigations in asthma.

1.1 Motivation and Rationale

Chronic pulmonary diseases impact gas-exchange through airway diseases such as asthma and chronic obstructive pulmonary disease (COPD), parenchymal diseases such as idiopathic pulmonary fibrosis, and vascular diseases such as pulmonary hypertension. Chronic respiratory disease affects approximately 7% of people worldwide (544.9 million in 2017) and prevalence has increased 40% since 1990.[2] 3.9 million deaths were caused by chronic respiratory disease in 2017 alone, accounting for 7% of all deaths worldwide.[2] Importantly, these data were acquired prior to the dramatic change in lifestyle and emergence of both acute and chronic illness tied to the recent global pandemic which has likely accelerated this trend.

Coronavirus disease 2019 (COVID-19) was a novel infection that emerged in December 2019 in Wuhan, China and rapidly developed into a global pandemic. Estimates suggest that approximately 150 million infections occurred in the United States by October 2021[3] and that 4.4 million infections occurred in Canada by December 2022.[4] Individuals infected with COVID-19 have reported symptoms that persist long after infections have ended, which has been referred to as post-acute COVID-19 syndrome (PACS),[5] post-acute

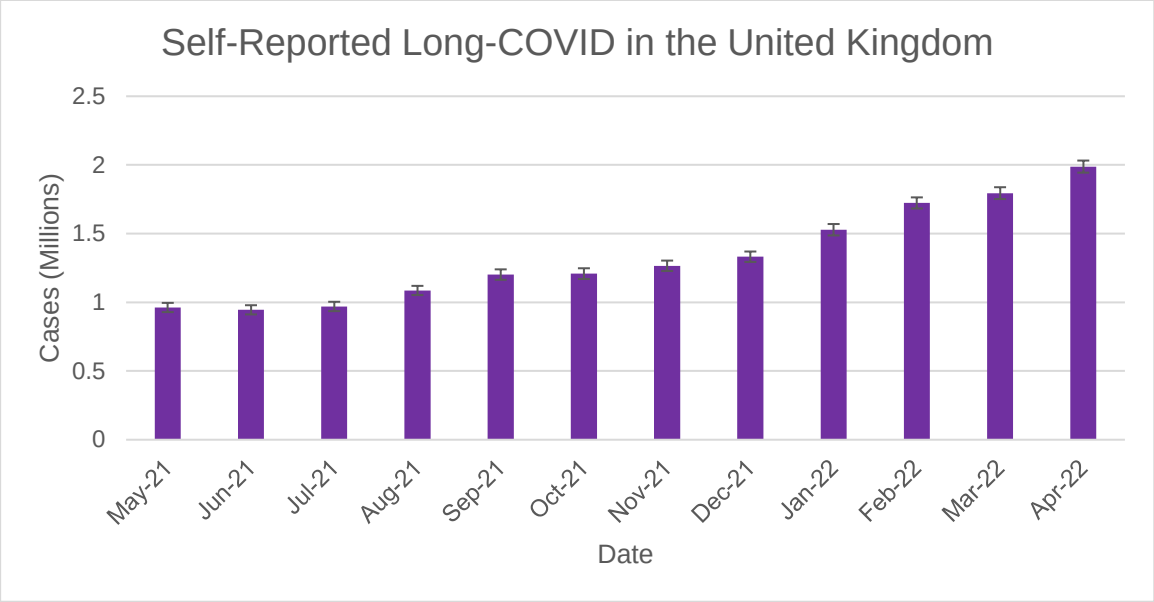

Figure 1-1 Self-reported long-COVID cases in the United Kingdom.
Figure adapted from data from the United Kingdom Office for National Statistics.[1]

sequelae of COVID-19[6] or more colloquially as "long-COVID." These different names include different definitions for the onset of long-COVID, between 4-12 weeks post infection.[5,7] The prevalence of long-COVID is difficult to ascertain, and studies have reported widely different results ranging from 6% to 81% prevalence among infected[8,9] however global meta-analyses report averages between 6% and 43%.[8,10] As COVID has become endemic, these numbers continue to rise. For instance, self-reported long-COVID numbers have doubled in the UK between April 2021 and April 2022[1] as shown in **Figure 1-1**. One estimate places the number of worldwide long-COVID cases at 65 million.[11]

As the population ages and COVID-19 becomes endemic, means of evaluating treatment and better understanding the mechanisms that drive disease progression will be important. Pulmonary function testing is currently used to diagnose diseases, monitor their progression, and evaluate their treatment. The most used pulmonary function test is spirometry, which measures flow and air volume at the mouth and reports values such as

the forced expiratory volume in one second (FEV_1). Gas-exchange abnormalities can be evaluated using the diffusing capacity of the lung for carbon monoxide (DL_{CO}) which measures the amount of carbon monoxide (as a surrogate for oxygen) that is absorbed in a breath-hold. These measurements are both acquired at the mouth and fail to consider the spatial distribution of heterogeneous disease in the lung.

Hyperpolarized gas magnetic resonance imaging (MRI) uses inhaled helium-3 or xenon-129 (^{129}Xe) gas to measure the distribution of gas in the lung. Ventilation can then be deduced by measuring the area of the lung with ^{129}Xe signal and pathological regions identified as having no signal. While helium originally was preferred for lung imaging, two factors have caused the field to convert to using xenon: xenon is less costly, and xenon is soluble in human tissues. This means that once inhaled, xenon can enter the bloodstream similarly to oxygen and can act as a surrogate for gas-transfer in the lung. ^{129}Xe presents a unique opportunity to measure gas transfer in the lung both by examining signal across the whole lung through spectroscopy and by constructing images showing the distribution of gas-exchange effectiveness in the lung. ^{129}Xe visualizes lung function and is complimented by x-ray computed tomography (CT) to visualize and measure lung structure. While ^{129}Xe previously focused on quantifying ventilation, there exists the possibility to probe beyond the airways to measure gas-exchange in pulmonary disease, directly at the alveolar interface.

This thesis focuses on the development and application of tools to measure gas-exchange in individuals with long-COVID and an individual with congenital heart disease, with the intention of discovering the underlying mechanisms of disease and how they relate to patient outcomes. The introductory chapter details the necessary biological, medical and

imaging physics information needed to place the research presented in **Chapters 2 to 5** in context**.** It begins with an overview of the anatomy and physiology of the lungs as well as a brief introduction to the cardiopulmonary circuit (**Chapter 1.2**). The underlying pathophysiology of long-COVID, pulmonary vascular pruning and congenital heart defects is presented next (**Chapter 1.3)**. Clinical tools to evaluate lung disease are presented (**Chapter 1.4)** to establish traditional measures of lung function and patient outcomes. Established imaging technologies are introduced (**Chapter 1.5**) followed by a detailed introduction of ^{129}Xe MR spectroscopy (MRS) and MRI (**Chapter 1.6)**. Finally, the hypotheses and objectives of this thesis will be outlined (**Chapter 1.7**). The body of the thesis will include a mathematical treatment of ^{129}Xe gas-exchange imaging (**Chapter 2**) followed by application of this technique in long-COVID cross-sectionally (**Chapter 3**) and longitudinally (**Chapter 4**). Next, a case-report of an apparently healthy volunteer with abnormal gas-exchange is presented (**Chapter 5**). The concluding chapter (**Chapter 6**) will tie together the work of the thesis and present proposed future directions for ^{129}Xe gas-exchange research along with preliminary data to motivate these proposals.

1.2 Structure and Function of the Lung

The primary purpose of the lung is gas-exchange, which maintains cell metabolism in the body by providing oxygen and removing waste carbon dioxide from the bloodstream. The lungs form part of the larger cardiopulmonary circuit along with the heart, which together oxygenate and distribute blood to the rest of the body. The lung is comprised of three sets of systems to facilitate gas-exchange: the airways, the vessels, and the alveolar membranes. The airways consist of branching passages, the bronchi and bronchioles, that terminate in airspaces called alveoli. Gas-exchange occurs in the alveolar zone where oxygen and

carbon dioxide diffuse across the alveolar membrane. The final system is the pulmonary vasculature, which originates in the right heart. Deoxygenated blood is pumped from the right heart, through the pulmonary artery and branching arterioles until it reaches the capillaries, the smallest vessels adjacent to the alveoli where gases are exchanged with the bloodstream. The capillaries are collected into pulmonary veins, which return the oxygenated blood to the left heart to pump to the rest of the body. In this section, these structures are discussed in more detail and their primary functions are examined.

1.2.1 Airways

Air is inhaled through the mouth and travels through the pharynx, larynx, and trachea to reach the airways. The trachea is ringed by cartilage to form a tube shape and splits to form two bronchi, which act as the first "generation" of airways. The first-generation forms paths to the left and right lungs which continue to branch into lobes, segments and subsegments, with each split forming a new generation of airways. **Figure 1-2** shows the 23 generations of airways; the first 16 generations are the conducting airways, which are responsible for moving air into the lungs, and the remaining seven the respiratory bronchioles lined with alveolar sacs where gas-exchange occurs. In the respiratory zone, bronchioles continue to branch with increasing numbers of alveoli until generation 23, at which point the airways terminate with more alveolar sacs. The geometric growth pattern of the airways ensures a large surface area in the conducting zone for efficient gas-exchange in the lung.

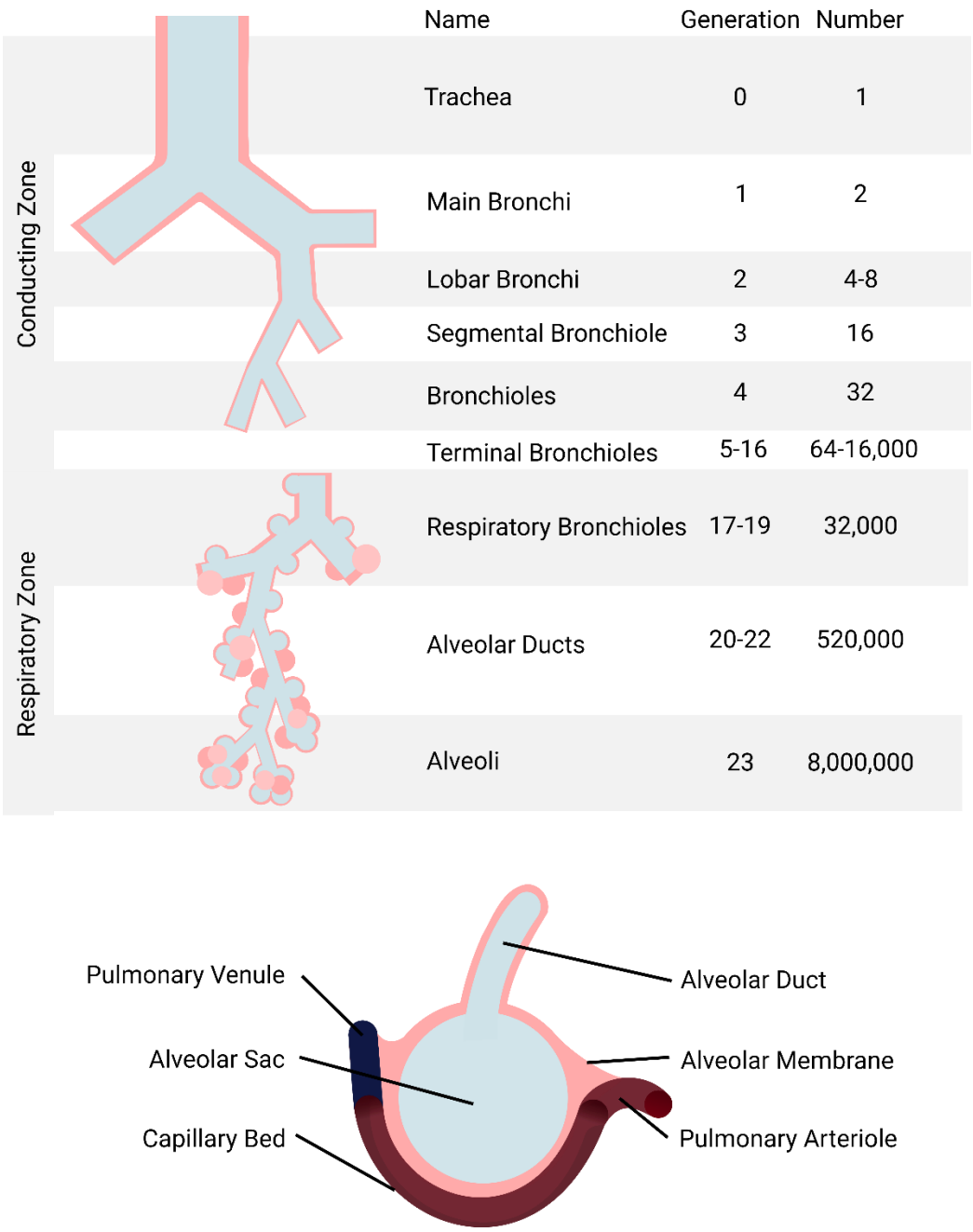

Figure 1-2 Diagram of the airway tree and alveolus.
Top: Airways branch from the trachea and continue to branch 23 further times before terminating in the alveoli. Adapted from Nunn's Applied Respiratory Physiology, 8th edition.[12] Bottom: airways terminate at an alveolus, which connects the respiratory and circulatory systems.

1.2.2 Alveoli

The alveolus is the fundamental unit of the lung where gas-exchange occurs. There are approximately 400 million individual alveoli in total, with a combined surface area of about 130m^2 for gas-exchange.[12] The alveoli are lined by a thin fluid film called surfactant; composed of phospholipids and proteins, the surfactant acts to reduce surface tension and prevent collapse of the alveolus.[13] The walls of the alveolar sacs are known as the alveolar septa, alveolar barrier, or alveolar membrane. A thin mesh of capillaries covers the alveoli, and two layers of cells, the alveolar epithelium and the capillary endothelium, separate the alveolar cavity from the bloodstream.

1.2.3 Vasculature

The pulmonary vasculature begins at the heart, branching out from the pulmonary artery and following the airways. The smallest arteries (diameter <100μm) are known as arterioles, which supply blood to the even smaller capillaries. The capillaries are narrow and approximately the width of a single red-blood-cell (7μm).[12] Pulmonary venules, analogous to the pulmonary arterioles, collect from the capillaries and then into the pulmonary veins. The pulmonary veins do not follow the airway tree, instead travelling along the septa at the margins of lung sections.

The lung has a second set of vessels known as the bronchial circulation. While the purpose of the pulmonary circulation is to oxygenate blood, the bronchial circulation is similar to the systemic circulation and provides blood to the lung tissue itself. About two-thirds of the blood flowing in the bronchial circulation drains into the pulmonary vasculature, and mixes with the oxygenated blood in the pulmonary veins.[14]

1.2.4 The Cardiopulmonary Circuit

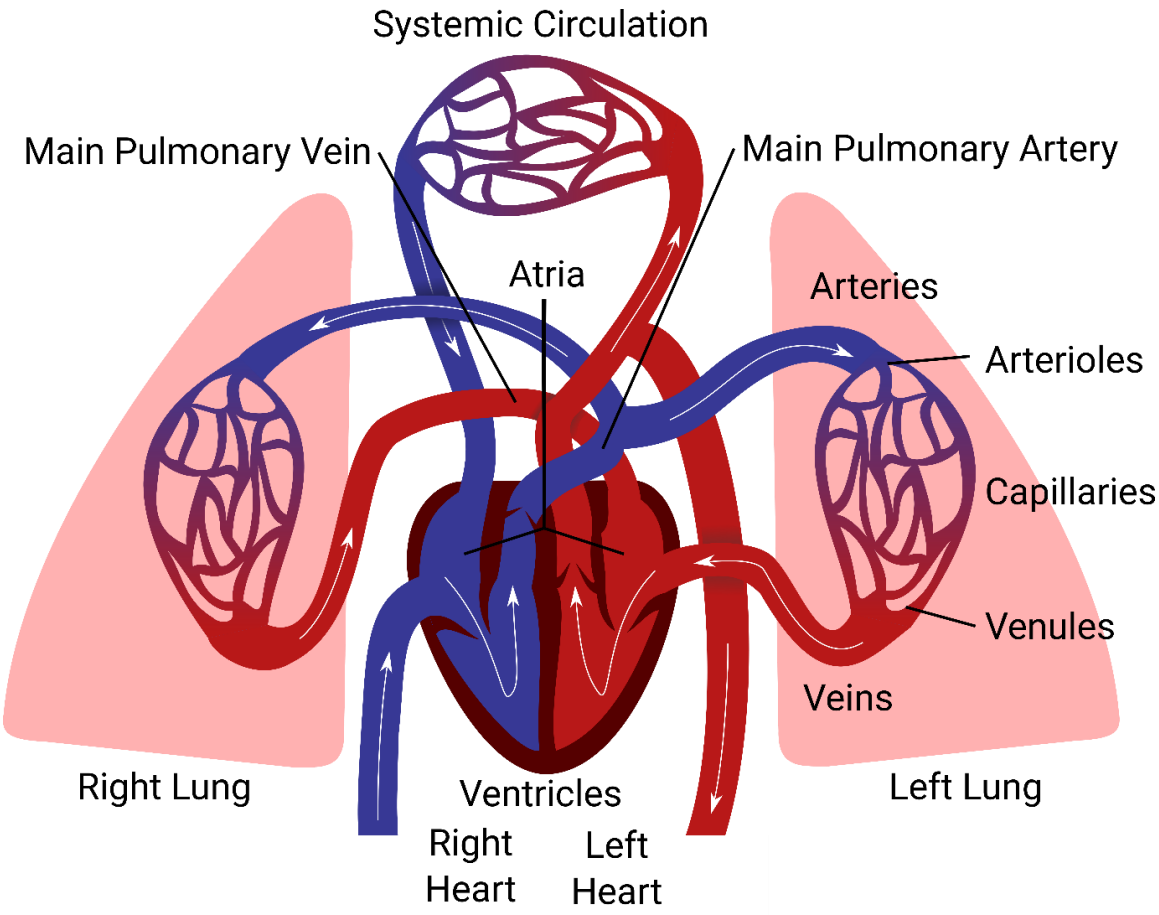

Figure 1-3 The cardiopulmonary circuit
Adapted from Tortora and Reynolds.[15]

Together, the heart and lungs form a circuit for the purposes of blood oxygenation. The heart composed of four chambers that pump blood in concert to the lungs and to the body. Blood is returned from the systemic circulation by the superior and inferior vena cava to the atrium of the right heart, drawn in during atrial diastole. The right atrium contracts, pumping blood through the tricuspid valve and into the right ventricle which contracts to pump blood through the pulmonic valve and into the pulmonary artery. Blood flows through the arteries and arterioles before travelling through capillary beds. The blood

drains into a pulmonary venule followed by a pulmonary vein, where it returns to the left heart during atrial diastole. At atrial systole, blood is pumped into the left ventricle through the mitral valve and then pumped during ventricular systole through the aortic valve to the systemic circulation.

1.2.5 Ventilation

Ventilation moves air from the environment to the alveoli through the respiratory tract and remove carbon dioxide along the same route. Pressure and volume changes in the lung are caused by muscle movement, primarily the intercostal muscles and the diaphragm. Ventilation is defined by the volume of gas moved per unit time (usually L/min) and can be calculated by measuring the tidal volume (VT) by the respiratory rate. The air volume that reaches the alveoli is known as the alveolar ventilation and undergoes gas-exchange, however some gas (150mL for an average adult) remains in the conducting airways, known as the "dead space."

1.2.6 Perfusion

Similar to ventilation, perfusion is the movement of blood in lung tissue measured as the blood flow (blood volume per unit time) per volume of tissue. Pulsatile blood flow is driven by the cardiac cycle, where muscle contractions drive blood though the pulmonary vasculature. Unlike the airways, the vessels are a complete loop, meaning there is no circulatory dead space. The Fick principle can be used to measure perfusion by comparing oxygen concentration in venous and arterial blood:

$$\dot{V}O_2 = \dot{Q}(C_a - C_v)$$

$$\dot{Q} = \frac{\dot{V}O_2}{(C_a - C_v)}$$

where VO_2 is oxygen consumption, Q is perfusion, C_a is the oxygen concentration of arterial blood, and C_v is the oxygen concentration of venous blood. These values can be measured directly through catheterization or indirectly through tracer gases.[12]

1.2.7 Gas Diffusion

Gas is exchanged between the airway and vascular systems as molecules diffuse across the alveolar membrane. Gases diffuse across pressure gradients from regions of high gas partial pressure to low gas partial pressure, causing oxygen to move from the alveoli to red-blood-cells (RBC) in the bloodstream and carbon dioxide to move from RBC to alveoli. Oxygen gas is uniformly distributed in the alveoli[12] and diffuses into the surrounding alveolar tissue. The alveolar tissue in healthy humans is only 0.5μm thick adjacent to the capillaries and is composed of the alveolar epithelium and the capillary endothelium separated by an interstitial space.[12] Contained within the capillary are RBC surrounded by blood plasma. Oxygen continues to diffuse into the RBC, where it binds to hemoglobin to form oxyhemoglobin.[16] Gas-exchange relies on body size, matched ventilation/perfusion, the thickness of the alveolar membrane and blood hemoglobin. Hemoglobin (Hb) measurements include concentration in blood, reported in g/dL, mean corpuscular volume (MCV), or the average volume of RBC reported in dL, and hematocrit, or the percentage of RBC in a volume of blood.[16,17]

1.3 Pathophysiology

Chronic lung disease is often characterized by abnormal gas-exchange, and this thesis focuses on three clinical examples of gas exchange: long-COVID, atrial septal defect (ASD) and preliminary research into asthma. Long-COVID symptoms are multi-systemic and range from broad symptoms such as fatigue and muscle pain to more specific respiratory symptoms such as dyspnea and impaired diffusing capacity in the lung.[5,18,19] Just as lung diseases can cause symptoms outside the lung, heart disease can also cause changes inside the pulmonary circuit and in anticipation of **Chapter 5** I present here a brief introduction to congenital heart defects.

1.3.1 Long-COVID

Long-COVID is a multi-organ disease with a wide variety of symptoms that persist long after the end of the infectious period of SARS-CoV-2. Pulmonary symptoms of long-COVID include fatigue, reduced exercise capacity, dyspnea, cough, hypoxia, and chest pain.[5] Surprisingly, long-COVID can develop regardless of COVID-19 infection severity.[20] Many early studies on COVID-19 follow-up focused on hospitalized individuals[9,21,22] but recent research has published on never-hospitalized cohorts as well.[23,24] Because this syndrome is tied to the recent emergence of SARS-CoV-2, the exact pathophysiology of long-COVID is unknown, although similarities to acute respiratory distress syndrome, middle eastern respiratory syndrome and SARS-CoV-1 offer clues.[5,20]

Damage from COVID-19 infection itself affects the post-COVID condition. The upper airways are the primary infection point,[25] where SARS-CoV-2 attacks angiotensin-converting enzyme 2 receptors (ACE2).[26] In some individuals, COVID progresses to

pneumonia filling large portions of the peripheral airways, causing alveolar damage. A hyperintense immune response driven by a proliferation of cytokines (a "cytokine storm") is common and may be related to COVID-19 severity.[27,28] A hypercoagulant state has also been noted, and an elevated risk of thromboembolic events persists chronically after infection.[29] How this state changes from acute infection to long-COVID is still under research, but proposed physiological mechanisms include viral damage to endothelial and epithelial cells, lingering inflammatory damage, microvascular injuries, and metabolic abnormalities.[5] Fibrotic changes in the lung are widely hypothesized[30-32] to contribute to long-COVID, as inflammatory processes can progress to fibrosis of the lung.

1.3.2 Atrial Septal Defects

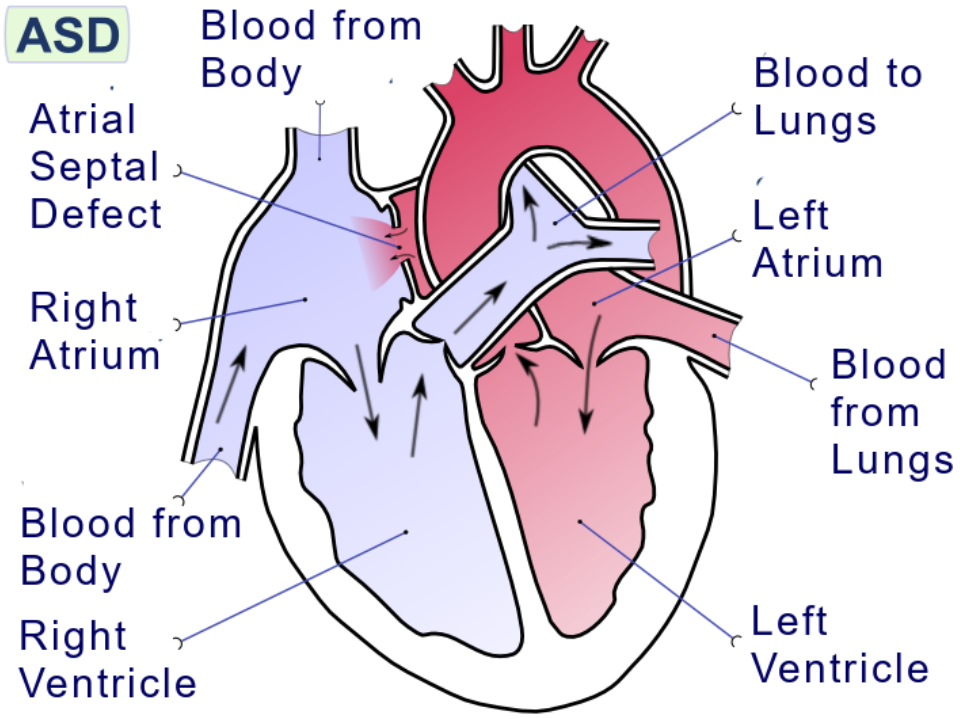

Figure 1-4 Blood flow in the heart in the presence of an atrial septal defect.
This image adapted from M Capac.[33] This illustration was published under a Creative Commons 3.0 license.

Atrial septal defects (ASD) are congenital, abnormal openings that connect the right and left atria and can lead to changes in hemodynamics and flow. There are four anatomical presentations of ASD: secundum, sinus venous, primum, and coronary sinus.[34] The most common,[34] the secundum ASD (~80% of cases), is located at the fossa ovalis, when the fetal foramen ovale does not properly close at birth.[35] A primum ASD occurs at the bottom of the fossa ovalis. A sinus ASD connects the vena cava to the left atrium, often through an opening in the superior vena cava to the pulmonary veins.[36] Finally, a coronary sinus ASD indirectly connects the atria through a hole between the coronary sinus and left atrium. An ASD does not typically present with symptoms until late into disease progression, often in adulthood,[34] at which point fatigue, dyspnea, chest pain, cyanosis and clubbed fingernails are observed.[37] ASD is characterized by shunting between the affected regions, determined by blood pressure gradients. Left-to-right shunts are more common,[34] due to the higher left atrial pressure. Other pathological changes develop due to chronic changes to flow from shunting including right atrial and ventricular dilation and pulmonary vessel remodeling. Progressive changes due to pressure can develop into Eisenmenger's syndrome, where pressures increase and shunting reverses. Pathological changes are then possible throughout the body as right-to-left shunts distribute de-oxygenated blood to the rest of the body.

1.3.3 Pulmonary Vascular Pruning

Pathophysiological changes related to gas-exchange may impact the pulmonary vessels through vascular remodeling, also known as "pruning," resulting in a loss of CT-visible vessels. **Figure 1-5** shows an example of pulmonary vascular pruning in COPD relative to a healthy volunteer. Pruning has been observed in diseases with a known cardiovascular

component like COPD,[38] pulmonary hypertension[39] and bronchiectasis[40] but also in asthma.[41] In COPD, pruning is correlated with FEV_1, measurements of exercise capacity and quality of life[38]. Bronchiectatic patients demonstrated worse vascular pruning[40] and pruning was more severe in asthma patients with worse-controlled disease.[41] Whether or not pruning represents a loss of vessels or a loss of detectability is uncertain, however interpretations for pruning include a loss of the vascular bed, vasoconstriction in response to hypoxia, or hyperinflation induced vascular compression.[42] Histologic studies in patients with COPD and pulmonary hypertension report that pruning was correlated with small pulmonary artery wall thickening.[39,43] Together, pruning in obstructive lung disease and pulmonary vascular disease suggests CT measurements of the pulmonary vasculature reflect small vessel structure and may be related to hypoxic mechanisms.

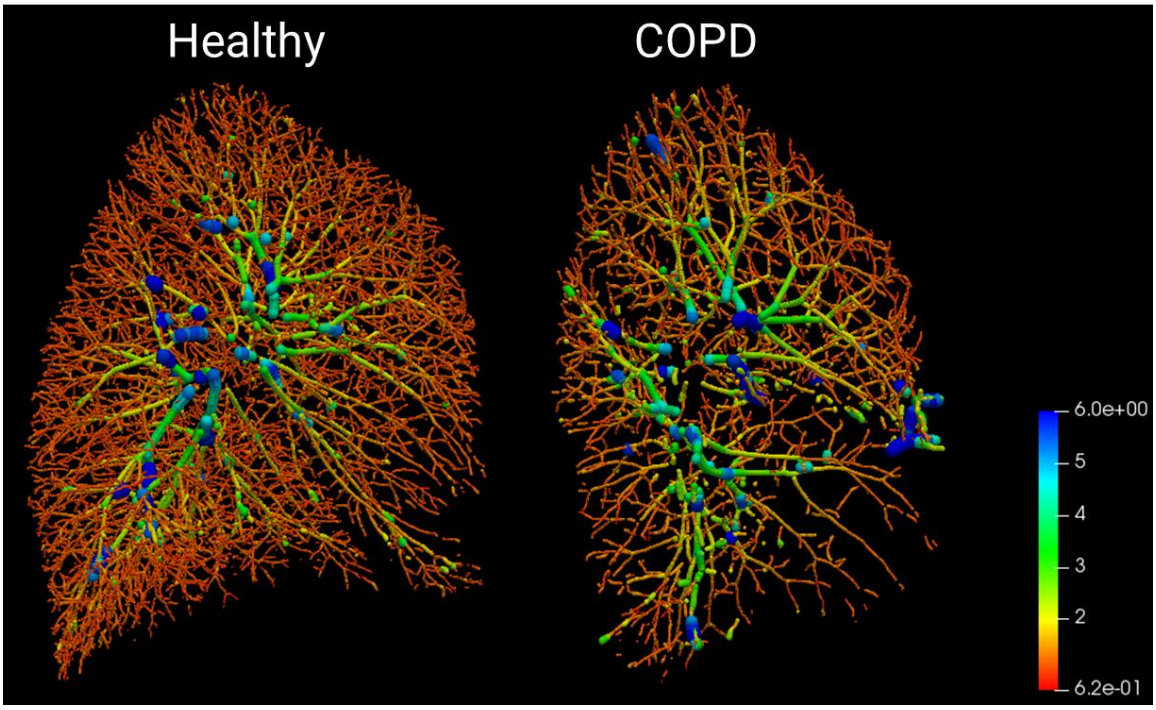

Figure 1-5 pulmonary vascular pruning observed in the vessel tree
Left: the pulmonary vascular tree in a healthy person displays many small vessels. Right: a pulmonary vascular tree in a person with COPD shows a loss of small vessels, which is often due to parenchymal destruction.

1.4 Clinical Measures of Lung Disease

Clinical measurements are used to characterize lung health and to determine disease severity, progression, and responses to treatment. Pulmonary function tests are the most common clinical measurements that use breathing maneuvers and in some cases tracer gases to determine lung airflow, lung volumes and gas transfer and include spirometry, plethysmography and DL_{CO}. Blood content and heart performance may also affect gas-exchange measurements. Finally, questionnaires are used to measure subjective patient experiences such as quality-of-life.

1.4.1 Spirometry

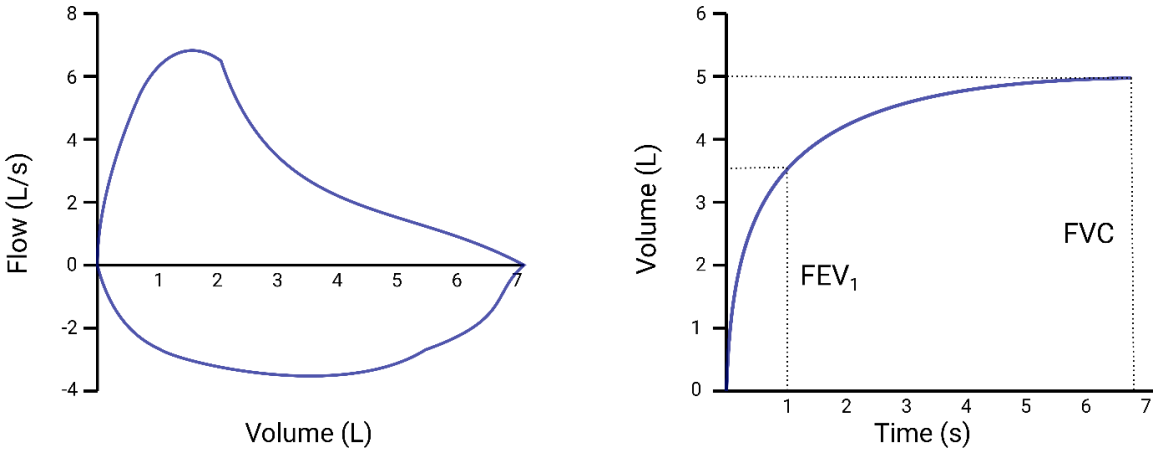

Figure 1-6 Spirometry curves as measured by spirometer
Left: flow/volume curves can be used to determine if airflow obstructions are present. Right: volume-time curves can be used to determine the FEV_1 and FVC during a forced exhalation maneuver.

Spirometry measures lung function using airflow and volume measurements obtained at the mouth using a device known as a spirometer. Participants must undergo a set of breathing maneuvers, which are coached by an administrator to ensure that lung volumes are measured from the appropriate points in the breathing cycle. Participants begin from normal, tidal breathing before completely inhaling (to total lung capacity [TLC]) followed

by forceful exhalation until the participant cannot exhale further. Measurements are recorded in time curves and flow-volume curves as shown in **Figure 1-6**, from which measurements such as FEV_1 and forced vital capacity (FVC) can be obtained and reported as percent predicted ($\%_{pred}$), using equations for a healthy population based on age, sex, height, and ethnicity. These two measurements are commonly used to classify lung disease. Flow volume curves can be used to characterize lung disease as obstructive (having a scoop shaped curve) or restrictive (having a low-volume curve).

1.4.2 Plethysmography

Plethysmography is a technique for measuring lung volumes using an enclosed chambre called a "body box." Boyle's law can be used to indirectly measure lung volumes by knowing that the product of the box air pressure and box volume is equal to the product of lung pressure and lung volume.[44] By using a sealed box, volumes can be kept constant between the participant and the box and pressure changes thus represent volume changes. A pressure transducer located at the mouth measures box pressure while a separate transducer is placed in a mouthpiece that the participant breathes through. A typical plythysmography maneuver consists of three parts: tidal breathing, panting, and full inspiration/expiration. Pressure changes during tidal breathing can be used to compute the tidal volume (VT). Next, the participant is instructed to perform a shallow pant and a shutter at the mouthpiece is closed. This prevents flow between the lungs and box; however the effort of the participant still causes their lungs to expand and contract. The volume change of the lungs can then be measured as a pressure change in the box and a pressure measurement at the mouth can measure the lung pressure. Finally, the participant performs a full inhalation and exhalation. This allows TLC to be calculated from the maximum lung

volume and RV to be calculated from the volume at full exhalation. Unlike spirometry, plethysmography maneuvers are not performed under maximum effort and participants can exhale at a comfortable pace.

1.4.3 Diffusing Capacity of the Lung for Carbon Monoxide

The effectiveness of gas transfer can be measured using DL_{CO}. Due to a strong binding affinity for hemoglobin in RBCs, CO follows the same gas-exchange path as oxygen detailed in **section 1.2.7** and can act as a tracer gas to measure the efficiency of oxygen transport. During this pulmonary function test, participants perform a full exhalation to empty the lungs to RV followed by a deep inhalation of a tracer gas mix from a mouthpiece attached to a pulmonary function test workstation. The participant then holds their breath for seven seconds to allow CO uptake and fully exhales the gas back out the mouthpiece, where a gas sample is taken after discarding gas collected from the respiratory dead space. The gas is passed through a gas chromatograph column to separate out the constituent tracer gases and measure the partial pressure of CO in the exhaled gas. Additional gases such as Neon allow CO pressures to be measured relative to the unabsorbed noble gas. DL_{CO} is reported in units of ml CO/min/kPa as well as percent predicted. Additional corrections can be performed for hemoglobin levels if blood tests are performed in participants. While DL_{CO} can describe the overall effectiveness of gas-exchange, it does not pinpoint the source of abnormalities, and a variety of factors may influence the final result including: parenchymal destruction, alveolar membrane thickening, loss of lung area, or impaired perfusion.[45] DL_{CO} is also sensitive to heart disease due to the relationship between the heart and pulmonary vasculature. Diminished DL_{CO} is also present in cases of heart disease such as left heart failure,[46] due to pulmonary vascular remodeling through

pulmonary hypertension. In addition, fluid filling of alveolar membrane and associated fibrosis of the membrane can worsen DL_{CO}.[47]

Unfortunately, DL_{CO} varies considerably and there is no consensus on which of the many prediction equations is "most correct." The European Respiratory Society suggests matching a patient population to a reference equation from a similar population, however as shown in **Figure 1-7** these reference equations produce a spread of possible values. It is therefore difficult to distinguish pathological changes from natural variability and establish clear normal thresholds.

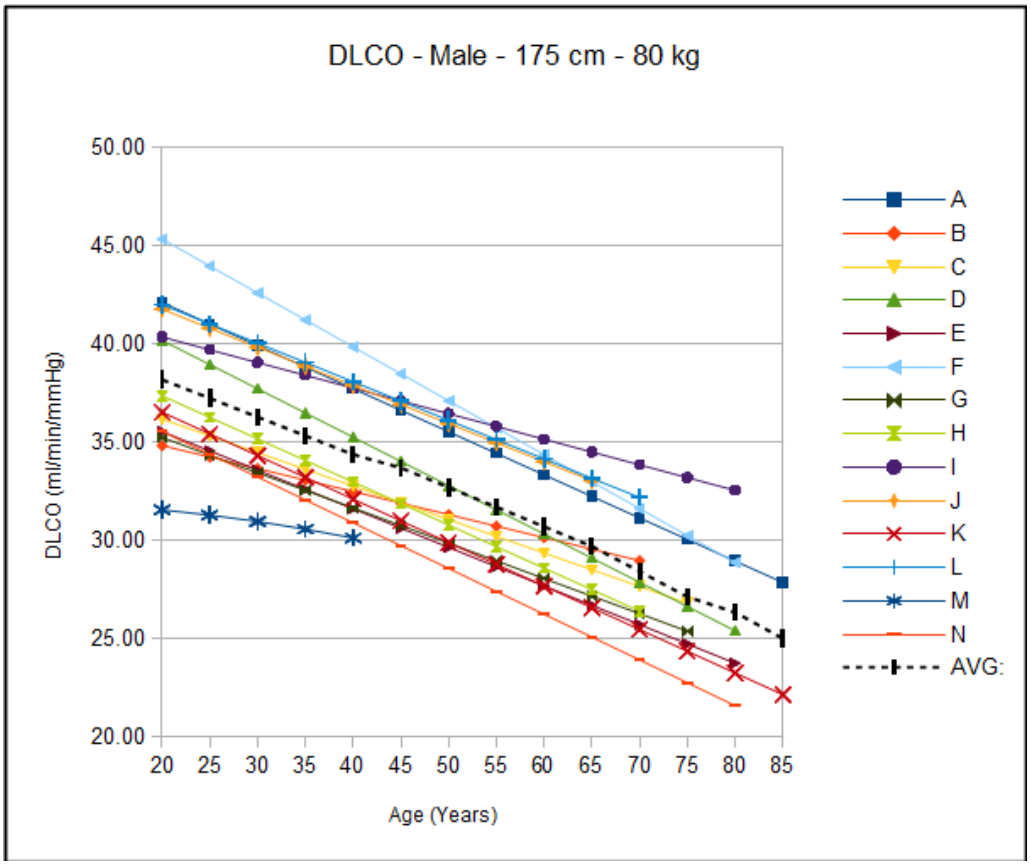

Figure 1-7 predicted DL_{CO} values for a single healthy male
Each line corresponds to a different equation for DL_{CO} over the lifespan: A,[48] B,[49] C,[50] D,[51] E,[52] F,[53] G,[54] H,[55] I,[56] J,[57] K,[58] L,[59] M,[60] N[61]. Figure reproduced from R Johnston[62] under a Creative Commons 4.0 license.

1.4.4 Complete Blood Count

A complete blood count (CBC) is a test to determine the cellular composition of blood, including RBCs, white blood cells, and platelets. Blood samples are collected by inserting a needle into a vein in the arm and draining a small volume of blood into a sample tube. Cell counts may be performed manually using a microscope or by an automated hematology analyzer. Samples are separated, diluted and lysed to obtain separate samples of RBC, white blood cells, and platelets. Automated hematology analyzers use volumetric impedance measurements to count cells. The apparatus uses two volumes of a solution connected by a small, cell-diameter inlet for single direction flow, with connected electrodes in each of the volumes forming a circuit. The separated blood samples are added to one of the volumes and the sample flows through the inlet. As cells enter the inlet, there is a momentary change in electrical impedance related to cell type and dimensions. Hematocrit, or the percentage of RBC in whole blood, can then be calculated using the RBC count and measured RBC volume relative to sample volume. Oxygenated hemoglobin (oxyhemoglobin) absorbs light at a different wavelength than deoxygenated hemoglobin (deoxyhemoglobin), so measurements of both forms can be obtained by measuring light passed through a sample to determine hemoglobin concentrations.

1.4.5 Oxygen Saturation

Oxygen saturation is a measurement to determine how much of the blood's hemoglobin is oxygenated. Measurements can be calculated from dissolved arterial oxygen (SaO_2) or by in-vivo estimation of peripheral blood saturation (SpO_2) where a sensor placed on a fingertip passes light through the tissue, including perfused capillaries in the finger. Fingertip estimations are more prone to error due to poor circulation or difficulty passing

light through a fingernail. A healthy resting-state SpO_2 is above 95% but desaturation (<95%) may occur due to gas-exchange problems in the lung or due to an imbalance between oxygen consumption and uptake during exercise.

1.4.6 Six Minute Walk Test

The six minute walk test (6MWT) is a simple measure of exercise capacity which can also act as an important predictor of future health.[63] It measures the distance travelled over six minutes while walking laps of a hard, flat, 100ft/30m track. The 6MWT is intended to reflect overall exercise health and exercise capacity during day-to-day life, so participants are able to select their own level of exertion when performing the test and are allowed to take breaks as needed, without stopping the clock. Both immediately before and after the tests, participants have oxygen saturation recorded, self-report dyspnea levels through the modified Borg Dyspnea Scale[64] and the Rating of Perceived Exertion[65] to provide further evidence of exercise impairment.[63] Despite its simplicity, the 6MWT outperforms many other measures of health and patient outcomes. The 6MWD is an accurate predictor of maximal oxygen consumption in end-stage lung disease[66] and is an independent predictor of mortality in interstitial pulmonary fibrosis[67] and COPD, outperforming spirometry.[68,69] Also, despite patients choosing the pace to walk, the test is very reproducible (intraclass correlation coefficient=0.93).[70] The primary limitation of the 6MWT is its broadness: there are many possible contributors to walking distance and it is not possible to isolate the impact of the lung on walking distance.

1.4.7 Patient Questionnaires

Some data cannot be acquired in a lab setting, either because it relates to a participant's subjective experience or because it requires knowledge of a participant's day to day activities. In these cases, patient questionnaires are used which correlate to established objective measures of patient health, accurately represent a participant's experiences outside the lab and report repeatable results. The St. George's Respiratory Questionnaire (SGRQ) was designed to measure patient quality-of-life in diseases with chronic airflow limitation.[71] It consists of 50 questions for patients to rate their agreement to statements such as "My cough or breathing is embarrassing in public." The questionnaire provides an overall health score and three sub-scores: symptoms, activity and impacts. The SGRQ correlates well with multiple other symptom scores and evaluations of psychological distress and worsens over time such that it correlates with worsening spirometry and dyspnea.[72] The International Physical Activity Questionnaire (IPAQ) was designed to meet a global need to measure poor physical activity.[73] It asks participants to report how long they spent in the last week performing certain activities such as walking, biking, sitting, or working related lifting. Scores are reported as metabolic-equivalent-of-task minutes (MET-minutes) which estimates the amount of time spent exercising during a week, with more vigorous activities having higher MET-minutes.

1.5 Imaging Pulmonary Structure and Function

The clinical tests discussed in **section 1.4** are gold-standards for diagnosing and monitoring pulmonary diseases such as asthma and COPD.[74-76] In long-COVID, however, these tests are not consistently abnormal in patients.[77,78] This may be due to the nature of COVID-19 infection – in severe cases COVID commonly manifests as heterogeneous pneumonia,[79]

however clinical tests fail to capture the regional information inherent in pulmonary disease because they only acquire measurements at the mouth. Because imaging was often used in the diagnosis of pneumonia through chest CT in people with severe COVID-19 infections,[80,81] imaging follow-up was performed early in the pandemic to monitor recovery.[82] Unfortunately, the emergence of long-COVID even in people with mild COVID-19 infections has prompted more imaging in long-COVID at the site of infection – the lung. Some imaging techniques examine the lung structure – the airways, parenchyma, vessels, etc. Other techniques examine the associated functions of these structures – ventilation, perfusion, and diffusion. This chapter examines imaging techniques used in COVID-19 and ASDs to examine structure (x-ray, CT, proton MRI, ultra-short echo time MRI and echocardiography) and function (CT pulmonary angiograph [CTPA], CT perfusion and ventilation/perfusion single photon emission computed tomography [VQ-SPECT]). ^{129}Xe gas-exchange MRI, the focus of this thesis, will be examined in more detail in **section 1.6**.

1.5.1 Planar Chest X-ray

Planar x-ray was the first radiographic technology invented and has been in use for over a century. Radiographs can probe the inside of the body using high energy photons (at the x-ray portion of the electromagnetic spectrum) that are energetic enough to pass through the body, but not so energetic that they pass through without interacting. As photons pass through the body, some are attenuated through Compton scattering, photoelectric absorption, Rayleigh scattering, and pair production, though predominantly the first two. Photons act to cast a “shadow” of regions with higher attenuation, which are displayed as

white regions on an image, such as shown in **Figure 1-8**. Unfortunately, radiation-induced ionization breaks DNA bonds and x-ray techniques should therefore be used with some caution to ensure minimal risk to patients. A typical chest x-ray has a dose of 0.05mSv[83], which can be compared to the typical annual dose in Toronto of 1.59mSv/year.[84] X-rays are emitted by a x-ray tube consisting of a cathode and anode separate by a gap, with a corresponding current and potential difference. X-ray photons pass through the body and hit a detector, which use scintillating crystal elements to convert x-ray photons to electrons which are subsequently measured. Tissues such as bone with a high mass attenuation coefficient do not permit as many photons to pass and show up as white on a radiograph. Other tissues with low mass attenuation coefficients such as air-filled lung show up as black. X-rays travel on paths that may include many tissues, and the overall attenuation of that path is the integral of attenuation along the path. This means that a single image is a projection through a body, showing structures superimposed on top of each other, which may make differentiating overlapping structures difficult. Images may be obtained in multiple planes (e.g. coronal, sagittal) to adjust for this.

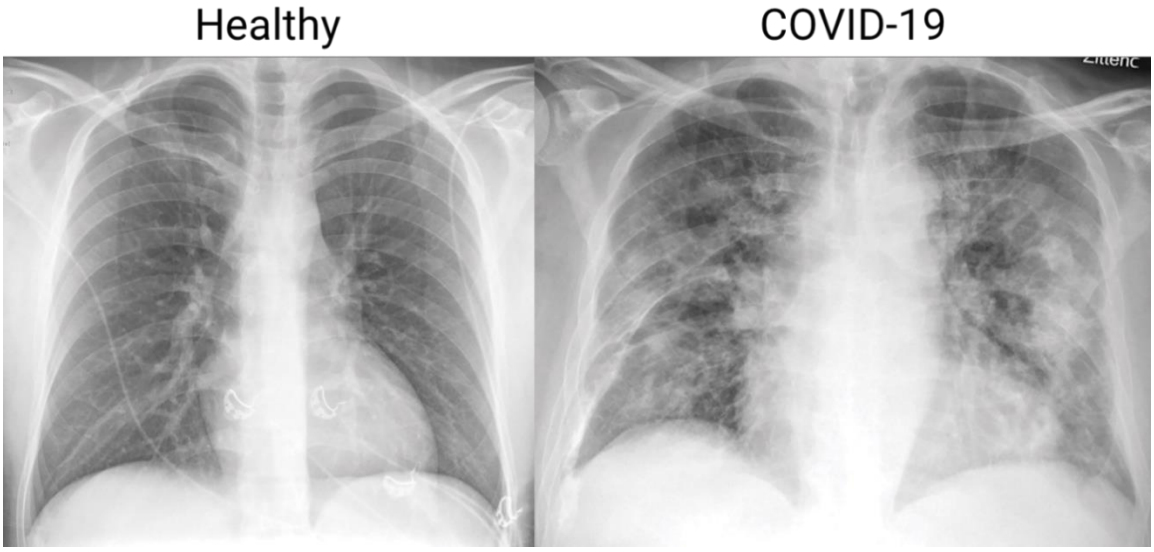

Figure 1-8 Chest radiographs of a healthy individual and an individual with COVID-19 pneumonia
Left: an image of a 30-year-old male with a negative polymerase chain reaction (PCR) test for COVID-19.
Right an image of a 74-year-old male with a positive PCR test for COVID-19. Patchy ground glass opacities are typical of COVID-19 pneumonia.
Image adapted courtesy of Murphy et al.[85] Image was published under PMC Open Access.

In cases of COVID-19 pneumonia, alveoli become filled with trapped fluid that form patches of higher attenuation opacities. Abnormalities were commonly present in the periphery (40-90% of cases with abnormalities) and in the lower lungs (50-7-% of cases with abnormalities).[86,87] Chest x-ray was common for diagnostic purposes during the initial waves of the pandemic due to limited access to molecular testing, however not all individuals positive for COVID-19 demonstrated abnormalities.[86,87]

1.5.2 X-ray Computed Tomography

X-ray computed tomography (CT) relies on the same principle as planar x-ray: the detection of attenuated x-rays to determine internal body structures. CT, however, obtains multiple images at different angles and then uses algorithms (computed) to reconstruct spatial information and make a three-dimensional representation (tomography) of the

attenuating tissues of the body. A CT scanner is comprised of a similar x-ray source and detector as a planar x-ray; however, these components are mounted on a spinning gantry that rotates 360° around the region of interest. Patients are placed on an adjustable table that moves the patient along the axis of rotation of the gantry. Data from the CT are stored as a sinogram representing the x-ray attenuation along the width of the detector on one axis, with the angle of rotation along the other axis. A sinogram can be converted to a three-dimensional volume representation by three methods: filtered back projection, radon transform, or iterative reconstruction. As the CT acquired in **Chapter 3** used back projection, the other two methods will not be discussed. Back projection is simply projecting the attenuation values for a given acquisition angle over the reconstruction space. By adding the projections at each angle, the original attenuation can be recovered, but with substantial blurring. By applying a high-pass filter prior to back projection, blurring can be reduced. A reconstructed CT consists of voxels representing the spatial distribution of tissue with each voxel intensity reported in Hounsfield Units (HU), which relate the radiodensity of tissue compared to two reference substances: air (-1000 HU) and water (0 HU).

As an extension of x-ray radiography, CT also subjects patients to ionizing radiation. Compared to x-ray doses of 0.05mSv, conventional clinical chest CT varies substantially between clinics from 1.7mSv to 24mSv with a median dose of 8.2mSv.[88], all greater than an average background dose. In research contexts, technical advances are helping to develop low-dose and ultra-low dose strategies with some scans achieved with <0.8mSv[89] of radiation at the cost of image quality. Studies in younger populations are difficult due to increased risk of developing cancer over a patient's lifetime. Studies on treatment effects

and disease progression also require careful consideration of the benefits of acquiring multiple images versus the risk of multiple radiation doses.

CT imaging is a structural technique with resolution typically in the sub-millimeter range. This permits clear visualization of the gross structure of the lung (lobes, diaphragm, major airways, etc.) as well as small structures (fissures, small airways, small vessels). For the detection of airways, a CT scan with a common resolution of 0.625mm can detect an airway of diameter 1.875mm or greater (equivalent to two wall voxels and one lumen voxel), and vessels of 0.625mm or greater. CT airway and vessel segmentations can be performed with commercial software such as VIDAVision (VIDA Diagnostics, Coralville, IA) or open-source tools like Chest Imaging Platform (Brigham and Women's Hospital, Boston, MA). Vessels can be detected by filtering for tube-like structures using algorithms such as the Frangi vesselness filter.[90] Discrete convolution kernels based on second-order derivatives (Hessians) can create higher-dimension maps of curvature at different scales and the eigenvalues of these maps can identify regions with high curvature in two dimensions and none in the third (tubes). Advanced particle systems detect vessels by travelling along gradients in Hessian maps and minimizing their energy.[91] Information about vessel structure can be derived from vascular tree segmentations, including the total blood volume (TBV) segmented and volumes in different caliber vessels including the blood volume in vessels with cross-sectional-area $<5mm^2$ (BV_5).[38]

While the alveolar region is beyond the resolution of CT, alveolar pathology can still be inferred from CT attenuation such as in emphysema where attenuation <-950HU corresponds to tissue destruction. Conversely, regions of high attenuation such as ground

glass opacities or consolidation can correspond to fluid-filled or collapsed alveoli, interstitial thickening (e.g. edema or fibrosis), or increased blood volume.[92]

CT played an important role in the detection and diagnosis of COVID-19 pneumonia early in the pandemic before wide-spread availability of molecular testing.[93] Abnormalities were similar to those reported in chest radiograph, with ground glass opacities (GGOs) (57%), consolidation (29%), crazy-paving pattern (19%) and a predominantly peripheral distribution (33%) being the most common CT findings.[81] Consolidation and GGOs are demonstrated in a COVID-19 patient in **Figure 1-9**. Following recovery, CT abnormalities may persist, with only 38% of those hospitalized with COVID-19 having resolved at 6-months post infection[77] and 49-75% resolved at 1-year, although recovery slowed after 6-months.[94,95] Because of the prolonged inflammatory state and autopsy evidence, the possible development of permanent fibrosis is a concern.[94-96] Age, sex, hospitalization duration, acute respiratory distress syndrome and infection severity were associated with persistent abnormalities or development of fibrosis-like abnormalities.[77,94] Most imaging studies have followed previously hospitalized patients with long-COVID, including those in intensive care. Among never-hospitalized participants, there was a significantly lesser prevalence of opacities (3.7%) on CT however evidence of gas-trapping was present in never-hospitalized, ever-hospitalized and intensive care unit (ICU) -hospitalized patients suggesting a small airways component to long-COVID.[97]

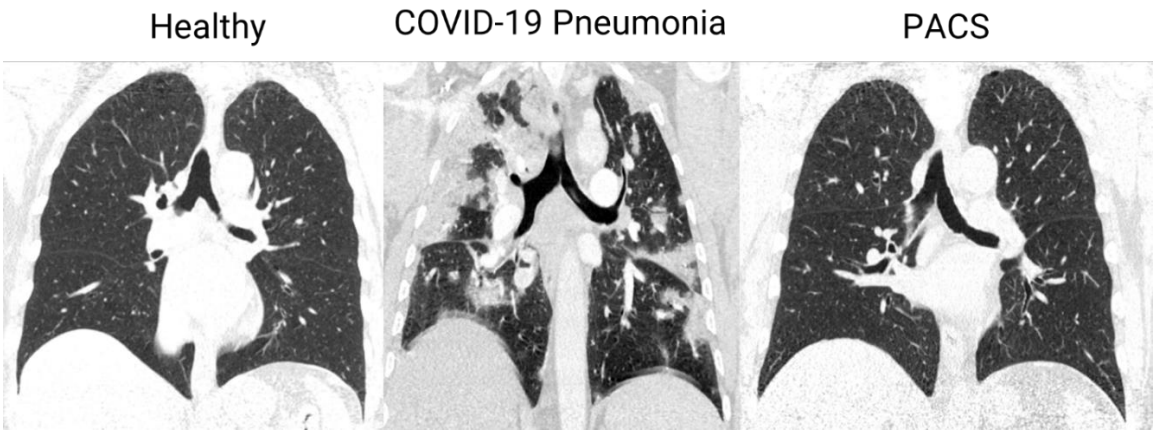

Figure 1-9 CT images in healthy and diseased lungs
Coronal x-ray CT images for a healthy participant, participant with COVID-19 pneumonia during infection, and a participant with PACS, post COVID-infection.
Left: a 76-year old female with no history of respiratory disease.
Middle: a 57 year-old male hospitalized with an active COVID-19 infection. CT shows bilateral consolidation and ground glass opacities, especially in the right upper lobe.
Right: a 41-year-old never-hospitalized male with long-COVID and no abnormal CT findings to suggest disease

1.5.3 Proton Magnetic Resonance Imaging

Magnetic resonance imaging is a technique to image the body using non-ionizing radiofrequency (RF) radiation. It images the body using nuclear magnetic resonance, where nuclei precessing in an external magnetic field can be manipulated by the application of RF waves at the precession frequency described by the Larmor equation:

$$\omega = -\gamma B$$

where ω is the resonant frequency, γ the gyromagnetic ratio and B the magnetic field strength. Atoms with odd number of protons and/or neutrons, such as ^{1}H (or protons) and ^{129}Xe, have a magnetic moment that will precess in an external magnetic field. Because of its abundance in tissue, clinical MRI targets ^{1}H to image body structures. Historically, ^{1}H MRI has not targeted lungs because of the low proton density (0.15g/mL)[98] and large susceptibility differences between air and tissue that create a heterogeneous magnetic

field.[99] These susceptibility gradients cause nuclei within a voxel to experience slightly different magnetic field strengths and quickly de-phase, known as T_2* or spin-spin relaxation. This rapid dephasing (T_2*=0.9-2.2ms in ^{1}H at 1.5T) destroys what little signal the lung tissue provides. In these images the lungs appear like a dark void, which can still be used to segment the thoracic cavity for image processing and analysis.[100]

During imaging, external magnetic gradients are applied to encode spatial information into the precession frequency of the nuclei. These gradients also have the effect of de-phasing the spins, however this can be reversed by using a gradient-recalled-echo (GRE). In this scheme, the applied gradient is reversed after the initial RF excitation. Any de-phasing that occurs during this time is cancelled out as the opposing gradient re-phases the spins in an "echo" at time TE. Modern sequences, known as ultra-short echo time (UTE) sequences, aim to minimize TE and acquire data before T_2* destroys the lung parenchyma signal. UTE sequences can image the thoracic cavity to provide similar information to CT, albeit at a lower resolution. **Figure 1-10** shows that CT findings in COVID-19 infections such as ground glass opacities and consolidation were also visible on UTE and COVID scoring systems showed excellent agreement between methods.[101,102]

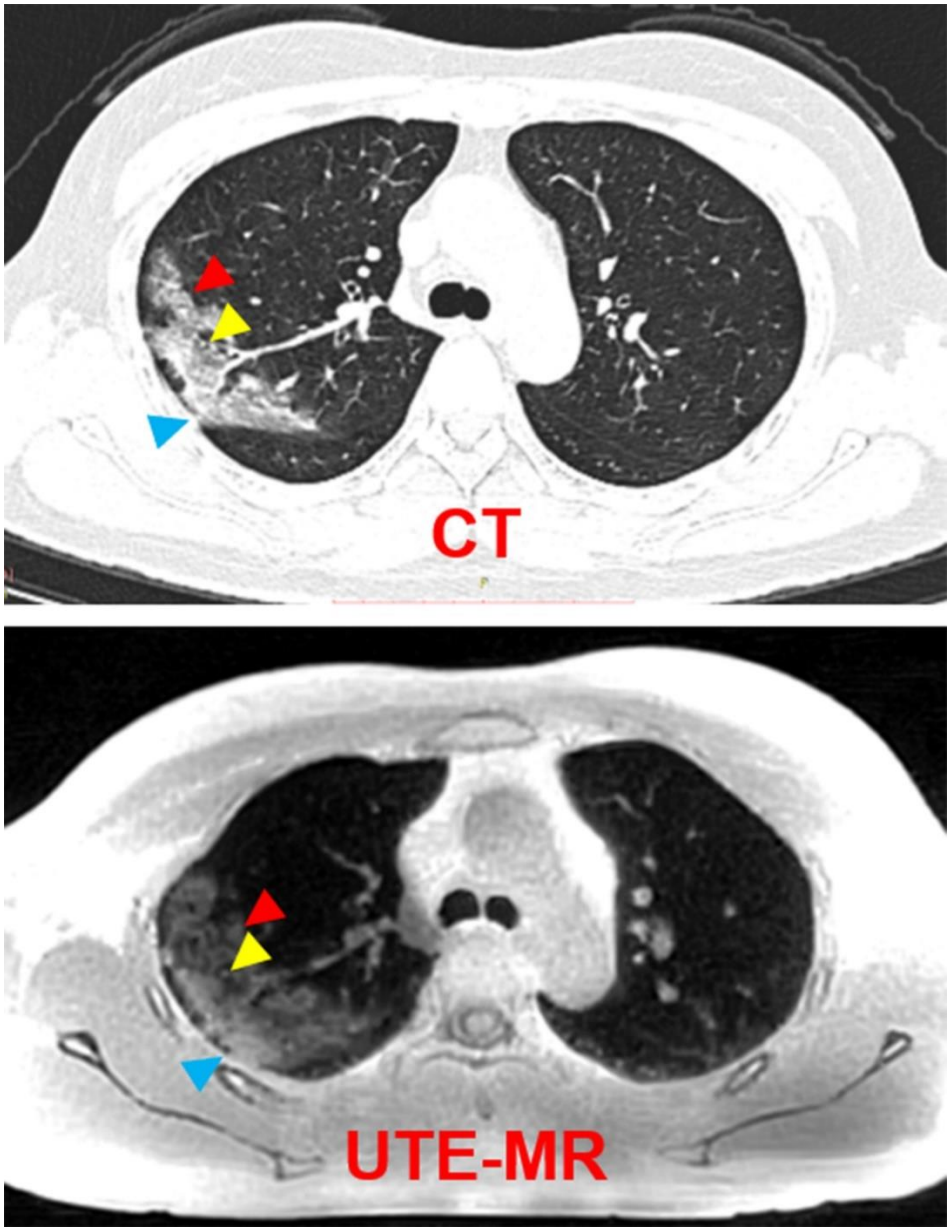

Figure 1-10 Ultra-short echo-time MRI in a person with COVID-19 pneumonia, compared to CT
Red arrow: region of ground-glass opacity, yellow arrow: vessel expansion, Blue arrow: pleural thickening
Figure reproduced from Yang et al.[101]

1.5.4 Echocardiography

The preceding sections concerned lung imaging, but as will be shown in Chapter 5, the structure of the heart may have functional consequences on the pulmonary vasculature. Echocardiography uses ultrasound to image tissues, using a transducer to send ultrasonic

sound waves into tissue. Sound waves are reflected back by the tissue and the time for reflections to return to the transducer can be used to determine tissue structure, such as the echocardiogram shown in **Figure 1-11**. Like MRI it is free of ionizing radiation, but can be performed with smaller, more inexpensive equipment and at a high resolution. Additionally, heart motion and wall motion can be examined and blood flow patterns visualized by adding agitated saline to the bloodstream, which produces bubbles.[103]

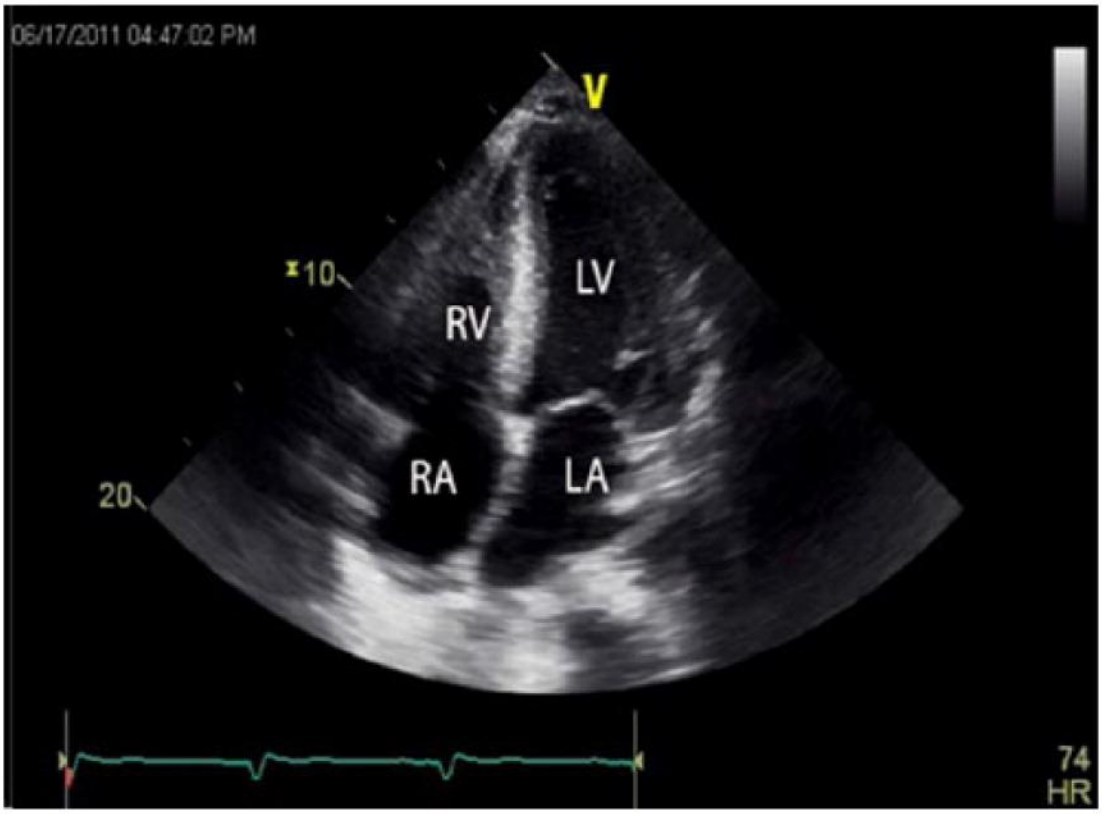

Figure 1-11 Echocardiogram in the four-chamber plane acquired near the apex
Image reproduced from Mayer.[104]

Because of the dramatic difference between acoustic properties of bone and soft tissue, sound waves are mostly reflected and cannot penetrate past bone. To image the heart, a transducer may be oriented between the ribcage to avoid bone. Alternatively, the transducer may be attached to a gastroscope and guided down the esophagus to image through the

esophageal wall from underneath the heart. Transthoracic echocardiography is less invasive and provides a clear view of the anterior ventricles while transesophageal echocardiography provides a clearer view of the atria and has better resolution due to lower required depth penetration.[105] Echocardiography is the primary tool for imaging ASDs, and is used to determine the size, shape, shunting and structural remodeling in response to aberrant flow.[103,106] In cases of ASD, transesophageal echocardiography is often used to better access the atria, especially if the visible window between the ribs does not cover the region of interest. In cases of secundum ASD, defects may vary considerably in size and shape, and transesophageal acquisition may provide beneficial imaging planes for 3-dimensional reconstruction.[103,106] Echocardiography is also essential for surgical planning and post-surgical monitoring of closure devices.[103,106]

1.5.5 CT Pulmonary Angiogram and CT Perfusion

CT pulmonary angiogram (CTPA) is used to image pulmonary perfusion by the injection of an iodine-based contrast agent into the blood. Scans are timed, often by tracking attenuation in a narrow region of interest in the pulmonary artery, to maximize the contrast generated by the bolus in the arteries.[107] CTPA is central to diagnosis of pulmonary embolism,[107] where contrast agent does not enter clotted vessels and clots can be identified as regions of lower opacification. **Figure 1-12** shows an example CTPA with contrast bolus visible and an embolism present in the left lung of a recovering COVID-19 patient. Clots may be due to emboli transported from other parts of the body, or locally occurring thrombi. Quantitative analysis may be able to further distinguish between acute and chronic thromboemboli.[108] Parenchymal perfusion maps can be generated from CTPA by subtracting an anatomic CT from the CTPA to obtain an map of attenuation differences

due to perfusion of the contrast agent. An alternative technique is dual-energy CT, which acquires two different images at different x-ray tube voltages. Imaging is acquired following injection of an iodine contrast agent. Iodine has greater x-ray attenuation thus the attenuation difference between the two images can be measured and the distribution of the iodine can be calculated to estimate perfusion.[109]

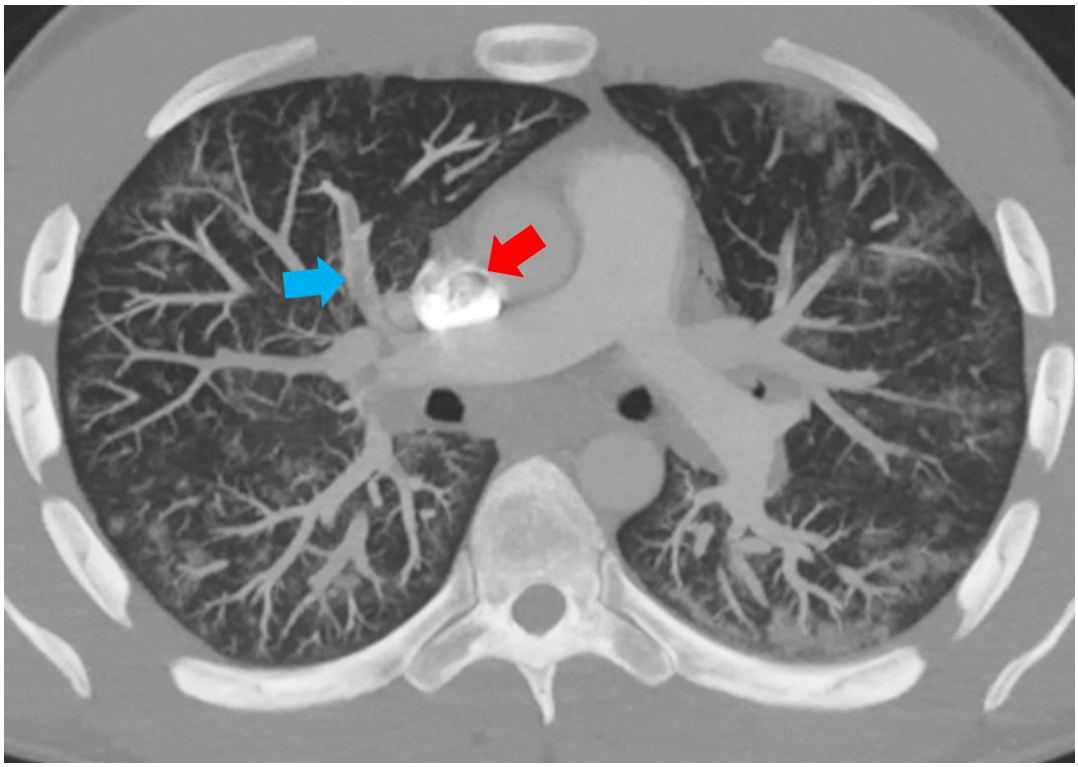

Figure 1-12 CT pulmonary angiogram in a patient with COVID-19 pneumonia
This axial, maximum-intensity-projection image shows the contrast agent entering the heart through the superior vena cava (red arrow) as well as an embolism (blue arrow)

Pulmonary embolism is a common symptom occurring in 5-23% of COVID-19 cases requiring hospitalization.[110,111] Elevated D-dimers in patients with COVID-19 point to a "hypercoagulative state" common across infections. Beyond diagnosis of embolism, CTPA has uncovered pulmonary vascular dilation and a tree-in-bud pattern, also common in COVID-19.[112] CTPA has been less studied in long-COVID, due to difficulty in resolving

small-vessel clotting, which may form a more common phenotype in people with long-COVID.[30] Pulmonary embolism has been noted in people recovering from COVID infection, including in cases of mild disease, however most cases (77%) occurred within 36 days of infection.[113]

1.5.6 Ventilation Perfusion SPECT

Single-photon emission computed tomography (SPECT) is a functional imaging technique that employs radionuclide contrast agents to examine ventilation and perfusion (VQ) through two different scans. For ventilation, either an aerosolized (e.g. ^{99m}Tc-technegas) or gaseous (^{81m}Kr or ^{133}Xe) radionuclide is inhaled and travels to the alveoli so that aerosol distribution is related to ventilation function.[114] For perfusion, a technetium-labeled albumin is administered intravenously that travels to the lung and shows perfused regions.[114] As the radionuclide decays, gamma photons are emitted that can be detected by a gamma camera. As shown in **Figure 1-13**, ventilation and perfusion planar images may be obtained as well as three-dimensional tomography reconstructed in a similar manner to x-ray CT.

VQ-SPECT is often used to look at ventilation/perfusion mismatch or detect emboli. The physiology of the lung seeks to maintain an equilibrium between ventilation and perfusion for efficient lung function, and many diseases are characterized by ventilation/perfusion mismatch, such as in COPD.[115] Functional defects usually appear as dark wedge-shape defects corresponding to unventilated/unperfused lung segments. Ventilated but unperfused segments indicate an embolism. VQ-SPECT in long-COVID has shown that perfusion defects are common – one study in never hospitalized people observed perfusion

defects in 57% of participants.[116] Ventilation defects have also been reported in 88% of ever-hospitalized and 44% of never-hospitalized participants.[117]

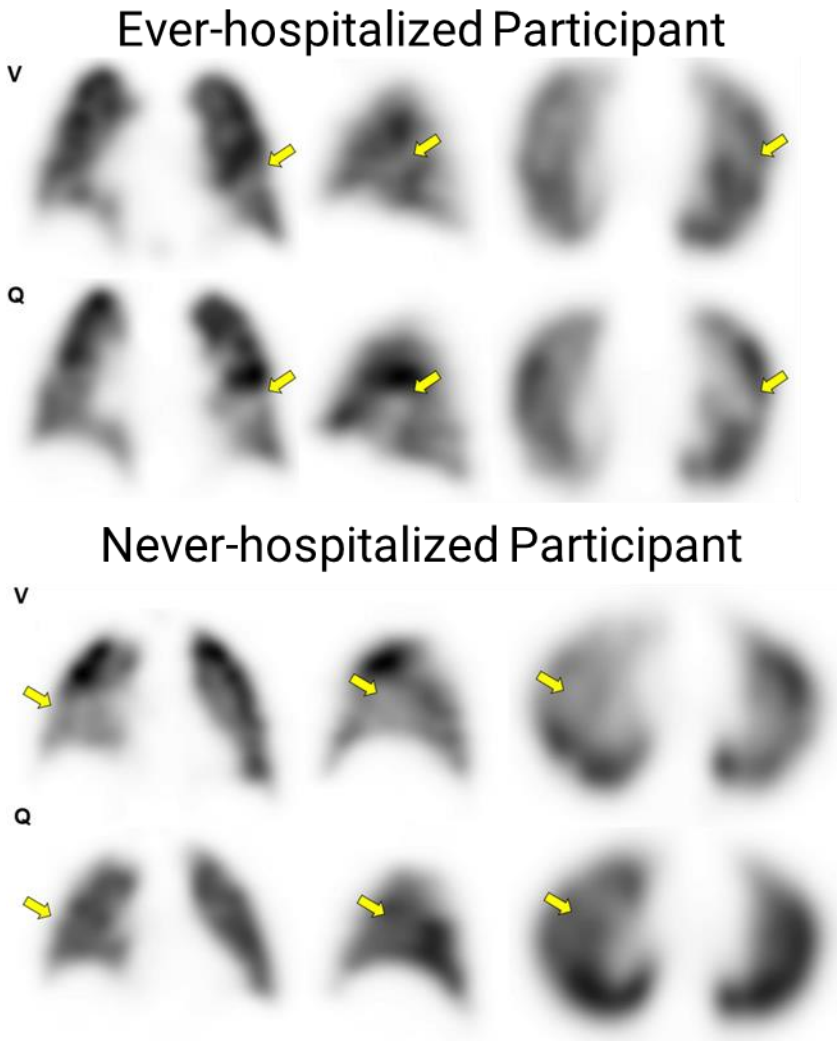

Figure 1-13 SPECT tomographic coronal, sagittal and axial images of participants with COVID-19 infection.
SPECT demonstrates regions of matching poor ventilation (V) and perfusion (Q) indicated by yellow arrows. Image reproduced from Venegas *et al.*[117]

1.6 ^{129}Xe Magnetic Resonance Imaging

This section will present a detailed account of the associated hardware, software, and applications of ^{129}Xe MRI and MRS in the lung. Hyperpolarized gas MRI was created in 1994[118] to image anesthetic gas in the brain, however experiments showed gases introduced

to mouse lungs produced maps of ventilation. Within three years, experiments showed that ^{129}Xe exhibited different magnetic resonant frequencies as it travelled through the different regions of gas-exchange: airspaces, alveolar membrane/blood plasma, and RBC.[119] These discoveries, and the subsequent discovery of functional abnormalities in pathological lungs,[120] have motivated an expanding area of research with the ultimate goal of imaging the complete process of gas-exchange in the lung in a single breath-hold for the diagnosis and characterization of lung disease.

1.6.1 Hyperpolarization

Unlike other contrast methods that rely on changing tissue properties or relaxation for imaging with conventional ^{1}H MRI, ^{129}Xe MRI directly measures xenon atoms in the airspaces and tissue. The detection of ^{129}Xe signal in MRI is challenging however, due to a much lower concentration of atoms in gaseous xenon than ^{1}H in tissue and due to a gyromagnetic ratio 4 times lower than that of ^{1}H, creating a relatively small population difference between up/down spin states.[121] Together these factors reduce the net magnetization available for manipulation with MRI. While the first factor may have limited solutions due to dosing limitations, the fraction of spin up/down can be addressed through hyperpolarization. Spin-exchange optical polarization (SEOP) uses circularly polarized laser light at 795.7nm to induce a spin flip in electrons of an alkali metal, such as rubidium, which then interacts to transfer magnetic spin to a noble gas nucleus.[121,122] SEOP hyperpolarization is performed in a polarizer, as shown in **Figure 1-14**. The system is contained within an oven to heat rubidium into a vapor and surrounded by Helmholtz coils to place the interactions in a uniform magnetic field. A laser is aimed at a glass cell containing rubidium vapor and unpolarized ^{129}Xe flows into the cell and undergoes spin

exchange. Polarized ^{129}Xe gas flows out of the cell and into a glass cooling finger surrounded by liquid nitrogen: ^{129}Xe freezes to the interior, separating it from other buffer gases.[123] Thawing of the cold finger releases polarized gas which is collected in a Tedlar bag and mixed with ^{4}He gas to normalize the total volume to 1.0L and reduce the viscosity of the gas for easy inhalation.[124]

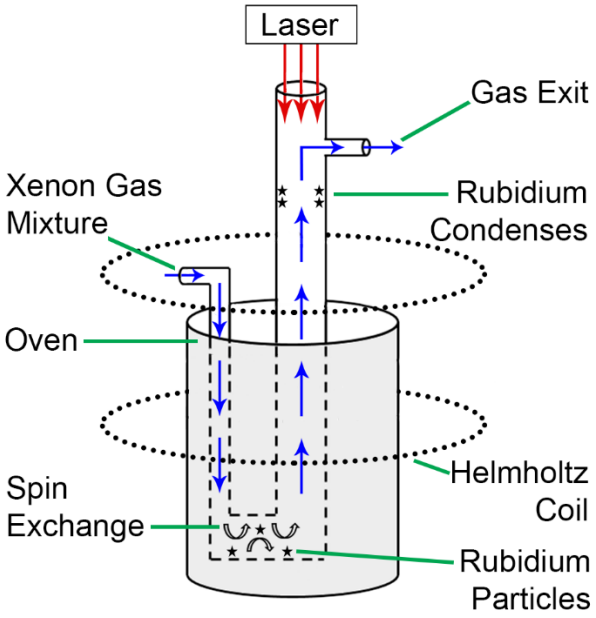

Figure 1-14 Schematic diagram of polarizer apparatus
Image reproduced from Matheson et al.[125]

1.6.2 ^{129}Xe Magnetic Resonance Spectroscopy

Like ^{1}H MRI, ^{129}Xe experiences changes in chemical shift based on the local magnetic environment in tissues. ^{129}Xe exhibits four distinct resonance frequencies at equilibrium in the lung: gas (0ppm), alveolar membrane tissue (197ppm), blood plasma (194ppm), and RBC (222ppm).[126,127] Magnetic resonance spectroscopy (MRS) works similarly to MRI using an RF pulse to excite and measure spins, but without extra magnetic gradients that

encode spatial information and instead simultaneously collects whole-lung data. By using an RF pulse with sufficient spectral selectivity in the frequency domain, all ^{129}Xe compartments may be excited and measured. In lower spectral resolution acquisitions, only three peaks may be visible due to the overlap of tissue and plasma peaks, as shown in **Figure 1-15**.[128] Further shifting of the resonant frequencies up to 5ppm is caused by variations in blood oxygenation due to interactions with oxygenated hemoglobin.[128,129]

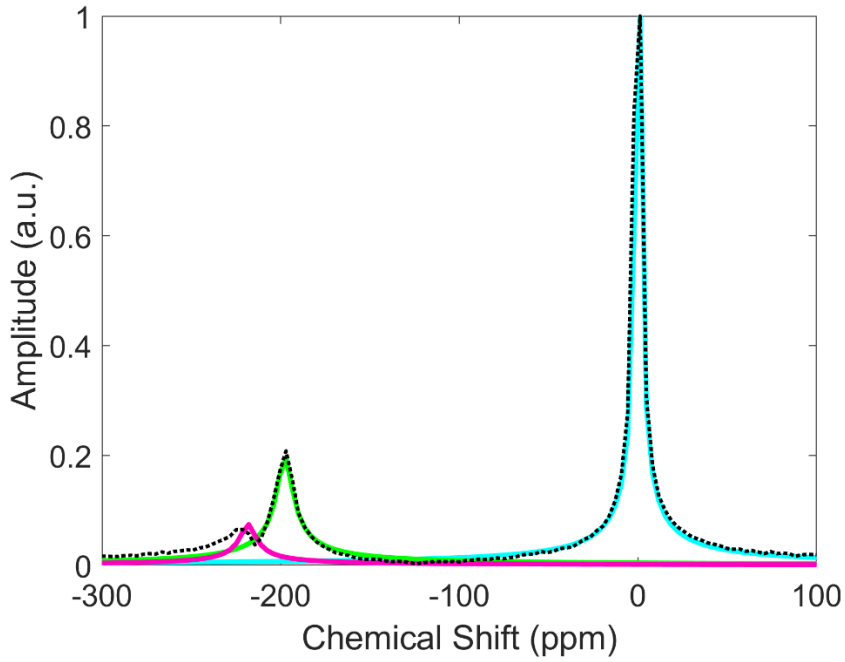

Figure 1-15 ^{129}Xe magnetic resonance spectrum in a healthy individual
Dotted line indicates raw spectrum. Colored lines indicate individual xenon compartments: gas (cyan), alveolar membrane (green), and RBC (magenta).

The most commonly reported spectroscopic measurement is the ratio of RBC area-under-the-curve (AUC) to membrane AUC (RBC:barrier, RBC:tissue-plasma, or RBC:membrane).[130-134] This thesis will use the recently accepted RBC:membrane, however some chapters use other terms that were more common at the time of publishing.

RBC:membrane represents the effectiveness of gas-exchange by measuring how xenon diffuses through the membrane and binds to RBC. Interpretation of this ratio can be challenging, as changes can be due to abnormalities in either the RBC or membrane compartments. The RBC:membrane has been observed to correlate with DL_{CO}[135] and more advanced multivariate models including ventilation information strongly correlate (R^2=.75).[136] Individual compartments may be analyzed using peak AUC or other ratios like RBC:gas.[135] Abnormally low RBC:membrane has been observed in non-specific interstitial pneumonia,[137] COPD,[138] and pediatric bone-marrow transplantation patients[133] and has been related to FVC in patients with idiopathic pulmonary fibrosis.[135] Preliminary investigations have revealed gas-exchange abnormalities in previously hospitalized COVID-19 patients in China and the United Kingdom however relations between Gas-exchange and clinical measurements as well as measurements in never-hospitalized patients were not performed in these small cohorts.[139,140]

Once inhaled, ^{129}Xe spectroscopy undergoes temporal changes both due to relaxation and physiological effects. T_1 decay is variable and decreases with oxygen desaturation (T_1=3s-14s *in vivo*)[141] and additional decay occurs with successive RF pulses, producing a net monotonic decay. The RBC spectral peak also undergoes periodic oscillations at the cardiac frequency termed "cardiogenic oscillations".[128,132] These oscillations are visible in multiple spectral parameters including peak height, full-width-half-maximum, chemical shift and complex phase.[128,132] An example of RBC cardiogenic oscillations is shown in **Figure 1-16**. These oscillations are proposed to reflect blood pulsation in the pulmonary capillaries, which increase available xenon binding sites as well as changing the local susceptibility environment, causing changes in phase and chemical shift over time.

Oscillations in the tissue-plasma compartment have also been reported, although inconsistently.[128,132]

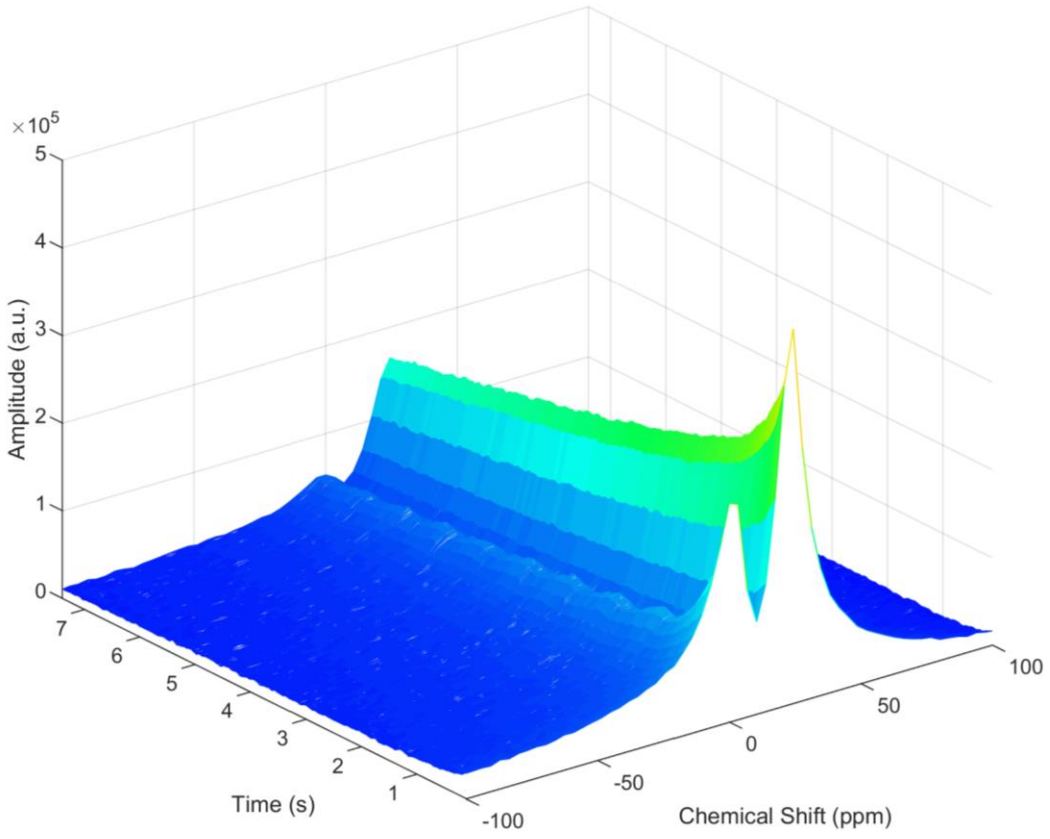

Figure 1-16 ^{129}Xe dynamic spectroscopy acquired in a healthy participant
Two spectral peaks are shown above, with the RBC peak to the left (-2ppm) and alveolar membrane to the right (22ppm). Cardiogenic oscillations are visible in the RBC peak.

1.6.3 ^{129}Xe Ventilation Imaging

^{129}Xe MRI is similar to MRS but can target specific compartments of the Gas-exchange process and recover information about the spatial distribution of ^{129}Xe in that compartment. An RF pulse centered on the ^{129}Xe gas compartment resonance frequency excites atoms for imaging. Although the pulse may excite ^{129}Xe in other compartments, the gas signal is 50 times stronger than xenon in the membrane and RBC compartments so signal can safely be assumed to be due to ^{129}Xe in the airspaces. Similar to ^{1}H MRI covered in section 1.5.3,

magnetic gradients can encode spatial information through a GRE to form ^{129}Xe ventilation images, organized in slices.

Ventilation imaging maps the distribution of gaseous ^{129}Xe in the airspaces in the lung, resulting in signal in regions that are ventilated and signal voids termed "ventilation defects" in regions that are not.[100] Ventilation defect percent is a percentage of ventilation defect volume (VDV) to total lung volume (TLV):

$$\mathrm{VDP} = \frac{\mathrm{VDV}}{\mathrm{TLV}} \times 100\%$$

Because images are acquired under breath hold, they are known as "static ventilation" images, whereas ventilation is traditionally conceived as a change in air volume over time.[142]

Ventilation imaging has been established as a well-tolerated[143-145] imaging technique with strong single-site[146,147] and multi-site reproducibility.[148] Ventilation defects have been demonstrated to correlate with FEV_1 in asthma[149], cystic fibrosis[150] and COPD,[138] decreases in asthma bronchodilator response,[151] and responds to treatments.[152,153] Prior research in COPD failed to detect a relationship between VDP and pulmonary small vessel volume.[154] A preliminary investigation reported ventilation defects in previously hospitalized COVID-19 patients[139] and an investigation with overlapping participants to those in chapters 3 and 4 reported abnormal VDP in PACS participants that was significantly greater in hospitalized participants and related to 6MWD and SpO_2.[155] **Figure 1-17** shows representative static ventilation images and ventilation defects for a representative healthy participant, a participant with COPD and a participant with PACS.

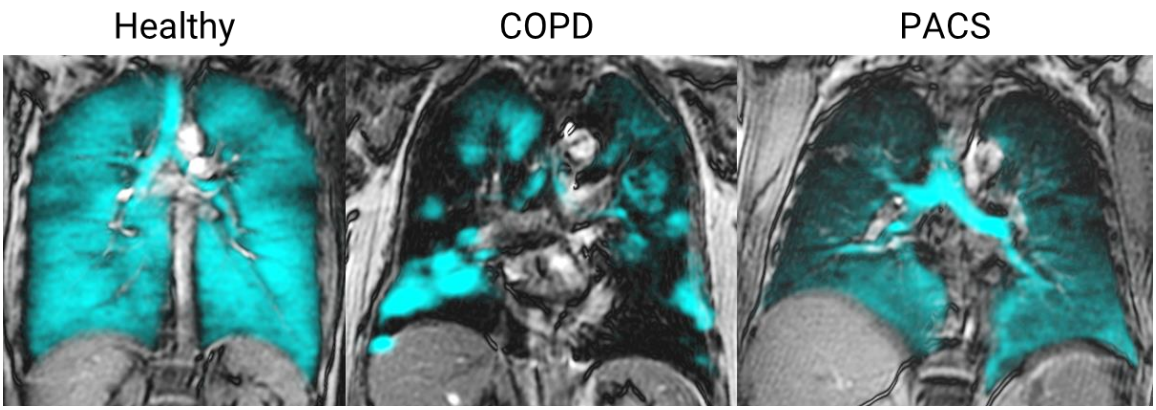

Figure 1-17 ^{129}Xe MRI static ventilation images
Cyan colour denotes the presence of ^{129}Xe. Healthy people (example left) have homogeneous ventilation, while obstructive lung disease often results in heterogeneous ventilation disrupted by ventilation defects (COPD example centre). People with PACS have been noted to have mildly abnormal ventilation patterns (example right). Ventilation images are cyan color and overlaid on ^{1}H anatomic images.

1.6.4 ^{129}Xe Gas-Exchange Imaging

Imaging of the multi-spectral nature of ^{129}Xe in the membrane and RBC compartments was historically challenging due to many limitations: inadequate ^{129}Xe polarization causing poor membrane and RBC signals, low density of membrane and RBC tissue to dissolve in, difficulty in separating two spectral peaks separated by ~20ppm, a low T_2* (1.5-2.4ms at 1.5T)[156] for ^{129}Xe in dissolved compartments and the need to accomplish imaging in a single breath-hold. Over time, improvements in polarization,[157,158] hardware, k-space trajectories[159,160] and decomposition algorithms[131] have made gas-exchange imaging possible.

The separation of membrane and RBC signals in ^{129}Xe is similar to the separation of water and fat images in ^{1}H MRI, which was solved using the Dixon method.[161] In the simplest Dixon scheme, two images are acquired at different TE where the fat component is in-phase in one image and out-of-phase in another. By combining the two images, either the water or fat can be removed and additional images can provide corrections for different

magnetic inhomogeneities. Three point Dixon and iterative decomposition of water and fat with echo asymmetry and least-squares estimation (IDEAL) acquisitions were implemented based on these principles and successful in separating gas-exchange data.[162,163] The technique used in this thesis is a one-point Dixon technique, based on a sequence with interleaved gas and dissolved-phase data acquisition. A one-point Dixon approach acquires dissolved-phase data at a time TE_{90} such that the membrane and RBC compartments are 90° out-of-phase and each compartment is directed to a different perpendicular quadrature channel.[131] A separate spectroscopic calibration is performed to determine a participant-specific TE_{90} based on spectral phase and chemical shift prior to imaging. Using the gas compartment data acquired from interleaved imaging, a phase correction to correct for field inhomogeneities can be applied to all compartments such that the gas compartment has a uniform phase. Finally, membrane and RBC compartments may not be exactly aligned to the quadrature channels, so the raw data are iteratively rotated in the complex plane until the whole-lung RBC:membrane calculated from images matches that obtained during the spectroscopy calibration scan. **Figure 1-18** shows a set of images acquired using the interleaved single-point Dixon method. A recent four-point approach proposes to avoid the perfect 90° phase difference assumption of single-point Dixon by using a mathematical inversion model to solve for each of the three compartments.[164]

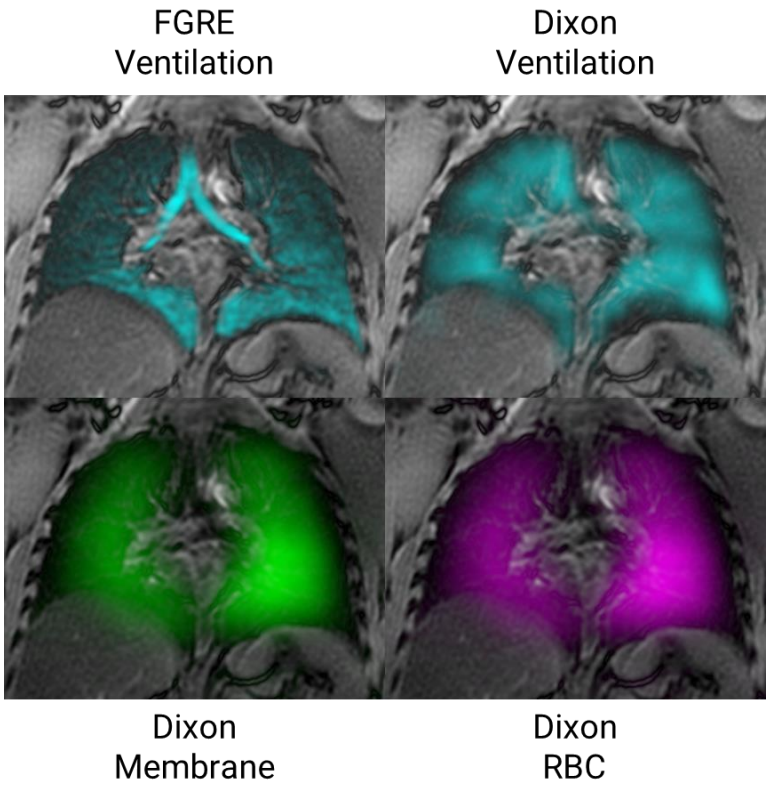

Figure 1-18 Multi-compartment ^{129}Xe MR images
All three ^{129}Xe MR compartments are acquired in a single breathhold with a radial one-point Dixon sequence: gas/ventilation (top right), alveolar membrane (bottom left) and RBC (bottom right). Gas compartment imaging acquired during Dixon acquisition was lower resolution than in ventilation imaging acquired by an FGRE sequence (top left) but was used for B1 field corrections.

^{129}Xe MRI has detected gas-exchange abnormalities in the membrane correlated with CT measurements of emphysema, and in the RBC correlated with DL_{CO}.[138] Imaging in nonspecific interstitial pneumonia and idiopathic pulmonary fibrosis has revealed elevated barrier patterns in most, but not all, participants[137] that corresponds to regions of fibrosis on CT images.[165] Reticulation, ground glass opacities, honeycombing and traction bronchiectasis findings have also been spatially related to regions of elevated barrier signal.[135] Overall barrier uptake maps showed poor correlation with CT fibrosis scores,

which Wang *et al.*[135] propose is evidence of probing alveolar abnormalities rather than the features apparent at CT resolution.

1.7 Thesis Hypotheses and Objectives

Gas-exchange imaging has the potential to probe deeper into the gas-exchange process by providing spatial information to determine how regional, structural changes relate to the individual components of gas-exchange. By isolating these components at the alveolar level, ^{129}Xe gas-exchange MRI has the potential to explain the fine-scale pathophysiology that drives chronic pulmonary disease. The development of gas-exchange MRI has focused on the development of acquisition, reconstruction, analysis tools and novel biomarkers to enable research to expand into this space, however the connection between these novel tools and established pulmonary function tests, patient outcomes, and underlying physiology requires further investigation. Biomarkers such as RBC:membrane have been observed to be abnormal, but how do complex measurements like these relate to what is occurring at the alveolar level and what can it tell us about how patients feel and progress? The overarching objective of this thesis was the development of sensitive pulmonary imaging and spectroscopic measurements to interrogate individual components of the gas-exchange process and understand the underlying pathophysiology that drives symptoms and outcomes in chronic pulmonary disease. The specific hypotheses and objectives in each chapter that support this overarching hypothesis are outlined below.

I first aimed to deconstruct the ^{129}Xe gas-exchange MRI techniques used in measuring gas-exchange to better understand how acquisition parameters, technical assumptions and the simultaneous measurement of gas-exchange compartments affects imaging measurements. In **Chapter 2** I developed a mathematical model of the processes involved from excitation

through reconstruction with the objective of better understanding how the assumptions used in the development of single-point Dixon affect acquired signals. A linear systems approach was used as I hypothesized that the various steps in image formation and acquisition could be represented or approximated by combinations of linear operators.

In **Chapter 3** I aimed to determine the contribution of abnormal gas-exchange and pulmonary vascular structure to persistent respiratory symptoms and exercise in people with long-COVID. Despite common respiratory symptoms of dyspnea, cough and exercise limitation, the source of these symptoms was not apparent from standard pulmonary function tests and imaging. We performed gas-exchange MRI, pulmonary CT, pulmonary function tests and questionnaires to search for abnormalities in people with long-COVID. We hypothesized that abnormal gas-exchange measurements in participants with PACS would be associated with symptoms and that there would be differences in imaging measurements between never-hospitalized and ever-hospitalized participants.

While preliminary studies[139,140] had been published on hyperpolarized ^{129}Xe gas-exchange imaging in people immediately following COVID-19 infection and in people with PACS, all information was collected at a single time-point and follow-up studies were necessary to determine the progression or resolution of PACS. **Chapter 4** examined a subgroup of participants from Chapter 3 that returned to examine longitudinal changes in gas-exchange. Therefore, the objective of this chapter was to determine if gas-exchange measurements normalized over time in people with long-COVID. I also sought to determine if participant symptoms and quality of life improved and to determine if any potential changes in gas-exchange had an impact on participant symptoms.

In **Chapter 5** my objective was to determine the underlying cause of an abnormally high RBC:membrane ratio discovered in the control arm of the long-COVID study detailed in **Chapter 3**. Because the abnormality appeared to stem from a high RBC signal on spectroscopy, the participant was referred to a clinical team for additional clinical tests and imaging. I also developed a hypothesis to explain the physiological mechanism behind the MRS abnormality in relation to clinical findings that emerged during investigation by the care team. Following surgical intervention into the ASD that was discovered, I then aimed to determine if MRS abnormalities has resolved. I tested the previously hypothesized mechanism to determine if the abnormality resolved in line with the normalization of clinical measures.

In **Chapter 6** I conclude this thesis with a summary discussion of the key results from body **Chapters 2-5**. The limitations present in the thesis, both in general for the techniques used in this thesis and for each chapter are presented next. A discussion of future directions for research building on this thesis is also provided.

1.8 References

1. Ayoubkhani D, Pawelek P. Prevalence of ongoing symptoms following coronavirus (COVID-19) infection in the UK: 1 June 2022. In: Statistics OfN, editor. 2022.

2. Collaborators GBDCRD. Prevalence and attributable health burden of chronic respiratory diseases, 1990-2017: a systematic analysis for the Global Burden of Disease Study 2017. Lancet Respir Med. 2020;8(6):585-96.

3. Estimated COVID-19 Burden Web: United States Centers for Disease Control and Prevention; 2021 [updated October 2 2021. Available from: https://www.cdc.gov/coronavirus/2019-ncov/cases-updates/burden.html.

4. Dong E, Du H, Gardner L. An interactive web-based dashboard to track COVID-19 in real time. Lancet Infect Dis. 2020;20(5):533-4.

5. Nalbandian A, Sehgal K, Gupta A, Madhavan MV, McGroder C, Stevens JS, et al. Post-acute COVID-19 syndrome. Nature Medicine. 2021;27(4):601-15.

6. Proal AD, VanElzakker MB. Long COVID or Post-acute Sequelae of COVID-19 (PASC): An Overview of Biological Factors That May Contribute to Persistent Symptoms. Front Microbiol. 2021;12:698169.

7. National Institute of Health and Care Excellence. COVID-19 Rapid Guideline: Managing COVID-19. NICE; 2021.

8. Global Burden of Disease Long CC, Wulf Hanson S, Abbafati C, Aerts JG, Al-Aly Z, Ashbaugh C, et al. Estimated Global Proportions of Individuals With Persistent Fatigue, Cognitive, and Respiratory Symptom Clusters Following Symptomatic COVID-19 in 2020 and 2021. JAMA. 2022;328(16):1604-15.

9. Fernandez-de-las-Penas C, Palacios-Cena D, Gomez-Mayordomo V, Rodriuez-Jimenez J, Palacios-Cena M, Velasco-Arribas M, et al. Long-term post-COVID symptoms and associated risk factors in previously hospitalized patients: A multicenter study. J Infection. 2021;83(2):271-4.

10. Chen C, Haupert SR, Zimmermann L, Shi X, Fritsche LG, Mukherjee B. Global Prevalence of Post-Coronavirus Disease 2019 (COVID-19) Condition or Long COVID: A Meta-Analysis and Systematic Review. J Infect Dis. 2022;226(9):1593-607.

11. Davis HE, McCorkell L, Vogel JM, Topol EJ. Long COVID: major findings, mechanisms and recommendations. Nat Rev Microbiol. 2023:1-14.

12. Lumb AB. Nunn's applied respiratory physiology. Eighth edition. ed. Edinburgh ; New York: Elsevier; 2017. xii, 544 pages p.

13. Han S, Mallampalli RK. The Role of Surfactant in Lung Disease and Host Defense against Pulmonary Infections. Ann Am Thorac Soc. 2015;12(5):765-74.

14. Front Matter. In: Lumb AB, editor. Nunn's Applied Respiratory Physiology (Eighth Edition): Elsevier; 2017. p. i-ii.

15. Tortora GJ, Reynolds S. Principles of anatomy and physiology. 10th ed: Wiley; 2003.

16. Billett HH. Hemoglobin and Hematocrit. In: Walker HK, Hall WD, Hurst JW, editors. Clinical methods: the history, physical, and laboratory examinations. 3 ed. Boston: Butterworths; 1990.

17. Karakochuk CD, Hess SY, Moorthy D, Namaste S, Parker ME, Rappaport AI, et al. Measurement and interpretation of hemoglobin concentration in clinical and field settings: a narrative review. Ann N Y Acad Sci. 2019;1450(1):126-46.

18. Mendez R, Latorre A, Gonzalez-Jimenez P, Feced L, Bouzas L, Yepez K, et al. Reduced Diffusion Capacity in COVID-19 Survivors. Ann Am Thorac Soc. 2021;18(7):1253-5.

19. Shah AS, Wong AW, Hague CJ, Murphy DT, Johnston JC, Ryerson CJ, et al. A prospective study of 12-week respiratory outcomes in COVID-19-related hospitalisations. Thorax. 2021;76(4):402-4.

20. Yong SJ. Long COVID or post-COVID-19 syndrome: putative pathophysiology, risk factors, and treatments. Infect Dis (Lond). 2021;53(10):737-54.

21. Bellan M, Baricich A, Patrucco F, Zeppegno P, Gramaglia C, Balbo PE, et al. Long-term sequelae are highly prevalent one year after hospitalization for severe COVID-19. Sci Rep. 2021;11(1):22666.

22. Chopra V, Flanders SA, O'Malley M, Malani AN, Prescott HC. Sixty-Day Outcomes Among Patients Hospitalized With COVID-19. Ann Intern Med. 2021;174(4):576-8.

23. Bell ML, Catalfamo CJ, Farland LV, Ernst KC, Jacobs ET, Klimentidis YC, et al. Post-acute sequelae of COVID-19 in a non-hospitalized cohort: Results from the Arizona CoVHORT. Plos One. 2021;16(8).

24. Bliddal S, Banasik K, Pedersen OB, Nissen J, Cantwell L, Schwinn M, et al. Acute and persistent symptoms in non-hospitalized PCR-confirmed COVID-19 patients. Sci Rep-Uk. 2021;11(1).

25. Mulay A, Konda B, Garcia G, Jr., Yao C, Beil S, Villalba JM, et al. SARS-CoV-2 infection of primary human lung epithelium for COVID-19 modeling and drug discovery. Cell Rep. 2021;35(5):109055.

26. Scialo F, Daniele A, Amato F, Pastore L, Matera MG, Cazzola M, et al. ACE2: The Major Cell Entry Receptor for SARS-CoV-2. Lung. 2020;198(6):867-77.

27. Gursoy B, Surmeli CD, Alkan M, Satici C, Altunok ES, Kamat S, et al. Cytokine storm in severe COVID-19 pneumonia. J Med Virol. 2021;93(9):5474-80.

28. Hu B, Huang S, Yin L. The cytokine storm and COVID-19. J Med Virol. 2021;93(1):250-6.

29. Kanne JP, Little BP, Schulte JJ, Haramati A, Haramati LB. Long-Term Lung Abnormalities Associated with COVID-19 Pneumonia. Radiology. 2022:221806.

30. Dhawan RT, Gopalan D, Howard L, Vicente A, Park M, Manalan K, et al. Beyond the clot: perfusion imaging of the pulmonary vasculature after COVID-19. Lancet Respir Med. 2021;9(1):107-16.

31. Ojo AS, Balogun SA, Williams OT, Ojo OS. Pulmonary Fibrosis in COVID-19 Survivors: Predictive Factors and Risk Reduction Strategies. Pulm Med. 2020;2020:6175964.

32. P KM, Sivashanmugam K, Kandasamy M, Subbiah R, Ravikumar V. Repurposing of histone deacetylase inhibitors: A promising strategy to combat pulmonary fibrosis promoted by TGF-beta signalling in COVID-19 survivors. Life Sci. 2021;266:118883.

33. Capac M. File:Atrial septal defect-tr.png. Wikimedia Commons2020.

34. Brida M, Chessa M, Celermajer D, Li W, Geva T, Khairy P, et al. Atrial septal defect in adulthood: a new paradigm for congenital heart disease. Eur Heart J. 2022;43(28):2660-71.

35. Kheiwa A, Hari P, Madabhushi P, Varadarajan P. Patent foramen ovale and atrial septal defect. Echocardiography. 2020;37(12):2172-84.

36. Attenhofer Jost CH, Connolly HM, Danielson GK, Bailey KR, Schaff HV, Shen WK, et al. Sinus venosus atrial septal defect: long-term postoperative outcome for 115 patients. Circulation. 2005;112(13):1953-8.

37. Sun R, Liu M, Lu L, Zheng Y, Zhang P. Congenital Heart Disease: Causes, Diagnosis, Symptoms, and Treatments. Cell Biochem Biophys. 2015;72(3):857-60.

38. Estepar RS, Kinney GL, Black-Shinn JL, Bowler RP, Kindlmann GL, Ross JC, et al. Computed tomographic measures of pulmonary vascular morphology in smokers and their clinical implications. Am J Respir Crit Care Med. 2013;188(2):231-9.

39. Synn AJ, Margerie-Mellon C, Jeong SY, Rahaghi FN, Jhun I, Washko GR, et al. Vascular remodeling of the small pulmonary arteries and measures of vascular pruning on computed tomography. Pulm Circ. 2021;11(4):20458940211061284.

40. Diaz AA, Maselli DJ, Rahaghi F, Come CE, Yen A, Maclean ES, et al. Pulmonary vascular pruning in smokers with bronchiectasis. ERJ Open Res. 2018;4(4).

41. Ash SY, Rahaghi FN, Come CE, Ross JC, Colon AG, Cardet-Guisasola JC, et al. Pruning of the Pulmonary Vasculature in Asthma. The Severe Asthma Research Program (SARP) Cohort. Am J Respir Crit Care Med. 2018;198(1):39-50.

42. Pistenmaa CL, Nardelli P, Ash SY, Come CE, Diaz AA, Rahaghi FN, et al. Pulmonary Arterial Pruning and Longitudinal Change in Percent Emphysema and Lung Function: The Genetic Epidemiology of COPD Study. Chest. 2021;160(2):470-80.

43. Magee F, Wright JL, Wiggs BR, Pare PD, Hogg JC. Pulmonary vascular structure and function in chronic obstructive pulmonary disease. Thorax. 1987;43:183-9.

44. Criée CP, Sorichter S, Smith HJ, Kardos P, Merget R, Heise D, et al. Body plethysmography – Its principles and clinical use. Respiratory Medicine. 2011;105(7):959-71.

45. van der Lee I, Zanen P, van den Bosch JM, Lammers JW. Pattern of diffusion disturbance related to clinical diagnosis: The K(CO) has no diagnostic value next to the DL(CO). Respir Med. 2006;100(1):101-9.

46. Hoeper MM, Meyer K, Rademacher J, Fuge J, Welte T, Olsson KM. Diffusion Capacity and Mortality in Patients With Pulmonary Hypertension Due to Heart Failure With Preserved Ejection Fraction. JACC: Heart Failure. 2016;4(6):441-9.

47. Gehlbach BK, Geppert E. The pulmonary manifestations of left heart failure. Chest. 2004;125(2):669-82.

48. Crapo RO, Morris AH. Standardized single breath normal values for carbon monoxide diffusing capacity. Am Rev Respir Dis. 1981;123(2):185-9.

49. Gaensler EA, Smith AA. Attachment for automated single breath diffusing capacity measurement. Chest. 1973;63(2):136-45.

50. Gulsvik A, Bakke P, Humerfelt S, Omenaas E, Tosteson T, Weiss ST, et al. Single breath transfer factor for carbon monoxide in an asymptomatic population of never smokers. Thorax. 1992;47(3):167-73.

51. Gutierrez C, Ghezzo RH, Abboud RT, Cosio MG, Dill JR, Martin RR, et al. Reference values of pulmonary function tests for Canadian Caucasians. Can Respir J. 2004;11(6):414-24.

52. Ip MS, Lam WK, Lai AY, Ko FW, Lau AC, Ling SO, et al. Reference values of diffusing capacity of non-smoking Chinese in Hong Kong. Respirology. 2007;12(4):599-606.

53. Knudson RJ, Kaltenborn WT, Knudson DE, Burrows B. The single-breath carbon monoxide diffusing capacity. Reference equations derived from a healthy nonsmoking population and effects of hematocrit. Am Rev Respir Dis. 1987;135(4):805-11.

54. Marsh S, Aldington S, Williams M, Weatherall M, Shirtcliffe P, McNaughton A, et al. Complete reference ranges for pulmonary function tests from a single New Zealand population. N Z Med J. 2006;119(1244):U2281.

55. Miller A, Thornton JC, Warshaw R, Anderson H, Teirstein AS, Selikoff IJ. Single breath diffusing capacity in a representative sample of the population of Michigan, a large industrial state. Predicted values, lower limits of normal, and frequencies of abnormality by smoking history. Am Rev Respir Dis. 1983;127(3):270-7.

56. Neder JA, Andreoni S, Peres C, Nery LE. Reference values for lung function tests. III. Carbon monoxide diffusing capacity (transfer factor). Braz J Med Biol Res. 1999;32(6):729-37.

57. Paoletti P, Viegi G, Pistelli G, Di Pede F, Fazzi P, Polato R, et al. Reference equations for the single-breath diffusing capacity. A cross-sectional analysis and effect of body size and age. Am Rev Respir Dis. 1985;132(4):806-13.

58. Roberts CM, MacRae KD, Winning AJ, Adams L, Seed WA. Reference values and prediction equations for normal lung function in a non-smoking white urban population. Thorax. 1991;46(9):643-50.

59. Roca J, Rodriguez-Roisin R, Cobo E, Burgos F, Perez J, Clausen JL. Single-breath carbon monoxide diffusing capacity prediction equations from a Mediterranean population. Am Rev Respir Dis. 1990;141(4 Pt 1):1026-32.

60. Vijayan VK, Kuppurao KV, Venkatesan P, Sankaran K, Prabhakar R. Pulmonary function in healthy young adult Indians in Madras. Thorax. 1990;45(8):611-5.

61. Yang SC, Yang SP, Lin PJ. Prediction equations for single-breath carbon monoxide diffusing capacity from a Chinese population. Am Rev Respir Dis. 1993;147(3):599-606.

62. Johnston R. PFT Blog [Internet]. Internet2014 November 18, 2016. [cited 2023]. Available from: https://www.pftforum.com/blog/whats-normal-about-dlco/.

63. Laboratories ATSCoPSfCPF. ATS statement: guidelines for the six-minute walk test. Am J Respir Crit Care Med. 2002;166(1):111-7.

64. Borg GAV. Psychophysical bases of perceived exertion. Med Sci Sports Exerc. 1982;14(5):377-81.

65. Borg G. Borg's perceived exertion and pain scales. Champaign, IL, US: Human Kinetics; 1998. viii, 104-viii, p.

66. Cahalin L, Pappagianopoulos P, Prevost S, Wain J, Ginns L. The relationship of the 6-min walk test to maximal oxygen consumption in transplant candidates with end-stage lung disease. Chest. 1995;108(2):452-9.

67. du Bois RM, Albera C, Bradford WZ, Costabel U, Leff JA, Noble PW, et al. 6-Minute walk distance is an independent predictor of mortality in patients with idiopathic pulmonary fibrosis. Eur Respir J. 2014;43(5):1421-9.

68. Karanth MS, Awad NT. Six Minute Walk Test: A Tool for Predicting Mortality in Chronic Pulmonary Diseases. J Clin Diagn Res. 2017;11(4):OC34-OC8.

69. Pesonen I, Gao J, Kalafatis D, Carlson L, Sköld M, Ferrara G. Six-minute walking test outweighs other predictors of mortality in idiopathic pulmonary fibrosis. A real-life study from the Swedish IPF registry. Respiratory Medicine: X. 2020;2:100017.

70. Hernandes NA, Wouters EF, Meijer K, Annegarn J, Pitta F, Spruit MA. Reproducibility of 6-minute walking test in patients with COPD. Eur Respir J. 2011;38(2):261-7.

71. Jones PW, Quirk FH, Baveystock CM. The St George's Respiratory Questionnaire. Respir Med. 1991;85 Suppl B:25-31; discussion 3-7.

72. Jones PW, Quirk FH, Baveystock CM, Littlejohns P. A self-complete measure of health status for chronic airflow limitation. The St. George's Respiratory Questionnaire. Am Rev Respir Dis. 1992;145(6):1321-7.

73. Craig CL, Marshall AL, Sjostrom M, Bauman AE, Booth ML, Ainsworth BE, et al. International physical activity questionnaire: 12-country reliability and validity. Med Sci Sports Exerc. 2003;35(8):1381-95.

74. Graham BL, Brusasco V, Burgos F, Cooper BG, Jensen R, Kendrick A, et al. 2017 ERS/ATS standards for single-breath carbon monoxide uptake in the lung. Eur Respir J. 2017;49(1).

75. Graham BL, Steenbruggen I, Miller MR, Barjaktarevic IZ, Cooper BG, Hall GL, et al. Standardization of Spirometry 2019 Update. An Official American Thoracic Society and European Respiratory Society Technical Statement. Am J Respir Crit Care Med. 2019;200(8):e70-e88.

76. Global Initiative for Chronic Obstructive Lung D. 2019 Report: Global Initiative for Chronic Obstructive Lung Disease; 2019 [155]. Available from: http://www.goldcopd.org/.

77. Han X, Fan Y, Alwalid O, Li N, Jia X, Yuan M, et al. Six-month Follow-up Chest CT Findings after Severe COVID-19 Pneumonia. Radiology. 2021;299(1):E177-E86.

78. van Gassel RJJ, Bels JLM, Raafs A, van Bussel BCT, van de Poll MCG, Simons SO, et al. High Prevalence of Pulmonary Sequelae at 3 Months after Hospital Discharge in

Mechanically Ventilated Survivors of COVID-19. American Journal of Respiratory and Critical Care Medicine. 2021;203(3):371-4.

79. Guan WJ, Ni ZY, Hu Y, Liang WH, Ou CQ, He JX, et al. Clinical Characteristics of Coronavirus Disease 2019 in China. N Engl J Med. 2020;382(18):1708-20.

80. Wang YXJ, Liu WH, Yang M, Chen W. The role of CT for Covid-19 patient's management remains poorly defined. Ann Transl Med. 2020;8(4):145.

81. Chung M, Bernheim A, Mei X, Zhang N, Huang M, Zeng X, et al. CT Imaging Features of 2019 Novel Coronavirus (2019-nCoV). Radiology. 2020;295(1):202-7.

82. Gassel RJJv, Bels JLM, Raafs A, Bussel BCTv, Poll MCGvd, Simons SO, et al. High Prevalence of Pulmonary Sequelae at 3 Months after Hospital Discharge in Mechanically Ventilated Survivors of COVID-19. American Journal of Respiratory and Critical Care Medicine. 2021;203(3):371-4.

83. Zimmermann GS, Fingerle AA, Renger B, Laugwitz KL, Hautmann H, Sauter A, et al. Dark-field chest x-ray imaging: first experience in patients with alpha1-antitrypsin deficiency. Eur Radiol Exp. 2022;6(1):9.

84. Natural Background Radiation in Canada - Annual Effective Dose Values for Select Canadian Cities Internet: Natural Resources Canada; 2023 [updated 3 February 2014.

85. Murphy K, Smits H, Knoops AJG, Korst M, Samson T, Scholten ET, et al. COVID-19 on Chest Radiographs: A Multireader Evaluation of an Artificial Intelligence System. Radiology. 2020;296(3):E166-E72.

86. Rousan LA, Elobeid E, Karrar M, Khader Y. Chest x-ray findings and temporal lung changes in patients with COVID-19 pneumonia. BMC Pulm Med. 2020;20(1):245.

87. Wong HYF, Lam HYS, Fong AH, Leung ST, Chin TW, Lo CSY, et al. Frequency and Distribution of Chest Radiographic Findings in Patients Positive for COVID-19. Radiology. 2020;296(2):E72-E8.

88. Smith-Bindman R, Lipson J, Marcus R, Kim KP, Mahesh M, Gould R, et al. Radiation dose associated with common computed tomography examinations and the associated lifetime attributable risk of cancer. Arch Intern Med. 2009;169(22):2078-86.

89. Taekker M, Kristjansdottir B, Graumann O, Laursen CB, Pietersen PI. Diagnostic accuracy of low-dose and ultra-low-dose CT in detection of chest pathology: a systematic review. Clin Imaging. 2021;74:139-48.

90. Frangi AF. Medical Image Computing and Computer-Assisted Intervention — MICCAI'98 Multiscale vessel enhancement filtering. 1998:130-7.

91. Estepar RSJ, Ross JC, Krissian K, Schultz T, Washko GR, Kindlmann GL. Computational Vascular Morphometry for the Assessment of Pulmonary Vascular Disease

Based on Scale-Space Particles. 2012 9th Ieee International Symposium on Biomedical Imaging (Isbi). 2012:1479-82.

92. Hansell DM, Bankier AA, MacMahon H, McLoud TC, Muller NL, Remy J. Fleischner Society: glossary of terms for thoracic imaging. Radiology. 2008;246(3):697-722.

93. Rubin GD, Ryerson CJ, Haramati LB, Sverzellati N, Kanne JP, Raoof S, et al. The Role of Chest Imaging in Patient Management During the COVID-19 Pandemic: A Multinational Consensus Statement From the Fleischner Society. Chest. 2020;158(1):106-16.

94. Luger AK, Sonnweber T, Gruber L, Schwabl C, Cima K, Tymoszuk P, et al. Chest CT of Lung Injury 1 Year after COVID-19 Pneumonia: The CovILD Study. Radiology. 2022;304(2):462-70.

95. Pan F, Yang L, Liang B, Ye T, Li L, Li L, et al. Chest CT Patterns from Diagnosis to 1 Year of Follow-up in Patients with COVID-19. Radiology. 2022;302(3):709-19.

96. Li Y, Wu J, Wang S, Li X, Zhou J, Huang B, et al. Progression to fibrosing diffuse alveolar damage in a series of 30 minimally invasive autopsies with COVID-19 pneumonia in Wuhan, China. Histopathology. 2021;78(4):542-55.

97. Cho JL, Villacreses R, Nagpal P, Guo J, Pezzulo AA, Thurman AL, et al. Quantitative Chest CT Assessment of Small Airways Disease in Post-Acute SARS-CoV-2 Infection. Radiology. 2022;304(1):185-92.

98. Bergin CJ, Glover GM, Pauly J. Magnetic resonance imaging of lung parenchyma. J Thorac Imaging. 1993;8(1):12-7.

99. Bergin CJ, Glover GH, Pauly JM. Lung parenchyma: magnetic susceptibility in MR imaging. Radiology. 1991;180(3):845-8.

100. Kirby M, Heydarian M, Svenningsen S, Wheatley A, McCormack DG, Etemad-Rezai R, et al. Hyperpolarized 3He magnetic resonance functional imaging semiautomated segmentation. Acad Radiol. 2012;19(2):141-52.

101. Yang S, Zhang Y, Shen J, Dai Y, Ling Y, Lu H, et al. Clinical Potential of UTE-MRI for Assessing COVID-19: Patient- and Lesion-Based Comparative Analysis. J Magn Reson Imaging. 2020;52(2):397-406.

102. Campbell-Washburn AE, Suffredini AF, Chen MY. High-Performance 0.55-T Lung MRI in Patient with COVID-19 Infection. Radiology. 2021;299(2):E246-E7.

103. Johri AM, Rojas CA, El-Sherief A, Witzke CF, Chitty DW, Palacios IF, et al. Imaging of atrial septal defects: echocardiography and CT correlation. Heart. 2011;97(17):1441-53.

104. Mayer P. At the Heart of the Matter:An Overview of Adult Echocardiography for the Non–Cardiac Sonographer. Journal of Diagnostic Medical Sonography. 2015;31(4):221-32.

105. Shillcutt SK, Bick JS. Echo didactics: a comparison of basic transthoracic and transesophageal echocardiography views in the perioperative setting. Anesth Analg. 2013;116(6):1231-6.

106. Silvestry FE, Cohen MS, Armsby LB, Burkule NJ, Fleishman CE, Hijazi ZM, et al. Guidelines for the Echocardiographic Assessment of Atrial Septal Defect and Patent Foramen Ovale: From the American Society of Echocardiography and Society for Cardiac Angiography and Interventions. J Am Soc Echocardiogr. 2015;28(8):910-58.

107. Moore AJE, Wachsmann J, Chamarthy MR, Panjikaran L, Tanabe Y, Rajiah P. Imaging of acute pulmonary embolism: an update. Cardiovasc Diagn Ther. 2018;8(3):225-43.

108. Wittram C. How I do it: CT pulmonary angiography. AJR Am J Roentgenol. 2007;188(5):1255-61.

109. Mamourian AC, Mamourian AC. 1History and Physics of CT Imaging. CT Imaging: Practical Physics, Artifacts, and Pitfalls: Oxford University Press; 2013. p. 0.

110. Grillet F, Behr J, Calame P, Aubry S, Delabrousse E. Acute Pulmonary Embolism Associated with COVID-19 Pneumonia Detected with Pulmonary CT Angiography. Radiology. 2020;296(3):E186-E8.

111. Al-Samkari H, Karp Leaf RS, Dzik WH, Carlson JCT, Fogerty AE, Waheed A, et al. COVID-19 and coagulation: bleeding and thrombotic manifestations of SARS-CoV-2 infection. Blood. 2020;136(4):489-500.

112. khalifa MH, Samir A, Baess AI, Hendawi SS. COVID-19-induced vascular angiopathy: CTPA signs in critically ill patients other than acute pulmonary embolism and high-lung opacity scores. Egyptian Journal of Radiology and Nuclear Medicine. 2021;52(1):112.

113. Mouzarou A, Ioannou M, Leonidou E, Chaziri I. Pulmonary Embolism in Post-CoviD-19 Patients, a Literature Review: Red Flag for Increased Awareness? SN Compr Clin Med. 2022;4(1):190.

114. Roach PJ, Schembri GP, Bailey DL. V/Q scanning using SPECT and SPECT/CT. J Nucl Med. 2013;54(9):1588-96.

115. Rodriguez-Roisin R, Drakulovic M, Rodriguez DA, Roca J, Barbera JA, Wagner PD. Ventilation-perfusion imbalance and chronic obstructive pulmonary disease staging severity. J Appl Physiol (1985). 2009;106(6):1902-8.

116. Evbuomwan O, Engelbrecht G, Bergman MV, Mokwena S, Ayeni OA. Lung perfusion findings on perfusion SPECT/CT imaging in non-hospitalized de-isolated patients diagnosed with mild COVID-19 infection. Egyptian Journal of Radiology and Nuclear Medicine. 2021;52(1):144.

117. Venegas C, Marriott CJC, Ho T, Son K, Jamil R, Jamal M, et al. Ventilation and perfusion abnormalities following recovery from noncritical COVID-19. Canadian Journal of Respiratory, Critical Care, and Sleep Medicine. 2022;6(5):304-13.

118. Albert MS, Cates GD, Driehuys B, Happer W, Saam B, Springer CS, et al. Biological magnetic resonance imaging using laser-polarized 129Xe. Nature. 1994;370:199-201.

119. Sakai K, Bilek K, Oteiza E, Walsworth RL, Balamore D, Jolesz FA, et al. Temporal Dynamics of Hyperpolarized 129Xe Resonances in Living Rats. Journal of Magnetic Resonance. 1996;111:300-4.

120. Kauczor HU, Ebert M, Kreitner KF, Nilgens H, Surkau R, Heil W, et al. Imaging of the Lungs Using 3He MRI: Preliminary Clinical Experience in 18 Patients with and without Lung Disease. J Magn Reson Imaging. 1997;7:538-43.

121. Schroder L. Xenon for NMR biosensing - Inert but alert. Phys Medica. 2013;29(1):3-16.

122. Bouchiat MA, Carver TR, Varnum CM. Nuclear Polarization inHe3Gas Induced by Optical Pumping and Dipolar Exchange. Physical Review Letters. 1960;5(8):373-5.

123. Roos JE, McAdams HP, Kaushik SS, Driehuys B. Hyperpolarized Gas MR Imaging: Technique and Applications. Magn Reson Imaging Clin N Am. 2015;23(2):217-29.

124. Kirby M, Svenningsen S, Kanhere N, Owrangi A, Wheatley A, Coxson HO, et al. Pulmonary ventilation visualized using hyperpolarized helium-3 and xenon-129 magnetic resonance imaging: differences in COPD and relationship to emphysema. J Appl Physiol (1985). 2013;114(6):707-15.

125. Matheson AM, Thompson C, Parraga G. Chapter 14 - Inhaled Gas Magnetic Resonance Imaging: Advances, Applications, Limitations, and New Frontiers. In: Ross BD, Gambhir SS, editors. Molecular Imaging (Second Edition): Academic Press; 2021. p. 245-63.

126. Wolber J, Cherubini A, Dzik-Jurasz AS, Leach MO, Bifone A. Spin-lattice relaxation of laser-polarized xenon in human blood. Proc Natl Acad Sci U S A. 1999;96(7):3664-9.

127. Marshall H, Stewart NJ, Chan HF, Rao M, Norquay G, Wild JM. In vivo methods and applications of xenon-129 magnetic resonance. Prog Nucl Magn Reson Spectrosc. 2021;122:42-62.

128. Norquay G, Leung G, Stewart NJ, Wolber J, Wild JM. 129Xe chemical shift in human blood and pulmonary blood oxygenation measurement in humans using hyperpolarized 129Xe NMR. Magnetic Resonance in Medicine. 2017;77(4):1399-408.

129. Wolber J, Cherubini A, Leach MO, Bifone A. Hyperpolarized 129Xe NMR as a probe for blood oxygenation. Magnetic Resonance in Medicine. 2000;43(4):491-6.

130. Kaushik SS, Freeman MS, Yoon SW, Liljeroth MG, Stiles JV, Roos JE, et al. Measuring diffusion limitation with a perfusion-limited gas--hyperpolarized 129Xe gas-transfer spectroscopy in patients with idiopathic pulmonary fibrosis. J Appl Physiol (1985). 2014;117(6):577-85.

131. Kaushik SS, Robertson SH, Freeman MS, He M, Kelly KT, Roos JE, et al. Single-breath clinical imaging of hyperpolarized (129)Xe in the airspaces, barrier, and red blood cells using an interleaved 3D radial 1-point Dixon acquisition. Magn Reson Med. 2016;75(4):1434-43.

132. Bier EA, Robertson SH, Schrank GM, Rackley C, Mammarappallil JG, Rajagopal S, et al. A protocol for quantifying cardiogenic oscillations in dynamic (129) Xe gas exchange spectroscopy: The effects of idiopathic pulmonary fibrosis. NMR Biomed. 2019;32(1):e4029.

133. Willmering MM, Walkup LL, Niedbalski PJ, Wang H, Wang Z, Hysinger EB, et al. Pediatric (129) Xe Gas-Transfer MRI-Feasibility and Applicability. J Magn Reson Imaging. 2022;56(4):1207-19.

134. Weatherley ND, Stewart NJ, Chan HF, Austin M, Smith LJ, Collier G, et al. Hyperpolarised xenon magnetic resonance spectroscopy for the longitudinal assessment of changes in gas diffusion in IPF. Thorax. 2019;74(5):500-2.

135. Wang JM, Robertson SH, Wang Z, He M, Virgincar RS, Schrank GM, et al. Using hyperpolarized (129)Xe MRI to quantify regional gas transfer in idiopathic pulmonary fibrosis. Thorax. 2018;73(1):21-8.

136. Wang Z, Rankine L, Bier EA, Mummy D, Lu J, Church A, et al. Using hyperpolarized (129)Xe gas-exchange MRI to model the regional airspace, membrane, and capillary contributions to diffusing capacity. J Appl Physiol (1985). 2021;130(5):1398-409.

137. Mummy DG, Bier EA, Wang Z, Korzekwinski J, Morrison L, Barkauskas C, et al. Hyperpolarized (129)Xe MRI and Spectroscopy of Gas-Exchange Abnormalities in Nonspecific Interstitial Pneumonia. Radiology. 2021;301(1):211-20.

138. Myc L, Qing K, He M, Tustison N, Lin ZX, Manichaikul AW, et al. Characterisation of gas exchange in COPD with dissolved-phase hyperpolarised xenon-129 MRI. Thorax. 2021;76(2):178-81.

139. Li H, Zhao X, Wang Y, Lou X, Chen S, Deng H, et al. Damaged lung gas exchange function of discharged COVID-19 patients detected by hyperpolarized (129)Xe MRI. Sci Adv. 2021;7(1).

140. Grist JT, Chen M, Collier GJ, Raman B, Abueid G, McIntyre A, et al. Hyperpolarized (129)Xe MRI Abnormalities in Dyspneic Patients 3 Months after COVID-19 Pneumonia: Preliminary Results. Radiology. 2021;301(1):E353-E60.

141. Albert MS, Kacher DF, Balamore D, Venkatesh AK, Jolesz FA. T1 of 129Xe in Blood and the Role of Oxygenation. Journal of Magnetic Resonance. 1999;140:264-73.

142. West JB, West JB. Respiratory physiology--the essentials. 4th ed. Baltimore: Williams and Wilkins; 1990. x, 185 p. p.

143. Shukla Y, Wheatley A, Kirby M, Svenningsen S, Farag A, Santyr GE, et al. Hyperpolarized 129Xe magnetic resonance imaging: tolerability in healthy volunteers and subjects with pulmonary disease. Acad Radiol. 2012;19(8):941-51.

144. Driehuys B, Martinez-Jimenez S, Cleveland ZI, Metz GM, Beaver DM, Nouls JC, et al. Chronic obstructive pulmonary disease: safety and tolerability of hyperpolarized 129Xe MR imaging in healthy volunteers and patients. Radiology. 2012;262(1):279-89.

145. Walkup LL, Thomen RP, Akinyi TG, Watters E, Ruppert K, Clancy JP, et al. Feasibility, tolerability and safety of pediatric hyperpolarized (129)Xe magnetic resonance imaging in healthy volunteers and children with cystic fibrosis. Pediatr Radiol. 2016;46(12):1651-62.

146. Stewart NJ, Chan HF, Hughes PJC, Horn FC, Norquay G, Rao M, et al. Comparison of (3) He and (129) Xe MRI for evaluation of lung microstructure and ventilation at 1.5T. J Magn Reson Imaging. 2018.

147. Santyr G, Kanhere N, Morgado F, Rayment JH, Ratjen F, Couch MJ. Hyperpolarized Gas Magnetic Resonance Imaging of Pediatric Cystic Fibrosis Lung Disease. Academic Radiology. 2019;26(3):344-54.

148. Svenningsen S, McIntosh M, Ouriadov A, Matheson AM, Konyer NB, Eddy RL, et al. Reproducibility of Hyperpolarized (129)Xe MRI Ventilation Defect Percent in Severe Asthma to Evaluate Clinical Trial Feasibility. Acad Radiol. 2020.

149. Altes TA, Mugler JP, 3rd, Ruppert K, Tustison NJ, Gersbach J, Szentpetery S, et al. Clinical correlates of lung ventilation defects in asthmatic children. J Allergy Clin Immunol. 2016;137(3):789-96 e7.

150. Marshall H, Voskrebenzev A, Smith LJ, Biancardi AM, Kern AL, Collier GJ, et al. 129Xe and Free-Breathing 1H Ventilation MRI in Patients With Cystic Fibrosis: A Dual-Center Study. Journal of Magnetic Resonance Imaging.n/a(n/a).

151. Svenningsen S, Kirby M, Starr D, Leary D, Wheatley A, Maksym GN, et al. Hyperpolarized (3) He and (129) Xe MRI: differences in asthma before bronchodilation. J Magn Reson Imaging. 2013;38(6):1521-30.

152. Svenningsen S, Haider EA, Eddy RL, Parraga G, Nair P. Normalisation of MRI ventilation heterogeneity in severe asthma by dupilumab. Thorax. 2019.

153. McIntosh MJ, Kooner HK, Eddy RL, Jeimy S, Licskai C, Mackenzie CA, et al. Asthma control, Airway mucus and (129)Xe MRI ventilation after a single Benralizumab dose. Chest. 2022.

154. Barker AL, Eddy RL, MacNeil JL, McCormack DG, Kirby M, Parraga G. CT Pulmonary Vessels and MRI Ventilation in Chronic Obstructive Pulmonary Disease: Relationship with worsening FEV(1) in the TINCan cohort study. Acad Radiol. 2021;28(4):495-506.

155. Kooner HK, McIntosh MJ, Matheson AM, Venegas C, Radadia N, Ho T, et al. ¹²⁹Xe MRI ventilation defects in ever-hospitalised and never-hospitalised people with post-acute COVID-19 syndrome. BMJ Open Respiratory Research. 2022;9(1):e001235.

156. Cleveland ZI, Cofer GP, Metz G, Beaver D, Nouls J, Kaushik SS, et al. Hyperpolarized Xe MR imaging of alveolar gas uptake in humans. PLoS One. 2010;5(8):e12192.

157. Hersman FW, Ruset IC, Ketel S, Muradian I, Covrig SD, Distelbrink J, et al. Large production system for hyperpolarized 129Xe for human lung imaging studies. Acad Radiol. 2008;15(6):683-92.

158. Freeman MS, Emami K, Driehuys B. Characterizing and modeling the efficiency limits in large-scale production of hyperpolarized (129)Xe. Phys Rev A. 2014;90(2):023406.

159. Driehuys B, Cofer GP, Pollaro J, Mackel JB, Hedlund LW, Johnson GA. Imaging alveolar-capillary gas ttransfer using hyperpolarized 129Xe MRI. Proceedings of the National Academy of Sciences of the United States of America. 2006;103(48):18278-83.

160. Ruppert K, Brookeman JR, Hagspiel KD, Mugler JP, 3rd. Probing Lung Physiology with Xenon Polarization Transfer Contrast (XTC). Magn Reson Med. 2000;44:349-57.

161. Dixon WT. Simple proton spectroscopic imaging. Radiology. 1984;153(1):189-94.

162. Doganay O, Wade T, Hegarty E, McKenzie C, Schulte RF, Santyr GE. Hyperpolarized 129Xe imaging of the rat lung using spiral IDEAL. Magnetic Resonance in Medicine. 2016;76(2):566-76.

163. Muradian I, Patz S, Butler JP, Topulos GP, Hrovat MI, Covrig S, et al. Hyperpolarized 129Xe Human Pulmonary Gas Exchange with 3-point Dixon Technique. Proceedings of the International Society for Magnetic Resonance in Medicine. 2006;14.

164. Collier GJ, Eaden JA, Hughes PJC, Bianchi SM, Stewart NJ, Weatherley ND, et al. Dissolved (129) Xe lung MRI with four-echo 3D radial spectroscopic imaging: Quantification of regional gas transfer in idiopathic pulmonary fibrosis. Magn Reson Med. 2021;85(5):2622-33.

165. Mata J, Guan S, Qing K, Tustison N, Shim Y, Mugler JP, 3rd, et al. Evaluation of Regional Lung Function in Pulmonary Fibrosis with Xenon-129 MRI. Tomography. 2021;7(3):452-65.

CHAPTER 2

2 A LINEAR SYSTEMS DESCRIPTION OF MULTI-COMPARTMENT PULMONARY ^{129}XE MAGNETIC RESONANCE IMAGING METHODS

To better understand the evolution of ^{129}Xe MR signals in each gas-exchange compartment, I developed a linear systems model of image acquisition using the one-point Dixon technique to model how signal mixing, RF pulse shape, decay processes and reconstruction impact final images.

The contents of this chapter were previously published in the proceedings of SPIE: Alexander M Matheson, Grace Parraga and Ian A Cunningham. Proc SPIE 2021; 11600. Copyright of this article was maintained by the authors. Since publishing the term "membrane" has become preferred in the literature to "barrier" – the original term used in publishing is maintained here for fidelity.

2.1 Introduction

In patients with chronic lung diseases such as asthma and COPD, functional lung imaging using xenon-129 magnetic resonance imaging (^{129}Xe MRI) methods provides a way to quantify functional abnormalities or "ventilation defects".[1-3] Recently however, the entire process- from inhalation of the gas to transmembrane diffusion and delivery to the blood may be quantified on a regional basis using multi-compartment (gas, tissue, blood) ^{129}Xe MRI methods. These methods have been pioneered to explore and quantify the pathologies that drive breathlessness, severe exercise limitation and poor quality of life in patients. By taking advantage of the modest solubility of ^{129}Xe in biologic tissues,[4] spectroscopic MR methods may be used to detect, measure and image the distinct ^{129}Xe resonant frequencies as the atom fills the airspaces, diffuses through the alveolar membrane and into the plasma and red-blood-cell (RBC) membranes.[5] Multi-compartment (and

sometimes called "dissolved phase") ^{129}Xe MRI presents numerous obstacles to high spatial resolution imaging, including a 20 times lower signal in tissue and RBC compartments[6] than in the gaseous phase, an extremely low $T2^*$ for xenon in the lung (on the order of 2ms at 1.5T for dissolved xenon[7]) and an overlap of xenon resonant frequencies when resident in tissue and RBC. To overcome these challenges, a single-point Dixon technique has been developed[8,9] to simultaneously acquire and split the signal emanating from the three separate compartments by taking advantage of MRI quadrature hardware. Because MR acquisitions require ultra-fast speed to capture the xenon signal, post processing techniques are required to correct for phase evolution, magnetic inhomogeneities, and non-Cartesian acquisition trajectories.[9] To our knowledge, a complete mathematical and graphical framework does not exist to generate accurate and quantifiable models of multi-compartment ^{129}Xe MRI. To date, modelling has been limited to common relaxation terms,[7] however a general model may better describe more complex physiology such as the effects of surfactant (or abnormal surfactant-alveolar membrane homeostasis), plasma and/or epithelial peak effects or other tissues with heterogeneous relaxation properties.

2.2 Methods

2.2.1 Image Acquisition

MRI acquisition parameters were specified for a whole-body 3T Discovery MR350 scanner with broadband capabilities (General Electric Health Care, Wisconsin, USA) using a quadrature vest coil (Clinical MR Solutions, WI, USA). Multi-compartment imaging was specified according to a single-point Dixon scheme. Imaging was modelled according to a 3D radial pulse sequence (TR = 7.5ms; flip-angle=$1^o/22^o$; bandwidth = 31.25 kHz; field-of-view = 40x40x40cm; matrix = 32x32x32; 1001 rays; 79 samples/ray) with interleaved gas-compartment and dissolved

compartment k-space trajectories by alternating RF carrier frequency (208ppm) during a 15s during breath-hold. The pulse sequence diagram for the acquisition sequence is shown in **Figure 2-1**.

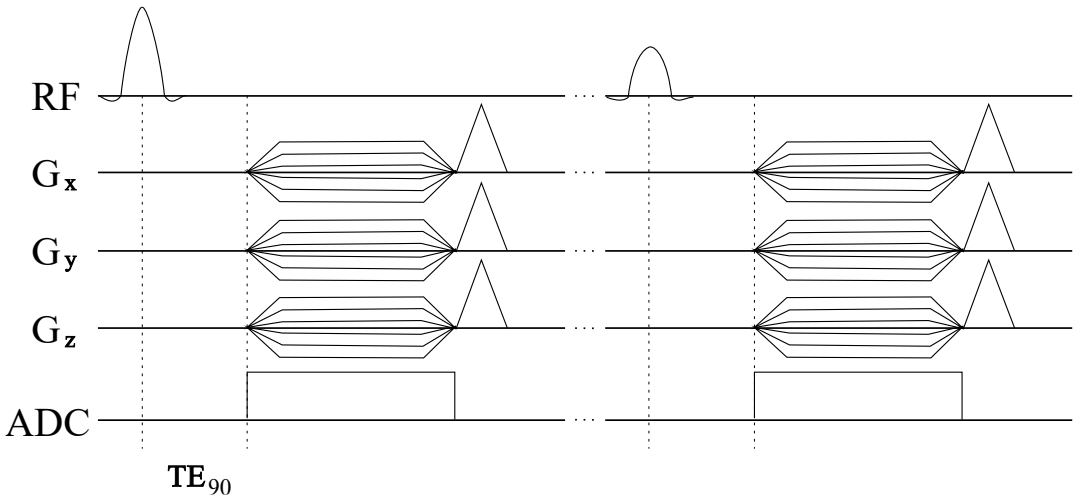

Figure 2-1 Pulse sequence diagram of MR imaging sequence (not to scale).
RF flip angles are 1° and 22° respectively. The sequence alternates between imaging of dissolved and gas compartments, represented by the left and right diagrams above. Gradients are activated after a delay time TE_{90} alongside the analogue to digital converter (ADC). Finally, spoiler gradients destroy any residual transverse magnetization.

2.2.2 Linear Systems Analysis

We employed a linear-systems model to describe free-induction-decay (FID) excitation, FID acquisition, domain transformation, and post-processing corrections required to produce simultaneous ventilation, tissue, and RBC images. For this analysis, we assumed that all systems were linear (or could be closely approximated as linear under certain conditions) and shift invariant.

Following inhalation of gases, ^{129}Xe enters the lung alveoli in the gas compartment. Due to a modest Ostwald solubility (~0.09 in blood plasma)[4], ^{129}Xe atoms immediately begin to diffuse across the alveolar septum and into the plasma where they also bind to red-blood-cells. In the

presence of a strong magnetic field, each compartment exhibits a characteristic resonance frequency represented as local magnetization $s(t)$ in the time domain and an associated representation in the frequency domain $S(\omega)$. Magnetic precession may be represented as a sum of complex exponentials in the time domain or a series of delta functions in the frequency domain:

$$s(t) = \sum_{j \in \Phi} a_j \exp(i\omega_j t), \ \Phi = \{gas, tissue, RBC\} \quad (1)$$

$$S(\omega) = \sum_{j \in \Phi} A_j \delta(\omega - \omega_j) \quad (2)$$

Disconnecting the measurements from the unique different ^{129}Xe compartments is crucial to understanding their related and different pathophysiological processes in the lung. This is challenging because of the spectroscopic overlap of resonant frequency peaks. For example, distinguishing the independent tissue and RBC signal peaks is especially challenging due to a small chemical shift (~19ppm[10]) between peaks. However, by acquiring data when these two compartments (peaks) are 90° out-of-phase (denoted time to echo for 90°, TE_{90}), each compartment may be aligned with either the real or imaginary quadrature channel.

To achieve this, MRI acquisitions were made possible during a feasible breath-hold timeframe by using a fast, 3D radial k-space trajectory. For simplicity, the model was visualized in one dimension along a radial trajectory for a single ^{129}Xe source. A 3D model may be conceptualized by adding together the rays in both k-space and the associated Fourier-transforms in image-space.

2.3 Results

2.3.1 RF Excitation

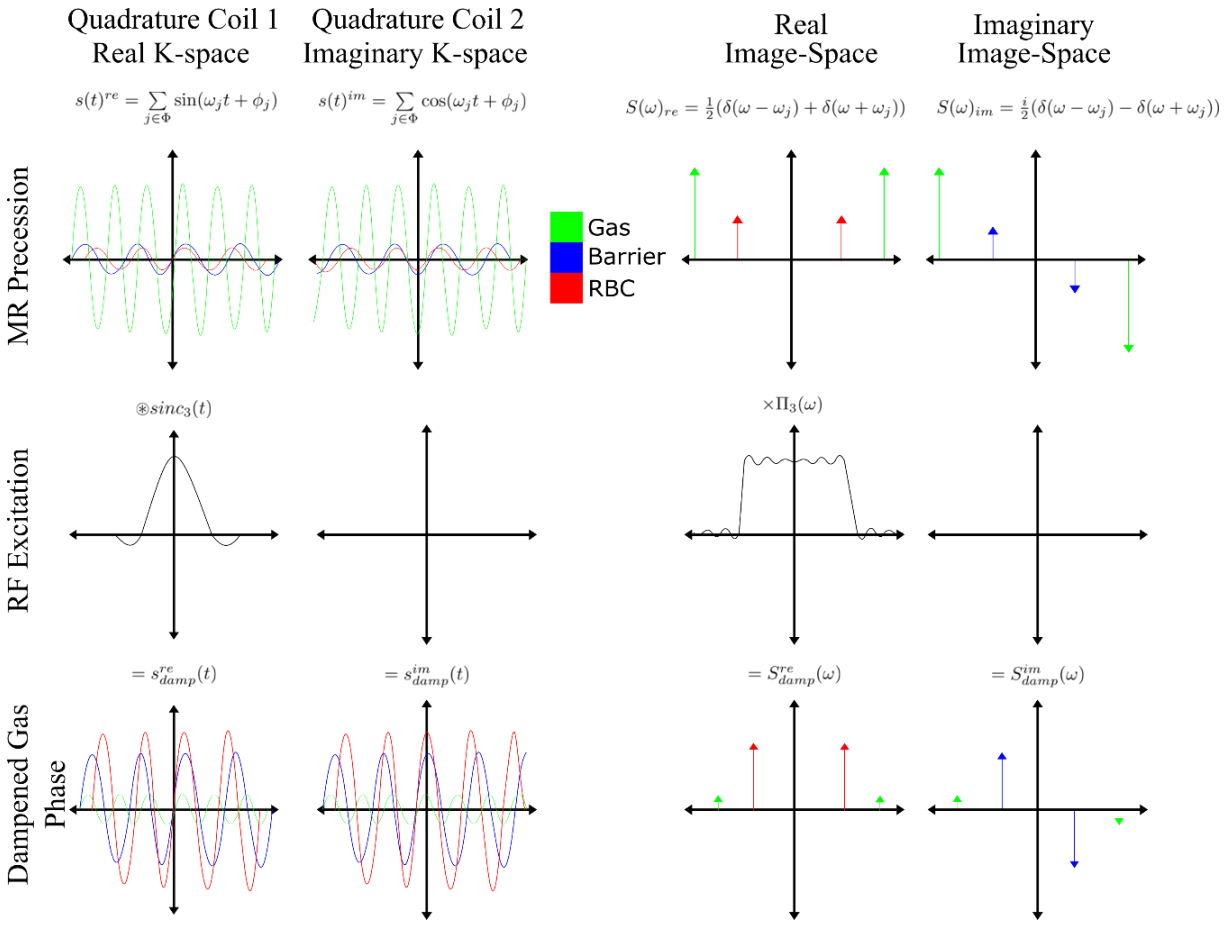

Figure 2-2 The effect of selective RF pulses on three compartments of xenon in vivo.
The magnetic precession signal s(t) is excited by an RF pulse to produce a signal $s_{damp}(t)$ with tissue and RBC compartments excited and the gas compartment dampened. Barrier and RBC images are assumed to be in perfect alignment with the real and imaginary channels for this analysis; misalignment is retrospectively corrected in practice. An imperfect square pulse in the frequency domain results in minor excitation of the gas compartment signal in the stop band.

RF excitation is typically non-linear but may be approximated as a Fourier transform between the RF amplitude in the time domain and spin response in the frequency domain for low flip angles[11] ($\alpha<30^o$). Whilst a rectangular excitation window of width $\Delta\omega$ is desirable in the frequency domain, breath-hold time limits mean that the excitation must be approximated using a single lobe sinc

pulse in the time domain. A single-lobe Shinnar-Le Roux pulse used for excitation may be approximated by multiplying a sinc pulse with a rectangular pulse of width *Δt* in the time domain.

$$rf(t) = 2\,\mathrm{sinc}(\tfrac{\Delta\omega t}{2}) \times \Pi_{\Delta t}(t) \quad (3)$$

$$RF(\omega) = \Pi_{\Delta\omega}(\omega) \circledast 2\,\mathrm{sinc}(\tfrac{\Delta t\omega}{2}) \quad (4)$$

Due to the much larger gas signal, ringing in the tissue and RBC compartment excitation causes some contamination of the excitation due to convolution (denoted by $\circledast$), as shown in **Figure 2-1**.

2.3.2 Line Broadening

Magnetization evolution following excitation results in exponential decay with a time constant T_2^* in the time domain. This may be represented by multiplication by an exponential decay function *f(t)* in the positive time domain, which is equivalent to convolution with a complex Lorentzian distribution in the frequency domain.

$$f(t) = \exp(-\tfrac{t}{T_2^*}),\ t > 0 \quad (5)$$

$$F(t) = \tfrac{1}{1+\omega^2 T_2^{*2}} - i\tfrac{\omega T_2^{*2}}{1+\omega^2 T_2^{*2}} \quad (6)$$

Spatial encoding of MRI data is accomplished with magnetic gradients and recorded as an "echo"; the Dixon method is not considered a true echo as there is no signal refocusing. While the gradient is active, sub-voxel dephasing occurs due to the difference in magnetic field across the voxel, in a similar manner to T_2^* decay. This decay is represented by a dispersion function *d(t)* that may be calculated by integrating over the phase distribution of a voxel as shown in equation 7.

$$d(t) = \frac{1}{V}\int_V \exp(i\Delta\omega_j(x,y,z)t)dV \quad (7)$$

Phase difference is accrued according to the local Larmor frequency. For radial acquisitions such as those used in the Dixon technique, gradients in the x, y, and z directions are simultaneously activated to produce a linear gradient along a desired radial direction, denoted here as *r*. As the net gradient only varies along *r*, this reduces to a one-dimensional integral as shown in equation 8.

$$d(t) = \frac{1}{\Delta r}\int_{\frac{-\Delta r}{2}}^{\frac{\Delta r}{2}} \exp(i\gamma G_r r t)dr \qquad (8)$$

$$d(t) = \mathrm{sinc}\left(\gamma G_r \frac{\Delta r}{2} t\right) \qquad (9)$$

Note that the dispersion function is normalized to *d(0)* = 1 in equation 9. In k-space, this process causes blurring due to convolution with a rectangular (the sinc Fourier transform pair) dispersion function *D(ω)*.

$$D(w) = \frac{4\pi}{|\gamma G_r \Delta r|}\Pi\left(\frac{\omega}{\gamma G_r \Delta r}\right) \qquad (10)$$

Dephasing does not begin immediately but following a delay of TE_{90} as shown in equation 11 to ensure that tissue and RBC compartments are 90° out of phase when the gradients are activated. According to the Fourier shift theorem, this is reflected in an additional exponential term in the frequency domain.

$$d(t) = \mathrm{sinc}\left(\gamma G_r \frac{\Delta r}{2}(t - TE_{90})\right) \qquad (10)$$

$$D(w) = \frac{4\pi}{|\gamma G_r \Delta r|}\Pi\left(\frac{\omega}{\gamma G_r \Delta r}\right)\exp(-i\omega TE_{90}) \qquad (12)$$

Figure 2-2 shows the impact of both $T2^*$ decay and gradient de-phasing on the magnetic precession signal.

2.3.3 Gradient Encoding

Until this point, the frequency response of ^{129}Xe has been modeled with individual frequencies ω_{tissue} and ω_{RBC}. However, spatial information is imparted to the signal by frequency encoding gradients that shift the resonance frequency such that $\omega_j = \omega_j(x,y,z)$. The total signal is the sum of spin signals across all space:

$$\omega_j(t) = \omega_{0,j} + \gamma \int_0^t (g_x(t') + g_y(t') + g_z(t'))dt' \tag{13}$$

$$s(t) = \int_x \int_y \int_z \sum_{j\in\Phi} \rho_j(x,y,z) \exp(i\omega_j(x,y,z)t)dxdydz \tag{14}$$

2.3.4 Free-induction Decay Acquisition and Demodulation

Data from quadrature channels are acquired separately and processed through an analog-to-digital converter (ADC) in the time domain. The recording period of the ADC may be represented mathematically by multiplying the continuous signal by rectangular unit-height window of width τ in the time domain, as shown in **Figure 2-4**, which corresponds to convolution with a sinc pulse in the frequency domain. This 'ringing' in the frequency domain cause spectral leakage of the signal of interest as well as ringing from the gas compartment contamination.

The ADC samples signal during the recording window which may be represented by multiplication with a Dirac comb function in the time domain to generate samples spaced according to dwell time Δt, which may be represented by convolution by a Dirac comb with spacing Δt^{-1} in the frequency domain. Following sampling, the data from each quadrature orientation were separated and each treated as "real" signals, with one representing the tissue compartment and the other, the RBC compartment.

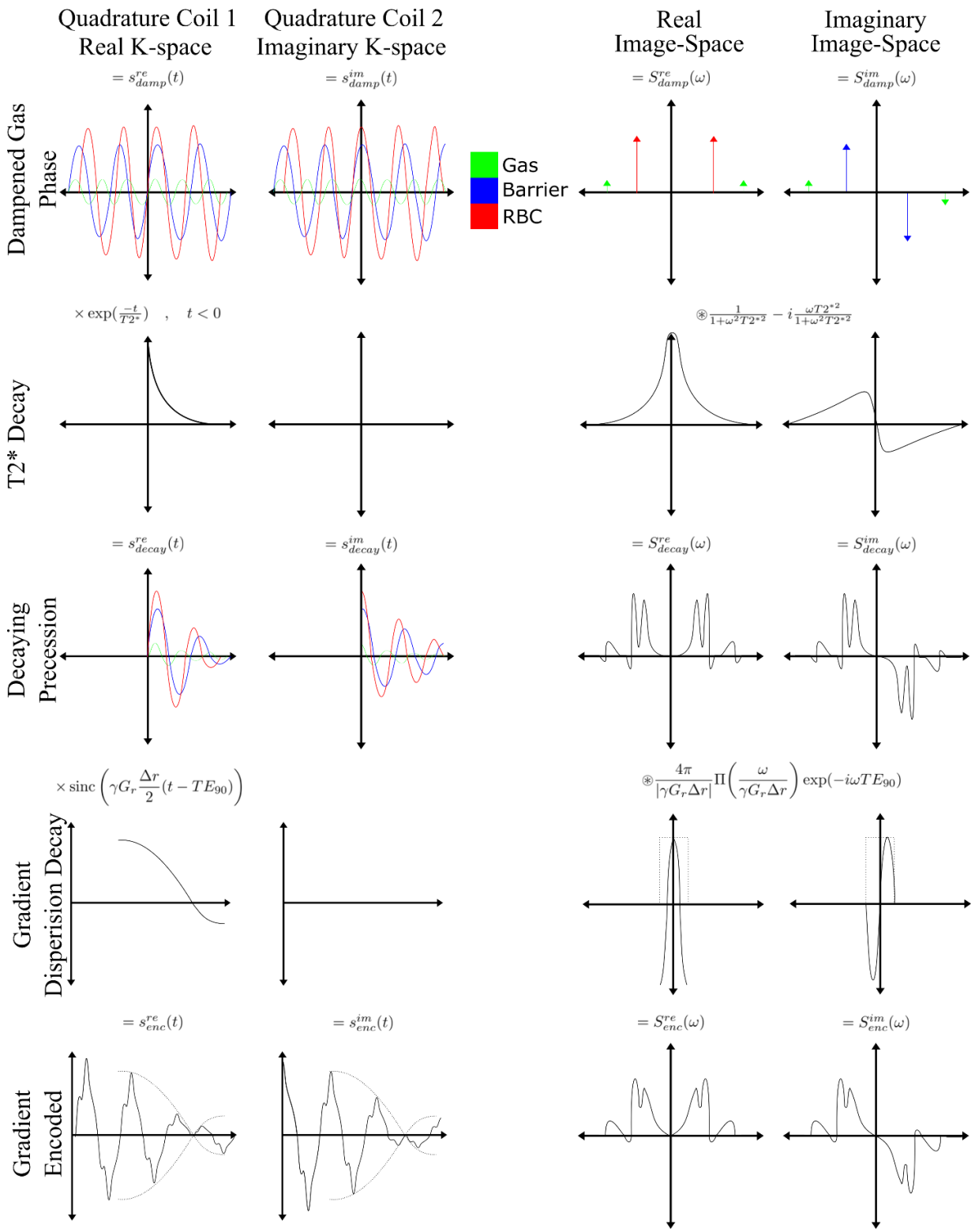

Figure 2-3 Signal decay over time due to magnetic relaxation.
Relaxation stems from spin-spin interactions in inhomogeneous fields ($T2^*$) as well as deliberately applied gradient echos. The excited spins magnetization, $s_{damp}(t)$, decay over time as shown by $s_{decay}(t)$. Dotted lines denote envelopes of gradient de-phasing.

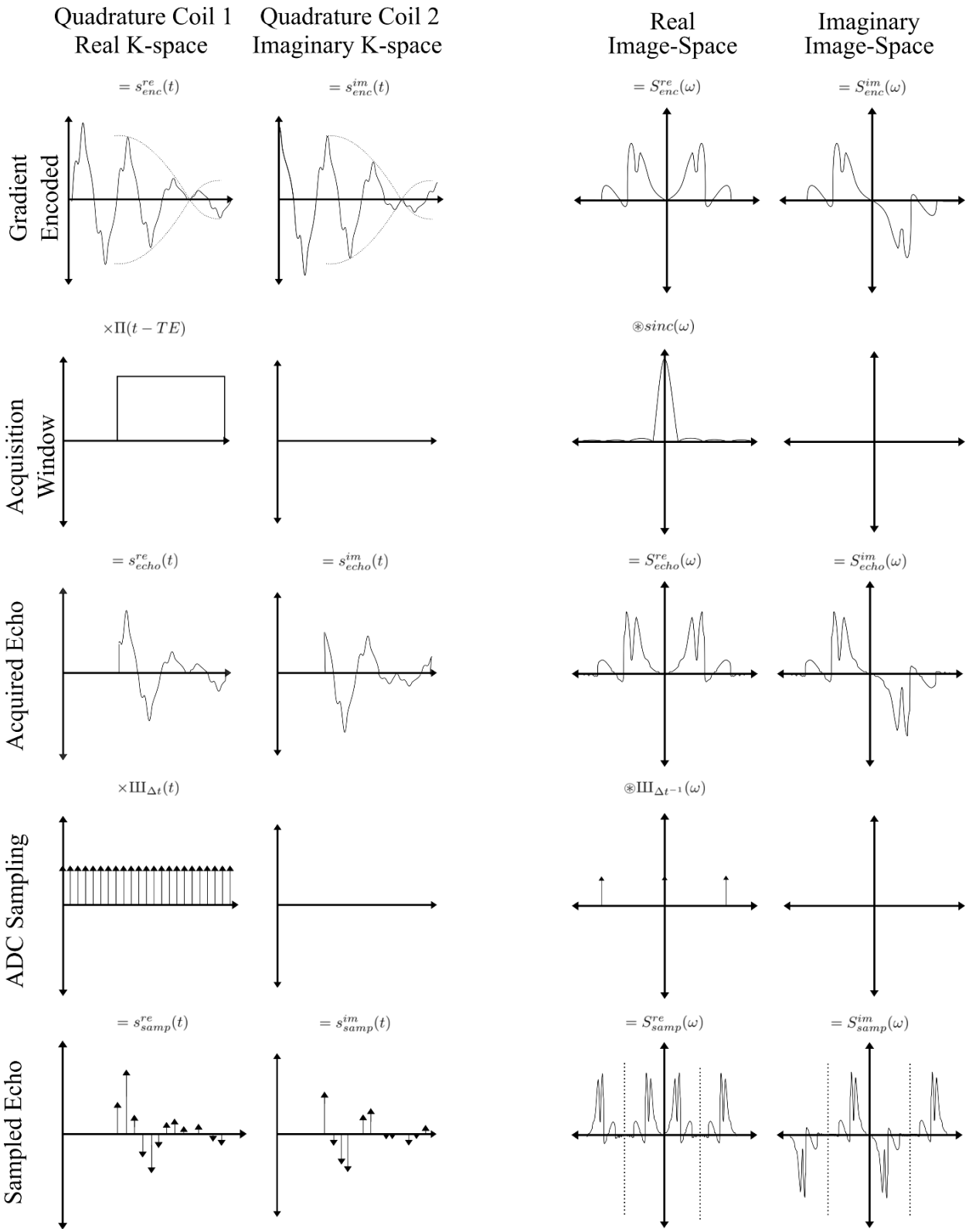

Figure 2-4 Sampling of the FID performed by analog-to-digital converter (ADC).
Dotted lines in the k-space representations represent the boundaries of the Nyquist limit. The frequency encoded signal $s_{enc}(t)$ is acquired as an "echo" $s_{echo}(t)$ by the ADC and sampled, $s_{samp}(t)$.

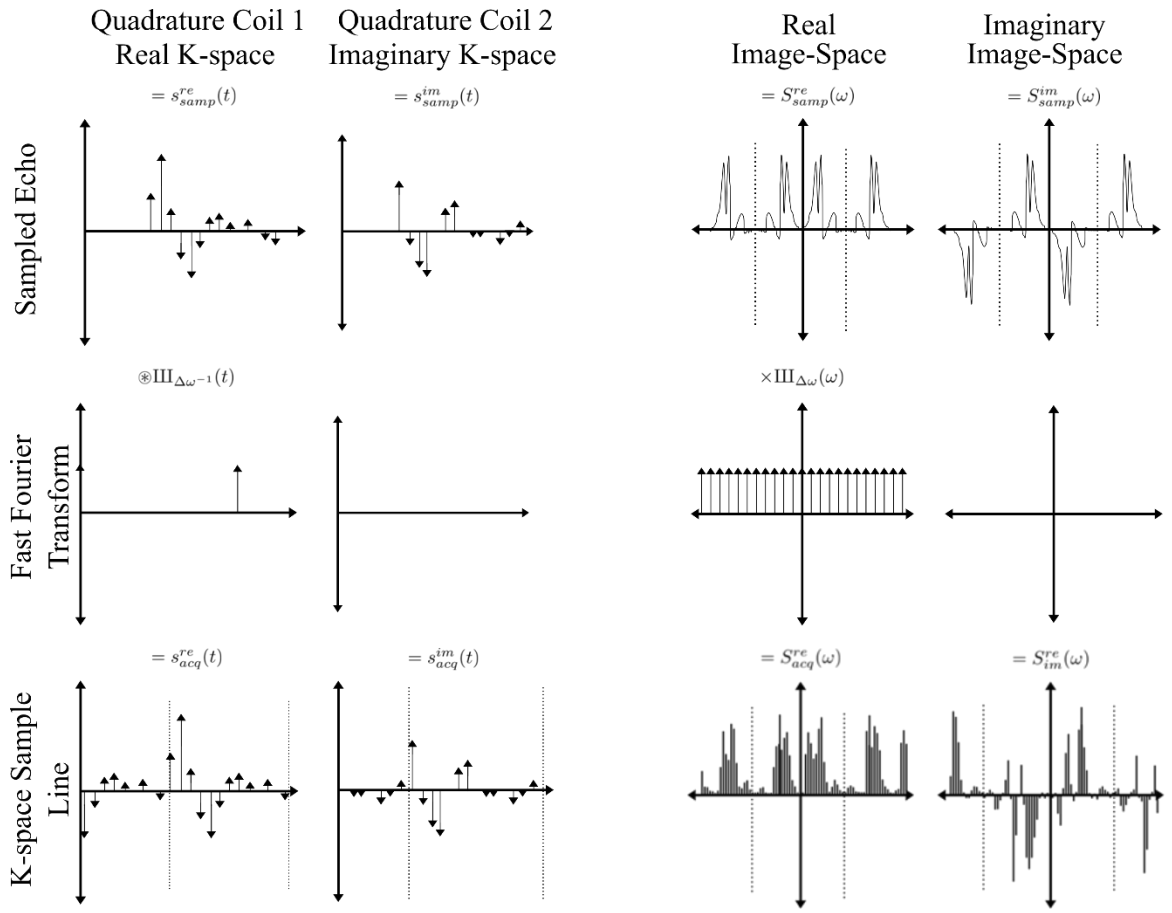

Figure 2-5 Discrete Fourier transformation (DFT)
A DFT may be represented as a convolution of the sampled distribution $S_{samp}(\omega)$ with a Dirac comb, resulting in discretized k-space samples $S_{acq}(\omega)$ with possible spectral leakage artifacts

The discrete, time-series data are used to obtain image data points through a discrete Fourier transform (DFT), as shown in **Figure 2-4**. This is represented by sampling (multiplying) with a Dirac comb in the frequency domain with uniform spacing $\omega_s = 2\omega_{ny}/N$ where ω_{ny} is the Nyquist frequency and N the number of samples.

Each acquisition traced out a radial trajectory through k-space, which when superimposed evenly created a separate, radially sampled distribution of discrete k-space for each xenon compartment.

2.3.5 Non-uniform Fast Fourier Transform

A three-dimensional radial k-space sampling scheme is used to ensure complete data acquisition within a breath hold and to make results more robust against motion artifacts. Because of a non-uniform sampling scheme, a traditional fast-Fourier transform (FFT) is not possible to convert k-space data to the image domain. The computational cost and time required for a discrete Fourier transform is undesirable, therefore a non-uniform fast-Fourier transform (NUFFT) algorithm is used.[12] The NUFFT algorithm convolves all discrete sample points with a sampling function to reconstruct an estimate of the original continuous k-space function. The continuous estimate is then re-sampled to a Cartesian grid for use in an FFT. The choice of sampling function $\Psi(k_x, k_y, k_z)$ dictates the accuracy of the method and the NUFFT algorithm solves a least-squares problem to determine a function with the minimum error based on the sampling distribution used.[12] This implementation has the benefit of being linear, shift invariant, and consistent for all acquisitions once the scheme specific $\Psi(k_x, k_y, k_z)$ is calculated.[12] First, the discrete points are convolved with the derived sampling function to reconstruct the continuous representation followed by multiplication with a Cartesian-spaced (t_c) Dirac comb in k-space to create a new set of discrete points. Gas, tissue, and RBC images may then be obtained through a three-dimensional DFT of the corresponding k-space pair, similarly to the one-dimensional DFT in section 3.4.

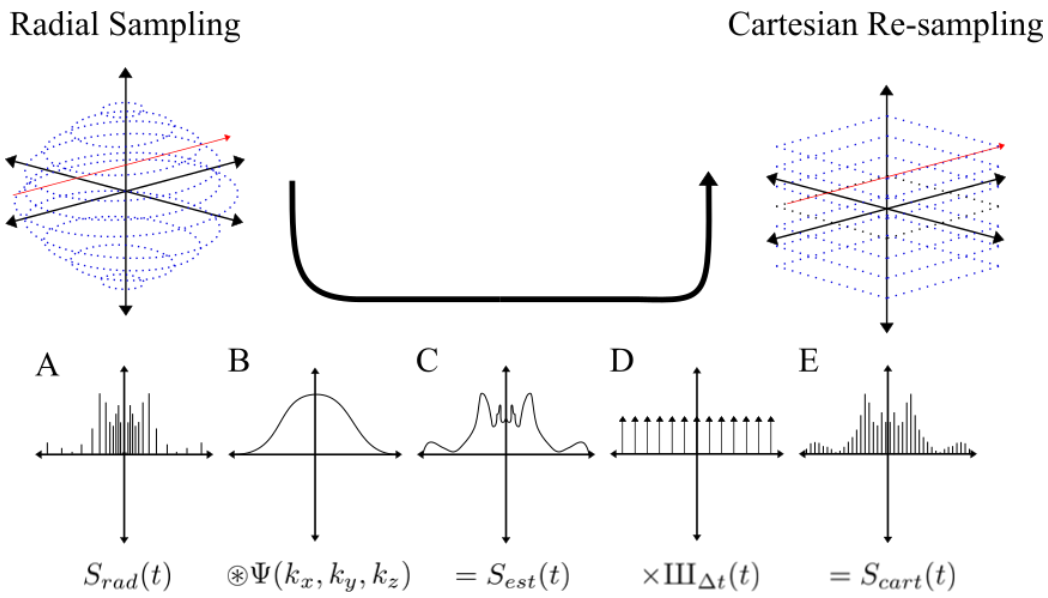

Figure 2-6 Spatial resampling from a radial to a Cartesian coordinate system performed during non-uniform fast Fourier transform (NUFFT).
A one-dimensional strip of the 3D radial distribution is considered, shown as a red trajectory in the radial sampling diagram. Resampling results in data points equally distributed in x, y, and z axes that may be transformed using a standard FFT. A single trajectory $S_{rad}(\omega)$ is convolved with a sampling function $\Psi(k_x, k_y, k_z)$ to reconstruct the continuous function $S_{est}(\omega)$ from which $S_{cart}(\omega)$ is sampled.

2.3.6 Post-processing Corrections

The one-point Dixon method requires the tissue and RBC magnetic phases to be precisely 90° out-of-phase and aligned with orthogonal quadrature coils. Local magnetic field inhomogeneities, however, prevent a uniform phase difference at all points in space. Since the gas compartment is acquired in both quadrature coils, local phase information may be calculated. In a uniform field, the gas compartment should have uniform phase. Therefore, any phase deviation $\Delta\theta$ is purely due to inhomogeneities and an opposite direction shift may be applied to all images as a correction.

Finally, although TE_{90} ensures tissue and RBC phases are 90° out-of-phase the final orientation is not guaranteed to be parallel to the quadrature orientation due to a system specific offset ϕ_0. A correction, $\Delta\phi$, may be derived from the calibration NMR spectra by determining the ratio *R* of the

areas of the tissue peak to the RBC peak. $\Delta\phi$ may be determined by applying phase shifts from 0° to 180° to the tissue and RBC images and determining $\Delta\phi$ that best matches *R*.

$$S^{\dagger}_{tissue}(x,y,z) = S_{tissue}(x,y,z)\exp(i\Delta\theta(x,y,z))\exp(i\Delta\phi) \qquad (11)$$

2.4 New or Breakthrough Work

We developed a linear systems description of the multi-compartment, single-point Dixon hyperpolarized gas MRI method that allows for a mathematical and graphical description of the free-induction decay, k-space and resultant images. For the first time, this approach provides a step-by-step breakdown of the origins and the mixing of signals from different compartments. This provides a foundation for describing acquisition optimizations through parameter tuning and for the characterization of peak shape in heterogeneous or abnormal tissues.

2.5 Discussion and Conclusion

This work considered the single-point Dixon method as a perfectly linear, shift invariant system. While the assumptions made in this work suitably approach linearity, some small deviations from these approximations, such as the non-linearity of the Bloch equations, must be acknowledged. Minor but non-trivial magnetic field inhomogeneities and the dielectric properties of human tissue also introduce some shift-invariance across space. The least-squares approximation of a sampling interpolation also introduces inaccuracies.

We developed a graphical and mathematical linear systems analysis of the acquisition and post processing steps required for image generation. This model describes all steps as a series of multi-channel, multi-domain operations using only multiplication and convolution shift-invariant

processes. This model will permit simulation and quantification of compartment overlap due to imperfections and phase evolution not currently accounted for multi-compartment studies. Future refinement of Shinnar-Le Roux pulse shape and NUFFT sampling distribution shapes will allow calculation of the degree of overlap between target compartments and contaminating compartments as well as simulations of k-space artifacts due to magnetization evolution.

The linear systems model we constructed considered both time and frequency domains as separable into both real and imaginary components. Because of quadrature separation, these components provide a deeper understanding of the shapes of individual peaks as opposed to simply considering the magnitude in either domain. Instead, it is useful to think of the signal in the image domain as a complex vector that projects onto real and imaginary planes. Ideally, a phase difference of 90° aligns these vectors entirely in real or imaginary planes, however phase differences act to rotate the vector and split the signal between real and imaginary components.

Current multi-compartment ^{129}Xe MRI research focuses on gas, plasma, RBC, and tissue barrier compartments,[5,7,9,13] Current three and four-compartment models also do not incorporate different lipid structures (e.g. surfactant) or tissues (e.g. epithelium) present in lung alveolar and airway system. By developing a more generalized model of multi-compartment MRI, future work will help to model new compartments or tissues with heterogeneous properties (e.g. T2*) using inhaled ^{129}Xe MRI.

2.6 References

1. Dregely I, Mugler JP, 3rd, Ruset IC, Altes TA, Mata JF, Miller GW, et al. Hyperpolarized Xenon-129 gas-exchange imaging of lung microstructure: first case studies in subjects with obstructive lung disease. J Magn Reson Imaging. 2011;33(5):1052-62.

2. Driehuys B, Martinez-Jimenez S, Cleveland ZI, Metz GM, Beaver DM, Nouls JC, et al. Chronic obstructive pulmonary disease: safety and tolerability of hyperpolarized 129Xe MR imaging in healthy volunteers and patients. Radiology. 2012;262(1):279-89.

3. Kirby M, Svenningsen S, Kanhere N, Owrangi A, Wheatley A, Coxson HO, et al. Pulmonary ventilation visualized using hyperpolarized helium-3 and xenon-129 magnetic resonance imaging: differences in COPD and relationship to emphysema. J Appl Physiol (1985). 2013;114(6):707-15.

4. Chen RYZ, Fan FC, Kim S, Jan KM, Usami S, Chien S. Tissue-blood partition coefficient for xenon: temperature and hematocrit dependence. Journal of Applied Physiology. 1980;49(2):178-83.

5. Sakai K, Bilek K, Oteiza E, Walsworth RL, Balamore D, Jolesz FA, et al. Temporal Dynamics of Hyperpolarized 129Xe Resonances in Living Rats. Journal of Magnetic Resonance. 1996;111:300-4.

6. Sato H, Enmi J, Hayashi T, Takei N, Iwadate Y, Abe S, et al. Development of a hyperpolarized 129Xe system on 3T for the rat lungs. Magn Reson Med Sci. 2004;3(1):1-9.

7. Kammerman J, Hahn AD, Cadman RV, Malkus A, Mummy D, Fain SB. Transverse relaxation rates of pulmonary dissolved-phase Hyperpolarized (129) Xe as a biomarker of lung injury in idiopathic pulmonary fibrosis. Magn Reson Med. 2020;84(4):1857-67.

8. Kaushik SS, Freeman MS, Cleveland ZI, Davies J, Stiles J, Virgincar RS, et al. Probing the regional distribution of pulmonary gas exchange through single-breath gas- and dissolved-phase 129Xe MR imaging. J Appl Physiol (1985). 2013;115(6):850-60.

9. Kaushik SS, Robertson SH, Freeman MS, He M, Kelly KT, Roos JE, et al. Single-breath clinical imaging of hyperpolarized (129)Xe in the airspaces, barrier, and red blood cells using an interleaved 3D radial 1-point Dixon acquisition. Magn Reson Med. 2016;75(4):1434-43.

10. Driehuys B, Cofer GP, Pollaro J, Mackel JB, Hedlund LW, Johnson GA. Imaging alveolar-capillary gas ttransfer using hyperpolarized 129Xe MRI. Proceedings of the National Academy of Sciences of the United States of America. 2006;103(48):18278-83.

11. Wu S, Ma H, Iya P, David S, Pasa-Tolic L. The Encyclopedia of Spectroscopy and Spectrometry, 3rd edition2017.

12. Song J, Liu Y, Gewalt SL, Cofer G, Johnson GA, Liu QH. Least-square NUFFT methods applied to 2-D and 3-D radially encoded MR image reconstruction. IEEE Trans Biomed Eng. 2009;56(4):1134-42.

13. Niedbalski PJ, Bier EA, Wang Z, Willmering MM, Driehuys B, Cleveland ZI. Mapping cardiopulmonary dynamics within the microvasculature of the lungs using dissolved (129)Xe MRI. J Appl Physiol (1985). 2020;129(2):218-29.

CHAPTER 3

3 PERSISTENT ^{129}XE MRI PULMONARY AND CT VASCULAR ABNORMALITIES IN SYMPTOMATIC INDIVIDUALS WITH POST-ACUTE COVID-19 SYNDROME

To understand the mechanisms underlying disease in people with post-acute COVID-19 syndrome, we performed ^{129}Xe MRI and pulmonary CT in never- and ever-hospitalized participants with PACS. We compared MR and CT measurements to clinical and participant-reported measures of lung health to relate gas-exchange abnormalities to symptoms, exercise capacity and quality-of-life.

The contents of this chapter were previously published in Radiology: Alexander M Matheson, Marrissa J McIntosh, Harkiran K Kooner, Justin Lee, Vedanth Desaigoudar, Elianna Bier, Bastiaan Driehuys, Sarah Svenningsen, Giles E Santyr, Miranda Kirby, Mitchell S Albert, Yurii Shepelytskyi, Vira Grynko, Alexei Ouriadov, Mohamed Abdelrazek, Inderdeep Dhaliwal, J Michael Nicholson, Grace Parraga. Radiology 2022; 305(2):466-476. As author of the original article, Radiology does not require permission to re-use beyond citing the original source. Since publishing this manuscript, long-COVID has become the accepted term for long-term sequelae following COVID infection. The term PACS is maintained in this chapter as it was relevant to the discussion of different post-COVID definitions. The term "membrane" has also become preferred in the literature to "barrier."

3.1 Introduction

The acute and post-acute phase of SARS-CoV-2 infection presents with a variety of symptoms,[1] in patients who experienced mild infection[2] and those hospitalized with more severe infection, requiring hospital-based care.[3] The prevalence of post-acute COVID-19 symptomatic findings, including dyspnea at rest and on exertion, tachypnea, fatigue, exercise limitation, muscle weakness and cognition deficits, ranges from 20%[4] to 81%.[3] Such symptoms have been described with the

umbrella term “post-acute COVID-19 syndrome” (PACS) defined as persistent symptoms or sequelae at least 12 weeks post-infection.[5] Post-acute COVID symptoms are difficult to treat because the literature has reported varying degrees of abnormality in spirometry (FEV_1 2-20% below LLN [lower limit of normal])[6,7] and diffusing-capacity-of-the-lung for carbon-monoxide (22-88% below LLN)[6,7] alongside various CT abnormalities including ground glass opacities (41-89% present),[6,7] reticular patterns (0-67% present)[6,7] and atelectasis (33% present).[7] A recent study showed that never-hospitalized patients also reported normal or nearly normal pulmonary function tests (6-37% abnormal at 4-month follow-up)[8] and imaging was rarely available in these patients. A recent CT pulmonary vascular investigation in hospitalized patients undergoing treatment has also suggested a shift in blood distribution from smaller to larger vessels,[9] potentially due to microemboli and vascular remodelling affecting small-vessel resistance.^{129}Xe gas-transfer MRI provides an opportunity to probe capillary-level abnormalities by detecting inhaled ^{129}Xe dissolved in the alveolar membrane (quantified as barrier area-under-the-curve [AUC]) and red-blood-cells (quantified as RBC AUC). The ratio of ^{129}Xe uptake (RBC:barrier ratio) has been observed to reflect impaired gas transfer in obstructive and restrictive disease[10] and was also recently shown to detect low alveolar to red-blood-cell gLLNas-exchange in hospitalized COVID-19 patients 3-months post-discharge.[11,12] Although some long-term symptoms were reported in these patients, ^{129}Xe MRI has not been performed in patients with PACS.

Most COVID-19 studies have been performed in ever-hospitalized patients,[3,12] and report poor quality-of-life post-discharge. One recent study investigated symptoms post-infection in never-hospitalized patients.[2] The most recent wave of COVID-19 infection has affected unprecedented numbers of people but with an apparently decreased rate of hospitalization due to less severe

infection.[13] Understanding the relationship between COVID-19 infectious severity and post-infection symptoms will be critical for health care planning as COVID-19 becomes endemic.

We hypothesized that long haul COVID-19 symptoms in the presence of normal pulmonary function would be associated with abnormal ^{129}Xe MRI gas-exchange and CT pulmonary vascular density measurements and that such imaging measurements would differ in ever- and never-hospitalized PACS. Hence, in ever-COVID participants with PACS, we aimed to determine the relationship of persistent symptoms and exercise limitation to ^{129}Xe MRI and CT pulmonary vascular measurements.

3.2 Materials and Methods

3.2.1 Study Participants

We prospectively evaluated individuals 18-80 years of age who provided written-informed consent to an ethics board (HSREB # 113224) Health Canada approved and registered protocol (ClinicalTrials.gov: NCT04584671). Study participants with a proven positive PCR COVID-19 test were prospectively recruited from a quaternary-care COVID-19 clinic between April and October 2021. Inclusion criteria consisted of: age ≥ 18 and <80 years, a documented case by positive RT_PCR test of COVID-19 infection that resulted in symptoms post-infection. Exclusion criteria consisted of: contraindications to MRI such as implants and severe claustrophobia, mental or legal incapacitation or could not read or understand written material, inability to perform spirometry or plethysmography maneuvers, and pregnancy. Healthy controls aged ≥ 18 and <80 years, with no prior history of COVID-19 or any other respiratory infection during the period February 2020- study visit date were recruited as a convenience sample in June 2021. Controls were excluded if there were clinically relevant incidental findings.

3.2.2 Study Design

The study design consisted of Visit 1 (3-months post +COVID test), an optional Visit 2 (9-months post +COVID test) and Visit 3 (15-months post +COVID test). Participants were administered salbutamol upon arrival at our centre and 15 minutes later performed post-bronchodilator (BD) spirometry and DL_{CO} immediately prior to MRI. Research thoracic CT was acquired within 30 minutes of MRI and then participants completed the six-minute-walk-test (6MWT) and Questionnaires (St. George's Respiratory Questionnaire (SGRQ),[14] modified Medical Research Council (mMRC) Questionnaire, Chronic Obstructive Pulmonary Disease Assessment Test (CAT),[15] post-COVID-19 Functional Status scale,[16] International Physical Activity Questionnaire (IPAQ),[17] modified Borg Dyspnea Scale (mBDS).[18,19] ^{129}Xe gas-exchange MRI was performed at either Visit 1, 2 or 3. SpO_2 and heart rate were measured using an 8500 series handheld pulse oximeter (Nonin Medical Inc.) upon participant arrival as well as before and just after the 6MWT. For participants with PACS, the research visit was 35±25 weeks (range=6-79) post-COVID-19 infection with positive tests ranging from March 2020 to April 2021. Controls were evaluated in June 2021 after at least a single COVID-19 vaccine dose and none had experienced symptomatic respiratory illness for the period February 2020 up to and including the study visit date.

3.2.3 Pulmonary Function Tests

Pulmonary function tests were performed according to American Thoracic Society guidelines[20,21] using an *ndd EasyOne Pro LAB system* (ndd Medical Technologies). Post-BD measurements were performed 15 minutes after inhalation of 4×100 µg/inhalation salbutamol sulfate norflurane (Ivax Pharmaceuticals) using an *AeroChamber* (Trudell Medical International). Participants withheld inhaled medications before study visits according to American Thoracic Society guidelines (e.g. short-acting β-agonists ≥6 hours, long-acting β-agonists ≥12 hours, long-acting muscarinic

antagonists ≥24 hours).[20] Questionnaires and the 6MWT were self-administered under supervision of study personnel.

3.2.4 ^{129}Xe MRI

Anatomic ^{1}H and ^{129}Xe MRI were acquired using a 3.0 Tesla scanner (Discovery MR750; GE Healthcare) as previously described.[22] ^{129}Xe MRI were acquired using a flexible vest quadrature coil (Clinical MR Solutions). Gas-exchange ^{129}Xe MRI and spectroscopy were performed, as described in the online supplement,[22] following coached inhalation and breath-hold of a 1.0L gas mixture (4/1 by volume ^{4}He/^{129}Xe for MRS, 1/1 by volume ^{4}He ^{129}Xe for MRI) from functional residual capacity. ^{129}Xe magnetic resonance spectroscopy data were fit to three complex Lorentzian distributions to determine frequency and area under the curve (AUC). The RBC:barrier ratio was calculated as the ratio of RBC AUC to barrier AUC. Gas-transfer MRI data were reconstructed as described;[22] additional detail is provided in the online supplement.

3.2.5 Thoracic CT

Within 30 minutes of MRI, CT was acquired post-BD after inhalation of 1.0L N_2 from functional residual capacity, as previously described[22] using a 64-slice LightSpeed VCT system (General Electric Healthcare; parameters: 64×0.625 collimation, 120 peak kilovoltage, 100 mA, tube rotation time=500ms, pitch=1.25, standard reconstruction kernel, slice thickness=1.25mm, field-of-view=40cm^2), as previously described.[22]

Pulmonary vascular measurements included total blood volume (TBV), volume of pulmonary blood vessels ≤5mm^2 (BV5), between 5-10mm^2 (BV5-10) and >10mm^2 (BV10), as detailed in the online supplement. CT data were qualitatively evaluated by a single chest CT radiologist with >10 years' experience (MA) for diagnostic and incidental findings. The qualitative reader was not

blinded. CT data were also quantitatively evaluated by a single experienced observer (AMM) who was blinded to participant identification and clinical measurements using automated (Chest Imaging Platform, Brigham and Women's Hospital)[23] software.

3.2.6 Statistical Analysis

The ^{129}Xe MRI signal intensity ratio of RBC to alveolar tissue barrier was the primary endpoint. SPSS (SPSS Statistics 27.0; IBM) was used for all statistical analyses. Data were tested for normality using Shapiro-Wilk tests and nonparametric tests were performed for non-normally distributed data. Relationships were evaluated using Pearson (r) and Spearman (ρ) correlations. Intergroup differences were tested using Welch's t-tests for two-group or Welch's ANOVA for multi-group analyses. Fischer's exact tests were used for categorical variables. Results were considered statistically significant when the probability of making a type I error was <5% ($p<0.05$).

3.3 Results

3.3.1 Participant Characteristics

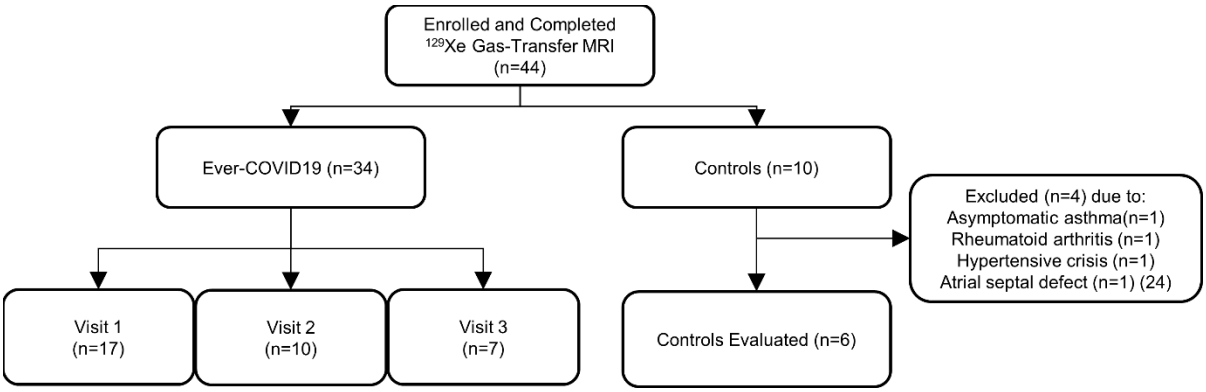

Figure 3-1 CONSORT Flow Diagram.

Table 3-1 Participant demographics

	All PACS (n=34)	Controls (n=6)	*PACS-control* (P value)	Never-Hospitalized PACS (n=22)	Ever-Hospitalized PACS (n=12)	*Never-ever hospitalized* (P value)
Age yrs	53 (13)	35 (15)	.02	51 (12)	57 (14)	.23
Females n (%)	18 (53)	3 (50)	.62	14 (64)	4 (33)	.09
BMI kg/m^2	30 (5)	25 (3)	.02	29 (6)	30 (4)	.46
Asthma n (%)	9 (26)	0 (0)		6 (27)	3 (25)	.61
COPD n (%)	4 (12)	0 (0)		3 (14)	1 (8)	.34
Pack-years	4 (10)	0 (0)		6 (11)	1 (3)	.08
Days Since +	238 (171)	-	-	236 (170)	244 (183)	.90
SpO_2 %	97 (2)	-	-	97 (2)	96 (3)	.13
SpO_2 post-exertion %	97 (4)	-	-	98 (1)	95 (6)	.13
FEV_1 $\%_{pred}$	93 (20)	100 (8)	.11	96 (21)	88 (17)	.19
FVC %	92 (17)	102 (7)	.02	94 (19)	88 (12)	.26
FEV_1/FVC	81 (13)	80 (5)	.89	81 (10)	81 (17)	.97
$DL_{CO}\%_{pred}$	85 (17)	-	-	86 (13)	84 (24)	.83
Quality-of-Life						
SGRQ	31 (17)	-	-	32 (17)	29 (19)	.65
CAT	13 (7)	-	-	13 (7)	13 (8)	.81
IPAQ MET-min/week	4865 (4189)	-	-	5401 (4202)	3883 (4160)	.32
PCFS	1.6 (1.3)	-	-	1.5 (1.2)	1.7 (1.4)	.80
mMRC dyspnea	1.0 (0.8)	-	-	1.0 (0.8)	1.0 (1.0)	>.99
6MWD m	429 (80)	-	-	426 (78)	434 (86)	.82
mBDS post-exertion	1.8 (1.4)	-	-	1.6 (1.4)	2.2 (1.3)	.29

PACS=post-acute COVID-19 syndrome; BMI=body mass index; COPD=chronic obstructive pulmonary disease; SpO_2=peripheral oxygen saturation; FEV_1=forced expiratory volume in 1 second; $\%_{pred}$=percent of predicted value; FVC=forced vital capacity; DL_{CO}=diffusing capacity of the lung for carbon monoxide; SGRQ=St. George's Respiratory Questionnaire; CAT=chronic obstructive pulmonary disease assessment test; IPAQ=International Physical Activity Questionnaire; MET=Metabolic Equivalent of Task; PCFS=Post-COVID-19 Functional Status; mMRC=Modified Medical Research Council; 6MWD=six-minute-walk-distance; mBDS=modified Borg Dyspnea Scale

As shown in **Figure 3-1**, of an initial 44 participants, data were acquired in 34 participants with PACS (mean age, 53 years ±13[SD], 18 women) and 10 control participants (mean age, 35 years ±15[SD], five men), of which four controls were excluded due to clinically relevant incidental

findings. Three control participants were excluded due to asymptomatic asthma, rheumatoid arthritis, and hypertensive crisis. Another participant was excluded due to an incidental finding that lead to the diagnosis of a large, asymptomatic atrial septal defect.[24]

For participants with PACS, the research visit was 35±25 weeks (range=6-79) post-COVID-19 infection with positive tests ranging from March 2020 to April 2021. Participants with PACS were infected prior to vaccine availability and prior to the release of COVID-19 specific anti-viral treatments. Never-COVID participants were evaluated in June 2021 after at least a single COVID-19 vaccine dose and none had experienced symptomatic respiratory illness for the period up to and including February 2020. **Table 3-1** summarizes participant demographic data for never- and ever-participants with PACS, as well as never- and ever-hospitalized participants with PACS. Control participants were younger (P=.02) than participants with PACS (controls 35±15 years, PACS 53±13 years) and had a lower BMI (controls 25±3 kg/m^2, PACS 30±5 kg/m^2; P=.02). Persistent symptoms that led to a diagnosis of PACS and follow-up by the London Health Sciences COVID clinic are summarized in **Table 3-3** in **Supplementary Material 3.6**. Most participants reported respiratory symptoms including exertional dyspnea as well as fatigue and brain fog. Among the ever-hospitalized COVID patients, two were treated in ICU and none required ventilation. Participant medications are summarized in **Table 3-4** in **Supplementary Material 3.6**.

3.3.2 Qualitative MRI and CT Findings

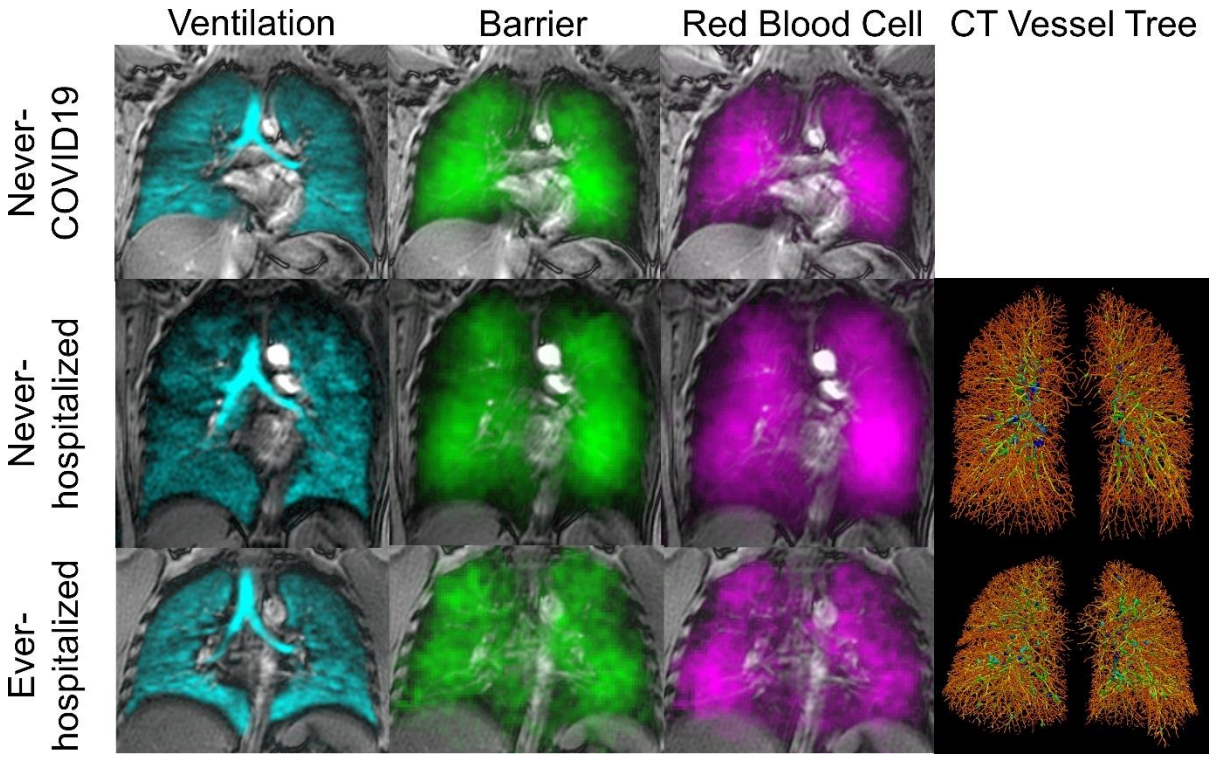

Figure 3-2 ^{129}Xe gas-transfer MRI and CT pulmonary vascular trees in never-COVID and ever-COVID participants.
Top: ^{129}Xe gas-transfer MRI in a 30-year-old male control participant with RBC:barrier ratio=0.52.
Middle: ^{129}Xe gas-transfer MRI and CT pulmonary vessels in a 59-year-old never-hospitalized female participant with PACS (RBC:barrier=0.26 and BV5/TBV= 62%).
Bottom: ^{129}Xe gas-transfer MRI and CT pulmonary vessels in a 42-year-old ever-hospitalized male participant with PACS (RBC:barrier=0.33 and BV5/TBV=54%).

Figure 3-2 shows representative ^{129}Xe MRI ventilation, alveolar-capillary tissue barrier and RBC maps and thoracic CT in a never-COVID-19 participant, a never-hospitalized and an ever-hospitalized PACS participant. In the never-COVID control participant, there were homogeneous signal intensities for ventilation, alveolar-capillary tissue barrier and RBC compartments. In the never- and ever-hospitalized participants with PACS, there were patchy alveolar-capillary tissue barrier and RBC signal intensity maps. As shown in **Figure 3-7**, in some participants with abnormal CT BV5/TBV, there was visual evidence of fewer small vessels and a greater density of

larger vessels without a visually obvious change in TBV. A summary of CT radiological findings is included in **Table 3-5** in **Supplementary Material 3.6**. In never-hospitalized participants the most common findings were nodules (8/22, 36%), bronchiectasis (3/22, 14%), ground glass opacity (4/22, 18%) and atelectasis (3/22, 14%). In ever-hospitalized participants the CT findings were similar but with greater frequencies for ground glass opacity (5/12 42%) and consolidation (2/12, 17%).

3.3.3 Differences Between Never- and Ever-hospitalized Participants

Table 3-2 Imaging measurements

Imaging Measurement mean (SD)	All PACS (n=34)	Controls (n=6)	*PACS-controls* (P value)	Never-Hospitalized PACS (n=22)	Ever-Hospitalized PACS (n=12)	*Never-ever hospitalized* (P value)
CT TBV mL	285 (55)*	-	-	289 (54)**	279 (59)†	.74
CT BV5 mL	150 (38)*	-	-	159 (39)**	134 (23)†	.09
CT BV5-10 mL	47 (19)*			45 (20)**	49 (21)†	.67
CT BV10 mL	85 (26)*	-	-	81 (24)**	96 (36)†	.39
CT BV5/TBV %	54 (10)*	-	-	56 (9)**	49 (10)†	.18
CT BV5-10/TBV %	17 (6)*			15 (5)**	19 (8)†	.38
CT BV10/TBV %	30 (6)*	-	-	28 (6)**	34 (6)†	.09
^{129}Xe MRI RBC:barrier	0.32 (0.06)	0.41 (0.10)	.06	0.33 (0.05)	0.31 (0.07)	.41
^{129}Xe MRI Barrier AUC	290 (120)	346 (144)	.40	340 (133)	241 (85)	.01
^{129}Xe MRI RBC AUC	90 (37)	139 (65)	.13	103 (39)	78 (31)	.01

TBV=total blood volume; BV5=blood volume in vessels with cross-sectional area ≤5mm^2; BV10=blood volume in vessels with cross-sectional area ≤10mm^2; RBC=red-blood-cell; AUC=area under the spectroscopy curve*n=24 **n=13 †n=11

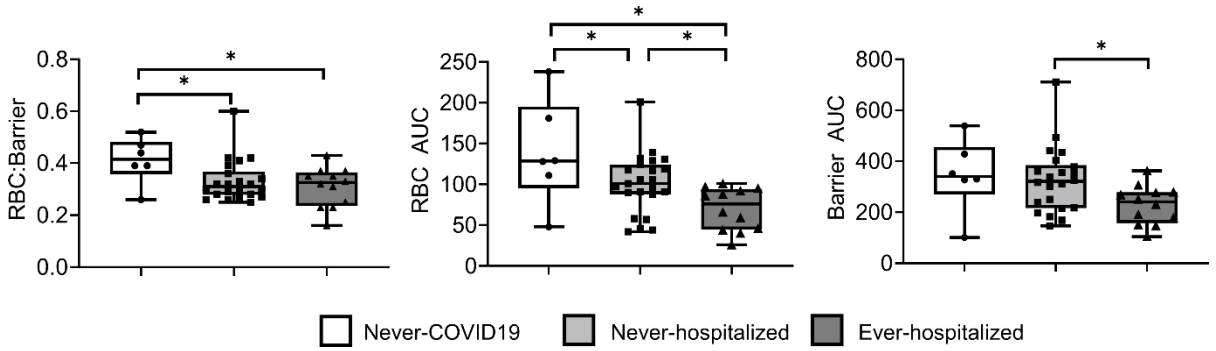

Figure 3-3 ^{129}Xe spectroscopy measurements for controls, never-hospitalized and ever-hospitalized participants with PACS.
Controls and never-hospitalized participants with PACS reported different ^{129}Xe MR spectroscopy measurements. A) red-blood-cell to barrier ratio (RBC:barrier): controls (0.41±0.10) and ever-hospitalized PACS (0.31±0.07), P=.04. B) RBC area-under-the-curve (AUC): controls (139±65) and ever-hospitalized PACS (78±31), P =.046, never-hospitalized PACS (103±39) and ever-hospitalized PACS, P=.01. C) Barrier AUC: Never-hospitalized PACS (340±133) and ever-hospitalized PACS (241±85), P=.01

Table 3-2 shows the MRI (n=34) and CT pulmonary vascular measurements (n=24) by hospitalization status and **Figure 3-3** shows some of these measurements in box and whisker plots. Five CT segmentations were excluded from the evaluation because of segmentation artifacts in regions of CT consolidation/opacities in ever-hospitalized participants.

As shown in **Table 3-2**, in all Participants with PACS as compared with controls participants, ^{129}Xe MRI RBC:barrier ratio (0.32±0.06 vs. 0.41±0.10 *P*=.06) trended toward a difference. The ^{129}Xe MRI barrier AUC (340±133 vs. 241±85, P=.01) and RBC AUC (103±39 vs. 78±31, P=.01) measures were greater in never- as compared with ever-hospitalized participants. There was no difference in BV5/TBV for never- (56±9) and ever-hospitalized participants (49±10; P=.14) although the trend observed was consistent with previous reports of vascular pruning in COVID-19.[9] **Figure 3-3** shows differences in box and whisker plots by participant group for ^{129}Xe MRI RBC:barrier ratio, RBC and barrier AUC. Differences in RBC AUC were observed between never-COVID, never-hospitalized PACS and ever-hospitalized PACS.

3.3.4 Relationships between Imaging Measurements, Symptoms, and Exercise Limitation

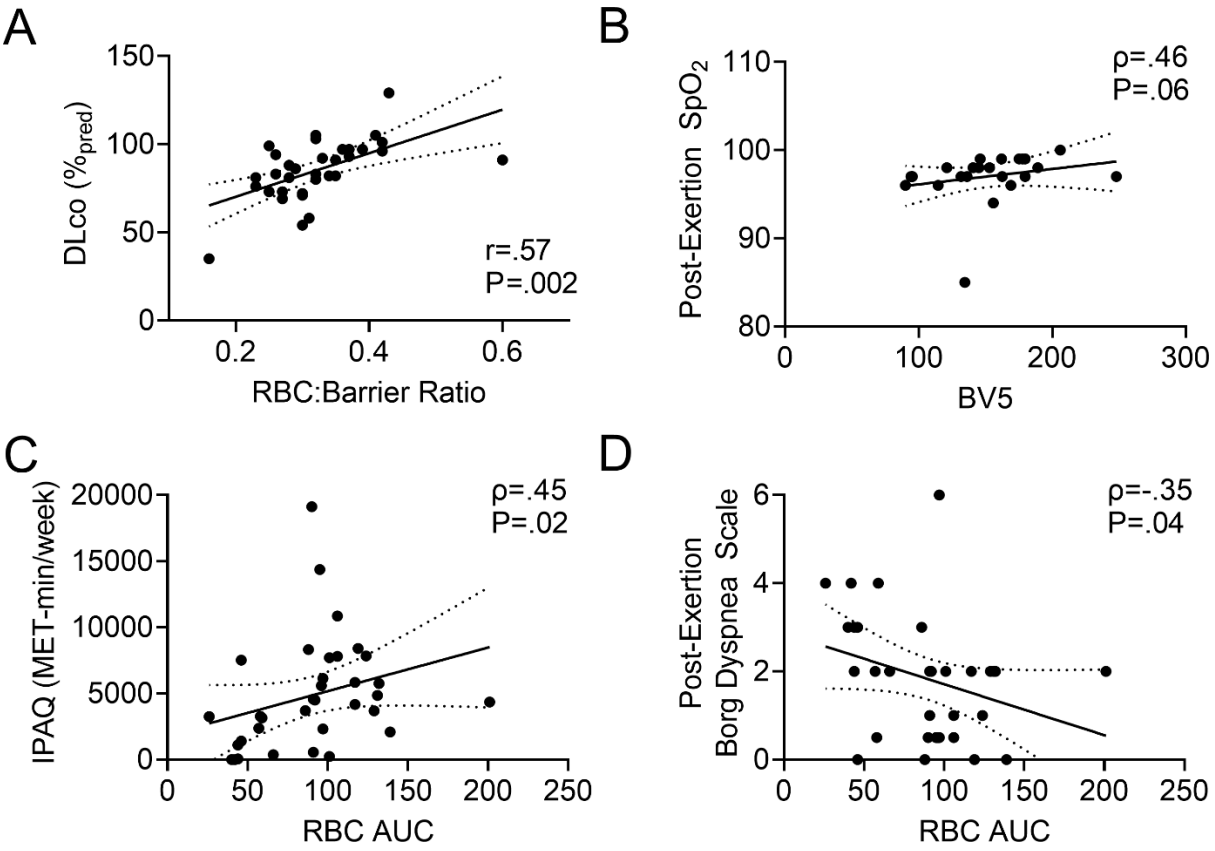

Figure 3-4 ^{129}Xe MR Spectroscopy measurement relationships with pulmonary function and exercise measurements in participants with PACS.
A) ^{129}Xe gas-transfer red-blood-cell to barrier ratio (RBC:barrier) measurements were related to (r=.57, Holm-Bonferonni P=.002) diffusing-capacity-of-the-lung for carbon monoxide (DL_{CO}).
B) ^{129}Xe MRI RBC area-under-the-curve (AUC) trended towards an association with CT blood volume in vessels with cross-sectional area ≤5mm^2 (BV5; ρ=.46, Holm-Bonferonni P=.06).
C) ^{129}Xe MR RBC AUC was related to International Physical Activity Questionnaire (IPAQ) exercise capacity (ρ=.45, Holm-Bonferonni P=.02).
D)^{129}Xe MR RBC AUC was related to dyspnea measured by post-exertion modified Borg Dyspnea Scale (ρ=-.35, Holm-Bonferonni P=.04).

Figure 3-4 shows the relationships for CT and MRI measurements with one another and with symptoms and exercise limitation. **Figure 3-4** shows that the ^{129}Xe MRI RBC:barrier ratio was correlated with DL_{CO} (r=.57, P=.002) and FEV_1 (ρ=35, P=.03). The ^{129}Xe MRI RBC AUC was correlated with CT BV5 (ρ=.44, P=.03), IPAQ score (ρ=.45, P=.02), post-exertional SpO_2 (ρ=.37,

P=.03) and post-6MWT Borg breathlessness (ρ=-.35, P=.04), but not SGRQ score (r=-.15, P=.40). BV5 was also correlated with post-exertional SpO_2 (ρ=.46, P=.03).

Figure 3-6 provides additional relationship data without statistical tests.

3.4 Discussion

Independent studies[11,12] have uncovered evidence of either MRI or CT pulmonary vascular abnormalities in previously hospitalized patients with COVID-19 who were recovered from infection but remained symptomatic. Here we endeavored to determine if ^{129}Xe MRI abnormalities were present in never-hospitalized Participants with PACS and to determine relationships between MRI and CT measurements with clinical and patient-centred measurements. We evaluated 40 participants, including 22 never-hospitalized and 12 ever-hospitalized participants with PACS, 35 ±25 weeks post COVID infection and observed: 1) different ^{129}Xe MRI RBC:barrier ratio (0.31±0.07 vs 0.41±0.10; P=.04) and RBC AUC (90±37 vs 139±65; P=.046) in ever- hospitalized participants with PACS with normal spirometry (but abnormal SGRQ, IPAQ, mMRC) as compared with controls, 2) differences in ever- as compared with never-hospitalized participants ^{129}Xe MRI RBC (78±31 vs 103±39; P=.01) and barrier AUC (241±85 vs 340±133; P=.01), 3) relationships for MRI RBC:barrier ratio with DL_{CO} (r=.57, P=.002) and FEV_1 (ρ=.35, P=.03), and, 4) relationships for MRI RBC AUC with CT BV5(ρ=.44, P=.03), IPAQ score (ρ=.45, P=.02), post-exertional SpO_2 (ρ=.46, P=.03) and post-6MWT dyspnea (ρ=-.35, P=.04).

In all patients with COVID-19, mean spirometry values were normal and SGRQ, IPAQ, and mMRC scores were abnormal. In addition, RBC:barrier ratio (controls 0.41±0.10, participants with ever-COVID 0.32±0.06; P=.06) trended toward a difference as compared with never-COVID controls. As in previous studies,[25] we used hospitalization status to dichotomize post-COVID

patients and detected MRI differences in never- and ever-hospitalized participants including ^{129}Xe MRI RBC and barrier AUC. Whereas the CT measurements in never-hospitalized participants were similar to never-COVID values previously reported (BV5/TBV=56%, BV10/TBV=28%),[9] CT pulmonary vascular measurements in ever-hospitalized COVID-19 patients were consistent with vascular pruning, similar to previous findings.[9] CT evidence of "vascular pruning" has been hypothesized to be due to vasoconstrictive remodelling of the capillary systems and small blood vessels.[9] While the capillaries are well beyond the spatial resolution of CT, histologic analyses[26] have indicated that capillary remodelling occurred in COPD patients when CT vascular pruning was also identified. In never-hospitalized patients, we observed ^{129}Xe MRI, but not CT abnormalities. Since MRI directly probes the function of the alveolar-capillary boundary, it may be more sensitive or more targeted than CT to microvascular abnormalities.

Together, the abnormal MRI and CT findings were consistent with abnormal gas-exchange stemming from the alveolar tissue barrier and pulmonary vascular compartments. Similar to previous reports of post-COVID coagulation and emboli,[1] it is possible that we were measuring micro-embolic or micro-thrombotic obstruction of small capillaries which explained the abnormal RBC signal. Other vascular changes, such as vascular injury, vascular remodelling or shunting may also be possible and has previously been hypothesized post-COVID-19.[5,9,25] Post-mortem micro-CT imaging of COVID-19 infection supports these interpretations as abnormal alveolar-level structures and occluded capillaries were observed.[27]

We observed relationships for ^{129}Xe MRI RBC:barrier ratio with DL_{CO}, FEV_1. Whilst modestly low DL_{CO} is common in PACS patients, post-COVID hospitalization,[28] a pilot ^{129}Xe MRI study unexpectedly did not find a DL_{CO} and MRI gas-transfer relationship.[12] In contrast, here we observed relationships for the ^{129}Xe MRI RBC:barrier ratio with DL_{CO} and FEV_1. The relationship

with DL_{CO} was not unexpected because previous work showed these relationships in both obstructive and restrictive lung disease.[29] RBC:Barrier and FEV_1 relationships have not previously been observed but could reflect underlying tissue changes in participants that also impact airway restriction. In our study, DL_{CO} was greater than $80\%_{pred}$ in both never- and ever-hospitalized participants and FEV_1 was also normal which together may suggest that the ^{129}Xe MRI RBC:barrier ratio is highly sensitive to pulmonary gas-transfer abnormalities.

We also observed a moderate correlation between BV5 and RBC AUC. This finding supports a link between RBC gas uptake and small-vessel abnormalities in PACS. Microvascular remodelling, shunting, thrombi, micro-embolisms, or some combination of these may play a role. Increased vascular resistance due to these structural modifications could also explain how such abnormalities are also visible throughout the vascular tree. Hemodynamic measurements were outside the scope of our study but may prove an important subject of future investigation into PACS mechanisms.

We were surprised to detect relationships for MRI RBC AUC with post-exertion SpO_2, exertional dyspnea (modified Borg Dyspnea Scale) and IPAQ score. Similar to previous studies of post-COVID patients,[5,25,30] in our study, there was abnormal SGRQ (31±17 vs. 6±9 in general population[31]), CAT (13±7, >90th percentile general population[32]) and mMRC dyspnea (1.0±0.7, >91st percentile general population[33]). Whilst there were no relationships for MRI and CT measurements with SGRQ (which is validated for use in COPD),[14] there was a correlation for IPAQ activity and MRI RBC AUC. Relationships between MRI, CT, pulmonary function and symptoms suggest a physiologic mechanistic link. Abnormal gas transfer, demonstrated by the relationship between RBC:barrier and DL_{CO}, would lead to poor oxygenation and vascular changes, possibly reflected in the trend towards a relationship between post-exertion SpO_2 and CT

BV5. Vascular abnormality-driven desaturation could explain commonly reported symptoms in PACS such as exercise limitation and dyspnea,[3] which we observed to be related to RBC AUC. As shown in **Figure 3-5** pulmonary vascular abnormalities including the low RBC signal (which is a surrogate for abnormal O_2 uptake) may stem from vascular remodeling, where narrowed vessels reduce the available blood volume, or eliminated altogether in regions with vascular shunting or persistent microemboli. For example, in cadaveric COVID lungs, there was histological evidence of severe endothelial damage and distorted, elongated vessels alongside microemboli.[34] Shunting has been observed during infection in patients with COVID[35] and perfusion of damaged or unventilated alveoli also would also reduce RBC signal in the lung. These potential mechanisms are supported by the relationship between the MRI RBC:barrier ratio and $DL_{CO,}$ and an RBC AUC relationship with SpO_2. Microvascular changes in flow and resistance could have upstream effects on the vasculature and may explain blood redistribution observed here and in other studies.[9] The relationship between RBC AUC, dyspnea scores and exercise capacity measured by IPAQ help explain dyspnea and exercise impairment in some post-COVID patients as pulmonary vascular gas-exchange dysfunction.

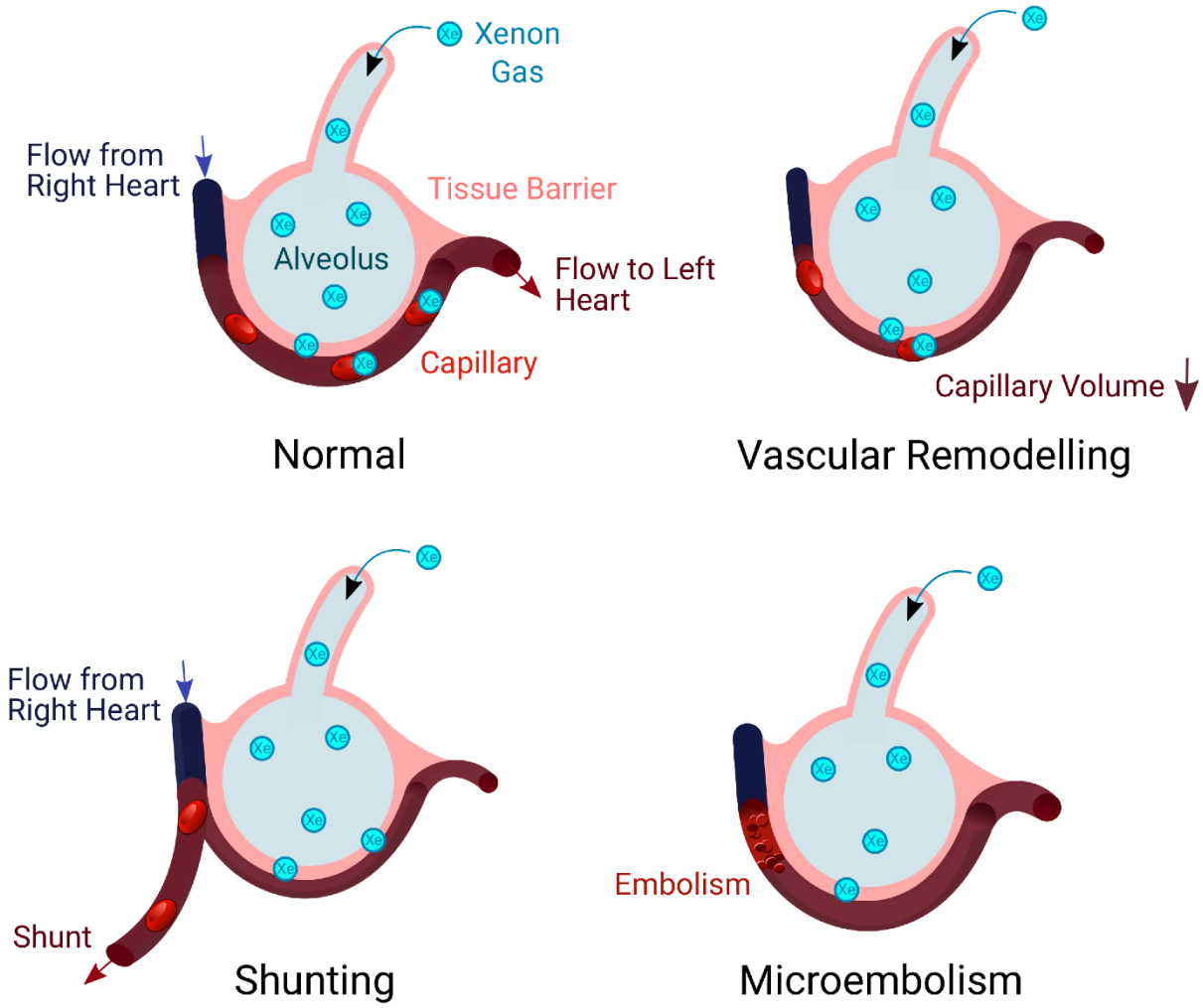

Figure 3-5 Proposed Mechanisms explaining relationships for ^{129}Xe MRI RBC AUC
Top left: Gas-exchange in a healthy individual occurs as xenon diffuses through the tissue barrier and attaches to RBC.
Top right: Vasoconstrictive remodeling following infection reduces the available blood volume for ^{129}Xe binding.
Bottom left: Changes to vascular resistance and flow pattens may result in redistributions of pulmonary blood through shunting away from ^{129}Xe ventilated regions.
Bottom right: Thrombus or microembolism blocks capillary-level bloodflow, preventing ^{129}Xe uptake in RBC and redistributing blood upstream in the vasculature

In our study, the range of follow-up was quite wide (6-79) weeks post-positive test with most COVID-19 testing at our centre performed approximately 1-week post-infection. While post-acute infectious symptoms were potentially possible, the emerging literature now describes the timelines for clinically relevant post-covid symptoms that include 4-6 weeks post-infection. For example,

The Centers for Disease Control and Prevention (CDC) coined the term post-COVID condition as "a wide range of new, returning, or ongoing health problems people can experience four or more weeks after first being infected with the virus that causes COVID-19"[36]. The World Health Organization (WHO) also describes the post-COVID-19 condition, typically three months from the onset of COVID-19.[37] As an alternative that blends both consensus definitions, The National Institute for Health and Care Excellence (NICE)[38], coined the term long-COVID as signs and symptoms that continue or develop following the acute infectious phase of COVID-19, which includes both ongoing symptomatic COVID-19 and post-COVID-19 syndrome all greater than 4 weeks post infection.[5] Hence our understanding and these definitions are still quite fluid. Given these definitions, the ever-COVID participants evaluated in our study can be considered as having post-acute COVID-19 syndrome or long COVID, based on their symptoms and timeframe since symptomatic infection.

We recognize a number of study limitations. For example, the relatively small sample size of the control and PACS subgroups, certainly limits the generalizability of our findings. Our study was not powered based on ^{129}Xe MRI spectroscopy measurements so our results must be considered exploratory and hypothesis generating. To provide a transparent snapshot of our results with the COVID-19 research community, we provided data in the online supplement without statistical tests so that other centres may utilize our results to help generate sample sizes for long term follow-up studies.

Other limitations include: 1) CT was not acquired in the control subgroup which prevented CT comparisons across all three subgroups; 2) all participants were referred from a COVID-19 clinic focusing on long-haul symptoms and therefore recruitment was likely biased towards symptomatic individuals seeking some form of explanation or intervention; 3) participants with PACS were

older than the controls (53±13 years vs 35±15). To our knowledge, the effect of age on ^{129}Xe gas-exchange biomarkers has not been reported. However, it is possible that similar to age-related changes observed for DL_{CO},[39] age may also influence MRI gas-transfer measurements; 4) COVID-19 antibody testing was not performed to verify COVID-infection status in the never-Covid volunteers, so while unlikely, it is possible that some may have previously experienced an asymptomatic infection prior to the study; 5) the mean RBC:barrier ratio estimated for the control subgroup was lower than previous reports[11,12] and this means that the differences detected for COVID patients may be conservative underestimates; 6) ^{129}Xe gas-exchange MRI was performed on one of Visit 1, 2 or 3 which broadened the time post-COVID infection to 35±25 weeks. As shown in the supplement, there was no bias over time towards improved gas-exchange but nevertheless, it will be important to evaluate those participants who performed MRI at Visit 1 for potential longitudinal differences; and finally, 7) MR image heterogeneity was not evaluated quantitatively in our study and we note that previous ^{129}Xe MRI COVID-19 investigations[11,12] also reported the RBC:barrier ratio which makes comparisons with our study possible. Unfortunately, gas-exchange imaging was not technically implemented at our centre until our COVID-19 study was already underway for a year and in these participants, MR spectroscopy was implemented first for our study.

Larger studies aimed at identifying mechanistic relationships between dyspnea and other symptoms with ^{129}Xe MRI abnormalities are complex to undertake in participants with PACS. The findings of abnormal ^{129}Xe MRI gas-exchange measurements in never-hospitalized COVID patients and the relationships between ^{129}Xe MRI and CT pulmonary vascular measurements have not been previously established in the literature. In our study, both CT and ^{129}Xe MRI suggest temporally persistent pulmonary vascular density and gas-transfer abnormalities that were related

to exercise limitation and exertional dyspnea. We observed abnormal ^{129}Xe MRI gas-exchange measurements in never-hospitalized participants with COVID and some ^{129}Xe MRI measurements were worse in ever-hospitalized patients compared to controls. We also detected relationships between ^{129}Xe MRI and CT pulmonary vascular measurements that point to persisting pulmonary vascular abnormalities including vessel density and gas-transfer abnormalities that were related to exercise limitation and exertional dyspnea. Furthermore, future studies will seek to determine if pulmonary vascular abnormalities can act as a predictor of long-term PACS outcomes and if abnormal gas-exchange measures can predict recovery. Pulmonary vascular pathologies play a role in PACS regardless of COVID-19 severity.

3.5 References

1. Nurek M, Rayner C, Freyer A, Taylor S, Jarte L, MacDermott N, et al. Recommendations for the recognition, diagnosis, and management of long COVID: a Delphi study. Br J Gen Pract. 2021;71(712):e815-e25.

2. Estiri H, Strasser ZH, Brat GA, Semenov YR, Patel CJ, Murphy SN, et al. Evolving phenotypes of non-hospitalized patients that indicate long COVID. Bmc Med. 2021;19(1).

3. Fernandez-de-las-Penas C, Palacios-Cena D, Gomez-Mayordomo V, Rodriuez-Jimenez J, Palacios-Cena M, Velasco-Arribas M, et al. Long-term post-COVID symptoms and associated risk factors in previously hospitalized patients: A multicenter study. J Infection. 2021;83(2):271-4.

4. Sandmann FG, Tessier E, Lacy J, Kall M, Van Leeuwen E, Charlett A, et al. Long-term health-related quality of life in non-hospitalised COVID-19 cases with confirmed SARS-CoV-2 infection in England: Longitudinal analysis and cross-sectional comparison with controls. Clin Infect Dis. 2022.

5. Nalbandian A, Sehgal K, Gupta A, Madhavan MV, McGroder C, Stevens JS, et al. Post-acute COVID-19 syndrome. Nature Medicine. 2021;27(4):601-15.

6. Huang C, Huang L, Wang Y, Li X, Ren L, Gu X, et al. 6-month consequences of COVID-19 in patients discharged from hospital: a cohort study. Lancet. 2021;397(10270):220-32.

7. van Gassel RJJ, Bels JLM, Raafs A, van Bussel BCT, van de Poll MCG, Simons SO, et al. High Prevalence of Pulmonary Sequelae at 3 Months after Hospital Discharge in Mechanically Ventilated Survivors of COVID-19. American Journal of Respiratory and Critical Care Medicine. 2021;203(3):371-4.

8. Munker D, Veit T, Barton J, Mertsch P, Mummler C, Osterman A, et al. Pulmonary function impairment of asymptomatic and persistently symptomatic patients 4 months after COVID-19 according to disease severity. Infection. 2022;50(1):157-68.

9. Lins M, Vandevenne J, Thillai M, Lavon BR, Lanclus M, Bonte S, et al. Assessment of Small Pulmonary Blood Vessels in COVID-19 Patients Using HRCT. Acad Radiol. 2020;27(10):1449-55.

10. Wang Z, Bier EA, Swaminathan A, Parikh K, Nouls J, He M, et al. Diverse cardiopulmonary diseases are associated with distinct xenon magnetic resonance imaging signatures. Eur Respir J. 2019;54(6).

11. Li H, Zhao X, Wang Y, Lou X, Chen S, Deng H, et al. Damaged lung gas exchange function of discharged COVID-19 patients detected by hyperpolarized (129)Xe MRI. Sci Adv. 2021;7(1).

12. Grist JT, Chen M, Collier GJ, Raman B, Abueid G, McIntyre A, et al. Hyperpolarized (129)Xe MRI Abnormalities in Dyspneic Patients 3 Months after COVID-19 Pneumonia: Preliminary Results. Radiology. 2021;301(1):E353-E60.

13. Maslo C, Friedland R, Toubkin M, Laubscher A, Akaloo T, Kama B. Characteristics and Outcomes of Hospitalized Patients in South Africa During the COVID-19 Omicron Wave Compared With Previous Waves. JAMA. 2021.

14. Jones PW, Quirk FH, Baveystock CM, Littlejohns P. A self-complete measure of health status for chronic airflow limitation. The St. George's Respiratory Questionnaire. Am Rev Respir Dis. 1992;145(6):1321-7.

15. Jones PW, Harding G, Berry P, Wiklund I, Chen WH, Kline Leidy N. Development and first validation of the COPD Assessment Test. Eur Respir J. 2009;34(3):648-54.

16. Klok FA, Boon GJAM, Barco S, Endres M, Geelhoed JJM, Knauss S, et al. The Post-COVID-19 Functional Status scale: a tool to measure functional status over time after COVID-19. European Respiratory Journal. 2020;56(1).

17. Craig CL, Marshall AL, Sjostrom M, Bauman AE, Booth ML, Ainsworth BE, et al. International physical activity questionnaire: 12-country reliability and validity. Med Sci Sports Exerc. 2003;35(8):1381-95.

18. Borg GAV. Psychophysical bases of perceived exertion. Med Sci Sports Exerc. 1982;14(5):377-81.

19. Enright PL. The Six-Minute Walk Test. Respiratory Care. 2003;48(8):783-5.

20. Miller MR, Hankinson J, Brusasco V, Burgos F, Casaburi R, Coates A, et al. Standardisation of spirometry. Eur Respir J. 2005;26(2):319-38.

21. Graham BL, Brusasco V, Burgos F, Cooper BG, Jensen R, Kendrick A, et al. 2017 ERS/ATS standards for single-breath carbon monoxide uptake in the lung. Eur Respir J. 2017;49(1).

22. Svenningsen S, Kirby M, Starr D, Leary D, Wheatley A, Maksym GN, et al. Hyperpolarized (3) He and (129) Xe MRI: differences in asthma before bronchodilation. J Magn Reson Imaging. 2013;38(6):1521-30.

23. Estepar RSJ, Ross JC, Krissian K, Schultz T, Washko GR, Kindlmann GL. Computational Vascular Morphometry for the Assessment of Pulmonary Vascular Disease Based on Scale-Space Particles. 2012 9th Ieee International Symposium on Biomedical Imaging (Isbi). 2012:1479-82.

24. Matheson A, Cunningham R, Bier E, Lu J, Driehuys B, Pickering J, et al. Hyperpolarized 129Xe pulmonary MRI and asymptomatic Atrial Septal Defect. Chest. 2022:(In Press).

25. McFann K, Baxter BA, LaVergne SM, Stromberg S, Berry K, Tipton M, et al. Quality of Life (QoL) Is Reduced in Those with Severe COVID-19 Disease, Post-Acute Sequelae of COVID-

19, and Hospitalization in United States Adults from Northern Colorado. Int J Environ Res Public Health. 2021;18(21).

26. Rahaghi FN, Argemi G, Nardelli P, Dominguez-Fandos D, Arguis P, Peinado VI, et al. Pulmonary vascular density: comparison of findings on computed tomography imaging with histology. Eur Respir J. 2019;54(2).

27. Walsh CL, Tafforeau P, Wagner WL, Jafree DJ, Bellier A, Werlein C, et al. Imaging intact human organs with local resolution of cellular structures using hierarchical phase-contrast tomography. Nat Methods. 2021.

28. Mendez R, Latorre A, Gonzalez-Jimenez P, Feced L, Bouzas L, Yepez K, et al. Reduced Diffusion Capacity in COVID-19 Survivors. Ann Am Thorac Soc. 2021;18(7):1253-5.

29. Wang ZY, Rankine L, Bier EA, Mummy D, Lu JL, Church A, et al. Using hyperpolarized Xe-129 gas-exchange MRI to model the regional airspace, membrane, and capillary contributions to diffusing capacity. Journal of Applied Physiology. 2021;130(5):1398-409.

30. Townsend L, Dowds J, O'Brien K, Sheill G, Dyer AH, O'Kelly B, et al. Persistent Poor Health after COVID-19 Is Not Associated with Respiratory Complications or Initial Disease Severity. Ann Am Thorac Soc. 2021;18(6):997-1003.

31. Ferrer M, Villasante C, Alonso J, Sobradillo V, Gabriel R, Vilagut G, et al. Interpretation of quality of life scores from the St George's Respiratory Questionnaire. Eur Respir J. 2002;19(3):405-13.

32. Pinto LM, Gupta N, Tan W, Li PZ, Benedetti A, Jones PW, et al. Derivation of normative data for the COPD assessment test (CAT). Respir Res. 2014;15:68.

33. Currow DC, Plummer JL, Crockett A, Abernethy AP. A community population survey of prevalence and severity of dyspnea in adults. J Pain Symptom Manage. 2009;38(4):533-45.

34. Ackermann M, Verleden SE, Kuehnel M, Haverich A, Welte T, Laenger F, et al. Pulmonary Vascular Endothelialitis, Thrombosis, and Angiogenesis in Covid-19. N Engl J Med. 2020;383(2):120-8.

35. Brito-Azevedo A, Pinto EC, de Cata Preta Corrêa GA, Bouskela E. SARS-CoV-2 infection causes pulmonary shunt by vasodilatation. J Med Virol. 2021;93(1):573-5.

36. Post-COVID Conditions: Centers for Disease Control and Prevention; 2021 [updated September 16, 2021. Available from: https://www.cdc.gov/coronavirus/2019-ncov/long-term-effects/index.html.

37. Soriano JB, Murthy S, Marshall JC, Relan P, Diaz JV, Condition WHOCCDWGoP-C-. A clinical case definition of post-COVID-19 condition by a Delphi consensus. Lancet Infect Dis. 2021.

38. National Institute of Health and Care Excellence. COVID-19 Rapid Guideline: Managing COVID-19. NICE; 2021.

39. Stanojevic S, Graham BL, Cooper BG, Thompson BR, Carter KW, Francis RW, et al. Official ERS technical standards: Global Lung Function Initiative reference values for the carbon monoxide transfer factor for Caucasians. Eur Respir J. 2017;50(3).

3.6 Supplemental Material

3.6.1 Methods

Table 3-3 Participant symptoms

Symptom n (%)	All PACS (n=34)	Never-Hospitalized PACS (n=22)	Ever-Hospitalized PACS (n=12)
Fatigue	12 (38)	5 (23)	7 (58)
Respiratory symptoms	21 (74)	13 (59)	8 (67)
Dyspnea	9 (26)	6 (27)	3 (25)
Dyspnea on exertion	14 (41)	7 (32)	7 (58)
Cough	4 (12)	4 (18)	0 (0)
Cardiac symptoms	8 (24)	5 (23)	3 (25)
Chest Tightness	5 (15)	4 (18)	1 (8)
Tachycardia	3 (9)	2 (9)	1 (8)
Palpitations	3 (9)	0 (0)	3 (25)
Headaches	5 (15)	4 (18)	1 (8)
Brain fog	13 (38)	9 (41)	4 (33)

Table 3-3 summarizes symptoms reported in PACS participants in this study.

Anatomic ^{1}H MRI was acquired using a fast-spoiled gradient-recalled-echo sequence (partial-echo acquisition; total acquisition time, 8 seconds; repetition-time msec/echo time msec, 4.7/1.2; flip-angle, 30°; field-of-view, 40×40cm^2; bandwidth, 24.4 kHz; 128×80 matrix, zero-filled to 128×128; partial-echo percent, 62.5%; 15-17×15mm slices). ^{129}Xe MR spectroscopy was acquired following inhalation breath-hold of a 1.0L gas mixture (4/1 by volume ^{4}He/^{129}Xe) from functional residual capacity (FRC) using a free-induction-decay whole-lung spectroscopy sequence (200 dissolved-phase spectra, TR=15ms, TE=0.7ms, flip=40°, BW=31.25kHz, 600μs 3-lobe Shinnar-Le Roux pulse). Spectroscopy was used to determine the echo time for a 90° barrier/RBC phase difference (TE_{90}). ^{129}Xe MRI was performed following inhalation of a 1.0L gas mixture (1/1 by volume ^{4}He/^{129}Xe) using an interleaved gas/dissolved-phase 3D radial sequence (TR=15ms TE=variable, flip=0.5^{o}/40°, FOV=40cm^3, matrix=72x72x72, BW=62.5kHz, 990 gas/dissolved projections,

600μs 3-lobe Shinnar-Le Roux pulse, frequency shift=7.664kHz). Supine participants were coached to inhale a 1.0L bag (Tedlar; Jensen Inert Products, Coral Springs, FL, USA) (500mL ^{129}Xe + 500mL ^{4}He for ^{129}Xe MRI and 1.0L N_2 for ^{1}H MRI) from the bottom of a tidal breath (functional residual capacity) with acquisition under breath-hold conditions. ^{129}Xe gas was polarized to 30-40% (Polarean; Xenispin 9820, Durham, NC, USA).[1]

Gas-transfer MRI data were reconstructed as previously described using a re-gridding method for non-cartesian acquisition.[2] Receiver phase-offset and local phase inhomogeneity were corrected as previously described.[3]

^{129}Xe gas-exchange MRI were corrected for local phase inhomogeneity using acquired interleaved gas-compartment data. Deviations from uniform phase in the gas image were assumed to result from phase inhomogeneity and voxel-wise phase corrections were applied to eliminate inhomogeneity effects. Receiver phase-offset was corrected using the spectroscopic RBC:barrier ratio. A phase correction $\Delta\phi$ was applied such that the ratio of real to imaginary channel signal matched the spectroscopic RBC:barrier ratio under the assumption that RBC and barrier signal should be perfectly aligned to the real and imaginary channels, respectively, at TE_{90}.

Within 30 minutes of MRI, CT was acquired post-BD after inhalation of 1.0L N_2 from functional residual capacity using a 64-slice LightSpeed VCT system (General Electric Healthcare, Milwaukee, WI, USA; parameters: 64×0.625 collimation, 120 peak kilovoltage, 100 mA, tube rotation time=500ms, pitch=1.25, standard reconstruction kernel, slice thickness=1.25mm, field-of-view=40cm^2) as previously described [4]. The total-effective-dose (1.8 mSv) was calculated using the ImPACT patient dosimetry calculator (UK Health Protection Agency NRPB-SR250 software). CT vessel measurements were performed in Chest Imaging Platform using a fully-automated pipeline. Images were filtered with a median filter before being passed to a thresholding script to

provide a basic segmentation of left and right lungs for region-of-interest identification. Next, a scale-space particle system[5] was used to identify vessels within the region-of-interest by computing multi-scalar maps of local Hessian features, i.e. calculating how tube-like local regions appear. An optimization moves sampling particles to tube-like regions of the image, where particle properties represent geometric properties of the underlying structure (radius/scale, shape, orientation). A kernel-density approach was used to compute a distribution of vessel-volumes at varying vessel cross-sections. This distribution was used to calculate BV5, BV5-10 and BV10. Vessel visualization was performed in Paraview (Kitware Inc., New York, NY, USA).

3.6.2 REFERENCES

1. Walker TG, Happer W. Spin-exchange optical pumping of noble-gas nuclei. Rev Mod Phys. 1997;69(2):629-42.

2. Robertson SH, Virgincar RS, He M, Freeman MS, Kaushik SS, Driehuys B. Optimizing 3D noncartesian gridding reconstruction for hyperpolarized 129Xe MRI—focus on preclinical applications. Concepts in Magnetic Resonance Part A. 2015;44(4):190-202.

3. Kaushik SS, Robertson SH, Freeman MS, He M, Kelly KT, Roos JE, et al. Single-breath clinical imaging of hyperpolarized (129)Xe in the airspaces, barrier, and red blood cells using an interleaved 3D radial 1-point Dixon acquisition. Magn Reson Med. 2016;75(4):1434-43.

4. Kirby M, Pike D, McCormack DG, Lam S, Coxson HO, Parraga G. Longitudinal Computed Tomography and Magnetic Resonance Imaging of COPD: Thoracic Imaging Network of Canada (TINCan) Study Objectives. Chronic Obstr Pulm Dis. 2014;1(2):200-11.

5. Estepar RSJ, Ross JC, Krissian K, Schultz T, Washko GR, Kindlmann GL. Computational Vascular Morphometry for the Assessment of Pulmonary Vascular Disease Based on Scale-Space Particles. 2012 9th Ieee International Symposium on Biomedical Imaging (Isbi). 2012:1479-82.

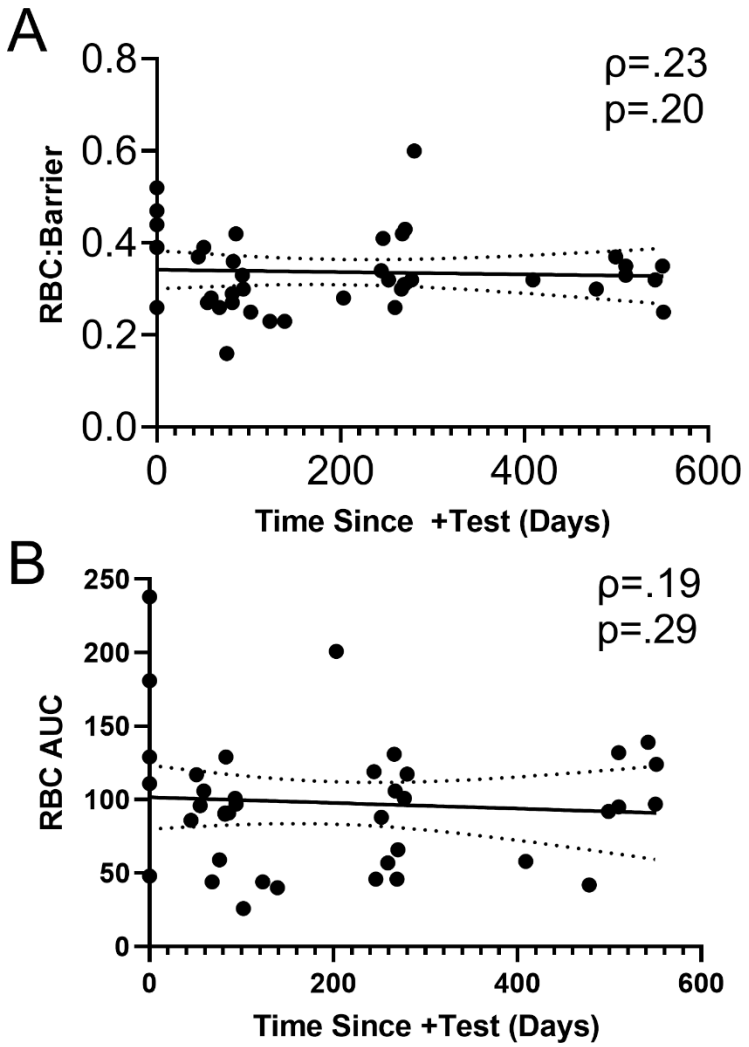

Figure 3-6 Gas-exchange measurements in never-COVID and PACS participants at varying imaging dates post-infection.
Never-COVID participant data were denoted as zero days since positive test.
A) RBC:barrier ratio was not significantly different over time (ρ=.23, P=.20)
B) RBC AUC was not significantly different over time (ρ=.19, p=.29)

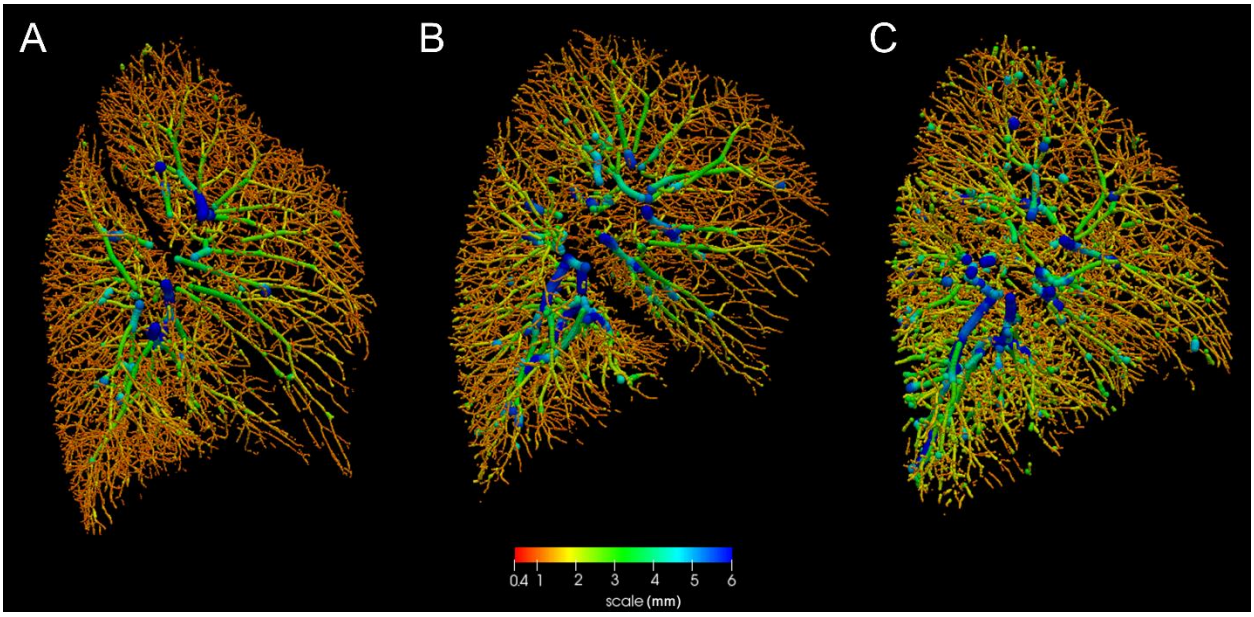

Figure 3-7 Evidence of pulmonary vascular abnormalities in participants with PACS.
Abnormal BV5/TBV was associate with greater vessel valiber as measured by CT without a change in TBV.
A) a 59-year-old never-hospitalized female with PACS, BV5/TBV=62%
B) a 69-year-old never hospitalized male with PACS, BV5/TBV=45%
C) a 70-year-old ever-hospitalized male with pre-existing COPD and PACS, BV5/TBV=35%

Table 3-4 Medications at research visit summary

Parameter n (%)	Ever-COVID (n=34)	Never-hospitalised (n=22)	Ever-hospitalised (n=12)
None	8 (24)	8 (36)	0 (0)
SABA	7 (21)	2 (9)	5 (42)
ICS	9 (26)	4 (18)	5 (42)
LABA	11 (32)	5 (23)	6 (50)
Anticoagulant	6 (18)	3 (14)	3 (25)
ACE inhibitors	5 (15)	2 (18)	3 (25)
Beta blockers	4 (12)	2 (18)	2 (17)
Other	20 (59)	12 (55)	7 (58)

SABA=short-acting beta-agonist; ICS=inhaled corticosteroid; LABA=long-acting beta-agonist; ACE=angiotensin-converting enzyme

Table 3-5 CT findings

Observation n (%)	All PACS (n=29)	Never-Hospitalized PACS (n=22)	Ever-Hospitalized PACS (n=12)
Ground Glass Opacity	9 (31)	4 (18)	5 (42)
Consolidation	3 (10)	1 (5)	2 (17)
Reticulation	0 (0)	0 (0)	0 (0)
Atelectasis	5 (17)	3 (14)[1]	2 (17)[2]
Emphysema	2 (7)	1 (0)	1 (8)
Honeycombing	0 (0)	0 (0)	0 (0)
Mosiac Attenuation	2 (7)	1 (5)	1 (8)
Nodules	9 (31)	8 (36)[3]	1 (8)[4]
Bronchiectasis	4 (19)	3 (14)	1 (6)

[1]2 participants with of minimal linear atelectasis
[2]1 participant with of minimal linear atelectasis
[3]1 participant with 3mm subpleural nodule, 1 participant with three 6-8mm nodules, 1 participant with three 5-6mm nodules, 1 participant with clustered 2-3mm nodules, 1 participant with 1-2mm subpleural nodules, 1 participant with 3mm nodule, 1 participant with 5mm nodule, one participant with three 2-8mm nodules.
[4]1 participant with nodular pulmonary infiltrates

Table 3-6 Relationships between pulmonary function tests, imaging and quality of life measurements

	BMI	FEV_1	FVC	FEV_1/FVC	DL_{CO}	6MWD	mBDS Post-exertion	SpO_2 Baseline	SpO_2 Post-exertion	SGRQ	mMRC	PCFS	CAT	IPAQ	RBC: Barrier	Barrier AUC	RBC AUC	TBV	BV5	BV5-10	BV10	BV5/TBV	BV5-10/TBV
	r/ρ	r/ρ	r/ρ	r/ρ	r/ρ	r/ρ	r/ρ	r/ρ	r/ρ	r/ρ	r/ρ	r/ρ	r/ρ	r/ρ	r/ρ	r/ρ	r/ρ	r/ρ	r/ρ	r/ρ	r/ρ	r/ρ	r/ρ
BMI	1.00	-.04	.00	-.12	.27	-.26	.07	-.27	-.27	.15	-.03	.04	.06	-.12	.13	-.37	-.26	.01	-.21	.44	.35	-.42	.51
FEV_1	-.04	1.00	.83	-.05	.44	.31	-.13	.51	.44	-.24	-.20	.02	-.24	.22	.35	-.19	.03	.20	.42	-.03	-.04	.20	-.09
FVC	.00	.83	1.00	-.45	.38	.33	.07	.35	.30	-.06	-.13	.11	-.09	.09	.32	-.22	-.02	.22	.24	.04	.06	.10	-.07
FEV_1/FVC	-.12	-.05	-.45	1.00	.02	.13	-.42	.28	.16	-.33	-.27	-.28	-.32	.24	.07	.36	.37	-.10	.05	-.15	-.19	.13	-.05
DL_{CO}	.27	.44	.38	.02	1.00	.32	-.42	.33	.20	-.34	-.39	-.12	-.41	.20	.59	-.23	.11	.15	.34	-.01	-.06	.21	-.09
6MWD	-.26	.31	.33	.13	.32	1.00	-.13	.24	.18	-.30	-.49	-.10	-.31	.20	.21	-.09	.00	.39	.24	.13	.15	.04	-.07
mBDS Post-exertion	.07	-.13	.07	-.42	-.42	-.13	1.00	-.17	.07	.74	.63	.62	.60	-.66	-.28	-.24	-.35	.02	-.12	.07	.05	-.12	.10
SpO_2 Baseline	-.27	.51	.35	.28	.33	.24	-.17	1.00	.74	-.11	-.12	-.10	-.25	.42	.29	.35	.55	.12	.57	-.25	-.35	.46	-.35
SpO_2 Post-exertion	-.27	.44	.30	.16	.20	.18	.07	.74	1.00	.04	.10	.24	-.04	.08	.11	.21	.37	.07	.46	-.19	-.26	.38	-.30
SGRQ	.15	-.24	-.06	-.33	-.34	-.30	.74	-.11	.04	1.00	.65	.63	.83	-.64	-.14	.00	-.03	.01	-.02	.09	.06	-.06	.08
mMRC	-.03	-.20	-.13	-.27	-.39	-.49	.63	-.12	.10	.65	1.00	.52	.68	-.53	-.29	.04	-.08	-.18	-.13	-.23	-.19	.04	-.11
PCFS	.04	.02	.11	-.28	-.12	-.10	.62	-.10	.24	.63	.52	1.00	.45	-.44	-.10	-.08	-.12	-.22	.13	-.22	-.26	.25	-.15
CAT	.06	-.24	-.09	-.32	-.34	-.31	.60	-.25	-.04	.83	.68	.45	1.00	-.65	-.08	-.10	-.11	.04	-.14	.15	.22	-.21	.17
IPAQ	-.12	.22	.09	.24	.20	.20	-.66	.42	.08	-.64	-.53	-.44	-.65	1.00	.17	.43	.45	-.06	.21	-.13	-.23	.27	-.17
RBC:Barrier	.13	.35	.32	.07	.59	.21	-.28	.29	.11	-.14	-.29	-.10	-.08	.17	1.00	-.14	.35	.48	.45	.25	.42	-.03	.09
Barrier AUC	-.37	-.19	-.22	.36	-.23	-.09	-.24	.35	.21	.00	.04	-.08	-.10	.43	-.14	1.00	.81	-.10	.10	-.24	-.47	.38	-.19
RBC AUC	-.26	.03	-.02	.37	.11	.00	-.35	.55	.37	-.03	-.08	-.12	-.11	.45	.35	.81	1.00	.22	.44	-.08	-.25	.37	-.11
TBV	.01	.20	.22	-.10	.15	.39	.02	.12	.07	.01	-.18	-.22	.04	-.06	.48	-.10	.22	1.00	.62	.50	.73	-.16	.11
BV5	-.21	.42	.24	.05	.34	.24	-.12	.57	.46	-.02	-.13	.13	-.14	.21	.45	.10	.44	.62	1.00	-.18	-.04	.64	-.51
BV5-10	.44	-.03	.04	-.15	-.01	.13	.07	-.25	-.19	.09	-.23	-.22	.15	-.13	.25	-.24	-.08	.50	-.18	1.00	.89	-.82	.88
BV10	.35	-.04	.06	-.19	-.06	.15	.05	-.35	-.26	.06	-.19	-.26	.22	-.23	.42	-.47	-.25	.73	-.04	.89	1.00	-.74	.72
BV5/TBV	-.42	.20	.10	.13	.21	.04	-.12	.46	.38	-.06	.04	.25	-.21	.27	-.03	.38	.37	-.16	.64	-.82	-.74	1.00	-.90
BV5-10/TBV	.51	-.09	-.07	-.05	-.09	-.07	.10	-.35	-.30	.08	-.11	-.15	.17	-.17	.09	-.19	-.11	.11	-.51	.88	.72	-.90	1.00

BMI =body mass index; FEV_1=forced expiratory volume in 1 second; FVC=forced vital capacity; DL_{CO}=diffusing capacity of the lung for carbon monoxide; 6MWD=six minute walk-distance; mBDS=modified Borg Dyspnea Scale; SpO_2= oxygen saturation; SGRQ=St. George's respiratory questionnaire; mMRC=modified medical research council dyspnea scale; PCFS=post-COVID-19 functional scale; CAT=chronic obstructive pulmonary disease assessment test; IPAQ=international physical activity questionnaire; RBC=red-blood-cell; AUC=area under the curve; TBV=total blood volume; BV5=blood volume in vessels with cross-sectional area $\leq 5mm^2$; BV5-10= BV5=blood volume in vessels with cross-sectional area $>5mm^2$ and $\leq 10mm^2$; BV5=blood volume in vessels with cross-sectional area ≤ 10

CHAPTER 4

4 LONGITUDINAL FOLLOW-UP OF POST-ACUTE COVID-19 SYNDROME: DL_{CO}, QUALITY-OF-LIFE AND MRI PULMONARY GAS-EXCHANGE ABNORMALITIES

*In **Chapter 3** we uncovered evidence of abnormal gas-exchange in participants with PACS that was related to symptoms. In this chapter, we sought to examine these measurements over time to determine if ^{129}Xe MR could detect changes in Gas-exchange over time or if other measurements of participant lung function, symptoms or quality-of-life improved over time*

The contents of this chapter were previously published in Thorax: Alexander M Matheson, Marrissa J McIntosh, Harkiran K Kooner, Mohamed Abdelrazek, Mitchell S Albert, Inderdeep Dhaliwal, J Michael Nicholson, A Ouriadov, S Svenningsen and G Parraga. Thorax 2022. This article was published as open access and copyright was retained by the authors under a creative commons non-commercial license. Since publishing this manuscript, long-COVID has become the accepted term for long-term sequelae following COVID infection. The term PACS is maintained in this chapter as it was relevant to the discussion of different post-COVID definitions. The term "membrane" has also become preferred in the literature, however the originally published "tissue-plasma" is used in this chapter.

4.1 Introduction

In patients with post-acute COVID-19 syndrome, fatigue, chest pain, brain fog and dyspnoea are common and contribute to poor quality-of-life (QoL).[1,2] Recent studies showed that 7-30%[1,3] of people with post-acute COVID-19 syndrome (PACS) remain symptomatic 1-6 months post-infection. Unfortunately, the underlying mechanisms and pathologies responsible for PACS are not well-understood.

Chest CT measurements of abnormal pulmonary vascular blood distribution[4] and fibrosis[5] have been reported in patients following recovery from COVID-19 infection. Hyperpolarised ^{129}Xe

MRI has also revealed alveolar gas-transfer abnormalities in PACS,[6,7] including in never-hospitalised people up to 41 weeks post-infection.[8] However, longitudinal ^{129}Xe measurements have not been reported and previous studies did not have access to pre-COVID imaging to inform on potential mechanisms linking symptoms and gas-exchange abnormalities.[7,8] Here we endeavoured to determine whether ^{129}Xe MRI gas-transfer measurements normalised over time in people with PACS and if such changes occurred in concert with improved QoL and DL_{CO} measurements.

4.2 Methods

We obtained written-informed consent from participants 18-80 years of age for this prospective, Health Canada and ethics board approved (HSREB#113224), registered protocol (ClinicalTrials.gov: NCT04584671). Participants with a previous positive PCR COVID-19 test and ongoing symptoms were recruited from a local COVID-19 clinic. Study visits were planned for 3±1 months (baseline) and 15±3 months (follow-up) post-COVID-19+ test. Participants underwent ^{129}Xe ventilation MRI, ^{129}Xe gas-transfer MRI, spirometry, diffusing capacity of the lung (DL_{CO}) measurement, fraction of exhaled nitric oxide (FeNO) measurement, six-minute-walk-test (6MWT) and the St. George's Respiratory Questionnaire (SGRQ). The ^{129}Xe MRI RBC to alveolar tissue-plasma ratio was the primary endpoint. SPSS (SPSS Statistics 27.0; IBM) was used for all statistical analyses. Data were tested for normality using Shapiro-Wilk tests and nonparametric tests were performed for non-normally distributed data. Correlations were evaluated using Pearson (r) and Spearman (ρ) correlations. Pearson and Spearman correlations at baseline and follow-up were compared using the Fisher's z-score. Repeated measures were tested using paired t-tests. Results were considered statistically

significant when the probability of making a type I error was <5% ($p<0.05$). Detailed methods are provided in the online supplement. Baseline results were previously reported.[8]

4.3 Results

At baseline, we enrolled 34 participants[8] and 21 of these (7 female, age=56±15 years) returned for follow-up. For these 21 participants with PACS, the baseline visit occurred 7±4 months post-COVID-19 infection with positive tests occurring during the period March 2020 to April 2021, which was prior to the population-based vaccination initiatives in our local area. The follow-up visit occurred 14±4 months post-COVID-19 infection. Participant demographics are detailed in **Supplementary Table 4-1**. Nine of these participants were hospitalised due to COVID-19 infection, and one required intubation during a 4-week intensive care unit admission. Five participants were diagnosed with pulmonary embolism (via CT angiogram) during their COVID-19 infectious period. Medications are summarised in **Table 3-4**.

A

	Baseline (n=21)	Follow-up (n=21)	Difference [95% CI]	Significance (p)
Days Since +	198 (131)	420 (120)	222 [199,245]	
FEV_1 $\%_{pred}$	92 (22)	92 (22)	-0.4 [-2.8,2]	.729
FVC $\%_{pred}$	91 (21)	93 (27)	3 [-5.2,11.2]	.555
FEV_1/FVC %	78 (11)	78 (13)	-0.4 [-4.4,3.6]	.888
FeNO	24 (16)*	21 (15)*	-3 [-6,-1]	.084
$DL_{CO}\%_{pred}$	81 (20)*	96 (23)*	14 [7,21]	**<.001**
Quality-of-Life				
SGRQ	33 (20)	27 (21)	-6 [-11,-1]	**.044**
Symptom	42 (23)	31 (26)	-11 [-20,-2]	**.032**
6MWD m	409 (75)	431 (88)	22 [0,44]	.079
mBDS post-exertion	2.0 (1.5)	1.5 (1.8)	-0.7 [-1.0,-0.4]	**.019**
^{129}Xe MRI				
VDP	5 (9)*	4 (9)*	-0.3 [-1.2,0.6]	.500
RBC:TP	0.32 (0.09)	0.35 (0.09)	0.03 [0.01,0.05]	.051
TP:gas	1.11 (0.28)	1.13 (0.26)	0.02 [-0.06,0.05]	.659
RBC:gas	0.35 (0.14)	0.40 (0.16)	0.05 [0.01,0.09]	.055

B

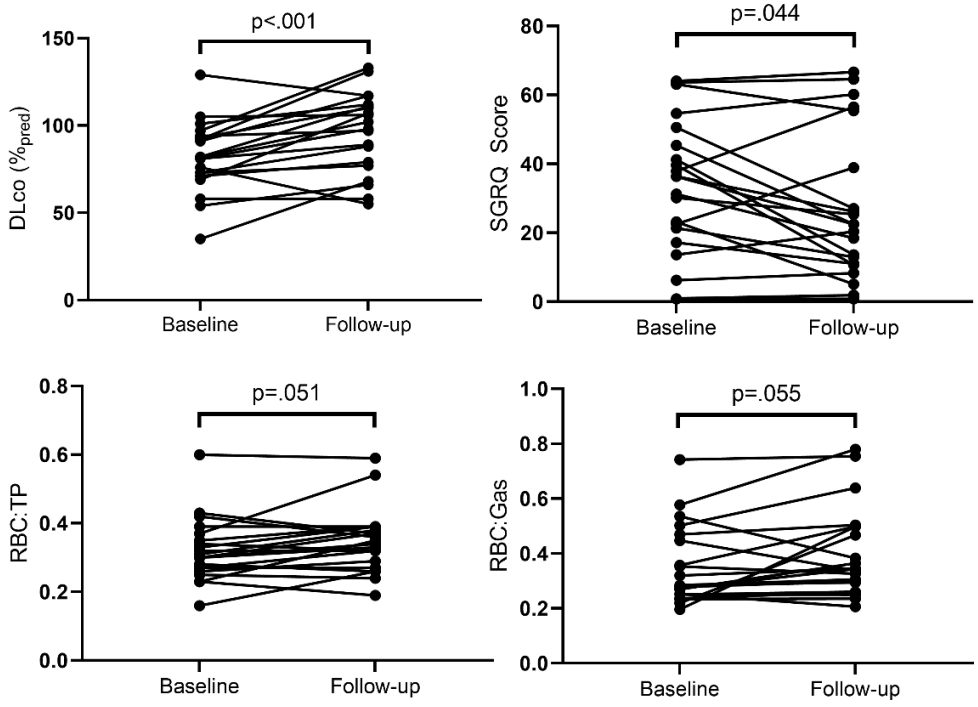

Figure 4-1 Clinical, quality-of-life and imaging measurements at baseline (7±4 months since PCR test) and follow-up (14±4 months since PCR test).
Top panel A shows tabulated baseline and follow-up measurements. Bottom panels B provide spaghetti plots for DL_{Co}, SGRQ score, ^{129}Xe MRI RBC:TP and RBC:gas measurements at baseline and follow-up. Differences were analysed for significance using paired t-tests.
FEV_1=forced expiratory volume in 1 second, $\%_{pred}$=percent of predicted value, FVC=forced vital capacity, FeNO=fractional exhaled nictric oxide, DL_{CO}=diffusing capacity of the lung for carbon monoxide; SGRQ=St. George's Respiratory Questionnaire, 6MWD=six-minute-walk-distance, mBDS=modified Borg Dyspnoea Scale, RBC=red-blood-cell, TP=tissue-plasma *n=20

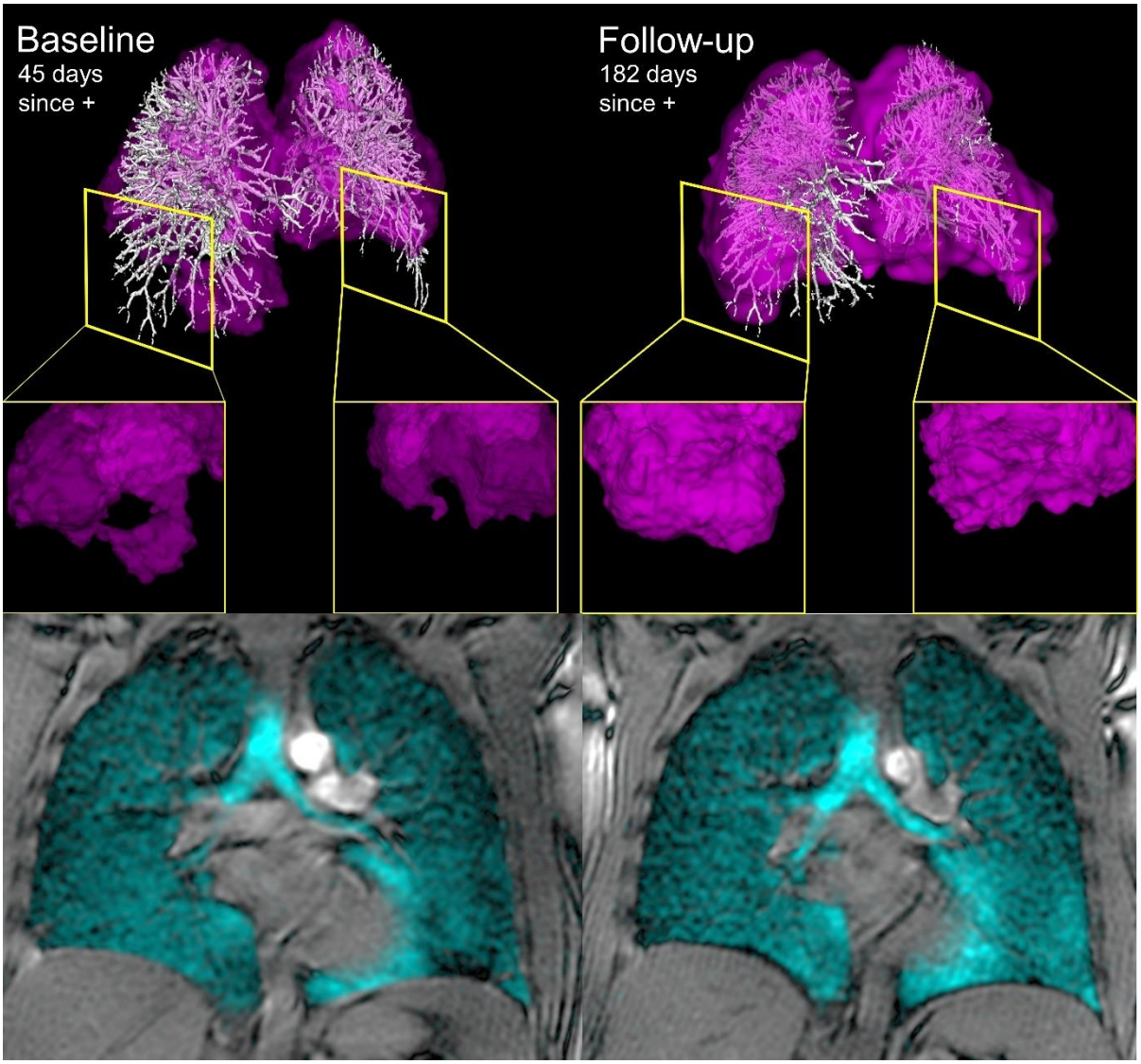

Figure 4-2 ^{129}Xe MRI and co-registered pulmonary vascular tree CT at baseline and follow-up. Left and right panels show ^{129}Xe MRI RBC map (pink) co-registered with CT pulmonary vascular tree (white) and bottom panels show ^{129}Xe ventilation images (cyan) for a previously healthy participant hospitalized with COVID symptoms and pulmonary embolism. At baseline 45 days post-COVID positive test, RBC:TP ratio was abnormally low (0.37) and insets provide examples of RBC map defects. At follow-up the RBC:TP ratio improved (0.54) as did the lower lobe red-blood-cell map defects shown in the right panel inset. DL_{CO} (baseline=93%$_{pred}$, follow-up=110%$_{pred}$) and total SGRQ score (baseline=23, follow-up=5) also improved at follow-up.

Figure 4-1 summarises baseline and follow-up clinical, QoL and imaging measurements in tabular format and spaghetti plots for DL_{CO}, SGRQ and ^{129}Xe MRI measurements. There were no significant differences in spirometry, 6MWD (Δ=22;95%CI=0,44, p=.084) and FeNO (Δ=-

3;95%CI=-6,-1, p=.084) between visits; FeNO measurements were normal across visits. DL_{CO} (Δ=14;95%CI=7,-21, p<.001), SGRQ-total (Δ=-6; 95%CI=-1,-11, p=.044) and symptom-score (Δ=-11;95%CI=-2,20, p=.032) significantly improved at follow-up. There was also significantly improved post-exertional dyspnoea (measured using the modified Borg Dyspnoea Scale [mBDS] post-six-minute-walk-test, Δ=-0.7;95%CI=-0.2,-1.2, p=.019) but not ^{129}Xe RBC:TP (Δ=0.03;95%CI=0.01,0.05, p=.051), ^{129}Xe RBC:gas (Δ=0.06;95%CI=0.02,0.10, p=.055) or FeNO (Δ=-3;95%CI=0,-6, p=.084) at 14-months. At baseline, two participants desaturated (ΔSpO_2=-9%, -7%) following the 6MWT while at follow-up, no participants desaturated.

Figure 4-2 shows representative three-dimensional ^{129}Xe MRI RBC maps co-registered with the corresponding segmented CT vessel tree for a single 31-year-old male participant at baseline and follow-up. ^{129}Xe MRI RBC map focal defects were obvious in the left and right lower lobes at baseline (shown in the insets) and this was coincident with an SGRQ total score of 23, post-exertional breathlessness score of 3 and RBC:TP ratio of 0.37. At follow-up, shown in the right panel, the RBC defects visually improved and this was coincident with clinically-relevant improvements[9] in SGRQ total score of 5, post-exertional breathlessness score of 1 and improved RBC:TP ratio (0.54). **Figure 4-4** shows multiple slices of ventilation and 2D raw red-blood-cell component of the dissolved phase images at both baseline and follow-up for additional participants.

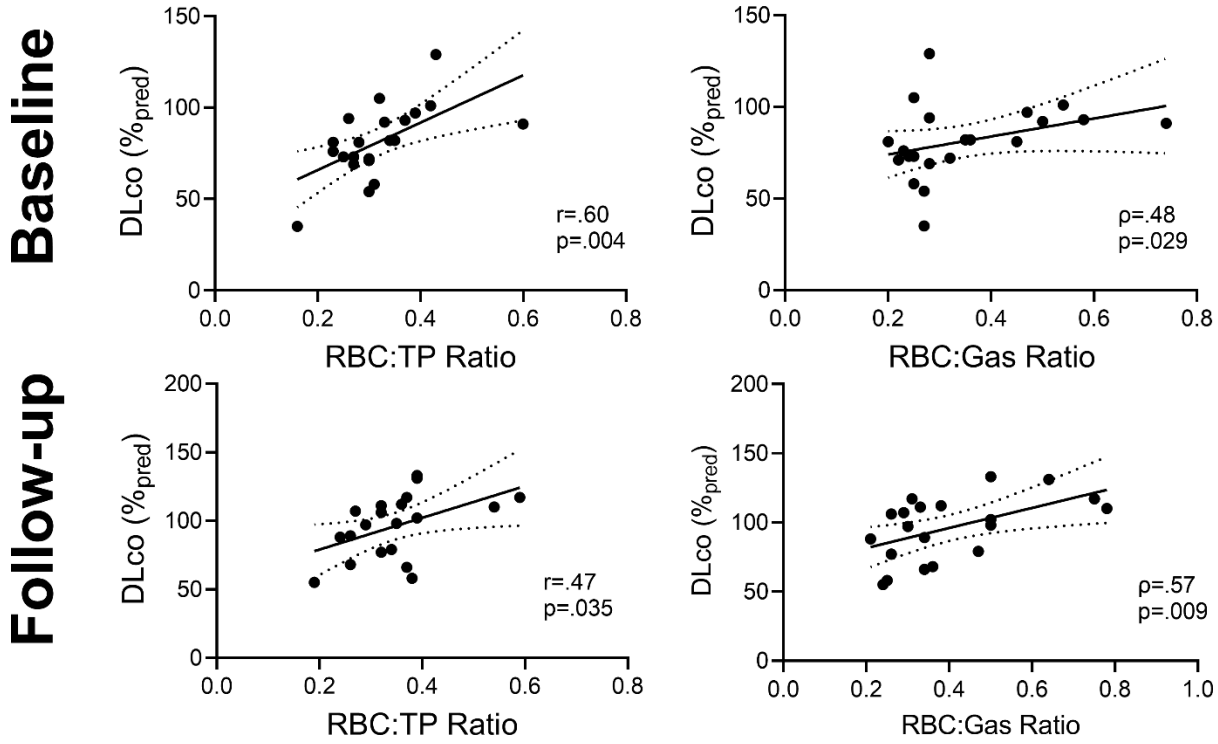

Figure 4-3 Correlations between DL_{CO} and ^{129}Xe MRI measurements.
At baseline and follow-up there were weak to moderate, significant correlations between DL_{CO} and ^{129}Xe MRI RBC:TP and RBC:gas ratios. (Participants with DL_{CO} measurement n=20)

Figure 4-3 shows weak-to-moderate correlations for DL_{CO} and ^{129}Xe MRI RBC:TP (r=.60 95%CI=.22 .82, p=.004) and RBC:Gas (ρ=.48, 95%CI=.04,.76, p=.029) at baseline. It also shows DL_{CO} correlations at follow-up (RBC:TP r=.47, 95%CI=.04,.76, p=.035; RBC:Gas, ρ=.57, 95%CI=.16, .81, p=.009). The correlations for DL_{CO} and RBC:TP at baseline (r=.60, p=.004) and follow-up (r=.47, p=.03) were not significantly different (z score=0.51, p=.609). **Supplemental Figure 4-5** shows significant correlations for the change in SGRQ at follow-up with the change in DL_{CO} (r=-.55, CI=-.14,-.80, p=.012) and post-exertional Borg dyspnoea (r=.68, 95%CI=.35,.86, p=.001).

4.4 Discussion

Previous work revealed the presence of ^{129}Xe gas-transfer abnormalities in people with PACS,[7,8] and showed that these abnormalities were related to dyspnoea and exercise limitation.[8] We examined a small group of 21 participants with PACS to measure SGRQ, DL_{CO} and ^{129}Xe MRI gas-exchange measurements, 7 months after a baseline visit and observed: 1) significant improvements in DL_{CO}, SGRQ scores and post-exertional dyspnoea, 2) persistently abnormal ^{129}Xe MRI RBC:TP values, (healthy volunteer RBC:TP=0.41±0.10)[8] and, 3) positive correlation for DL_{CO} with ^{129}Xe MRI RBC measurements, negative correlation for the change in DL_{CO} with the change in SGRQ and a positive correlation for the change in DL_{CO} with post-exertional dyspnoea at follow-up. Whether this snapshot in time, 14±2 months post-infection reflects a slow, ongoing recovery or permanent impairment, remains to be ascertained.

Previous work[8] detected a significant correlation between DL_{CO} and ^{129}Xe RBC:TP in PACS and here, we observed that this correlation persisted over time. This suggested that ^{129}Xe RBC:TP detected abnormal alveolar gas-exchange that remained abnormal in people with PACS, long after the infection had resolved. We also observed a correlation between post-exertional dyspnoea and DL_{CO} on SGRQ-score, underscoring the impact of dyspnoea and gas-exchange improvements on QoL improvements in PACS.

Together, these data suggest gas-exchange abnormalities at least partially resolved during a period of 7 months (and 14 months post-infection). While we do not know the precise cause of abnormal RBC:TP in these participants, a recently published study that evaluated post-mortem COVID-19 lungs described vasculo-pathologies including vascular congestion, perivascular inflammation, thrombo-emboli and infarcts unique to COVID-19 that could explain ongoing pulmonary vascular abnormalities.[10]

To our knowledge this is the first longitudinal ^{129}Xe gas-transfer MRI study of PACS. This study was limited by small sample size. ^{129}Xe spectroscopy had not previously been performed at our site and this study was therefore not powered for spectroscopy measurements. The sample size was also limited by incomplete retention of the original cohort of study participants. Retention difficulties stemmed from a number of reasons including the fact that fully recovered participants were less inclined to return for a follow-up visit during the COVID-19 pandemic and because of institutional requirements for fully vaccinated participants at follow-up. We also note that measurements were not available in these participants prior to infection, and this makes it difficult to distinguish abnormalities due to PACS or other sources. Seven patients had pre-existing asthma and one had pre-existing COPD which may have impacted gas-exchange measurements.

We measured improved SGRQ, DL_{CO} and post-exertional dyspnoea 14-months as compared to 7-months post-infection. Taken together, these findings provide hypothesis-generating insights which may help target future research on the mechanisms of gas-exchange abnormalities in people with PACS.

4.5 References

1. Xie Y, Bowe B, Al-Aly Z. Burdens of post-acute sequelae of COVID-19 by severity of acute infection, demographics and health status. Nat Commun. 2021;12(1):6571.

2. Nalbandian A, Sehgal K, Gupta A, Madhavan MV, McGroder C, Stevens JS, et al. Post-acute COVID-19 syndrome. Nature Medicine. 2021;27(4):601-15.

3. Yoo SM, Liu TC, Motwani Y, Sim MS, Viswanathan N, Samras N, et al. Factors Associated with Post-Acute Sequelae of SARS-CoV-2 (PASC) After Diagnosis of Symptomatic COVID-19 in the Inpatient and Outpatient Setting in a Diverse Cohort. J Gen Intern Med. 2022.

4. Lins M, Vandevenne J, Thillai M, Lavon BR, Lanclus M, Bonte S, et al. Assessment of Small Pulmonary Blood Vessels in COVID-19 Patients Using HRCT. Acad Radiol. 2020;27(10):1449-55.

5. McGroder CF, Zhang D, Choudhury MA, Salvatore MM, D'Souza BM, Hoffman EA, et al. Pulmonary fibrosis 4 months after COVID-19 is associated with severity of illness and blood leucocyte telomere length. Thorax. 2021;76(12):1242-5.

6. Li H, Zhao X, Wang Y, Lou X, Chen S, Deng H, et al. Damaged lung gas exchange function of discharged COVID-19 patients detected by hyperpolarized (129)Xe MRI. Sci Adv. 2021;7(1).

7. Grist JT, Collier GJ, Walters H, Kim M, Chen M, Abu Eid G, et al. Lung Abnormalities Depicted with Hyperpolarized Xenon MRI in Patients with Long COVID. Radiology. 2022:220069.

8. Matheson AM, McIntosh MJ, Kooner HK, Lee J, Desaigoudar V, Bier E, et al. Persistent 129Xe MRI Pulmonary and CT Vascular Abnormalities in Symptomatic Individuals with Post-Acute COVID-19 Syndrome. Radiology. 2022;0(0):220492.

9. Jones PW. Interpreting thresholds for a clinically significant change in health status in asthma and COPD. Eur Respir J. 2002;19(3):398-404.

10. Villalba JA, Hilburn CF, Garlin MA, Elliott GA, Li Y, Kunitoki K, et al. Vasculopathy and Increased Vascular Congestion in Fatal COVID-19 and ARDS. Am J Respir Crit Care Med. 2022.

4.6 Supplemental Material

4.6.1 Material and Methods

Study Participants

We prospectively evaluated people 18-80 years of age who provided written-informed-consent to an ethics-board (HSREB # 113224), Health-Canada approved and registered protocol (ClinicalTrials.gov: NCT04584671). Study participants with a proven positive PCR COVID-19 test were prospectively recruited from a quaternary-care COVID-19 clinic between April and October 2021. Inclusion criteria consisted of: age ≥ 18 and <80 years, a documented case by positive RT-PCR test of COVID-19 infection that resulted in symptoms post-infection. Exclusion criteria consisted of: contraindications to MRI such as implants and severe claustrophobia, mental or legal incapacitation or could not read or understand written material, inability to perform spirometry or plethysmography maneuvers, and pregnancy.

Study Design

The study design consisted of Visit 1 (3-months post +COVID test), an optional Visit 2 (9-months post +COVID test), Visit 3 (15-months post +COVID test) and Visit 4 (27-months post +COVID test). Participants were administered salbutamol upon arrival at our centre according to American Thoracic Society Guidelines[1] and 15 minutes later performed post-bronchodilator (BD) spirometry and DL_{CO} immediately prior to MRI. Participants completed the six-minute-walk-test (6MWT) and Questionnaires (St. George's Respiratory Questionnaire (SGRQ),[2] modified Medical Research Council (mMRC) Questionnaire, Chronic Obstructive Pulmonary Disease Assessment Test (CAT),[3] post-COVID-19 Functional Status scale,[4] International Physical Activity Questionnaire (IPAQ),[5] and modified Borg Dyspnoea Scale (mBDS).[6,7] ^{129}Xe gas-exchange MRI was performed in at least two visits. SpO_2 and heart rate were

measured using an 8500 series handheld pulse oximeter (Nonin Medical Inc.) upon participant arrival as well as before and just after the 6MWT.

Pulmonary Function Tests

Pulmonary function tests were performed according to American Thoracic Society guidelines[8,9] using a *ndd EasyOne Pro LAB system* (ndd Medical Technologies) or a *MedGraphics Elite Series* plethysmograph (MGC Diagnostics Corporation). Post-BD measurements were performed 15 minutes after inhalation of 4×100 µg/inhalation salbutamol sulfate norflurane (Ivax Pharmaceuticals) using an *AeroChamber* (Trudell Medical International). Participants underwent FeNO measurement according to guidelines[10] using a NIOX VERO system (Circassia Pharmaceuticals, Inc.). Participants withheld inhaled medications before study visits according to American Thoracic Society guidelines (e.g. short-acting β-agonists ≥6 hours, long-acting β-agonists ≥12 hours, long-acting muscarinic antagonists ≥24 hours).[8] Questionnaires and the 6MWT were self-administered under supervision of study personnel.

^{129}Xe MRI

Anatomic ^{1}H MRI was acquired using a fast-spoiled gradient-recalled-echo sequence (partial-echo acquisition; total acquisition time, 8 seconds; repetition-time msec/echo time msec, 4.7/1.2; flip-angle, 30°; field-of-view, 40×40cm^2; bandwidth, 24.4 kHz; 128×80 matrix, zero-filled to 128×128; partial-echo percent, 62.5%; 15-17×15mm slices). ^{129}Xe MR spectroscopy was acquired following inhalation breath-hold of a 1.0L gas mixture (4/1 by volume 4He/129Xe) from functional residual capacity (FRC) using a free-induction-decay whole-lung spectroscopy sequence (200 dissolved-phase spectra, TR=15ms, TE=0.7ms, flip=40°, BW=31.25kHz, 600µs 3-lobe Shinnar-Le Roux pulse). Spectroscopy was used to determine

the echo time for a 90º tissue-plasma/RBC phase difference (TE_{90}). ^{129}Xe MRI was performed following inhalation of a 1.0L gas mixture (1/1 by volume ^{4}He/^{129}Xe) using an interleaved gas/dissolved-phase 3D radial sequence (TR=15ms TE=variable, flip=0.5º/40º, FOV=40cm^3, matrix=72x72x72, BW=62.5kHz, 990 gas/dissolved projections, 600μs 3-lobe Shinnar-Le Roux pulse, frequency shift=7.664kHz). Supine participants were coached to inhale a 1.0L bag (Tedlar; Jensen Inert Products, Coral Springs, FL, USA) (500mL ^{129}Xe + 500mL ^{4}He for ^{129}Xe MRI and 1.0L N_2 for ^{1}H MRI) from the bottom of a tidal breath (functional residual capacity) with acquisition under breath-hold conditions. ^{129}Xe gas was polarised to 30-40% (Polarean; Xenispin 9820, Durham, NC, USA).[11]

Gas-transfer MRI data were reconstructed as previously described using a re-gridding method for non-cartesian acquisition.[12] Receiver phase-offset and local phase inhomogeneity were corrected as previously described.[13]

^{129}Xe gas-exchange MRI were corrected for local phase inhomogeneity using acquired interleaved gas-compartment data. Deviations from uniform phase in the gas image were assumed to result from phase inhomogeneity and voxel-wise phase corrections were applied to eliminate inhomogeneity effects. Receiver phase-offset was corrected using the spectroscopic RBC:TP ratio. A phase correction $\Delta\phi$ was applied such that the ratio of real to imaginary channel signal matched the spectroscopic RBC:TP ratio under the assumption that RBC and TP signal should be perfectly aligned to the real and imaginary channels, respectively, at TE_{90}.

4.6.2 Supplementary Tables

Table 4-1 Participant demographics

Parameter Mean (SD)	PACS (n=21)
Age yrs	56 (15)
Females n (%)	8 (38)
Hospitalized n (%)	9 (43)
BMI kg/m^2	31 (6)
Asthma n (%)	7 (33)
COPD n (%)	1 (5)
Pack-years	8 (19)

BMI=body mass index; COPD=chronic obstructive pulmonary disease

Table 4-2 Participant medications

Participant	Baseline Medications	Follow-up Medications
P01	Anticoagulant, ICS/LABA, SABA	Anticoagulant, ICS/LABA, SABA
P02	ICS/LABA, Anticholinergic, ICS	ICS/LABA, SABA
P03	ICS/LABA, ACE inhibitor, BP	ICS/LABA, ACE inhibitor, BP
P04	ICS/LABA	None
P05	Anticoagulant, stimulant	Anticoagulant, stimulant
P06	Diuretic, anticoagulant, thyroid hormone, BP	ICS/LABA, Diuretic, anticoagulant, thyroid hormone, BP
P07	Alpha blocker, beta blocker, anticoagulant, anti-cholesterol, BP, ICS	Alpha blocker, beta blocker, anticoagulant, anti-cholesterol, BP, ICS
P08	Antidepressant, ICS/LABA	ICS/LABA
P09	Antidepressant	Antidepressant
P10	ICS/LABA, Leukotriene antagonist, LABA, proton pump inhibitor	ICS/LABA, SABA, leukotriene antagonist, LABA, proton pump inhibitor, ICS
P11	ISC/LABA, SABA	ICS/LABA
P12	None	None
P13	BP, anti-cholesterol, alpha blocker, beta blocker, proton pump inhibitor, aspirin, ICS/LABA	BP, anti-cholesterol, alpha blocker, beta blocker, proton pump inhibitor, aspirin, diuretic, ICS/LABA
P14	Thyroid hormone, antidepressant	Thyroid hormone, contraceptive
P15	Insulin, acetaminophen, anti-cholesterol, anticoagulant, anti-inflammatory, proton pump inhibitor, ICS/LABA, SABA, beta agonist	Insulin, acetaminophen, anti-cholesterol, anticoagulant, ani-inflammatory, opioid, BP
P16	Acetaminophen, anticonvulsant, anti-inflammatory, hormone	Anticonvulsant, antidepressant, anti-inflammatory
P17	ACE inhibitor, BP, proton pump inhibitor, prostaglandin analog, anti-cholesterol, LABA, SABA, aspirin, ICS/LABA	ACE inhibitor, BP, proton pump inhibitor, prostaglandin analog, anti-cholesterol, LABA, SABA, aspirin, ICS/LABA
P18	Monoclonal antibody, digestive enzyme, ICS/LABA, SABA, LABA, anti-histamine	Monoclonal antibody, digestive enzyme, ICS/LABA, SABA, LAMA
P19	Antidepressant	ICS/LABA, BP
P20	Anti-cholesterol, prostaglandin analog, diuretic, antacid, SABA	Anti-cholesterol, prostaglandin analog, diuretic, antacid, SABA
P21	None	None

ICS=inhaled corticosteroids, LABA=long-acting beta-agonist, SABA=short-acting beta-agonist, ACE=angiotensin-converting enzyme, BP=blood pressure medication

4.6.3 Supplemental Figures

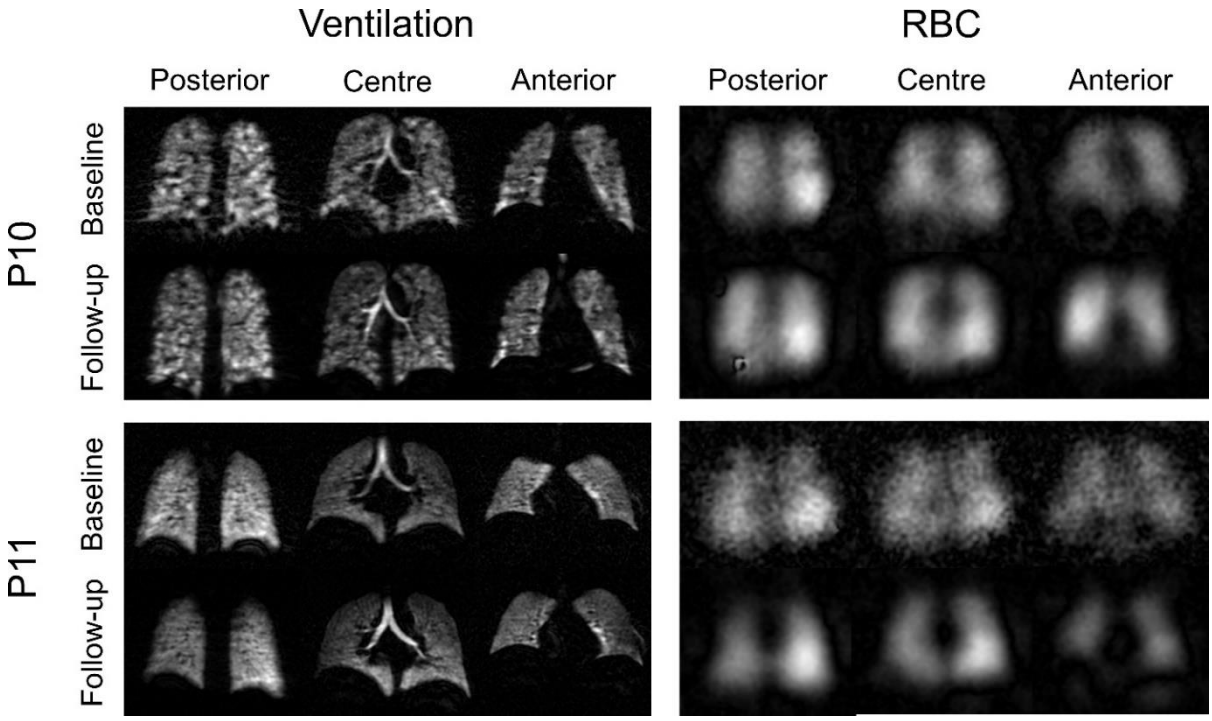

Figure 4-4 ^{129}Xe gas-exchange and ventilation MRI in two participants with PACS
Ventilation imaging and 2D (three central slices) raw red-blood-cell component of the dissolved phase images at baseline and follow-up for two participants.

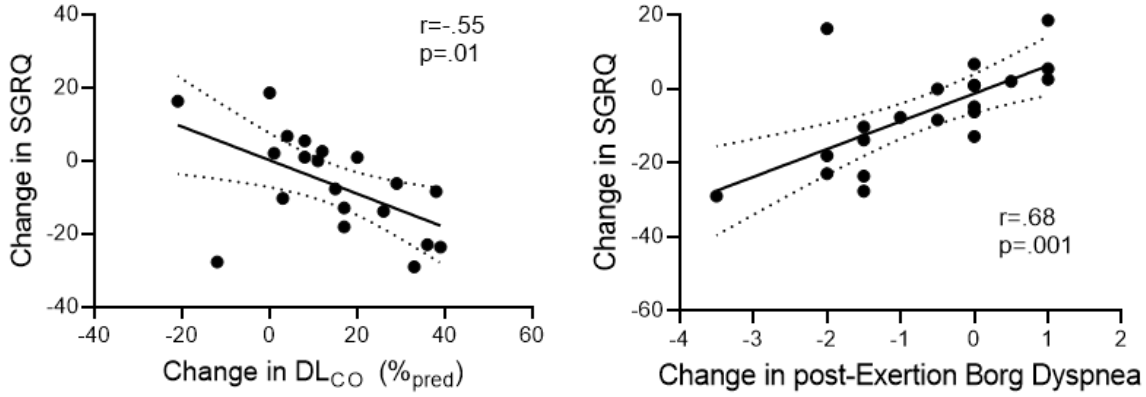

Figure 4-5 Correlations between changes in SGRQ score and clinical measurements.
There were moderate correlations between changes in SGRQ score and changes in DL_{CO} as well as post-exertion Borg dyspnoea. (Participants with DL_{CO} measurement n=20).

4.6.4 References

1. Graham BL, Steenbruggen I, Miller MR, Barjaktarevic IZ, Cooper BG, Hall GL, et al. Standardization of Spirometry 2019 Update. An Official American Thoracic Society and European Respiratory Society Technical Statement. Am J Respir Crit Care Med. 2019;200(8):e70-e88.

2. Jones PW, Quirk FH, Baveystock CM, Littlejohns P. A self-complete measure of health status for chronic airflow limitation. The St. George's Respiratory Questionnaire. Am Rev Respir Dis. 1992;145(6):1321-7.

3. Jones PW, Harding G, Berry P, Wiklund I, Chen WH, Kline Leidy N. Development and first validation of the COPD Assessment Test. Eur Respir J. 2009;34(3):648-54.

4. Klok FA, Boon GJAM, Barco S, Endres M, Geelhoed JJM, Knauss S, et al. The Post-COVID-19 Functional Status scale: a tool to measure functional status over time after COVID-19. European Respiratory Journal. 2020;56(1).

5. Craig CL, Marshall AL, Sjostrom M, Bauman AE, Booth ML, Ainsworth BE, et al. International physical activity questionnaire: 12-country reliability and validity. Med Sci Sports Exerc. 2003;35(8):1381-95.

6. Borg GAV. Psychophysical bases of perceived exertion. Med Sci Sports Exerc. 1982;14(5):377-81.

7. Enright PL. The Six-Minute Walk Test. Respiratory Care. 2003;48(8):783-5.

8. Miller MR, Hankinson J, Brusasco V, Burgos F, Casaburi R, Coates A, et al. Standardisation of spirometry. Eur Respir J. 2005;26(2):319-38.

9. Graham BL, Brusasco V, Burgos F, Cooper BG, Jensen R, Kendrick A, et al. 2017 ERS/ATS standards for single-breath carbon monoxide uptake in the lung. Eur Respir J. 2017;49(1).

10. American Thoracic S, European Respiratory S. ATS/ERS recommendations for standardized procedures for the online and offline measurement of exhaled lower respiratory nitric oxide and nasal nitric oxide, 2005. Am J Respir Crit Care Med. 2005;171(8):912-30.

11. Walker TG, Happer W. Spin-exchange optical pumping of noble-gas nuclei. Rev Mod Phys. 1997;69(2):629-42.

12. Robertson SH, Virgincar RS, He M, Freeman MS, Kaushik SS, Driehuys B. Optimizing 3D noncartesian gridding reconstruction for hyperpolarized 129Xe MRI—focus on preclinical applications. Concepts in Magnetic Resonance Part A. 2015;44(4):190-202.

13. Kaushik SS, Robertson SH, Freeman MS, He M, Kelly KT, Roos JE, et al. Single-breath clinical imaging of hyperpolarized (129)Xe in the airspaces, barrier, and red blood cells

using an interleaved 3D radial 1-point Dixon acquisition. Magn Reson Med. 2016;75(4):1434-43.

CHAPTER 5

5 HYPERPOLARIZED ^{129}XE PULMONARY MRI AND ASYMPTOMATIC ATRIAL SEPTAL DEFECT

*During recruitment of a healthy cohort for **Chapter 3** I discovered a novel MRS abnormality in an otherwise healthy teenager. This chapter details the investigation performed to determine the source of the abnormality and seeks to understand the underlying mechanism connecting a congenital heart abnormality to pulmonary gas-exchange measurements.*

The contents of this chapter were previously published in the journal CHEST: Alexander M. Matheson, Robin S.P. Cunningham, Elianna Bier, Junlan Lu, Bastiaan Dreihuys, J. Geoffrey Pickering, Pantelis Diamantouros, Ali Islam, J. Michael Nicholson, Grace Parraga, and Sarah Blissett. Chest 2022; 161(4):e199-e202. This chapter also includes a follow-up publication published as a letter to the editor: Alexander M. Matheson, Robin S.P. Cunningham, Grace Parraga, Michael W.A. Chu, Sarah Blissett. Chest 2022; 162(4):e205-e206. The right to include these works in a thesis or dissertation was retained at time of publication. The term "membrane" has become preferred in the literature to "barrier," used in this chapter.

5.1 Introduction

Hyperpolarized ^{129}Xe MRI provides a way to generate measurements of inhaled gas distribution (ventilation) as well as transmembrane diffusion into the alveolar-capillary tissue space and the red-blood-cells (RBC) (perfusion).

5.2 Case Report

An active, asymptomatic 19-year-old male with no history of cardiopulmonary disease, provided written-informed-consent to undergo hyperpolarized ^{129}Xe MRI as a participant in the control arm of a COVID19 study. ^{129}Xe was polarized (*Polarean 9820*, Polarean, Durham, NC) and ^{129}Xe MRI performed (Discovery MR750 General Electric Healthcare, Madison, WI) using a vest coil (Clinical MR Solutions, Brookfield, WI) as described.[1]

	5 July 2021	22 July 2021
PFT		
FEV_1 ($\%_{predicted}$)	106	106
FVC ($\%_{predicted}$)	117	120
FEV_1/FVC	76	75
TLC ($\%_{predicted}$)	104	107
RV ($\%_{predicted}$)	93	69
RV/TLC	20	15
DL_{CO} ($\%_{pred}$)	130	130
Blood Tests		
SaO_2	91	85
ERC (μL^{-1})		6.89
Hb (g/dL)		23.3
HCT		0.68
Reticulocyte (%)		151

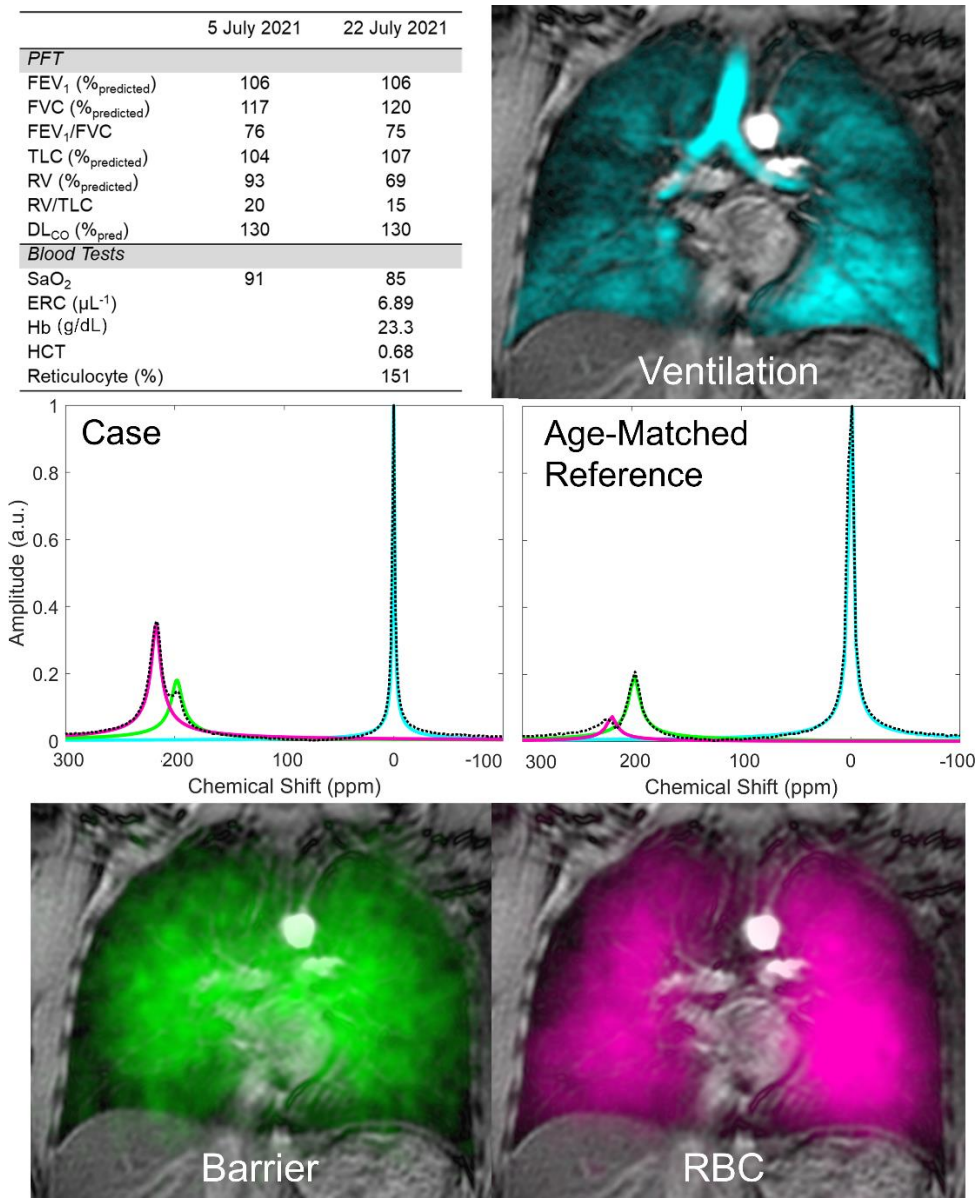

Figure 5-1 Initial findings using MRI and pulmonary function fests.
Table shows spirometry, plethysmography, and diffusing capacity for carbon monoxide (DL_{CO}) measurements acquired within 15 minutes of MRI in the research laboratory and clinical laboratory measurements, 5 weeks later. Blood tests were performed 2 weeks after the research laboratory PFTs. MR spectroscopy is shown in the gaseous (top panel left), tissue-dissolved, and RBC-dissolved states (bottom panel). Ventilation images and barrier images were homogenously filled without defects, whereas RBC images were also homogeneously filled, but with augmented signal intensity. Spectroscopic data (dotted black lines) were fitted to three Lorentzian distributions corresponding to gas (cyan), barrier (green), and RBC (magenta) ^{129}Xe phases. Fitted spectroscopy showed a substantially increased RBC peak (area under the curve [AUC] = 229) relative to an age-matched reference (AUC = 48). Image colormaps were scaled relative to the age-matched reference. a.u. = arbitrary unit; ERC = erythrocyte count; Hb = hemoglobin; HCT = hematocrit; PFT = pulmonary function test; ppm = parts part million; RV = right ventricle; SaO2 = oxygen saturation; TLC = total lung capacity.

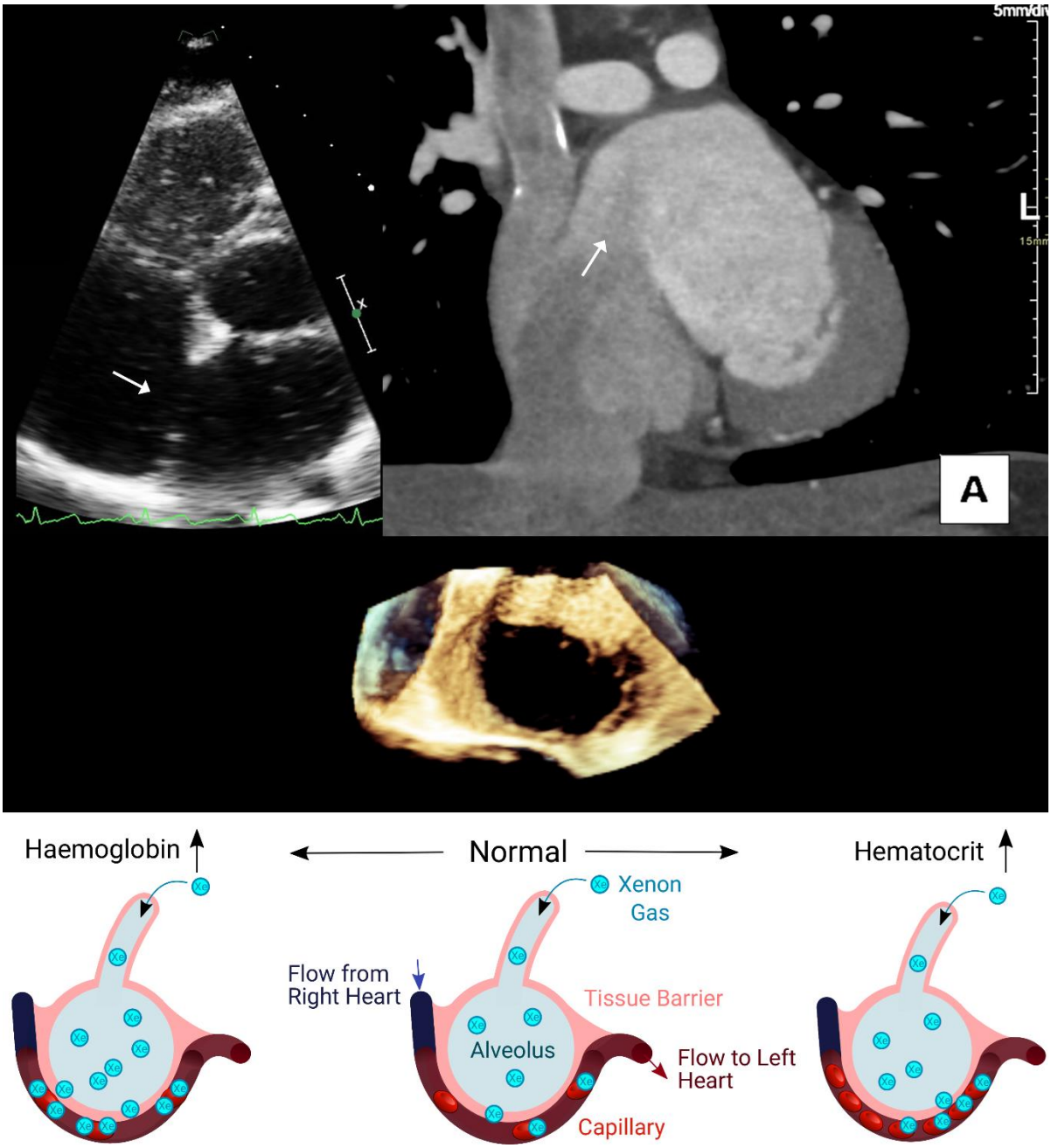

Figure 5-2 Cardiac imaging and proposed models explaining MRI result.
Top left panel shows transthoracic echocardiogram, which was consistent with right-to-left shunting through a moderate-to-large atrial septal defect (ASD). Top right panel shows a contrast-enhanced cardiac CT scan performed 6 weeks later (left panel) revealing unopacified flow from the inferior vena cava into the left atrium across the atrial septum. Transesophageal echocardiogram performed 7 weeks after the cardiac CT scan (middle panel shows 3-D reconstruction) shows large (20-27 mm) secundum ASD. Bottom panel shows proposed model explaining ^{129}Xe MRI/spectroscopy. Increased RBC signal was attributable to augmented hematocrit and corresponding increase in hemoglobin, resulting in more RBC available for xenon binding but with normal hemoglobin concentrations/RBC (mean corpuscular hemoglobin content [MCHC]).

Spectroscopy was performed after inhalation of a 1.0L gas mixture (4/1 by volume $^{4}He/^{129}Xe$) from functional residual capacity (FRC) using a free-induction-decay sequence as previously described.[2] Dissolved-phase ^{129}Xe MRI was acquired using an interleaved 3D radial sequence[2] and ^{129}Xe ventilation MRI was performed as described.[3] Image reconstruction[4] and single-point Dixon-method[5] were used to generate ^{129}Xe MRI red-blood-cell (RBC) and alveolar-to-capillary-tissue images.[5]

Figure 5-1 shows that spirometry, plethysmography and the diffusing-capacity-for-carbon-monoxide (top-panel) performed 20-minutes prior to MRI and according to guidelines,[6,7] were normal. ^{129}Xe spectroscopy revealed an elevated ^{129}Xe RBC spectroscopic peak with RBC:Barrier ratio=4.7x an age-matched participant, at the same frequency. ^{129}Xe MRI ventilation, alveolar-capillary tissue barrier and RBC images were without defects.

Pulse-oximetry performed during MRI revealed abnormally low digital and ear-lobe SaO_2 and there was evidence of clubbing and cyanosis. All other vital signs were normal.

Laboratory tests performed (**Figure 5-1**) were normal except for haematocrit (0.68, normal-range 0.40-0.54[8]) and haemoglobin (23.3 g/dL, normal-range 14-18 g/dL[8]).

As shown in **Figure 5-2**, transesophageal echocardiography demonstrated a large secundum atrial septal defect (ASD) with moderate dilation of the right atrium and mild dilation of the right ventricle. Contrast-enhanced CT confirmed the presence of a large ASD with contrast streaming suggestive of right-to-left shunting (**Figure 5-2**).

Cardiac catheterization revealed mildly elevated right and left atrial pressures (mean 8 mm Hg and 6 mm Hg respectively), normal pulmonary artery pressures (19/6, mean 13 mmHg) and a substantial right-to-left shunt (Qp:Qs 0.5). Trans-esophageal echocardiogram (**Figure 5-2**) provided the ASD dimensions and visualized a prominent Eustachian valve.

5.3 Discussion

To our knowledge, this is the first report of asymptomatic adult congenital heart disease diagnosed subsequent to novel ^{129}Xe MRI findings. In a teenaged male, ^{129}Xe MRI revealed a super-enhanced RBC signal and RBC to alveolar-capillary tissue ratio with normal ventilation, tissue-barrier images and super-normal RBC signal intensity. Further testing to evaluate the cause of the cyanosis revealed a large secundum ASD with right-to-left shunting. While most right-to-left shunting is due to pulmonary hypertension, the pulmonary pressures were normal in this patient suggesting that shunting was due to anatomic streaming. His height had recently rapidly increased, which may have changed the position of his heart in such a way that the IVC flow was now directed to the ASD by a prominent Eustachian valve. The resultant cyanosis lead to compensatory secondary erythrocytosis, elevating the haemoglobin and haematocrit. ^{129}Xe tissue barrier and RBC signal intensities and their ratios have been suggested to reflect fibrosis[9] and pulmonary hypertension[10], neither of which were observed in this case.

^{129}Xe MRI RBC values were previously shown to be related to DL_{CO}[11] which was interpreted to reflect capillary volume.[12] The current case however, suggests an alternative explanation (**Figure 5-2**) of increased ^{129}Xe binding due to augmented haemoglobin and haematocrit. When a haemoglobin correction was employed,[13] the corrected DL_{CO} was normalized ($110\%_{pred\text{-}Hb}$) which suggested that abnormally increased haemoglobin was partially responsible for the RBC finding. The mean corpuscular haemoglobin content (MCHC) was normal (342.6 g/L, normal range 320-360 g/L)[14] and therefore augmented haemoglobin was likely a consequence of augmented haematocrit. This is in keeping with the clinical history of ASD and the fact that compensatory polycythemia often accompanies this hemodynamic abnormality. Other explanations for the super-enhanced RBC peak include spectral-leakage

and nonuniform RF excitation of the tissue and RBC peaks. Whilst these are certainly possible, physiologic and hemodynamic explanations appear to dominate. This unexpected and novel case deepens our understanding of the pathophysiologic relevance of ^{129}Xe MRI findings.[10-12] While most secundum ASD cases are diagnosed in childhood, some patients do not present until adulthood (prevalence=0.88/1000).[15] Unlike other ASD cases which typically present with dyspnea and exercise limitation, this case was asymptomatic with no medical history that would point to congenital heart disease. Participation in a healthy volunteer arm of a ^{129}Xe MRI COVID19 study prompted this unexpected finding and early ASD identification and intervention. In the process we have gained an understanding of the sensitivity of ^{129}Xe MRI dissolved-phase measurements to cardiac abnormalities and compensatory hematologic mechanisms.

5.4 Follow-up: POST-CARDIAC SURGERY ATRIAL SEPTAL DEFECT REPAIR: NORMALIZATION OF HYPERPOLARIZED ^{129}XE MRI RBC-TO-BARRIER RATIO

We recently published a case of a large secundum atrial septal defect,[16] diagnosed in an active asymptomatic teenager subsequent to the detection of an abnormally enhanced hyperpolarized ^{129}Xe MRI signal in the red-blood-cells of the pulmonary capillaries.

Hyperpolarized ^{129}Xe MRI was previously developed[5] to provide a way to simultaneously generate pulmonary maps of inhaled ^{129}Xe gas in the airspaces, alveolar-capillary tissue and capillary red-blood-cells. In this case, we hypothesized that the super-normally elevated ^{129}Xe MRI RBC value was due to erythrocytosis reflected by abnormal hemoglobin (233g/L) and

hematocrit (0.68) values, both of which further increased over a 5-month period to 242g/L and 0.71, respectively.

The diagnosis of a large (20x27 mm) congenital secundum atrial septal defect with compensatory erythrocytosis in the absence of pulmonary hypertension was subsequently made on the basis of transthoracic echocardiogram, cardiac CT and cardiac catheterization. Minimally invasive cardiac surgery was performed and pericardial tissue was harvested and grafted to repair the 2cmx2cm ASD. Following surgery, hemoglobin (156 g/L) and hematocrit (0.46) diminished to normal values and continued to remain normal during the post-surgical period. The participant provided written informed consent to ^{129}Xe MR spectroscopy, which was performed 15-weeks post-surgery as shown in Figure 1. As compared to presurgical measurements, the ^{129}Xe RBC:barrier ratio was substantially decreased (RBC:barrier ratio pre-surgery=1.33, RBC:barrier post-surgery=0.46) to values equivalent to those of healthy male volunteers (mean ±SD RBC:barrier ratio=0.46 ±0.05),[17] and consistent with reported values in volunteers.[9] The post-surgical changes to hemoglobin, hematocrit and ^{129}Xe MRI RBC:barrier ratio values also supported our hypothesis that the abnormal RBC:barrier ratio reflected erythrocytosis secondary to right-to-left shunt through the large ASD.

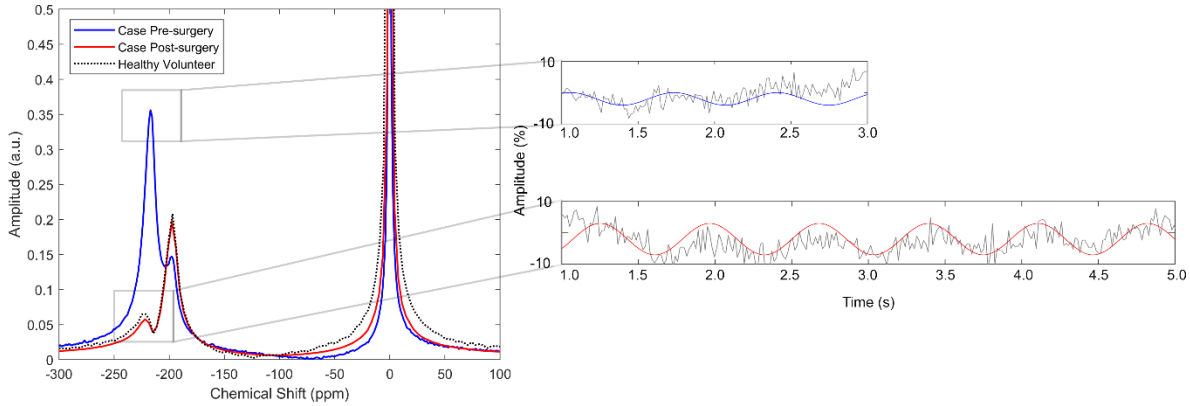

Figure 5-3 Pre- (blue) and Post- (red) surgery ^{129}Xe MRI Spectroscopy.
The large pre-surgery peak (blue) at ~-220ppm (RBC frequency) was substantially reduced post-surgery (red) and now similar to an age-matched healthy volunteer. The RBC:tissue barrier ratio also normalized. Inset boxes show pre and post-surgical cardiogenic oscillations over time for the RBC peak.

As shown in **Figure 5-3**, we observed low amplitude cardiogenic oscillations in this participant, with no evidence of pulmonary hypertension. ^{129}Xe cardiogenic oscillations have been previously observed in patients with confirmed pulmonary arterial hypertension, where lower amplitudes were thought to reflect increased vascular resistance. In contrast, following ASD closure in this participant, we observed oscillation amplitude changes which were consistent with the elimination of the cardiopulmonary shunt, which was confirmed by transthoracic echocardiogram (6 and 12-weeks post surgery) both of which showed sustained closure of the ASD.

^{129}Xe MRI gas-exchange measurements post-surgery provided real-time pulmonary evidence of normalization of the ^{129}Xe RBC pulmonary signal, reflecting the ASD closure, abrogation of right to left shunt and resolution of erythrocytosis.

5.5 References

1. Ouriadov A, Guo FM, McCormack DG, Parraga G. Accelerated Xe-129 MRI morphometry of terminal airspace enlargement: Feasibility in volunteers and those with alpha-1 antitrypsin deficiency. Magnetic Resonance in Medicine. 2020;84(1):416-26.

2. Niedbalski PJ, Hall CS, Castro M, Eddy RL, Rayment JH, Svenningsen S, et al. Protocols for multi-site trials using hyperpolarized (129) Xe MRI for imaging of ventilation, alveolar-airspace size, and gas exchange: A position paper from the (129) Xe MRI clinical trials consortium. Magn Reson Med. 2021.

3. Kirby M, Svenningsen S, Kanhere N, Owrangi A, Wheatley A, Coxson HO, et al. Pulmonary ventilation visualized using hyperpolarized helium-3 and xenon-129 magnetic resonance imaging: differences in COPD and relationship to emphysema. J Appl Physiol (1985). 2013;114(6):707-15.

4. Robertson SH, Virgincar RS, He M, Freeman MS, Kaushik SS, Driehuys B. Optimizing 3D noncartesian gridding reconstruction for hyperpolarized 129Xe MRI—focus on preclinical applications. Concepts in Magnetic Resonance Part A. 2015;44(4):190-202.

5. Kaushik SS, Robertson SH, Freeman MS, He M, Kelly KT, Roos JE, et al. Single-breath clinical imaging of hyperpolarized (129)Xe in the airspaces, barrier, and red blood cells using an interleaved 3D radial 1-point Dixon acquisition. Magn Reson Med. 2016;75(4):1434-43.

6. Graham BL, Brusasco V, Burgos F, Cooper BG, Jensen R, Kendrick A, et al. 2017 ERS/ATS standards for single-breath carbon monoxide uptake in the lung. Eur Respir J. 2017;49(1).

7. Graham BL, Steenbruggen I, Miller MR, Barjaktarevic IZ, Cooper BG, Hall GL, et al. Standardization of Spirometry 2019 Update. An Official American Thoracic Society and European Respiratory Society Technical Statement. Am J Respir Crit Care Med. 2019;200(8):e70-e88.

8. Billett HH. Hemoglobin and Hematocrit. In: Walker HK, Hall WD, Hurst JW, editors. Clinical methods: the history, physical, and laboratory examinations. 3 ed. Boston: Butterworths; 1990.

9. Wang JM, Robertson SH, Wang Z, He M, Virgincar RS, Schrank GM, et al. Using hyperpolarized (129)Xe MRI to quantify regional gas transfer in idiopathic pulmonary fibrosis. Thorax. 2018;73(1):21-8.

10. Wang Z, Bier EA, Swaminathan A, Parikh K, Nouls J, He M, et al. Diverse cardiopulmonary diseases are associated with distinct xenon magnetic resonance imaging signatures. Eur Respir J. 2019;54(6).

11. Weatherley ND, Stewart NJ, Chan HF, Austin M, Smith LJ, Collier G, et al. Hyperpolarised xenon magnetic resonance spectroscopy for the longitudinal assessment of changes in gas diffusion in IPF. Thorax. 2019;74(5):500-2.

12. Wang ZY, Rankine L, Bier EA, Mummy D, Lu JL, Church A, et al. Using hyperpolarized Xe-129 gas-exchange MRI to model the regional airspace, membrane, and capillary contributions to diffusing capacity. Journal of Applied Physiology. 2021;130(5):1398-409.

13. Marrades RM, Diaz O, Roca J, Campistol JM, Torregrosa JV, Barbera JA, et al. Adjustment of DLCO for hemoglobin concentration. Am J Respir Crit Care Med. 1997;155(1):236-41.

14. Sarma P. Red Cell Indices. In: Walker HK, Hall WD, Hurst JW, editors. Clinical Methods: The History, Physical, and Laboratory Examinations. 3 ed. Boston: Butterworths; 1990.

15. Marelli AJ, Mackie AS, Ionescu-Ittu R, Rahme E, Pilote L. Congenital heart disease in the general population: changing prevalence and age distribution. Circulation. 2007;115(2):163-72.

16. Matheson AM, Cunningham RSP, Bier E, Lu J, Dreihuys B, Pickering JG, et al. Hyperpolarized 129Xe Pulmonary MRI and Asymptomatic Atrial Septal Defect. Chest. 2022;161(4):e199-e202.

17. Matheson AM, McIntosh M, Kooner HK, Lee J, Desaigoudar V, Bier E, et al. Persistent 129Xe MRI Pulmonary and CT Vascular Abnormalities in Symptomatic Individuals with Post-acute COVID-19 Syndrome. Radiology. 2022;305.

CHAPTER 6

6 CONCLUSIONS AND FUTURE DIRECTIONS

In this chapter, I review the motivations and research question presented earlier in the thesis and present how this was reflected in the preceding chapters. Next, I discuss limitations both to the method of ^{129}Xe gas-exchange MRI and to each of the preceding chapters. I will suggest future directions for research, based both on the work presented here and building on other recent research in the literature. Finally, I will discuss the significance of this thesis and how it impacts the field of hyperpolarized imaging at large.

6.1 Overview and Research Questions

Chronic respiratory diseases affect over half-a-billion people worldwide[1] and the emergence of long-COVID means that tens to hundreds of millions[2] more have a chronic condition about which very little is known. An understanding of the underlying pathophysiology of long-COVID is necessary to begin developing targeted therapies. Mechanisms related to gas-exchange are central to this effort to understand long-COVID etiology, as symptoms such as dyspnea and reports of impaired DL_{CO} in some patients suggest.[3-5] Many clinical tests such as spirometry and plethysmography are normal in patients with long-COVID, therefore pulmonary structural and functional imaging can play a role in the detection and characterization of disease. Furthermore, clinical measurements of gas-exchange examine the entire process, and thus do not inform on regional differences, and cannot sensitively dissect the contributions of each compartment of the lung to Gas-exchange. Pulmonary imaging modalities such as chest x-ray, CT, CTPA and ^{1}H have proven helpful to analyzing lung structure and function but they do not perform measurements of the pulmonary alveoli. SPECT can examine gas-exchange at the alveoli through ventilation/perfusion mismatch but cannot

measure gas diffusion across the alveolar membrane. Hyperpolarized ^{129}Xe MRI addresses these obstacles by measuring all steps of gas-exchange in the alveolar zone in real time.

^{129}Xe gas-exchange MR spectroscopy and imaging take advantage of the tissue solubility of xenon to measure ventilation, diffusion through the alveolar membrane and binding to RBC. The most reported ^{129}Xe gas-exchange measurement is the RBC:membrane ratio, measuring how effectively xenon completes the gas-exchange process. Dynamic measurements in spectroscopy have observed gas-exchange peak height oscillations at the cardiac frequency – termed cardiogenic oscillations.[6-8] These oscillations have been proposed to relate to pulmonary vascular hemodynamics, suggesting that gas-exchange MR is sensitive to local capillary flow.[6] The interpretability of RBC:membrane can be challenging, due to abnormalities in either compartment contributing to an impaired ratio. Imaging techniques aim to move beyond ^{129}Xe MRS and provide spatial maps of RBC and membrane signal.[9,10] Abnormally low RBC:membrane has been reported in non-specific interstitial pneumonia[8], COPD,[11] and idiopathic fibrosis[12] and was related to FVC in idiopathic pulmonary fibrosis.[12] RBC:membrane measurements have also been found to correlate with clinical DL_{CO} measurements[12] and multivariate models have incorporated ventilation information for a more accurate result.[13] Preliminary studies used ^{129}Xe gas-exchange MRI in previously hospitalized COVID-19 patients, and saw abnormal RBC:membrane[14,15] but these studies did not examine never-hospitalized individuals, did not select participants on the basis of symptoms and did not relate abnormalities to clinical and quality-of-life variables.

The primary objective of this thesis was the development of sensitive pulmonary imaging and spectroscopic measurements to interrogate individual components of the gas-exchange process and understand the underlying pathophysiology that droves symptoms and outcomes in chronic

pulmonary disease. I addressed the following related research questions: 1) Can a linear systems framework be constructed to describe ^{129}Xe gas-exchange MRI and model how mathematical assumptions affect signal? (**Chapter 2**) 2) Are ^{129}Xe MRS measurements abnormal in both never- and ever-hospitalized people with COVID and are measurements related to symptoms and quality-of-life? (**Chapter 3**) 3) Do gas-exchange, long-COVID symptoms and exercise impairment persist over time in people with long-COVID? (**Chapter 4**) and 4) What is the cause of abnormally elevated RBC:membrane and why was it observed in an otherwise healthy teenage participant? (**Chapter 5**)

6.2 Summary and Conclusions

In **Chapter 2** I developed a mathematical model of ^{129}Xe gas-exchange MRI to better understand how technical considerations and mathematical assumptions impact the generated signals. Analysis was performed in both complex image-space and k-space using linear systems theory to relate operations in each domain through convolutions. The model began from the distribution of xenon atoms in different Gas-exchange compartments and included excitation, acquisition and reconstruction. The final model provided a system for deconstructing how decay constants, peak overlap and magnetization evolution impact final acquired measurements. As ^{129}Xe MRI methods for the lung and other organs continue to develop, this model may provide a tool for researching novel compartments and their interactions in disease.

In preparation for performing ^{129}Xe gas-exchange MRI, I developed and implemented MR acquisition and processing software. Prior to this thesis, no tools were available on-site for performing gas-exchange MRI. In collaboration with researchers at the University of Wisconsin, I installed, configured and calibrated a hybrid imaging/spectroscopy pulse

sequence. I also implemented updated specific absorption rate profiles for the ^{129}Xe RF coils used in these experiments, with assistance from the University of Wisconsin, to safely acquire data with the high-power sequence used. I developed new spectroscopic software for measuring spectroscopic ratios and cardiogenic oscillations. I also implemented and further developed image analysis software for ^{129}Xe MRI reconstruction based on a software package provided by Duke University. This software included an image reconstruction pipeline to extract k-space data from raw files, segment gas images, and bundle data for final processing with Duke's NUFFT reconstruction software.

In **Chapter 3** I evaluated ^{129}Xe gas-exchange MRI measurements in never- and ever-hospitalized people with long-COVID and compared them to healthy controls. I sought to relate previous, preliminary reports[14,16] of gas-exchange in ^{129}Xe MRI and pulmonary CT to each other and to measures of participant symptoms and exercise capacity. Previous studies had solely examined ever-hospitalized patients; this study analyzed ever-hospitalized versus never-hospitalized participants to determine the effect of infection severity on gas-exchange. I determined that the RBC:membrane ratio was lower in ever-hospitalized participants compared to healthy controls ($p=.04$). I also reported that CT pulmonary vascular BV_5 was correlated with ^{129}Xe MRI RBC AUC ($\rho=.44$, $p=.03$). Crucially, RBC AUC was related to patient-reported dyspnea ($\rho=-.35$, $p=.04$) and exercise capacity measured by IPAQ ($\rho=.45$, $p=.02$), suggesting a connection between the capillary component of gas-exchange and patient experiences that characterize long-COVID.

Chapter 4 detailed the longitudinal follow-up of 21 participants reported in **Chapter 3** to determine if ^{129}Xe gas-exchange MRI abnormalities changed over time in people with long-COVID and whether or not symptoms and quality-of-life changed at the same time. I evaluated

participants at 7±4 months after their baseline measurements and observed significant improvements in DL_{CO} (Δ=14%$_{pred}$, p<.001) and post-exertional dyspnea (Δ=-0.7, p=.02) but not RBC:membrane (Δ=0.03, p=.051). While gas-exchange measured by DL_{CO} improved, this was not reflected in RBC:membrane despite the fact that DL_{CO} correlated with RBC:membrane at both baseline (r=.60, p=.004) and follow-up (r=.47, p=.04). This work provided evidence that gas-exchange improves alongside quality-of-life and symptoms, however measurements did not fully normalize.

In **Chapter 5** I investigated a never-before-seen ^{129}Xe gas-exchange abnormality in an otherwise healthy 19-year-old male. I observed an abnormally elevated RBC:membrane ratio (1.33) which was driven by a large RBC signal 4.7 times as great as an age-matched participant. Despite abnormal ^{129}Xe MRI, pulmonary function tests were within normal ranges, although DL_{CO} (130%$_{pred}$) was high visual examination of the participant revealed mild cyanosis and clubbing. Blood tests uncovered elevated hematocrit (0.68) and hemoglobin concentrations (233g/L). Transesophageal ultrasound and contrast enhanced CT revealed a large (20-27mm) secundum ASD in the participant and cardiac surgery was performed to repair the defect. I hypothesized that the abnormal ^{129}Xe RBC signal was evidence of compensatory polycythemia to maximize oxygen uptake in the presence of a 50% right to left shunt, which had the effect of also increasing xenon uptake. Following surgery, ^{129}Xe MRI RBC:membrane normalized (0.46) alongside hemoglobin and hematocrit, supporting a hematologic origin of the MR abnormality. Although prior researched focused on abnormally diminished RBC signal, this case demonstrated that abnormally elevated signals were also pathological, that ^{129}Xe MRI could be sensitive to congenital heart defects, and that the content of blood should be considered when interpreting gas-exchange MRI measurements.

In summary, in this thesis I performed ^{129}Xe gas-exchange MRI with the goal of better understanding the underlying mathematical and physiological meaning of previously proposed biomarkers. First, I provided a mathematical description of ^{129}Xe gas-exchange MRI to better understand how technical processes affect gas-exchange measurements. Next, I applied gas-exchange MRI in long-COVID and related MRI measurements to CT vascular measurements, symptoms, and exercise capacity. In a follow-up study, I showed that gas-exchange improvements in long-COVID occurred alongside improvements in symptoms and quality of life. Finally, I recognized a novel elevated gas-exchange MRI signal that was revealed to be a compensatory mechanism in the blood, demonstrating how gas-exchange MRI measurements reveal important information about abnormalities in other compartments that were within clinical norms.

6.3 Limitations

In this section I discuss how limitations affected the specific studies presented in chapters 2-5, followed by a discussion of limitations of ^{129}Xe gas-exchange MRI and pulmonary imaging in general.

6.3.1 Study Specific Limitations

In **Chapter 2,** some assumptions were made of the mathematical model in order represent all steps as linear operations. First, all operations were presented as shift invariant although the nature of MRI hardware does not strictly follow this assumption. Inhomogeneities in the B_0 and B_1 fields produce varying fields and coil imperfections produce inhomogeneities. RF excitation was modelled as a linear operation, where selectivity in the frequency domain was equivalent to the Fourier transformation of the pulse shape, however this approximation breaks

down at higher flip angles (gas-exchange imaging was performed at 40°). This work also assumed that the subject being imaged was an ideal combination of blood, tissue and RBC. The plasma component was not modelled, although it could fit within the current framework. The model also assumed that the gas-exchange compartment properties were time-independent, when in-vivo experiments have reported cardiogenic oscillations in the RBC compartment.[6] In this chapter I considered the case of a single FID but despite crusher gradients used at the end of each TR, some residual magnetization may remain between pulses. Other temporal effects such as xenon transport upon uptake and gas-exchange prior to the start of imaging were likewise not considered.

In **Chapter 3**, dissolved-phase data were acquired at the first visit post-implementation of a gas-exchange MRI pulse sequence, resulting in a wide range of follow-up times (6-79 weeks post positive test). Recruitment through a clinic also biased data towards participants with more severe symptoms who sought treatment through the clinic. The LIVECOVIDFREE study was not initially conceived with gas-exchange MRI as the primary endpoint, and effect sizes were not previously known to determine an appropriately powered sample size.

Recruitment of healthy controls was also challenging during the pandemic due to public caution and restricted access to research facilities. Many participants had not had access to routine healthcare during the pandemic, and of 10 participants recruited, four were excluded due to unanticipated abnormalities discovered during testing (one with asthma, one with a hypertensive crisis, one with rheumatoid arthritis, one with an ASD). As a result, healthy controls were not matched to the demographics of the ever-COVID cohort and there were significant differences in age (35±15 vs 53±13, p=.02) and body-mass-index (BMI) (25±3 vs

30±5, p=.02). Research published after this work has shown there is an age-related decline in RBC:membrane that may explain some differences between cohorts.[17]

Variability in CT data were a further source of limitations. Research CT were not acquired in all participants as some (n=5) declined to undergo radiation-based imaging. Some participants (n=19) had received clinical CT imaging as part of treatment during the infectious phase and these were used in cases where image resolution did not produce large vessel segmentation errors. CT were also not acquired in healthy controls. These limitations prevented full inter-group comparisons and made it difficult to determine if small vessel volumes were abnormal in participants with long-COVID.

In **Chapter 4**, participant retention was a limitation as thirteen participants, including one pregnant participant and two unvaccinated participants, were lost to follow-up. The reduced dataset size made some analyses underpowered and made comparisons of never- to ever-hospitalized COVID difficult. Participants measured at follow-up may have been biased toward those who were still experiencing symptoms and those with improvements may have opted to not return. Not all participants had gas-exchange MRI performed at visit 1, and therefore measurements were obtained from the first two visits for each participant that included gas-exchange MRI. This may have impacted results if long-COVID recovery is not uniform over time. No additional CT data were acquired at follow-up in participants and therefore CT vessel structural abnormalities that were previously reported were unable to be monitored. This also prevented any analysis between structural changes and gas-exchange improvement.

In **Chapter 5**, the nature of a single-participant case report precludes drawing large conclusions for all participants with heart defects or hematological changes. The severity of erythrocitosis made blood testing challenging in this individual due to blood viscosity and the rapidness of clotting following collection and these values may be inaccurate. Blood collections were also performed on different days to imaging and may not reflect hematology at imaging due to the rapid changes and deterioration in this individual.

Follow-up performed in this participant included a preliminary analysis of cardiopulmonary oscillations. Spectroscopy acquisition parameters were changed between visits to acquire more spectra for fitting of oscillations – this may make comparisons between visits imperfect. Cardiopulmonary oscillations have previously been reported as a percentage of normalized peak height,[6] however this technique was performed in a relatively narrow range of peak heights. Whether low amplitude oscillation is truly the result of hemodynamic changes or a consequence of normalization to an intense peak is uncertain.

6.3.2 General Limitations

In **Chapters 3 and 4**, I examined participants with prior COVID-19 infections recruited between August 2020 and April 2021, however participants had infections as early as March 2020. During this time new viral variants emerged and the original wild type was supplanted by the alpha (arrived by December 2020),[18] beta (arrived by January 2021),[19] gamma (arrived by February 2021)[20] and delta (arrived by April 2021)[21] variants. Genomic sequencing was not performed in participants, therefore knowledge on how individual variants may have affected participant quality-of-life and gas-exchange was unavailable. Considering the alpha and beta variants tended to more severe infections[22-24] and the omicron to less severe infections,[25,26]

with different infection patterns in the bronchi and lungs[27] the infection variant might conceivably have an effect on abnormality severity. While the omicron variant emerged after the recruitment period for this study, research on self-reported long-COVID status suggests that omicron infections had a reduced proportion of people experiencing long-COVID compared to the delta variant.[28] The first vaccination against COVID-19 infection was approved on December 9, 2020[29] however vaccinations were not immediately available to Canadians due to a triaged release approach to vaccinate those most at risk. No participants included in this study were vaccinated prior to enrollment, therefore any analysis of long-COVID following vaccination was not possible. Some participants self-reported re-infection, however re-infection occurred later in the pandemic, when testing and molecular confirmation was unavailable.

A lack of data from the course of infection in never-hospitalized participants was a limitation in these COVID studies. In cases where participants did not want to undergo CT, hospitalized participants had access to imaging during their course of infection, which may have biased results toward more severe disease. In addition, hospitalized individuals may have been monitored for complications such as embolism, which was present within the health records of participants. VQ-SPECT perfusion defects in never-hospitalized people with COVID hints that subclinical emboli may have occurred in never-hospitalized participants.[30] As the case study in **Chapter 5** demonstrated, natural variability in blood hematocrit does influence the RBC:membrane ratio. Therefore healthy physiologic factors such as age,[17] sex and hemoglobin concentration may have also influenced RBC:membrane measurements.

All gas-exchange MR measurements in this manuscript were performed using spectroscopy, rather than images generated by ^{129}Xe gas-exchange Dixon imaging. For the main endpoint,

RBC:membrane, this distinction is moot as Dixon reconstruction includes a complex rotation in the final step to force the signal in RBC and membrane channels to match the spectroscopic ratio.[9] I reported RBC and membrane signal as either AUC or gas ratio measurements, and these whole-lung measurements did not include regional information that would be present in imaging-derived biomarkers. Recent publications have developed tools to quantify the fraction of the lung with "low RBC signal"[12] – such tools were not used as gas-exchange MRI image analysis protocols were still being developed during study data acquisition. The reconstructed images shown in this thesis are also limited by acquisition assumptions in the Dixon method, namely that imaging occurs precisely when compartments are 90° out-of-phase. While this may be true at $t=TE_{90}$, phase evolution will cause some mixing of compartment data as the k-space trajectory gets further from the origin. The Shinnar-Le Roux RF pulse used for excitation is also imperfect and causes some excitation of the gas-phase. Previous studies have made pulse sequence modifications and post-processing tools to remove gas contamination.[31,32] Gas contamination corrections were not performed in this thesis and dissolved-phase images may have some contamination present.

6.4 Future Directions

6.4.1 Physiologic Variability of ^{129}Xe MRI Gas-Exchange Measurements

^{129}Xe gas-exchange MRI has largely made comparisons between groups of healthy people and people with disease.[33] However, there is little understanding of how gas-exchange MRI measurements vary within a healthy population. An elevated RBC:membrane ratio was investigated in **Chapter 5** precisely because it was unknown if this fell within healthy limits. DL_{CO} has already demonstrated that gas-exchange efficiency depends on age, sex and height.[34]

The DL_{CO} relationships I uncovered in earlier chapters suggest that ^{129}Xe measures should be related to the same demographic and physiologic variance present in pulmonary function tests. **Chapter 3** also showed that hemoglobin/hematocrit should also be considered when interpreting natural variation in RBC:membrane. The objective of this preliminary work is to quantify the natural variance of RBC:membrane and determine relationships with demographic data.

I performed preliminary ^{129}Xe gas-exchange MRS in 16 healthy participants (age=37±17 years, 5/16 female). **Figure 6-1** shows correlations between RBC:membrane and age, divided by sex. RBC:membrane either correlated or approached (women r=.72, p=.07; men r=.56, p=.01) a statistically significant correlation with age. A multivariable model of RBC:membrane was also constructed, including age, sex, height, weight, BMI and hemoglobin concentration in healthy participants. Hemoglobin was estimated using a handheld, fingertip optical pulse oximeter. Variables were entered stepwise into the model, with sex, age, weight, and height as separate significant contributors to the final model, shown in **Table 6-1**. Surprisingly, both sex and hemoglobin were identified as separate, significant contributors, suggesting that sex differences in RBC:membrane measurements are not simply due to hemoglobin differences between sexes.

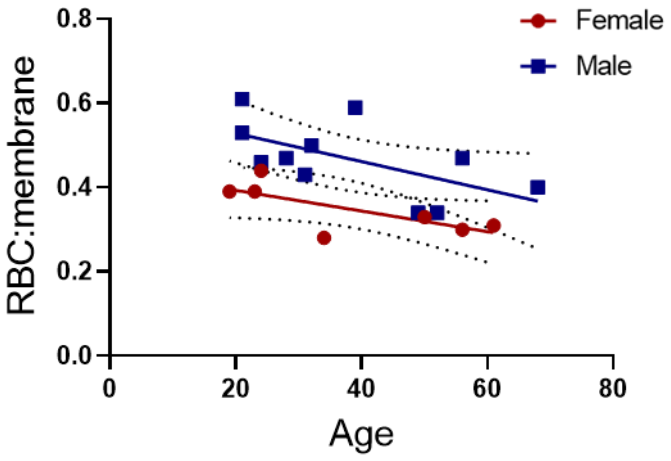

Figure 6-1 Gas-exchange measurements in healthy participants
Participants were grouped by age and sex. RBC:membrane neared a significant correlation with age in both groups for women (r=.72, p=.07) and men (r=.56, p=.01).

Table 6-1 Multivariable model for RBC:membrane in healthy participants

Variable	β	Standardized β	Significance p
Constant	-1.094		.02
Sex	.12	1.35	.03
Age	-.001	-.44	.02
Weight	-.004	-.25	.004
Hemoglobin	.13	-.56	.006

6.4.2 Gas-exchange in diverse pulmonary diseases

Gas-exchange imaging has so far focused on diseases with strong parenchymal components including idiopathic pulmonary fibrosis,[6,7,35,36] nonspecific interstitial pneumonia,[8] and COPD.[11,33] Work is also beginning to probe pulmonary hypertension.[33,37] As adoption of ^{129}Xe gas-exchange MRI is accelerating at sites that previously focused on ventilation, opportunities exist to better understand components of gas-exchange in other vascular and airways diseases.

While asthma is primarily understood as an airways disease with findings such as airway wall thickening, lumen obstruction and smooth muscle hypersensitivity, abnormalities have been observed in other tissues involved in Gas-exchange including collagen deposits observed in alveolar walls and pruning of the pulmonary vasculature.[38,39] Asthma may also induce pulmonary vascular changes through hypoxemic vasoconstriction in response to unventilated airways. CT ventilation and perfusion imaging in a pilot study before and after bronchodilation has shown decreased perfusion in broncho-constricted regions.[40] Together, these abnormalities suggest that probing alveolar gas-exchange in asthma may yield new insights into functional changes beyond the airways and a better understanding of how ventilation/perfusion mismatch produced changes in asthmatic lungs over time. This may be challenging to achieve, as gas-exchange imaging requires delivery of hyperpolarized ^{129}Xe gas to the alveoli, which would not occur in constricted regions. Either same-day dilation/constriction studies or methacholine challenge tests may aid in investigating short-term changes while treatment effect studies may be able to detect differences prior to and following treatment for smooth muscle dysfunction or mucus plugging.

Bronchopulmonary dysplasia (BPD) is a disorder in preterm infants that require supplemental oxygen at 28 days post-birth or a gestational age of 36 weeks.[41] Preterm birth can affect alveolarization[42] and can lead to lifelong pathological changes due to an abnormal growth trajectory.[41,43] Infants may experience pulmonary hypertension, with a staggering 47% mortality at 2 years.[44] Later in life, BPD has been associated with airway obstruction,[43] pulmonary hypertension through vascular remodelling,[45] and abnormal gas-exchange due to reduced alveolar surface area.[46] As a disease of the alveolar gas-exchange unit, ^{129}Xe gas-exchange MRI is well matched to measurements directly in the alveoli to track alveolar

development in infants, to determine targets for intervention and predictors of disease later in life. With dozens of treatments in animal models[45] targeting the various developmental abnormalities present, ^{129}Xe biomarkers may act as helpful evaluators of treatment efficacy. ^{129}Xe gas-exchange MRS in BPD animal models and detected altered alveolar dimensions and abnormal estimates of pulmonary capillary transit time[47] and feasibility tests show ^{129}Xe gas-exchange MRI was possible in 4 children with BPD with abnormal membrane signal reported.[48] With obstructive, parenchymal and pulmonary vascular abnormalities, BPD presents a well-suited, albeit challenging, application for gas-exchange MR.

6.4.3 Biomechanical Modelling of Cardiogenic Oscillations

Cardiogenic oscillations have been observed in healthy people and people with pulmonary disease. Based on the presence of different oscillation amplitudes in different diseases with abnormal pulmonary vascular pressures, cardiogenic oscillations have been proposed to relate to hemodynamics within the pulmonary capillaries.[6,37] Pulsatile, cardiogenic signals have previously been observed in nitrous oxide lung exams,[49] however whether these originate from mechanical compression of lung tissue by the heart or by hemodynamic properties is unclear. To better discern the relationship between cardiogenic oscillations and vessel geometry and hemodynamics, mathematical models could be constructed to predict oscillation amplitudes in pulmonary disease.

Current models of ^{129}Xe gas-exchange work under assumptions of constant blood flow and constant vessel geometry during acquisition.[50] A model may be constructed to consider vessel impedance where flow resistance is determined through vessel geometry and reactance due to vessel elastance. Previous spectroscopy investigation[51] has determined that blood plasma

contributes to a combined tissue-plasma spectroscopic compartment. Small oscillations previously observed[7] in the tissue-plasma compartment may allow modelling of plasma values, potentially allowing estimates of hematocrit. Conversely, pressure oscillations in the pulmonary capillaries may cause periodic dilation of the vessels, which would change vessel geometry and again could be modelled to relate to oscillations in the tissue-plasma system. Implementation of high-resolution spectroscopy (in the time and frequency domains) could help in determining whether one or both hypotheses are true.

In preliminary investigations into cardiogenic oscillations, I have observed oscillations in three compartments, including novel oscillations in the gas compartment. **Figure 6-2** shows cardiogenic oscillations in all three compartments for a healthy participant and a participant with asthma. A previous spectroscopic research during breath-hold has not reported gas oscillations, however earlier research in helium-3 MRI observed oscillations in lung signal during inhalation.[52,53] These oscillations also occur at the cardiac frequency, suggesting mechanical deformation of the lung causes gas redistribution during breath-hold. This signal could potentially be leveraged to compare the effects of mechanical deformation on signals versus the effects of pulsatile blood flow.

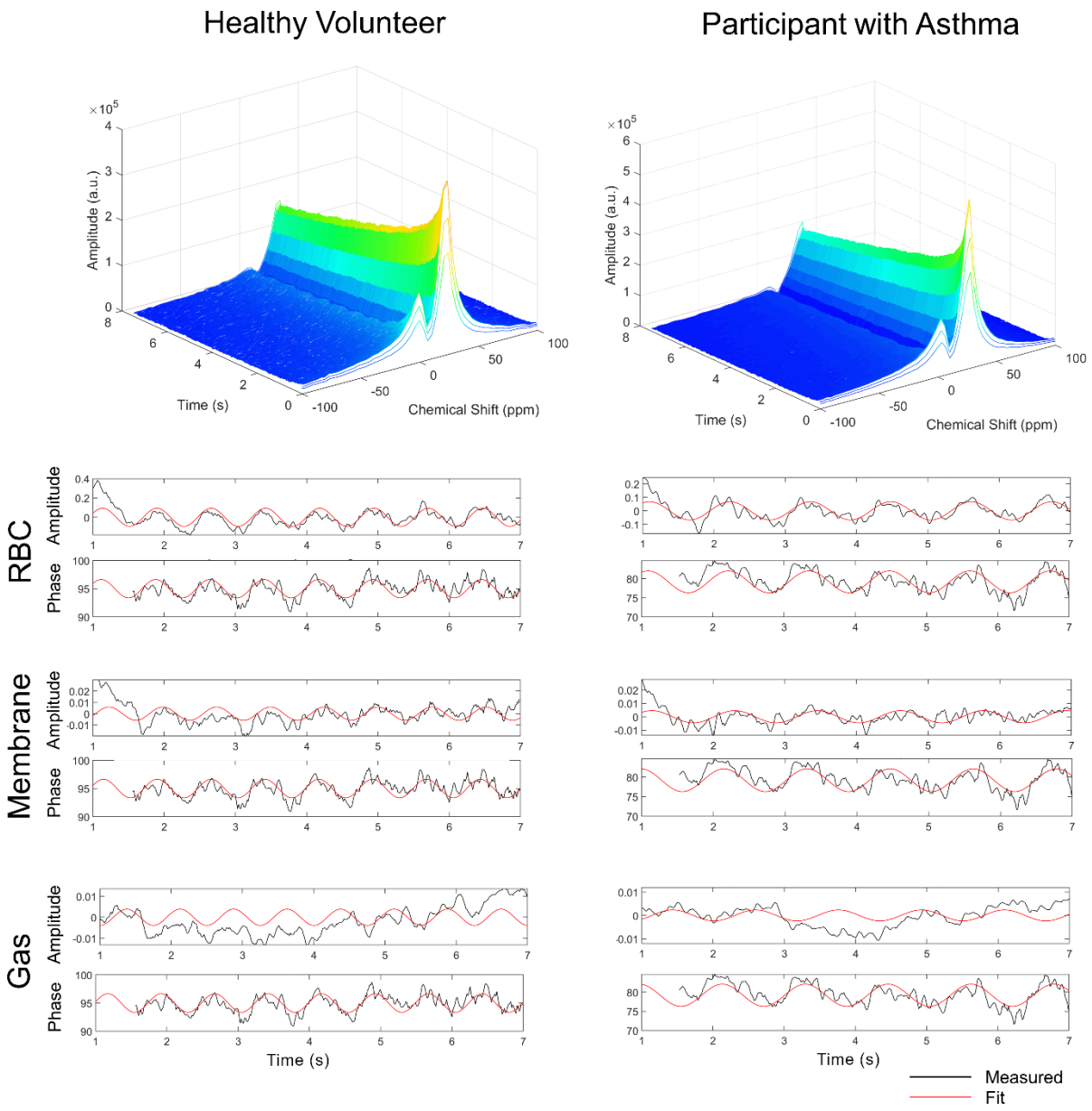

Figure 6-2 Cardiogenic oscillations in three compartments

Computational simulations of cardiogenic oscillations could be used to test the effect of different hemodynamic properties on ^{129}Xe signals and determine if specific oscillation patterns are unique to pre-capillary vs. post-capillary oscillations. Variation of the individual model parameters such as heart rate, resistance and elastance can be used alongside established histological measurements of capillary diameter, septal wall thickness and capillary pressure

to determine if the model produces predictions and results in line with published values. Comparisons between model predictions and animal models of disease may enable further insights as to what, if any, hemodynamic properties may be accurately measured without interventions such as cardiac catheterization.

6.5 Significance and Impact

Chronic pulmonary diseases result in reduced quality-of-life and exercise capacity by impeding gas-exchange in the lung through pathological changes to the airways, parenchyma and pulmonary vasculature. The prevalence of pulmonary disease has increased over the previous decades, and the recent stress to worldwide health, including the emergence of a new, chronic lung illness affecting millions, creates an urgent need for tools in pulmonary medicine. The current standard for measuring gas-exchange in the lung, the diffusing capacity of the lung for carbon monoxide, is an at-the-mouth test that can quickly perform a whole-lung measurement on the efficacy of gas-exchange. Unfortunately, DL_{CO} tests the entire gas-exchange process and cannot identify which of the components of gas-exchange is the source of abnormalities. As a whole-lung test, it also fails to determine the spatial distribution of gas-exchange in the lung, to match abnormal lung structure to function. Imaging technologies such as CT-perfusion and VQ-SPECT provide some measurement of gas-exchange, however these technologies lack the sensitivity to probe the alveolar membrane and radiation-dose burden makes these techniques unsuitable in pediatric populations and long-term monitoring of disease. Because ^{129}Xe is soluble in tissue, it can provide sensitive measures of each stage of the gas-exchange process in a single breath-hold through gas-exchange MRI. Furthermore, by measuring on

separate gas-exchange compartments, ^{129}Xe gas-exchange MRI can inform on the underlying pathophysiology of disease, providing a level of interpretability.

In this thesis, I have developed and applied ^{129}Xe gas-exchange MRI to better understand gas-exchange in cardiopulmonary disease. In the process, I provided valuable information on the pulmonary vascular nature of long-COVID, a disease which did not exist at the beginning of this thesis, showcasing the powerful and rapid way in which xenon MRI can be applied to pulmonary disease. ^{129}Xe MRI techniques have been in development for over 20 years, but are just starting to see progress towards clinical adoption. As this thesis has shown, xenon MRI can provide value to clinical settings, by providing sensitive information on lung function that helps give people evidence of lung dysfunction that relates to their daily, subjective experiences of lung disease.

6.6 References

1. Collaborators GBDCRD. Prevalence and attributable health burden of chronic respiratory diseases, 1990-2017: a systematic analysis for the Global Burden of Disease Study 2017. Lancet Respir Med. 2020;8(6):585-96.

2. Davis HE, McCorkell L, Vogel JM, Topol EJ. Long COVID: major findings, mechanisms and recommendations. Nat Rev Microbiol. 2023:1-14.

3. Nalbandian A, Sehgal K, Gupta A, Madhavan MV, McGroder C, Stevens JS, et al. Post-acute COVID-19 syndrome. Nature Medicine. 2021;27(4):601-15.

4. Shah AS, Wong AW, Hague CJ, Murphy DT, Johnston JC, Ryerson CJ, et al. A prospective study of 12-week respiratory outcomes in COVID-19-related hospitalisations. Thorax. 2021;76(4):402-4.

5. Mendez R, Latorre A, Gonzalez-Jimenez P, Feced L, Bouzas L, Yepez K, et al. Reduced Diffusion Capacity in COVID-19 Survivors. Ann Am Thorac Soc. 2021;18(7):1253-5.

6. Bier EA, Robertson SH, Schrank GM, Rackley C, Mammarappallil JG, Rajagopal S, et al. A protocol for quantifying cardiogenic oscillations in dynamic (129) Xe gas exchange spectroscopy: The effects of idiopathic pulmonary fibrosis. NMR Biomed. 2019;32(1):e4029.

7. Collier GJ, Eaden JA, Hughes PJC, Bianchi SM, Stewart NJ, Weatherley ND, et al. Dissolved (129) Xe lung MRI with four-echo 3D radial spectroscopic imaging: Quantification of regional gas transfer in idiopathic pulmonary fibrosis. Magn Reson Med. 2021;85(5):2622-33.

8. Mummy DG, Bier EA, Wang Z, Korzekwinski J, Morrison L, Barkauskas C, et al. Hyperpolarized (129)Xe MRI and Spectroscopy of Gas-Exchange Abnormalities in Nonspecific Interstitial Pneumonia. Radiology. 2021;301(1):211-20.

9. Kaushik SS, Robertson SH, Freeman MS, He M, Kelly KT, Roos JE, et al. Single-breath clinical imaging of hyperpolarized (129)Xe in the airspaces, barrier, and red blood cells using an interleaved 3D radial 1-point Dixon acquisition. Magn Reson Med. 2016;75(4):1434-43.

10. Wang Z, He M, Bier E, Rankine L, Schrank G, Rajagopal S, et al. Hyperpolarized (129) Xe gas transfer MRI: the transition from 1.5T to 3T. Magn Reson Med. 2018;80(6):2374-83.

11. Myc L, Qing K, He M, Tustison N, Lin ZX, Manichaikul AW, et al. Characterisation of gas exchange in COPD with dissolved-phase hyperpolarised xenon-129 MRI. Thorax. 2021;76(2):178-81.

12. Wang JM, Robertson SH, Wang Z, He M, Virgincar RS, Schrank GM, et al. Using hyperpolarized (129)Xe MRI to quantify regional gas transfer in idiopathic pulmonary fibrosis. Thorax. 2018;73(1):21-8.

13. Wang ZY, Rankine L, Bier EA, Mummy D, Lu JL, Church A, et al. Using hyperpolarized Xe-129 gas-exchange MRI to model the regional airspace, membrane, and capillary contributions to diffusing capacity. Journal of Applied Physiology. 2021;130(5):1398-409.

14. Li H, Zhao X, Wang Y, Lou X, Chen S, Deng H, et al. Damaged lung gas exchange function of discharged COVID-19 patients detected by hyperpolarized (129)Xe MRI. Sci Adv. 2021;7(1).

15. Grist JT, Chen M, Collier GJ, Raman B, Abueid G, McIntyre A, et al. Hyperpolarized (129)Xe MRI Abnormalities in Dyspneic Patients 3 Months after COVID-19 Pneumonia: Preliminary Results. Radiology. 2021;301(1):E353-E60.

16. Lins M, Vandevenne J, Thillai M, Lavon BR, Lanclus M, Bonte S, et al. Assessment of Small Pulmonary Blood Vessels in COVID-19 Patients Using HRCT. Acad Radiol. 2020;27(10):1449-55.

17. Plummer JW, Willmering MM, Cleveland ZI, Towe C, Woods JC, Walkup LL. Childhood to adulthood: Accounting for age dependence in healthy-reference distributions in 129Xe gas-exchange MRI. Magnetic Resonance in Medicine. 2023;89(3):1117-33.

18. Aziz S. Canada reports first cases of U.K. coronavirus variant. Here's what you need to know. Global News. 2020 December 27, 2020.

19. Heidenreich P, Gibson C. Officials confirm Canada's 1st case of South African variant of COVID-19 detected in Alberta. Global News. 2021 January 8, 2021.

20. Favaro A, Philip ES, Jones AM. Third variant detected in Canada, prompting concern from health experts. CTV News. 2021 February 8, 2021.

21. Little S. Dozens of cases of 'double mutant' COVID-19 variant confirmed in B.C. Global News. 2021 April 21, 2021.

22. Horby P, Huntley C, Davies N, Edmunds J, Ferguson N, Medley G, et al. NERVTAG paper on COVID-19 variant of concern B.1.1.7. In: Care UDoHaS, editor. Online: New and Emerging Respiratory Virus Threats Advisory Group; 2021.

23. Funk T, Pharris A, Spiteri G, Bundle N, Melidou A, Carr M, et al. Characteristics of SARS-CoV-2 variants of concern B.1.1.7, B.1.351 or P.1: data from seven EU/EEA countries, weeks 38/2020 to 10/2021. Eurosurveillance. 2021;26(16):2100348.

24. Ong SWX, Chiew CJ, Ang LW, Mak TM, Cui L, Toh MPHS, et al. Clinical and Virological Features of Severe Acute Respiratory Syndrome Coronavirus 2 (SARS-CoV-2)

Variants of Concern: A Retrospective Cohort Study Comparing B.1.1.7 (Alpha), B.1.351 (Beta), and B.1.617.2 (Delta). Clinical Infectious Diseases. 2021;75(1):e1128-e36.

25. Hyams C, Challen R, Marlow R, Nguyen J, Begier E, Southern J, et al. Severity of Omicron (B.1.1.529) and Delta (B.1.617.2) SARS-CoV-2 infection among hospitalised adults: A prospective cohort study in Bristol, United Kingdom. Lancet Reg Health Eur. 2023;25:100556.

26. Maslo C, Friedland R, Toubkin M, Laubscher A, Akaloo T, Kama B. Characteristics and Outcomes of Hospitalized Patients in South Africa During the COVID-19 Omicron Wave Compared With Previous Waves. JAMA. 2021.

27. Hui KPY, Ho JCW, Cheung M-c, Ng K-c, Ching RHH, Lai K-l, et al. SARS-CoV-2 Omicron variant replication in human bronchus and lung ex vivo. Nature. 2022;603(7902):715-20.

28. Antonelli M, Pujol JC, Spector TD, Ourselin S, Steves CJ. Risk of long COVID associated with delta versus omicron variants of SARS-CoV-2. Lancet. 2022;399(10343):2263-4.

29. Authorization of Pfizer-BioNTech COVID-19 Vaccine with English-only Carton and Vial Labels. In: Canada H, editor. Online: Government of Canada; 2020.

30. Evbuomwan O, Engelbrecht G, Bergman MV, Mokwena S, Ayeni OA. Lung perfusion findings on perfusion SPECT/CT imaging in non-hospitalized de-isolated patients diagnosed with mild COVID-19 infection. Egyptian Journal of Radiology and Nuclear Medicine. 2021;52(1):144.

31. Hahn AD, Kammerman J, Fain S. Removal of hyperpolarized 129Xe gas-phase contamination in spectroscopic imaging of the lungs. Magnetic Resonance in Medicine. 2018:2586-97.

32. Willmering MM, Cleveland ZI, Walkup LL, Woods JC. Removal of off-resonance xenon gas artifacts in pulmonary gas-transfer MRI. Magnetic Resonance in Medicine. 2021;86(2):907-15.

33. Wang Z, Bier EA, Swaminathan A, Parikh K, Nouls J, He M, et al. Diverse cardiopulmonary diseases are associated with distinct xenon magnetic resonance imaging signatures. Eur Respir J. 2019;54(6).

34. Park JO, Choi IS, Park KO. Normal predicted values of single-breath diffusing capacity of the lung in healthy nonsmoking adults. Korean J Intern Med. 1986;1(2):178-84.

35. Mata J, Guan S, Qing K, Tustison N, Shim Y, Mugler JP, 3rd, et al. Evaluation of Regional Lung Function in Pulmonary Fibrosis with Xenon-129 MRI. Tomography. 2021;7(3):452-65.

36. Weatherley ND, Stewart NJ, Chan HF, Austin M, Smith LJ, Collier G, et al. Hyperpolarised xenon magnetic resonance spectroscopy for the longitudinal assessment of changes in gas diffusion in IPF. Thorax. 2019;74(5):500-2.

37. Niedbalski PJ, Bier EA, Wang Z, Willmering MM, Driehuys B, Cleveland ZI. Mapping cardiopulmonary dynamics within the microvasculature of the lungs using dissolved (129)Xe MRI. J Appl Physiol (1985). 2020;129(2):218-29.

38. Weitoft M, Andersson C, Andersson-Sjoland A, Tufvesson E, Bjermer L, Erjefalt J, et al. Controlled and uncontrolled asthma display distinct alveolar tissue matrix compositions. Respir Res. 2014;15:67.

39. Ash SY, Rahaghi FN, Come CE, Ross JC, Colon AG, Cardet-Guisasola JC, et al. Pruning of the Pulmonary Vasculature in Asthma. The Severe Asthma Research Program (SARP) Cohort. Am J Respir Crit Care Med. 2018;198(1):39-50.

40. Kelly VJ, Hibbert KA, Kohli P, Kone M, Greenblatt EE, Venegas JG, et al. Hypoxic Pulmonary Vasoconstriction Does Not Explain All Regional Perfusion Redistribution in Asthma. Am J Respir Crit Care Med. 2017;196(7):834-44.

41. Duijts L, van Meel ER, Moschino L, Baraldi E, Barnhoorn M, Bramer WM, et al. European Respiratory Society guideline on long-term management of children with bronchopulmonary dysplasia. Eur Respir J. 2020;55(1).

42. Jobe AJ. The new BPD: an arrest of lung development. Pediatr Res. 1999;46(6):641-3.

43. Moschino L, Stocchero M, Filippone M, Carraro S, Baraldi E. Longitudinal Assessment of Lung Function in Survivors of Bronchopulmonary Dysplasia from Birth to Adulthood. The Padova BPD Study. Am J Respir Crit Care Med. 2018;198(1):134-7.

44. Khemani E, McElhinney DB, Rhein L, Andrade O, Lacro RV, Thomas KC, et al. Pulmonary artery hypertension in formerly premature infants with bronchopulmonary dysplasia: clinical features and outcomes in the surfactant era. Pediatrics. 2007;120(6):1260-9.

45. Lignelli E, Palumbo F, Myti D, Morty RE. Recent advances in our understanding of the mechanisms of lung alveolarization and bronchopulmonary dysplasia. Am J Physiol Lung Cell Mol Physiol. 2019;317(6):L832-L87.

46. Mitchell SH, Teague WG. Reduced gas transfer at rest and during exercise in school-age survivors of bronchopulmonary dysplasia. Am J Respir Crit Care Med. 1998;157(5 Pt 1):1406-12.

47. Fliss JD, Zanette B, Friedlander Y, Sadanand S, Lindenmaier AA, Stirrat E, et al. Hyperpolarized (129)Xe magnetic resonance spectroscopy in a rat model of bronchopulmonary dysplasia. Am J Physiol Lung Cell Mol Physiol. 2021;321(3):L507-L17.

48. Willmering MM, Walkup LL, Niedbalski PJ, Wang H, Wang Z, Hysinger EB, et al. Pediatric (129) Xe Gas-Transfer MRI-Feasibility and Applicability. J Magn Reson Imaging. 2022;56(4):1207-19.

49. Dahlstrom H, Murphy JP, Roos A. Cardiogenic oscillations in composition of expired gas; the pneumocardiogram. Journal of applied physiology. 1954;7(3):335-9.

50. Chang YV. MOXE: a model of gas exchange for hyperpolarized 129Xe magnetic resonance of the lung. Magn Reson Med. 2013;69(3):884-90.

51. Sakai K, Bilek K, Oteiza E, Walsworth RL, Balamore D, Jolesz FA, et al. Temporal Dynamics of Hyperpolarized 129Xe Resonances in Living Rats. Journal of Magnetic Resonance. 1996;111:300-4.

52. Collier GJ, Marshall H, Rao M, Stewart NJ, Capener D, Wild JM. Observation of cardiogenic flow oscillations in healthy subjects with hyperpolarized 3He MRI. J Appl Physiol (1985). 2015;119(9):1007-14.

53. Sun Y, Butler JP, Ferrigno M, Albert MS, Loring SH. "Ventilatory alternans": a left-right alternation of inspiratory airflow in humans. Respir Physiol Neurobiol. 2013;185(2):468-71.

Appendix A – FDMRI Unpublished Work

A PULMONARY FOURIER-DECOMPOSITION MAGNETIC RESONANCE IMAGING AND X-RAY COMPUTED TOMOGRAPHY OF LUNG PERFUSION AND PULMONARY VASCULAR DENSITY

A.1 Introduction

Chronic Obstructive Pulmonary Disease (COPD) is a leading cause of death worldwide,[1] and is predicted to cost healthcare systems in the US at least $49 billion this year.[2] Cardiovascular comorbidities are common, with pulmonary hypertension reported in half of patients with COPD.[3-5] Moreover, cardiovascular events account for a greater number of COPD deaths than do respiratory events, underscoring the critical importance of cardio- and pulmonary vascular health in these patients.[6] In support of these epidemiological findings, the Genetic Epidemiology of COPD study (COPDGene) reported that the CT measurement of the ratio of the pulmonary artery diameter to the aorta had a stronger association with COPD hospitalization and exacerbations than did breathlessness and the forced expiratory volume in one second (FEV_1).[7]

Recent computed tomography (CT) investigations have also uncovered evidence of pulmonary vascular density abnormalities – a loss of total blood vessel volume and fewer CT detected blood vessels < $5mm^2$ cross-sectional area.[8-11] In this previous work, so-called "vascular pruning" was associated with abnormal diffusing capacity of the lung for carbon monoxide (DL_{CO}), blood oxygen saturation (SaO_2), exercise capacity measured using the six-minute walking test distance (6MWD), quality of life measured using the St George's Respiratory Questionnaire (SGRQ) and an abnormally enlarged diameter of pulmonary artery relative to the aorta (PA:A).[9,12] In COPD patients, vasoconstriction and vascular remodeling may result

as a consequence of ventilation/perfusion (VQ) mismatch-driven hypoxia and hypercapnia.[4,13,14] In addition, emphysematous tissue destruction and compressive stress on the vascular bed due to hyperinflation may have an impact.[4] For all these reasons, imaging measurements of pulmonary vascular structure and function may serve as treatable traits or perhaps identify COPD patients at risk for hospitalization.

Simultaneous ventilation and perfusion measurements[15,16] may be provided using Fourier decomposition magnetic resonance imaging (FDMRI) which is a rapid (2 minutes) free-breathing MRI approach that measures the oscillatory frequency-spectrum power of local ^{1}H signal intensity changes over time. Power at the respiratory and heart rates correspond to the extent of local lung inflation and deflation (ventilation) and pulsatile blood flow (perfusion) respectively.[15] FDMRI has been used to measure ventilation defects in COPD, [17,18] and was recently enhanced using ^{1}H MRI phase-resolved functional lung MRI (PREFUL), which has opened up new opportunities for pulmonary research.[19,20]

FDMRI ventilation measurements were previously generated in a small group of patients with COPD and these were also directly compared with hyperpolarized ^{3}He MRI ventilation defects.[17] In this previous work, there was good agreement between FDMRI and hyperpolarized ^{3}He MRI ventilation defects. Based on this and other previous work,[21,22] we hypothesized that FDMRI perfusion measurements would be strongly related to CT measurements of emphysema. Until now however, to our knowledge, FDMRI perfusion measurements have never been directly compared with CT pulmonary vascular measurements. In previously described, preliminary work,[23] an image processing pipeline was created and tested for the generation of FDMRI pulmonary vascular perfusion maps in patients with asthma. Here, we optimized this algorithm pipeline to generate FDMRI perfusion

measurements in a larger group of ex-smokers with COPD from the TINCan cohort study.[24,25] We also directly compared these with thoracic CT measurements of the pulmonary vascular tree to interrogate spatial and structure-function relationships between the pulmonary vessels and FDMRI perfusion maps.

A.2 Materials and Methods

A.2.1 Study Participants

We evaluated male and female participants from the TINCan cohort study[24,25] for whom a complete FDMRI, CT and pulmonary function measurement dataset was acquired and for whom written informed consent was provided to an ethics-board approved protocol (NCT02279329, NCT02282202). COPD participants were included based on a clinical diagnosis of COPD as well as a predicted forced expiratory volume in 1 second (FEV1) >25% and predicted forced vital capacity (FVC) >25% and >0.5L.

All participants were stratified using Global Initiative for Chronic Obstructive Lung Disease (GOLD) grades[1] and underwent pulmonary function tests, multiple inert gas washout, low-dose thoracic CT, FDMRI, anatomical ^{1}H MRI and either ^{3}He or ^{129}Xe MRI. Participants completed a six- minute walk test (6MWT) and were monitored for blood oxygen saturation using digital pulse oximetry (Nonin Medical Inc. handheld oximeter, Plymouth, MN, USA) post exercise, when they also completed the BORG questionnaire.[26] Self-reported symptoms and quality-of-life were reported using the St. George's Respiratory Questionnaire (SGRQ).[12]

A.2.2 Pulmonary Function Tests

Spirometry and plethysmography were performed (*MedGraphics Elite Series* plethysmograph MGC Diagnostics Corporation, St. Paul, MN, USA) according to American Thoracic Society

and European Respiratory Society guidelines.[27-29] DL_{CO} was measured using the attached gas analyser.

A.2.3 ^{1}H MRI

All MRI was performed on a 3.0T Discovery MR 750 scanner (GE Healthcare, Milwaukee, WI) with multinuclear imaging capabilities. FDMRI was acquired between October 2013 and September 2019 in participants enrolled in the TINCan cohort study[24] and in whom there was sufficient time remaining after ^{1}H anatomical, ^{3}He and ^{129}Xe MRI acquisitions during a one-hour imaging session.

Dynamic FDMRI was acquired for a single coronal slice with a 32-channel torso coil (GE Health Care) including respiratory bellows and fingertip pulse oximeter to monitor respiratory rate, cardiac rate, and blood oxygen saturation. Dynamic acquisition was performed using a balanced steady-state free precession (bSSFP) sequence (TR/TE/flip = 1.9ms/0.6ms/15°; acquisition time = 125s; FOV = 40 x 40cm^{2}; BW=250kHz; matrix = 256x256; number of slices = 1; slice thickness=15mm; number of excitations = 1; number of frames = 500). Anatomic ^{1}H MRI was performed immediately prior to hyperpolarized gas imaging and performed in the same supine position. Anatomic ^{1}H were performed using a fast spoiled gradient recalled echo sequence (TR/TE/flip=4.7ms/1.2ms/30°; acquisition time = 12s; FOV = 40x40 cm^{2}; BW =24.4kHz; matrix = 128x80, zero-padded to 128x128; partial echo percent=62.5%; number of slices=15-18; slice thickness = 15mm) with a whole-body radiofrequency coil following inhalation of 1.0L N_2 from a tedlar bag.

A.2.4 Hyperpolarized Gas MRI

^{3}He gas was prepared using a commercial hyperpolarizer (HeliSpin, Polarean, Durham, NC) and diluted to 40% ^{3}He / 60% medical grade N_2. ^{129}Xe gas was prepared using a commercial hyperpolarizer (Polarean 9820, Polarean, Durham, NC, USA) and diluted to 40% ^{129}Xe / 60% ^{4}He. Participants were provided gas in a 1.0L Tedlar bag and coached from passive expiration to full hyperpolarized gas inhalation breath-hold while supine in the system bore. An optical digital -pulse oximeter was used to monitor oxygen saturation (SaO_2) during imaging and after the 6MWT. All MRI was performed on a 3.0T Discovery MR 750 scanner (GE Healthcare, Milwaukee, WI) with multinuclear imaging capabilities. Coronal ^{3}He MRI was acquired using a single-channel rigid elliptical thoracic coil (RAPID Biomedical GmbH, Wurzburg, Germany) and a two-dimensional multi-slice fast spoiled gradient recalled echo sequence with partial echo acceleration (TR/TE/flip angle = 3.8ms/1.0ms/7°; FOV = 40x40cm^2; BW=48.8kHz; matrix=128x80, zero-padded to 128x128; partial echo percent = 62.5%; number of slices = 15-18; slice thickness = 15mm).

Coronal ^{129}Xe MRI was acquired using a flexible vest coil (Clinical MR Solutions, Brookfield WI, USA) and a coronal plane 3D fast gradient recalled echo sequence (TE/TR/flip angle = 1.5ms/5.1ms/1.3°; FOV = 40x40 cm^2; BW=16kHz; matrix=128x128; number of slices = 15-18; slice thickness = 15mm).

A.2.5 CT

Thoracic CT images were acquired using a 64-slice LightSpeed VCT system (General Electric Healthcare, Milwaukee, WI, USA) as previously described[24,30] following inhalation of 1.0L N_2 gas from functional residual capacity (FRC+1) to ensure volume-matching between CT and ^{3}He or ^{129}Xe MRI. CT images were acquired within 30 minutes of MRI using the following

parameters: 64 x 0.625mm collimation, 100 mA effective tube current, 120 kVp tube voltage, 500 ms rotation time and 1.0 pitch. The total effective dose to participants was estimated as 1.8 mSv based on manufacturer settings and the ImPACT patient dosimetry calculator (based on UK Health Protection Agency NRBP-SR250).

A.2.6 Image Analysis

CT images were analysed using VIDAvision software (VIDA diagnostics Inc.; Coralville IA) to obtain vessel tree segmentations, total blood volume (TBV), volume of vessels < 1 voxel-radius (PV_1) and the relative area of the lung <-950 Hounsfield Units (RA_{950}).

FDMRI analysis was performed using a custom, in-house software pipeline[23] created using MATLAB (MATLAB R2019a; Mathworks, USA). A reference ^1H slice was identified midway between full inhalation and exhalation and selected as the target with which all other frames were deformed, using a modality independent neighbourhood descriptor[31] method as previously described.[32] The reference slice was also used to segment the thoracic cavity from the rest of the image using a continuous max-flow algorithm.[33] Individual image voxels were isolated from the deformed image series and Fourier transformed from time domain signal intensities to a frequency spectrum representation. Ventilation information was recovered from the magnitude of oscillations occurring at the respiratory frequency, identified as the largest magnitude peak occurring in the respiratory frequency range. The cardiac frequency was also identified as the largest magnitude peak in the cardiac frequency range. Gated data were used to verify respiratory and cardiac frequencies and the relevant respiratory and cardiac magnitudes were employed to generate ventilation and perfusion maps. Ventilation and perfusion maps were then segmented using a fuzzy c-means clustering algorithm into five intensity levels ranging from signal void and hypointense signal to hyperintense signal.[23,34]

The volume of the first signal intensity cluster (representing signal void in ventilation and perfusion maps) was divided by the total thoracic cavity volume to generate ventilation defect percent (VDP) and perfusion defect percent (QDP), respectively.

A.2.7 Statistics

Independent t-tests and were performed using IBM SPSS Statistics software, V25 (IBM; Armonk NY). Linear univariate regression and associated non-zero slope F statistics were performed using GraphPad Prism 8 (GraphPad Software; San Diego, CA). Linear correlations were measured using Pearson's correlation coefficient (*r)*. Results and models were considered significant if the two-tailed type I error probability was less than 5% ($p < .05$).

A.3 Results

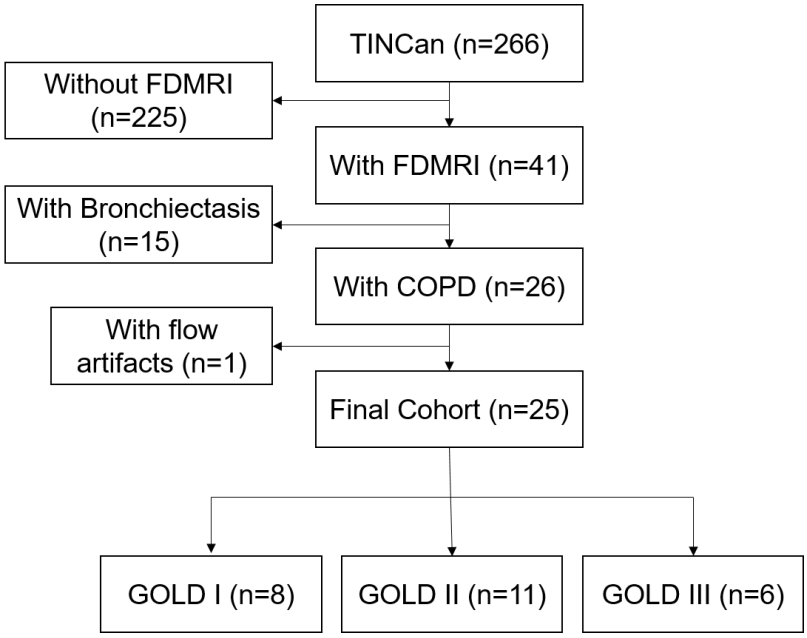

Figure A-1 Consort diagram for the participants analyzed using FDMRI.
Dynamic proton MRI was acquired in 41 of 266 participants; data for 15 of these participants were not evaluated because of a confirmed radiographic and clinical diagnosis of bronchiectasis. Flow artifacts stemming from the aorta in ^{1}H images interfered with FDMRI perfusion maps which resulted in the exclusion of a single participant from the final analysis in 25 participants.

A consort diagram in **Figure A-1** provides an overview of the participants originally enrolled (n=266) and evaluated with both FDMRI and hyperpolarized gas MRI (n=41). In this preliminary analysis, data for patients with confirmed bronchiectasis were not evaluated (n=15). In addition, a single enrolled participant was not included in the final analysis dataset (n=25) because pulsatile blood flow in the aorta generated flow artefacts in the FDMRI perfusion map on the left lung upper and lower lobes. **Figure A-2** shows the artefact in the original acquisition as well as its impact on the perfusion and ventilation maps.

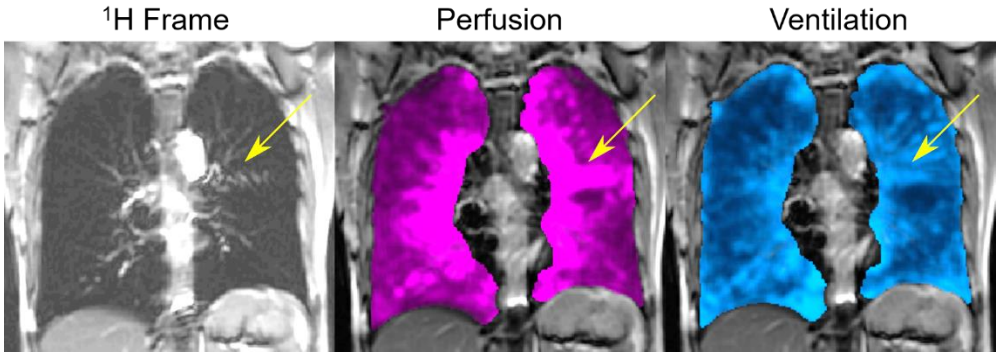

Figure A-2 Pulsatile blood flow artifact present in ^{1}H MRI.
An artifact originating in the aorta and extending in the phase-encode direction exhibited intensity fluctuations at the heart rate. The FDMRI perfusion map exhibited a hyperintense band in the same region. A small band was also present in the ventilation image. Participant was a female age=58, FEV_1=32%$_{pred,}$ FEV_1/FVC=31%, DL_{CO}=53%$_{pred}$, FD VDP=21%, QDP=15%, RA_{950}=11%, TBV/TLV=2.6% and PV_1=58%

Table A-1 provides participant demographics and pulmonary function measurements for all 26 participants and the subgroup of 25 participants evaluated including eight GOLD grade I, 11 GOLD grade II, and six GOLD grade III COPD participants. There were no significant differences between the "all participant" and the "evaluated participant" subgroups. ^{3}He MRI was also acquired in 17 participants (four GOLD I, seven GOLD II, and six GOLD III) and ^{129}Xe MRI in eight participants (four GOLD I, four GOLD II).

Table A-1 Participant demographics and pulmonary function measurements.

Parameter (mean ±SD)	All participants (n=26)	All participants evaluated (n=25)	Significance (*p* value)
Age years	67 (10)	67 (9)	.90
Male n	17	17	
BMI kg/m^2	26 (3)	27 (4)	.73
Pack years	45 (35)	45 (38)	.86
SGRQ	39 (18)	38 (19)	.82
FEV_1 $\%_{pred}$	67 (26)	69 (24)	.85
FEV_1/FVC %	53 (15)	54 (15)	.89
FVC $\%_{pred}$	91 (22)	92 (21)	.86
TLC $\%_{pred}$	111 (25)	110 (15)	.93
RV/TLC $\%_{pred}$	126 (31)	125 (23)	.86
DL_{CO} $\%_{pred}$	58 (24)	58 (25)	.93
6MWD m	411 (76)	422 (86)	.90
Post 6MWD SaO_2 %	92 (7)	92 (8)	.92

BMI=body mass index; SGRQ=St. George's Respiratory Questionnaire; FEV1=forced expiratory volume in 1 second; %pred=percent predicted; FVC=forced vital capacity; TLC=total lung capacity; RV=residual volume; DLCO=diffusing capacity of the lung for carbon monoxide; 6MWD=six-minute walk distance; SaO2=blood oxygen saturation

Table A-2 CT and MR Imaging measurements

Parameter Mean (±SD)	All participants N=26	All participants evaluated N=25	GOLD I N=8	GOLD II N=11	GOLD III N=6
RA_{950} %	10 (8)	9 (9)	3 (4)	12 (8)	19 (10)
TBV ml	144 (32)	143 (30)	132 (39)	145 (28)	146 (16)
TBV/TLV %	2.6 (0.4)	2.6 (0.4)	2.55 (0.47)	2.60 (0.31)	2.54 (0.38)
PV_1 %	54 (5)	54 (6)	53 (6)	55 (4)	54 (5)
^{3}He VDP %	21 (13)	20 (13)	8 (11)	19 (5)	31 (13)
^{129}Xe VDP %	-	18 (14)	18 (14)	18 (15)	-
FD VDP %	19 (12)	19 (12)	17 (12)	16 (11)	25 (13)
QDP %	24 (12)	24 (13)	19 (12)	21 (10)	37 (8)

TBV=total blood volume measured from CT vessel tree; TLV=total lung volume measured from CT segmented lung; RA_{950}=relative area of the lung with CT attenuation <-950 Hounsfield units (HU); PV_1=percent of pulmonary vessels with radius <1 voxel; FDMRI=Fourier decomposition magnetic resonance imaging; VDP=FDMRI ventilation defect percent; QDP=FDMRI perfusion defect percent.

Table **A-2** summarizes CT density and vessel measurements, hyperpolarized gas measurements and FDMRI ventilation and perfusion measurements by GOLD grade. In Fig.

3, box and whisker plots show that there were no differences between GOLD grade subgroups for PV_1 and this was also true for TBV, TBV/TLV (data not shown). MRI QDP was significantly different between GOLD III (37 ± 8%), GOLD II (21 ± 10%; p =.008) and GOLD I (19 ± 12 %; p =.011) subgroups. In addition, there was a significant difference in RA_{950} for GOLD I and GOLD III participants (p =.02).

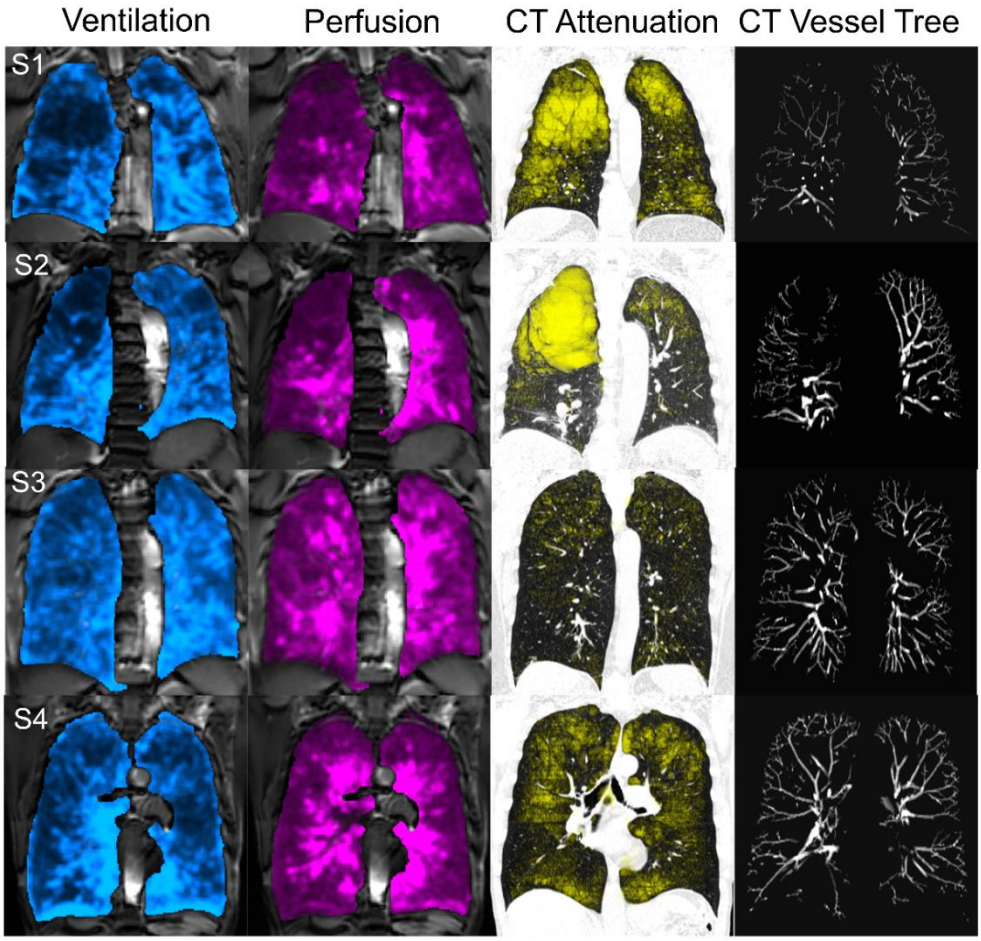

Figure A-3 FDMRI ventilation (blue) and perfusion (magenta) maps, CT attenuation<-950HU (yellow) and CT-segmented vessel trees for representative participants with COPD.
S1 is a male age=66 years with GOLD grade III COPD and FEV_1=48%$_{pred}$, FEV_1/FVC=36%, DL_{CO}=52%$_{pred}$, FD VDP=35%; QDP=37%, RA_{950}=24%, TBV/TLV=2.2% and PV_1=58%
S2 is a male age=79 years with GOLD grade I/II COPD and FEV_1=77%$_{pred}$, FEV_1/FVC=51%, DL_{CO}=31%$_{pred}$, FD VDP=20%, QDP=35%, RA_{950}=21%, TBV/TLV=3.1% and PV_1=48
S3 is a female age=56 years with GOLD grade II/III COPD and FEV_1=54%$_{pred}$, FEV_1/FVC=66%, DL_{CO}=55%$_{pred}$, FD VDP=7%, QDP=31%, RA_{950}=1%, TBV/TLV=2.6% and PV_1=54%
S4 is a female age=72 years with GOLD grade III COPD and FEV_1=37%$_{pred}$, FEV_1/FVC=57%, DL_{CO}=50%$_{pred}$ FD VDP=30%, QDP=42%, RA_{950}=10%, TBV/TLV=2.3% and PV_1=61%

Figure A-3 shows coronal FDMRI and CT images for four representative participants. FDMRI images are shown co-registered with a reference ^{1}H MRI slice and CT images are shown with an x-ray attenuation <-950HU (RA_{950}) mask in yellow co-registered to coronal CT slices. CT RA_{950} mask values and vessel trees were averaged over 21 slices to match the thickness of the MRI slices. In Fig. 4, for some participants, regions with marginal ventilation and perfusion

signal spatially corresponded with the RA_{950} emphysema mask (yellow). For example, in participant S1, regions of poor ventilation, perfusion and emphysema also qualitatively agreed with abnormal small vessel density, especially near bullae and the lung periphery. In participant S2, there were emphysematous bullae in the upper right lobes that spatially corresponded with MRI ventilation and perfusion defects. In participant S3 there was very minimal emphysema and in participant S4 with moderate, heterogeneously distributed

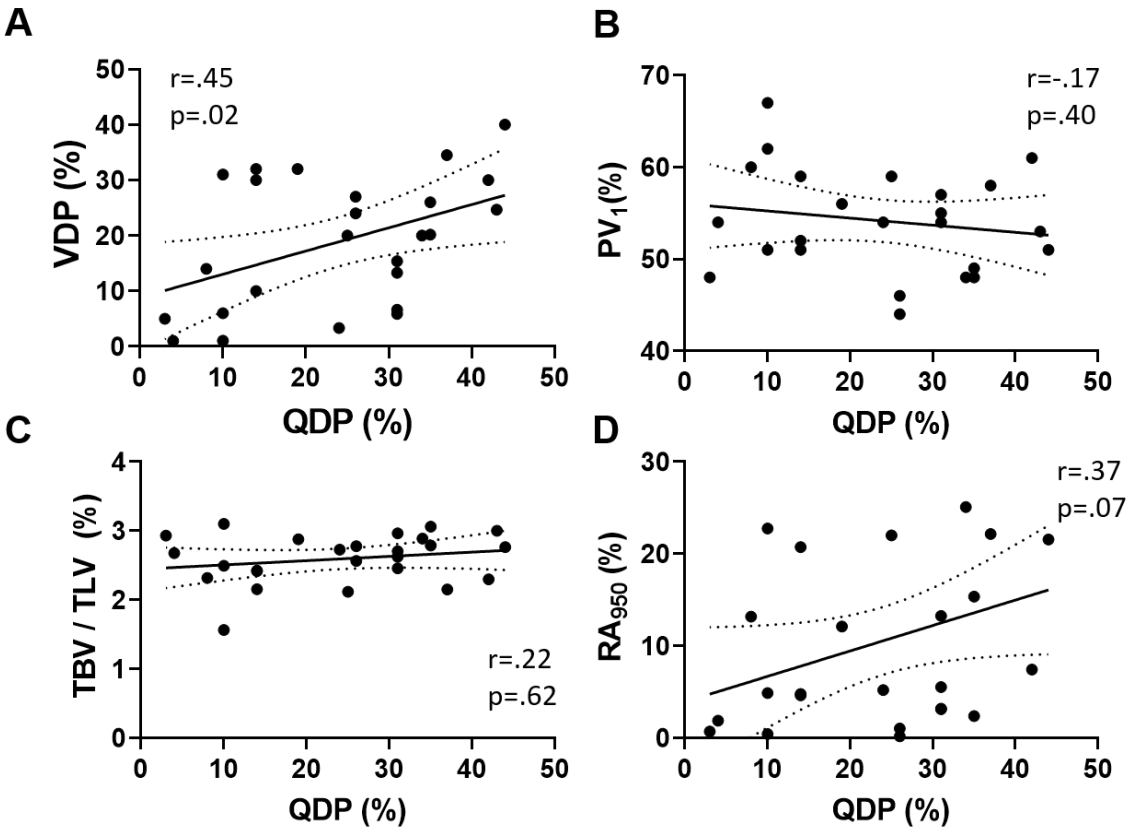

Figure A-4 Relationship of FDMRI QDP with pulmonary imaging measurements.
FDMRI QDP relationship with A) FDMRI VDP; r=.45, R^2=.20, p=.024, y = 0.42x + 9; B) CT-derived PV_1; r=-.17, R^2=.03, p=.62, y = -0.1x + 56; C) CT-derived TBV/TLV; r=.22, R^2=.05, p=0.86, y = 0.006x + 2.45; D) CT RA_{950}; r=.36, R^2=0.13, p=.07, y = 0.24x + 4.

emphysema, there was no qualitative evidence of this spatial correspondence.

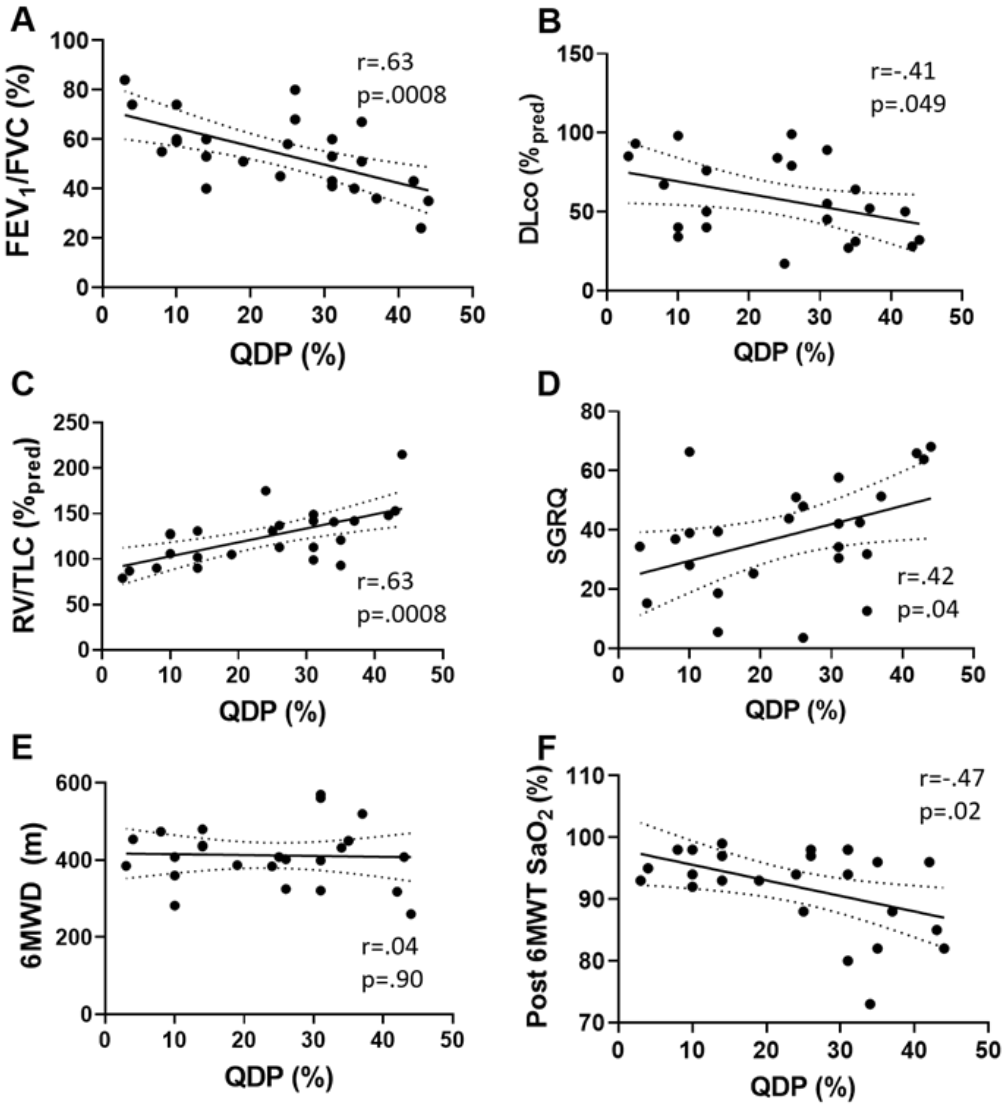

Figure A-5 FDMRI QDP relationships with pulmonary function, SGRQ and 6MWT measurements. FDMRI QDP relationship with A) FEV_1/FVC; r=.63, R^2=.39, p=.0008, y = -0.74x + 72 ; B) DL_{CO}; r=-.41, R^2=.18, p=.049, y = -0.79x + 77; C) RV/TLC; r=.63, R^2=.39, p=.0008, y = 1.54x + 88; D) SGRQ; r=.42, R^2=.17, p=.036, slope: y = 0.62x + 23; E) 6MWD; r=.04, R^2=.0013, p=.86, slope: y = -0.22x + 418; F) post-6MWT SaO_2; r=-.47, R^2=.22, p=.02, slope: y = -0.25x + 98

Figure A-4 shows the quantitative relationships for QDP and VDP (r=0.45; p=.02) and a trend towards a significant quantitative relationship between QDP and RA_{950} (r=0.37; p=.07). There was no significant relationship between FDMRI QDP and PV_1 (r =-0.17; p=.40) or TBV/TLV (r=0.22, p=.62). There were no other significant relationships observed between RA_{950} or DL_{CO} with PV_1 and TBV/TLV (data not shown).

Figure A-5 shows that FDMRI QDP was moderately correlated with FEV_1/FVC (r=-0.63; *p*=.001), DL_{CO} (r=-0.41; *p*=.04), RV/TLC (r=0.63; *p*=.001), SGRQ (r=0.42; *p*=.04) and the post-6MWT SaO_2 (r=-0.47; *p*=.02).

A.4 Discussion

Based on previous work in patients with COPD,[8-11] we hypothesized that FDMRI perfusion measurements would be quantitatively related to CT pulmonary vascular measurements and CT evidence of emphysema. Hence, in this preliminary evaluation in a relatively small group of COPD participants from the TINCan cohort study[24,25] we generated and evaluated FDMRI ventilation and perfusion measurements and directly compared these with CT measurements of emphysema and pulmonary vascular density. We made the following important observations: 1) FDMRI QDP was significantly different for the GOLD I and GOLD II subgroups with the GOLD III subgroup, while FDMRI VDP was not, 2) FDMRI ventilation and perfusion defects were quantitatively and spatially correlated with each other and spatially related to regional CT evidence of emphysema, 3) FDMRI QDP was not quantitatively related to CT PV_1 or TBV/TLV but there was a trend toward a significant relationship with RA_{950}, and, 4) FDMRI QDP was quantitatively related to FEV_1/FVC, DL_{CO}, RV/TLC, SGRQ, and post-6MWT SaO_2.

First, FDMRI QDP was significantly different between GOLD I and GOLD II subgroups as compared to the GOLD III subgroup while FDMRI VDP was not. Importantly however, and as expected, FDMRI QDP was also quantitatively correlated with FDMRI VDP. In regions with large bullae and tissue destruction, ventilation and perfusion defects appeared in most cases to be spatially matched. In some participants with diffuse regions of emphysema (male age 62, FEV_1=83%$_{pred}$, RA_{950}=2.4%, VDP= 26%, QDP=35%; age 76 male, FEV_1=86%$_{pred}$,

RA_{950}=13.26%, VDP=15%, QDP=31%), perfusion defects were larger than their corresponding ventilation abnormalities. This observation may be related to regional QDP/VDP mismatch or perhaps this simply suggests that FDMRI QDP is a more sensitive measurement of regional abnormalities in COPD participants. Moreover, while FDMRI ventilation and perfusion images were both generated using the same signal intensity segmentation algorithm, differences in the magnitude of ventilation and perfusion signal intensities may have contributed to the differences observed.

Second, while there was a trend towards a significant but modest relationship with RA_{950}, QDP was not related to CT PV_1 or TBV/TLV. This was unexpected given previous reports that revealed strong evidence of abnormally pruned CT pulmonary vasculature in participants with COPD.[8-11] We observed substantial gas trapping in the participants evaluated here which is important because gas trapping was previously shown to influence CT measurements of vascular density.[11] In the participants evaluated here, vasoconstriction and non-destructive remodeling processes may also be occurring, which themselves may not substantially influence CT measurements such as PV_1.[10,11] Furthermore, because the FDMRI signal originates from pulsatile flow patterns in the pulmonary vasculature, FDMRI may be sensitive to a number of different vascular abnormalities not detected using CT. It is also important to note that FDMRI QDP provides only single slice data and hence relationships may be difficult, if not impossible to quantify because CT PV_1 and TBV/TLV provide whole lung measures. Single-slice FDMRI acquisition also prevented lobar FDMRI analyses. For FDMRI, the acquisition of 3D volumes is challenging due to tradeoffs between spatial and temporal resolution and the need to adhere to the Nyquist limits for cardiac frequencies. Novel methods recently developed such as PREFUL[19] will provide a way to overcome this Nyquist limit.

Finally, we also observed that FDMRI QDP was quantitatively related to pulmonary function measurements such as FEV_1/FVC, DL_{CO} and RV/TLC as well as patient-relevant measurements such as SGRQ scores and post-6MWT SaO_2. Based on previous CT studies,[9,10] we were not surprised to observe a correlation between FDMRI QDP and airway obstruction. We hypothesized that FDMRI QDP and DL_{CO} would be related because parenchyma tissue destruction and emphysema have been previously shown to result in pulmonary vascular alterations.[9,35,36] The relationship between RV/TLC and QDP was somewhat unexpected and can be explained by vascular compression caused by gas trapping and the resulting pressure exerted on nearby tissue.[4] FDMRI may be especially sensitive to these effects because the ^1H MRI signal intensity is influenced by changes in lung tissue compliance.

In this relatively small study in 25 participants, we did not expect to find that FDMRI QDP would be related to post-exercise oxygen saturation, nor did we anticipate the relationship of QDP with quality-of-life scores. The COPDGene cohort study has provided strong evidence for the relationships between CT phenotypes and poor quality-of-life.[37] However, while COPDGene revealed modest correlations between CT vascular pruning measurements and oxygen saturation, there was no correlation with SGRQ.[9] Currently, COPD diagnosis is based on FEV_1, however this measure is a poor predictor of emphysema severity and of dyspnea and quality of life.[38] In other words, many COPD patients report worsening respiratory symptoms in the absence of worsening spirometry.[39] Thus, FDMRI QDP may be considered for studies where sensitivity to clinical targets is required that are poorly reflected by changes in spirometry.

Limitations of this work include the small number of participants in whom CT, FDMRI and full pulmonary function datasets were acquired which limits the generalizability of our results

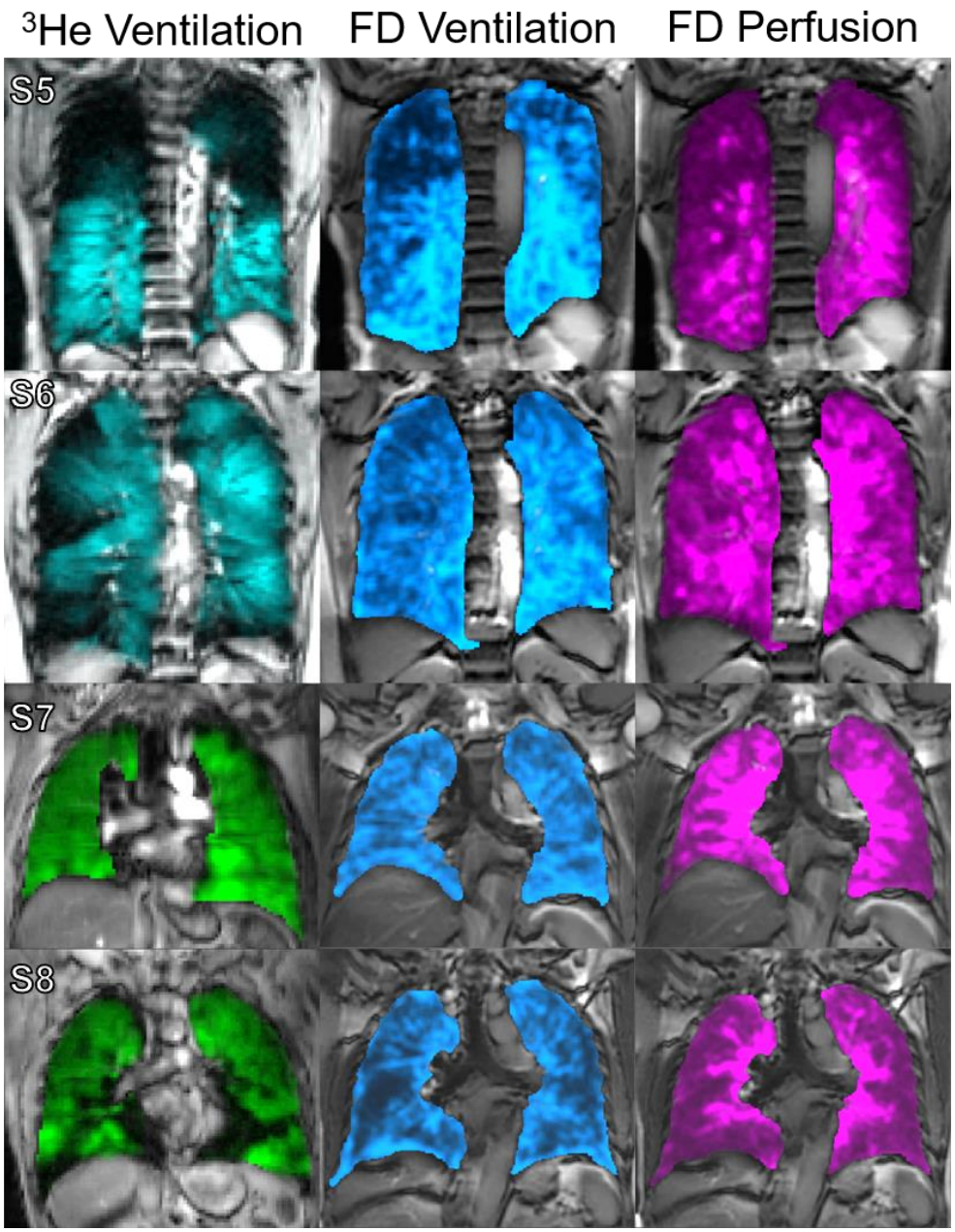

Figure A-6 Comparison of FDMR and ^{129}Xe MR images
Agreement (S5, S7) and disagreement (S6, S8) between hyperpolarized ^{3}He ventilation (cyan) or ^{129}Xe ventilation (green) and FD ventilation (blue) and perfusion (magenta).
S5 is a female age=73 years with GOLD grade III COPD and FEV_1=44%$_{pred}$, FEV_1/FVC=40%, DL_{CO}=27%$_{pred}$, ^{3}He VDP=29%, FD VDP=20%; QDP=34%, RA_{950}=25%, TBV/TLV=2.9% and PV_1=48%
S6 is a female age=56 years with GOLD grade II/III COPD and FEV_1=54%$_{pred}$, FEV_1/FVC=66%, DL_{CO}=55%$_{pred}$, ^{3}He VDP=17%, FD VDP=7%, QDP=31%, RA_{950}=1%, TBV/TLV=2.6% and PV_1=54%
S7 is a male age=72 years with GOLD grade I COPD and FEV_1=112%$_{pred}$, FEV_1/FVC=74%, DL_{CO}=93%$_{pred}$, ^{129}Xe VDP=4%, FD VDP=1%, QDP=4%, RA_{950}=1%, TBV/TLV=2.7% and PV_1=54%
S8 is a male age=87 years with GOLD grade III COPD and FEV_1=107%$_{pred}$, FEV_1/FVC=68%, DL_{CO}=93%$_{pred,}$ ^{129}Xe VDP=9%, FD VDP=27%, QDP=26%, RA_{950}=1%, TBV/TLV=2.8% and PV_1=54%

and likely limited our ability to detect significant relationships. Hence these findings should be considered preliminary and hypothesis generating for a larger cohort evaluation. We also noted that a single participant was not included in the evaluation subgroup because pulsatile blood flow disrupted the image contrast in the perfusion but not ventilation map, resulting in poor clustering algorithm performance. To our knowledge, such FDMRI artifacts have not been previously noted.[15,16] Out-of-slice excitation due to pulsatile flow may be responsible[40] and in future could be reduced by considering different acquisition plane geometries.

Sources of image contrast in FDMRI are still poorly understood and are a limitation of proton-based lung MRI. Ventilation abnormalities may be caused by blocked airways, compressed tissue, low regional compliance or tissue destruction however the relative contribution of each of these mechanisms to VDP is unknown.[16,41] As shown in **Figure A-6**, agreement between FDMRI and hyperpolarized ^{3}He and ^{129}Xe was inconsistent. Defects, such as large bullae, and healthy tissue showed agreement in some participants, although others exhibited defects in ^{3}He and ^{129}Xe that were not reflected in FDMRI, and vice versa. A better understanding of how different structural abnormalities are reflected in hyperpolarized gas and FDMRI signal intensity and distribution would help the interpretability of VDP and QDP.

Given the potential pathophysiological relevance of pulmonary vascular abnormalities in COPD and that vascular disease as an important predictor of COPD mortality[8,10] we think that MRI measurements of pulmonary vascular function such as QDP may be helpful to consider in clinical trials, especially in situations whereby regional VQ mismatch or perfusion abnormalities cannot be detected using CT. ^{1}H MRI techniques such as FDMRI and PREFUL[19,20] are highly suited to longitudinal and serial investigations. In addition to improved temporal resolution,[19] PREFUL provides important phase information which is

sensitive to local hemodynamics,[42] and which may be helpful in COPD clinical trials, as the pioneers of this method recently reported.[43,44]

In conclusion, in a relatively small group of COPD patients with a range of disease severity, we observed that FDMRI ventilation defects were spatially and quantitatively correlated with FDMRI perfusion defects which were also correlated with CT emphysema, DL_{CO}, post-exercise SaO_2 and quality-of-life measurements but not CT PV_1. These findings support the further development of rapid ^1H MRI methods to measure dynamic ventilation and perfusion abnormalities in COPD patients.

A.5 References

1. Global Initiative for Chronic Obstructive Lung D. 2019 Report: Global Initiative for Chronic Obstructive Lung Disease; 2019 [155]. Available from: http://www.goldcopd.org/.

2. Ford ES, Murphy LB, Khavjou O, Giles WH, Holt JB, Croft JB. Total and state-specific medical and absenteeism costs of COPD among adults aged >/= 18 years in the United States for 2010 and projections through 2020. Chest. 2015;147(1):31-45.

3. Falk JA, Kadiev S, Criner GJ, Scharf SM, Minai OA, Diaz P. Cardiac disease in chronic obstructive pulmonary disease. Proc Am Thorac Soc. 2008;5(4):543-8.

4. Criner GJ, Cordova F, Sternberg AL, Martinez FJ. The National Emphysema Treatment Trial (NETT): Part I: Lessons learned about emphysema. Am J Respir Crit Care Med. 2011;184(7):763-70.

5. Divo M, Cote C, de Torres JP, Casanova C, Marin JM, Pinto-Plata V, et al. Comorbidities and risk of mortality in patients with chronic obstructive pulmonary disease. Am J Respir Crit Care Med. 2012;186(2):155-61.

6. Sin DD, Anthonisen NR, Soriano JB, Agusti AG. Mortality in COPD: Role of comorbidities. Eur Respir J. 2006;28(6):1245-57.

7. Wells JM, Washko GR, Han MK, Abbas N, Nath H, Mamary AJ, et al. Pulmonary arterial enlargement and acute exacerbations of COPD. N Engl J Med. 2012;367(10):913-21.

8. Rahaghi FN, Wells JM, Come CE, De La Bruere IA, Bhatt SP, Ross JC, et al. Arterial and Venous Pulmonary Vascular Morphology and Their Relationship to Findings in Cardiac Magnetic Resonance Imaging in Smokers. J Comput Assist Tomogr. 2016;40(6):948-52.

9. Estepar RS, Kinney GL, Black-Shinn JL, Bowler RP, Kindlmann GL, Ross JC, et al. Computed tomographic measures of pulmonary vascular morphology in smokers and their clinical implications. Am J Respir Crit Care Med. 2013;188(2):231-9.

10. Washko GR, Nardelli P, Ash SY, Vegas Sanchez-Ferrero G, Rahaghi FN, Come CE, et al. Arterial Vascular Pruning, Right Ventricular Size, and Clinical Outcomes in Chronic Obstructive Pulmonary Disease. A Longitudinal Observational Study. Am J Respir Crit Care Med. 2019;200(4):454-61.

11. Rahaghi FN, Argemi G, Nardelli P, Dominguez-Fandos D, Arguis P, Peinado VI, et al. Pulmonary vascular density: comparison of findings on computed tomography imaging with histology. Eur Respir J. 2019;54(2).

12. Jones PW, Quirk FH, Baveystock CM, Littlejohns P. A self-complete measure of health status for chronic airflow limitation. The St. George's Respiratory Questionnaire. Am Rev Respir Dis. 1992;145(6):1321-7.

13. Rabe KF, Hurd S, Anzueto A, Barnes PJ, Buist SA, Calverley P, et al. Global strategy for the diagnosis, management, and prevention of chronic obstructive pulmonary disease: GOLD executive summary. Am J Respir Crit Care Med. 2007;176(6):532-55.

14. Voelkel NF, Tuder RM. Hypoxia-induced pulmonary vascular remodeling: a model for what human disease? J Clin Invest. 2000;106(6):733-8.

15. Bauman G, Puderbach M, Deimling M, Jellus V, Chefd'hotel C, Dinkel J, et al. Non-contrast-enhanced perfusion and ventilation assessment of the human lung by means of fourier decomposition in proton MRI. Magn Reson Med. 2009;62(3):656-64.

16. Kjorstad A, Corteville DMR, Henzler T, Schmid-Bindert G, Zollner FG, Schad LR. Non-invasive quantitative pulmonary V/Q imaging using Fourier decomposition MRI at 1.5T. Z Med Phys. 2015;25(4):326-32.

17. Capaldi DP, Sheikh K, Guo F, Svenningsen S, Etemad-Rezai R, Coxson HO, et al. Free-breathing pulmonary 1H and Hyperpolarized 3He MRI: comparison in COPD and bronchiectasis. Acad Radiol. 2015;22(3):320-9.

18. Kaireit TF, Gutberlet M, Voskrebenzev A, Freise J, Welte T, Hohlfeld JM, et al. Comparison of quantitative regional ventilation-weighted fourier decomposition MRI with dynamic fluorinated gas washout MRI and lung function testing in COPD patients. J Magn Reson Imaging. 2018;47(6):1534-41.

19. Voskrebenzev A, Gutberlet M, Klimes F, Kaireit TF, Schonfeld C, Rotarmel A, et al. Feasibility of quantitative regional ventilation and perfusion mapping with phase-resolved functional lung (PREFUL) MRI in healthy volunteers and COPD, CTEPH, and CF patients. Magn Reson Med. 2018;79(4):2306-14.

20. Kaireit TF, Voskrebenzev A, Gutberlet M, Freise J, Jobst B, Kauczor HU, et al. Comparison of quantitative regional perfusion-weighted phase resolved functional lung (PREFUL) MRI with dynamic gadolinium-enhanced regional pulmonary perfusion MRI in COPD patients. J Magn Reson Imaging. 2019;49(4):1122-32.

21. Capaldi DPI, Zha N, Guo F, Pike D, McCormack DG, Kirby M, et al. Pulmonary Imaging Biomarkers of Gas Trapping and Emphysema in COPD: 3He MR Imaging and CT Parametric Response Maps. Radiology. 2016;279(2):597-608.

22. Kirby M, Svenningsen S, Kanhere N, Owrangi A, Wheatley A, Coxson HO, et al. Pulmonary ventilation visualized using hyperpolarized helium-3 and xenon-129 magnetic resonance imaging: differences in COPD and relationship to emphysema. J Appl Physiol (1985). 2013;114(6):707-15.

23. Matheson AM, Capaldi DPI, Guo F, Eddy RL, McCormack DG, Parraga G, et al. Fourier decomposition free-breathing 1H MRI perfusion maps in asthma. Proc SPIE. 2019;10949:272-80.

24. Kirby M, Pike D, McCormack DG, Sin DD, Lam S, Coxson HO, et al. Longitudinal Computed Tomography and Magnetic Resonance Imaging of COPD: Thoracic Imaging Network of Canada (TINCan) Study Objectives. Journal of the COPD Foundation. 2014;1(2):200-11.

25. Svenningsen S, Paulin GA, Sheikh K, Guo F, Hasany A, Kirby M, et al. Oscillatory Positive Expiratory Pressure in Chronic Obstructive Pulmonary Disease. Copd. 2016;13(1):66-74.

26. Borg GAV. Psychophysical bases of perceived exertion. Med Sci Sports Exerc. 1982;14(5):377-81.

27. Miller MR, Hankinson J, Brusasco V, Burgos F, Casaburi R, Coates A, et al. Standardisation of spirometry. Eur Respir J. 2005;26(2):319-38.

28. Wanger J, Clausen JL, Coates A, Pedersen OF, Brusasco V, Burgos F, et al. Standardisation of the measurement of lung volumes. Eur Respir J. 2005;26(3):511-22.

29. Macintyre N, Crapo RO, Viegi G, Johnson DC, van der Grinten CP, Brusasco V, et al. Standardisation of the single-breath determination of carbon monoxide uptake in the lung. Eur Respir J. 2005;26(4):720-35.

30. Kirby M, Pike D, Sin DD, Coxson HO, McCormack DG, Parraga G. COPD: Do Imaging Measurements of Emphysema and Airway Disease Explain Symptoms and Exercise Capacity? Radiology. 2015;277(3):872-80.

31. Krol A, Gimi B, Guo F, Capaldi DPI, Di Cesare R, Fenster A, et al. Registration pipeline for pulmonary free-breathing 1H MRI ventilation measurements. Proc SPIE. 2017;10137:61-8.

32. Guo F, Capaldi DPI, McCormack DG, Fenster A, Parraga G. A framework for Fourier-decomposition free-breathing pulmonary (1) H MRI ventilation measurements. Magn Reson Med. 2019;81(3):2135-46.

33. Guo F, Svenningsen S, Eddy RL, Capaldi DPI, Sheikh K, Fenster A, et al. Anatomical pulmonary magnetic resonance imaging segmentation for regional structure-function measurements of asthma. Med Phys. 2016;43(6):2911-26.

34. Kirby M, Heydarian M, Svenningsen S, Wheatley A, McCormack DG, Etemad-Rezai R, et al. Hyperpolarized 3He magnetic resonance functional imaging semiautomated segmentation. Acad Radiol. 2012;19(2):141-52.

35. Cordasco EM, Beerel FR, Vance JW, Wende RW, Toffolo RR. Newer aspects of the pulmonary vasculature in chronic lung disease. A comparative study. Angiology. 1968;19(7):399-407.

36. Thurlbeck WM, Simon G. Radiographic appearance of the chest in emphysema. AJR Am J Roentgenol. 1978;130(3):429-40.

37. Lowe KE, Regan EA, Anzueto A, Austin E, Austin JHM, Beaty TH, et al. COPDGene((R)) 2019: Redefining the Diagnosis of Chronic Obstructive Pulmonary Disease. Chronic Obstr Pulm Dis. 2019;6(5):384-99.

38. Vestbo J, Anderson W, Coxson HO, Crim C, Dawber F, Edwards L, et al. Evaluation of COPD Longitudinally to Identify Predictive Surrogate End-points (ECLIPSE). Eur Respir J. 2008;31(4):869-73.

39. Regan EA, Lynch DA, Curran-Everett D, Curtis JL, Austin JH, Grenier PA, et al. Clinical and Radiologic Disease in Smokers With Normal Spirometry. JAMA Intern Med. 2015;175(9):1539-49.

40. Markl M, Alley MT, Elkins CJ, Pelc NJ. Flow effects in balanced steady state free precession imaging. Magn Reson Med. 2003;50(5):892-903.

41. Couch MJ, Munidasa S, Rayment JH, Voskrebenzev A, Seethamraju RT, Vogel-Claussen J, et al. Comparison of Functional Free-Breathing Pulmonary (1)H and Hyperpolarized (129)Xe Magnetic Resonance Imaging in Pediatric Cystic Fibrosis. Acad Radiol. 2020.

42. Behrendt L, Voskrebenzev A, Klimes F, Gutberlet M, Winther HB, Kaireit TF, et al. Validation of Automated Perfusion-Weighted Phase-Resolved Functional Lung (PREFUL)-MRI in Patients With Pulmonary Diseases. J Magn Reson Imaging. 2020;52(1):103-14.

43. Vogel-Claussen J, Schonfeld CO, Kaireit TF, Voskrebenzev A, Czerner CP, Renne J, et al. Effect of Indacaterol/Glycopyrronium on Pulmonary Perfusion and Ventilation in Hyperinflated Patients with Chronic Obstructive Pulmonary Disease (CLAIM). A Double-Blind, Randomized, Crossover Trial. Am J Respir Crit Care Med. 2019;199(9):1086-96.

44. Vogel-Claussen J, Kaireit T, Voskrebenzev A, Schoenfeld C-O, Czerner C, Renne J, et al. Indacaterol/Glycopyrronium improves pulmonary ventilation and ventilation inhomogeneity in the CLAIM Study. European Respiratory Journal. 2018;52.

B FULLY-AUTOMATED HYPERPOLARIZED GAS MAGNETIC RESONANCE VENTILATION IMAGING SEGMENTATION AND REGISTRATION USING CONVOLUTIONAL NEURAL NETWORKS

B.1 Introduction

Abnormal lung function in pulmonary disease has clinically been measured as whole-lung impairment but advances in imaging show that lung function in conditions such as asthma,[1] chronic obstructive pulmonary disease (COPD),[2] and cystic fibrosis[3] is heterogeneous with regions of low to non-existent function called defects.[1] Pulmonary functional magnetic resonance imaging (MRI) is a method to image pulmonary ventilation using an inhaled contrast agent of helium-3 (^{3}He) or xenon-129 (^{129}Xe). The extent of defects may be quantified using ventilation defect percent (VDP),[4] a measure of the volume-ratio of low-signal tissue to thoracic cavity volume:

$$VDP = \frac{Volume_{defect}}{Volume_{Thoracic\ Cavity}} \times 100\%$$

VDP has emerged as a key biomarker for measuring disease severity in asthma,[1,5-10] chronic obstructive pulmonary disease (COPD),[2,11-17] and radiation induced lung injury.[18,19] Furthermore, VDP has emerged as a measure of functional improvement treatments such as bronchial thermoplasty,[20] anti-type 2 therapy in asthma,[21] and cystic fibrosis (CF).[22] Despite its advantages as a sensitive biomarker of lung function, clinical uptake has been limited, partly due to the technical knowledge needed to analyze images.

Early attempts at quantifying ventilation relied on manual segmentation[23,24] and scoring,[3] however these methods proved time-consuming. Later attempts to streamline the process used semi-automated segmentation and registration tools based on seeded region growing and

landmark-based rigid registration algorithms.[4,25] Anatomical proton (^{1}H) MRI are acquired under breath-hold of functional residual capacity (FRC) + 1.0L N_2 to ensure a constant lung volume that can be registered to noble gas images by an affine transformation and then automatically segmented with manual corrections by trained observers. While these techniques have been shown to be repeatable and reproducible[4,25,26] inter-observer variability introduces uncertainty and must be mitigated by extensive observer training. Furthermore, the use of semi-automated tools are time-consuming, requiring up to 45 minutes per data set for manual corrections and impeding the use of these tools in clinical environments. Faster, automated algorithms such as maximum flow and iterative shape descriptor algorithms have demonstrated limitations at higher defect volume[27] or in the presence of cardiac motion artifacts[28].

Recently, convolutional neural networks (CNNs) have been shown to be rapid and accurate tools for performing segmentation in medical imaging.[29,30] The U-Net architecture[29] and its derivatives have become the de-facto choice for medical image segmentation due to their fast processing speed and generalizability across modalities and anatomy. U-Net approaches have recently been applied to separately segment proton[31] and hyperpolarized gas[32,33] images on augmented, small-scale ($\leq$73 image volumes) data sets. In contrast, there is not one standard architecture family for registration tasks. Non-neural-network approaches to automatic rigid registration have used iterative techniques to maximize an image similarity metric between target and moving images.[34] These methods are poorly suited to hyperpolarized gas imaging, as registration occurs between structural ^{1}H MRI and hyperpolarized gas MRI, which have drastically different image texture, anatomical features, and contrast. Neural network approaches to rigid registration aim to learn a whole-image transformation and evaluate the

transform either by regression of the transform parameters[35] or by computing image similarity between proposed and ground-truth images.[36,37]

^{129}Xe MRI has gradually replaced ^{3}He in lung imaging due to its ability to image alveolar tissue and red-blood-cell signals.[38] Due to differences in gas properties different spatial distributions of lung ventilation have been observed depending on the contrast gas used and signal-to-noise ratio is reduced in ^{129}Xe.[39,40] Although ^{3}He images have smaller defects than ^{129}Xe images, similar contrast mechanisms and defect shapes suggest that a single network could accurately process both ^{3}He and ^{129}Xe MRI. We hypothesized that CNNs could derive relevant features from image sets to transform features into rigid transformations that exhibited low translation and rotation mean absolute error. Therefore, our objective was to train segmentation and registration CNNs using both ^{3}He and ^{129}Xe data. In contrast to previous attempts,[31,33] our approach would train on larger data sets (n=305), incorporate registration networks, simultaneously consider hyperpolarized gas and ^{1}H image features, and be validated against external datasets to assess overfitting and generalizability. We hypothesized that a general-purpose hyperpolarized gas network would successfully segment and register both ^{3}He and ^{129}Xe images, and that the resulting segmentations would exhibit high Dice similarity coefficients (DSC).

B.2 Materials and Methods

B.2.1 Study Participants

Participants from five prior studies were retrospectively combined to maximize the number of available training images. Source studies for which informed consent was provided to an ethics board approved protocol were compiled including the TINCan cohort[41] of ex-smoker participants and participants with COPD (NCT02279329, NCT02282202), participants with

asthma (NCT02351141), participants with asthma undergoing bronchial thermoplasty (NCT02263794), participants with asthma prior to treatment with Benralizumab (NCT03733535), participants previously infected with COVID-19 (NCT04584671) and healthy volunteers (NCT02483403). Participants with COPD were enrolled based on a clinical diagnosis of COPD, a predicted forced expiratory volume in 1 second (FEV_1) >25% and predicted forced vital capacity (FVC) >25% and >0.5L. Participants with a history of poorly-controlled asthma (asthma control questionnaire ≥1.5) were enrolled between ages 18-70 with smoking history of <1 pack years, >12 months prior treatment with inhaled corticosteroids and a long-acting β2 agonist, predicted FEV_1 <80%, significant bronchodilator reversibility ≥12%, blood eosinophils ≥ 300 cells/μL. Participants with a prior documented COVID-19 infection (by positive COVID-19 test or clinical history) between ages 18 and 80 were enrolled approximately three months post-recovery. Healthy participants between ages 60-90 with a smoking history <0.5 pack-years were also enrolled. Participants in all constituent studies underwent pulmonary function tests, anatomical ^1H MRI and hyperpolarized gas MRI.

B.2.2 Pulmonary Function Tests

Spirometry and plethysmography tests were performed (*MedGraphics Elite Series* plethysmograph MGC Diagnostics Corporation, St. Paul, MN, USA; EasyOne Pro LAB ndd Medizintechnik AG, Zurich, CH) according to American Thoracic Society and European Respiratory Society guidelines.[42-44] FEV_1, forced vital capacity (FVC), residual volume (RV) and total lung volume (TLV) were obtained.

B.2.3 MRI

^{1}H, ^{3}He and ^{129}Xe MRI were acquired using a 3.0T Discovery MR750 scanner (GE Healthcare, WI) with broadband imaging capabilities. Images were acquired between December 2009 and January 2021 in participants in ethics-board approved studies. Gas hyperpolarization was performed using a Helispin hyperpolarizer (Polarean, NC) or Polarean 9820 hyperpolarizer (Polarean, NC). ^{1}H MRI were acquired during participant breath-hold of 1.0L nitrogen (N_2, Spectra Gases NJ) with a whole-body coil and fast spoiled gradient-recalled-echo (FGRE) sequence (TR/TE/flip=4.7ms/1.2ms/30°, field-of-view=40x40cm^{2}, slice thickness=15mm, number of slices=16-18, bandwidth=24.4kHz, matrix=128x80 padded to 128x128, partial echo=62.5%). ^{3}He MRI were acquired during participant breath-hold of 1.0L of a 40%/60% $3He/N_2$ mixture using a FGRE sequence (TE/TR/flip=3.8ms/1.0ms/7°, field-of-view=40x40cm^{2}, slice thickness=15mm, number of slices=16-18 bandwidth=48.8kHz, matrix=128x80 padded to 128x128, partial echo coverage=62.5%). ^{129}Xe were acquired during a participant inhalation of 1.0L 40%/60% $^{129}Xe/^{4}He$ gas using a coronal plane 3D FGRE sequence (TR/TE/flip=5.1ms/1.5ms/1.3^{o}, field-of-view=40x40x24cm^{3}, bandwidth=16kHz, matrix=128x128x16-18).

B.2.4 Data Processing, Annotation and Generation

MR images were reconstructed in Matlab software (version R2019b; Mathworks).A semiautomated segmentation pipeline[4] generated masks of the thoracic cavity, co-registered image sets, and calculate VDP using a seeded region growing segmentation algorithm and landmark based affine registration.

Image data were passed to the neural network using custom Keras data-generators. Image data were loaded sequentially and normalized on the range [0, 1] to prevent the network from

learning based on raw signal intensity. Previously co-registered hyperpolarized gas data were transformed according to a random transformation composed of scaling, shifting and rotation. The range of random values used were set to ±15º rotation, ±10% scaling, and ±13 pixels translation (10% of image width/height). Randomly generated translation, scaling and rotation matrices were multiplied together to produce a single transformation matrix that was normalized and passed to the network for training.

B.2.5 Pipeline and Network Design

The semiautomated pipeline consisted of segmentation and registration components implemented in a custom Matlab script. Hyperpolarized noble gas images were segmented using automated thresholding, then manually adjusted to remove artifacts and remove the trachea from the mask. Three to six landmarks were manually placed on both 1H and gas images and a 2D affine transform was calculated by linear regression on the landmark coordinates. The transform was applied to the gas mask. Next, the gas mask was used as a seed for region growing within the thoracic cavity of the ^{1}H image. The proposed ^{1}H segmentation was manually corrected by a trained observer. K-means clustering classified voxels into five intensity clusters in hyperpolarized gas images. The volume of the lowest intensity cluster and thoracic cavity segmentation volume were used to calculate VDP.

The automated pipeline was constructed in python 3.7.5. Neural networks were constructed with Keras 2.2.4 based on a Tensorflow 2.1.0 backend (Google, Mountainview, CA) and executed on an NVIDIA GTX 1080Ti graphics processing unit (NVidia, Santa Clara, CA).

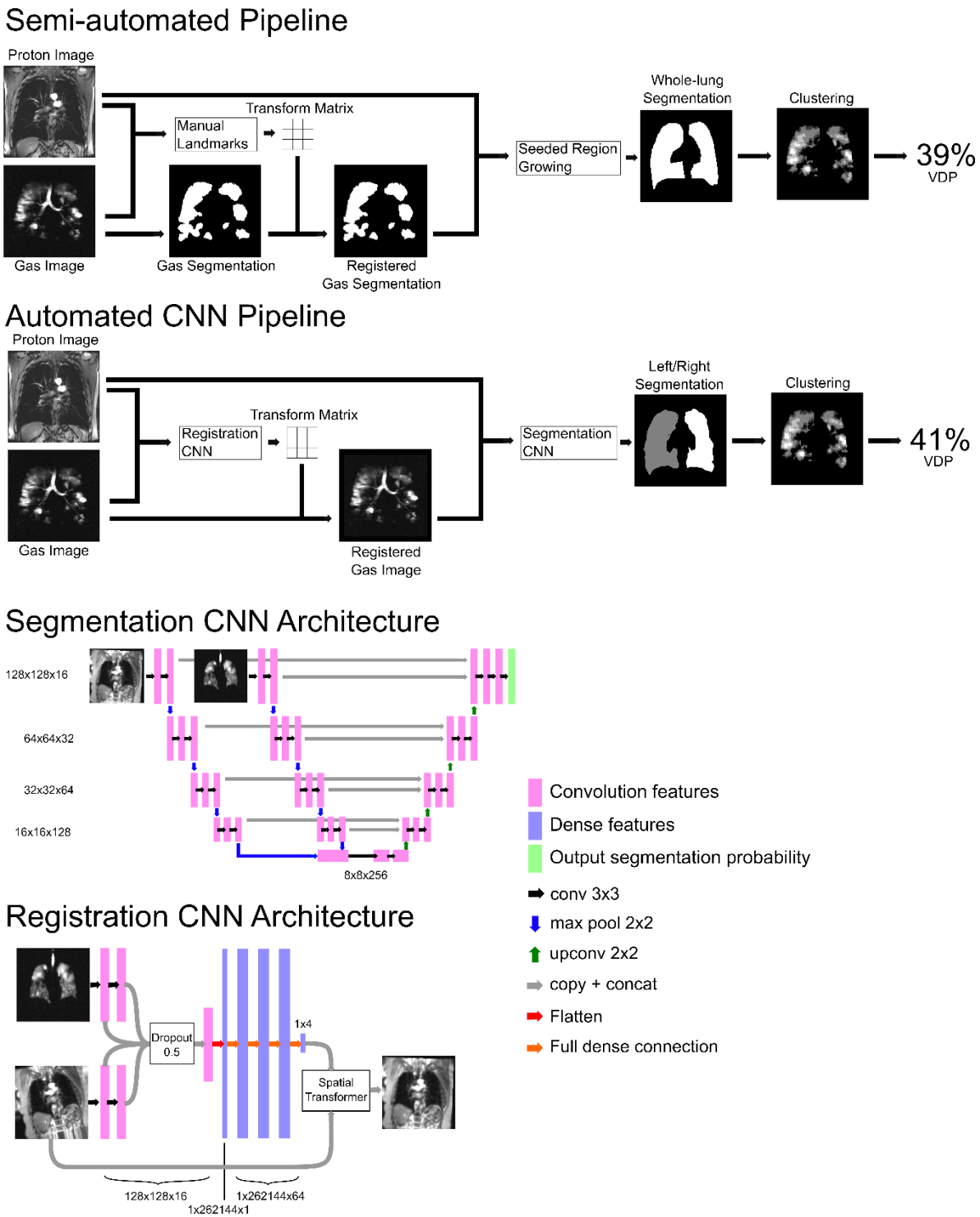

Figure B-1 Ventilation defect percent semi-automated and fully-automated CNN methods.

Figure B-1 illustrates the network architectures for both segmentation and registration networks. Semi-automated pipeline: acquired hyperpolarized gas images are segmented using

automated thresholding and then manually adjusted to remove artifacts and trachea data. Three to six landmarks are manually placed on both ^{1}H and hyperpolarized gas images and a 2D affine transform is calculated by linear regression on the landmark coordinates. The transform is applied to the hyperpolarized gas mask. Next, the gas mask is used as a seed for region growing within the thoracic cavity of the ^{1}H image. The proposed proton segmentation undergoes manual correction from a trained observer. The hyperpolarized gas image undergoes k-means clustering on an intensity basis, classifying voxels into five intensity clusters. The volume of the lowest intensity cluster and thoracic cavity segmentation volume are used to calculate VDP. Fully-automated CNN pipeline: ^{1}H and hyperpolarized gas MRI are input slice-wise into a pre-trained registration CNN that outputs slice-wise affine transform matrices. These transforms are applied to the gas image to generate a new registered image. The ^{1}H image and registered hyperpolarized gas image are input slice-wise to a pre-trained segmentation CNN that outputs a 128x128x3 matrix with channels corresponding to background, left lung and right lung. The hyperpolarized gas image is clustered and VDP calculated using the same procedure as the semi-automated pipeline. Registration CNN architecture: convolution layers extracted low-level ^{1}H and gas features separately, before concatenating and flattening features and passing through a series off fully connected layers. A 1x4 output array of degrees of freedom was subsequently converted to an affine transform matrix and applied to the input ^{1}H image. Segmentation CNN architecture: based on a UNet architecture, convolutional layers extracted features at multiple image scales in separate downsampling feature paths for ^{1}H and gas images. Features were concatenated together to form a single upscale path that output a three-channel output array representing voxel-wise class probability for background, left lung and right lung.

Two dimensional networks were employed instead of three-dimensional networks due to the low resolution along the sagittal axis. The segmentation was based on a U-net architecture[29] subdivided into block units comprised of three convolutional layers followed by a max-pooling layer to form encoding blocks, and up-sampling, concatenation, and three convolutional layers to form decoding blocks. Separate ^{1}H and hyperpolarized gas features were extracted in down-sampling layers and merged into a single up-sampling layer. All convolutions, pooling and sampling operations used 3x3 kernels with stride=1 and a rectified linear unit (ReLU) activation function. A final convolution layer used a softmax function to generate class probability maps on the range 0 to 1. Both networks were compiled using Adam optimization[45]. The segmentation network output was evaluated using a loss function consisting of DSC and categorical cross-entropy:

$$\mathcal{L} = \mathcal{L}_{DSC} + \mathcal{L}_{CCE}$$

Since DSC is defined for an overlap of two binary images, a generalized DSC (gDSC) was used to account for overlap between multiple binary channels.[46]

$$gDSC = 1 - 2\,\frac{\sum_{m=1}^{3} w_m \sum_n r_{mn} p_{mn}}{\sum_{m=1}^{3} w_m \sum_n r_{mn} + p_{mn}}$$

where a weighting term is introduced to correct for volume differences between classes.

$$w_m = \frac{1}{\left(\sum_{n=1}^{N} r_{mn}\right)^2}$$

Categorical cross-entropy was defined as:

$$CCE = -\sum_{m=1}^{3} \sum_n r_m \log p_m$$

The registration network used a combination of convolutional layers and fully-connected layers as depicted in **Figure B-1**. Convolutional layers generated low-level features for each nucleus which were input into fully connected layers to relate low level features across the entire image. The network output a 1x4 array representing four degrees of freedom: rotation, scaling, x-translation and y-translation. The four-degree representation was chosen opposed to a transformation matrix to prevent the network from over-fitting to redundant matrix elements. A custom Tensorflow layer converted the degrees of freedom into the corresponding transform matrix, then passed the matrix to a spatial transformer layer[47] to generate a transformed output. Registration network loss was calculated by a loss function composed of mean absolute error (MAE) of the degrees of freedom and the structural similarity index measure (SSIM) of the proposed proton image.

$$\mathcal{L} = \mathcal{L}_{MAE} + \mathcal{L}_{SSIM}$$

MAE was calculated by:

$$MAE = \frac{1}{N}\sum_{n=1}^{N}|r_n - p_n|$$

where r_n denotes the ground-truth data, p_n the predicted data, and N the number of data points. SSIM was calculated by:

$$SSIM = \frac{\left(2\mu_r\mu_p + (0.01L)^2\right)\left(\sigma_{rp} + (0.03L)^2\right)}{\left(\mu_r^2 + \mu_p^2 + (0.01L)^2\right)\left(\sigma_r^2 + \sigma_p^2 + (0.03L)^2\right)}$$

where μ is image mean, σ_r variance, σ_{rp} the covariance and L the dynamic range of image pixels.

B.2.6 Training, Validation and Testing

Training was performed with input batches of 16 ^{1}H / hyperpolarized gas slice pairs. Registration data sets were randomly transformed at the time of batch creation. Network validation occurred at epoch-end. The network was trained five epochs at a time until validation loss diverged from training loss and subsequently plateaued. Testing data sets input to trained networks for statistical analyses.

B.2.7 External Validation

Data were compiled from two external sites (site 2: McMaster University, site 3: University of British Columbia) for validation of the network. Participants at site 2 provided written, informed consent to an ethics board approved protocol for participants recovering from COVID-19 infection (NCT04584671), or for development of utilities in ^{129}Xe MRI in healthy volunteers and participants with lung disease (NCT03455686). Participants at site 3 provided written informed consent to an ethics-board approved protocol for an observational cohort imaging registry (NCT05102825). Data for both sites were acquired using a Discovery MR750 3.0T scanner (General Electric Health Care; Milwaukee WI) with a rigid quadrature-asymmetric bird-cage coil at site 2 and a flexible vest quadrature coil at site 3. All sites used the same pulse sequence software, described above. Polarizer systems (site 2: Polarean 9800, site 3: Polarean 9820) were used to polarize isotopically enriched ^{129}Xe gas (site 2: 500mL, site 3: 400mL) for static ventilation imaging and mixed in 1.0L Tedlar bags (site 2: $^{129}Xe/N_2$ mixture, site 3: $^{129}Xe/^{4}He$ mixture). Anatomical ^{1}H images were acquired using the built-in MRI whole-body radiofrequency coil using the same ^{1}H FGRE sequence described above. Functional ^{129}Xe images were acquired using the same ^{129}Xe 3D FGRE sequence described above.

Image registration and segmentation were performed using semi-automated software pipelines based on previously described software[4] and performed by a trained observer. Raw data, registered data, segmented data, and ventilation defect measurements were supplied to compare to neural network output. Raw data were split into slices, padded to 17-slice thickness and supplied to the registration and segmentation networks successively. Networks were configured with weights from the optimal epoch of fold 1 for both registration and segmentation. Registration was applied to center slices (slices 5-9) and the transforms for each participant was averaged and applied to all slices to ensure a consistent affine transform for the whole-lung dataset. Output segmentations were used to calculate DSC for neural network outputs compared to semiautomated outputs and to calculate VDP.

B.2.8 Statistical Analysis

Statistical tests were performed using SPSS software (IBM; Armonk, NY). Between-groups differences were evaluated using independent-samples t-tests. Relationships between variables were evaluated using linear regression. Bland-Altman tests were performed to evaluate the agreement between semi-automated and fully-automated analysis pipelines. Tests were reported as significantly significant at a significance level of $p<.05$.

B.3 Results

B.3.1 Participant Demographics

Table B-1 Participant demographics, pulmonary function tests and imaging measurements.

	All (n=305)	Healthy (n=51)	Asthma (n=47)	COPD (n=179)	COVID-19 (n=28)
Demographics					
Age (yrs)	66 (12)	73 (6)	54 (14)	69 (9)	57 (12)
Female n (%)	141 (46)	25 (51)	29 (62)	72 (40)	15 (54)
BMI	28 (5)	27 (4)	29 (5)	28 (5)	32 (6)
PFT					
FEV_1 ($\%_{pred}$)	81 (29)	106 (19)	69 (25)	76 (29)	87 (22)
FEV_1 / FVC (%)	67 (17)	77 (6)	67 (17)	63 (19)	77 (11)
RV ($\%_{pred}$)	129 (46)	109 (27)	134 (52)	137 (47)	95 (22)
RV/TLV ($\%_{pred}$)	45 (12)	41 (8)	42 (14)	47 (11)	38 (12)
Imaging					
^{129}Xe MRI n (%)	95 (31)	0 (0)	45 (100)	22 (12)	28 (100)
^{3}He MRI n (%)	210 (69)	52 (100)	0 (0)	157 (88)	0 (0)
^{3}He VDP	11 (10)	9 (9)	-	15 (10)	-
^{129}Xe VDP	14 (11)	-	9 (8)	22 (16)	11 (15)

Values reported as mean (standard deviation). BMI = body mass index, PFT = pulmonary function tests, FEV_1 = forced expiratory volume in 1 second, FVC = functional vital capacity, RV = residual volume, TLV = total lung volume, VDP = ventilation defect percent

Participant demographics, pulmonary function test results, and imaging measurements are provided in **Table B-1** for all participants (n=305), and by participant groups: asthma (n=47), COPD (n=179), post-COVID-19 (n=28) and healthy participants (n=51). External validation datasets included post- COVID-19 (site 2: n=13, site 3: n=22) and healthy participants (site 2: n=24, site 3: n=10).

B.3.2 Model Training and Network Parameters

Segmentation training was performed over 120 epochs with model weights saved after every epoch. Segmentation validation loss was observed to plateau after approximately 40 epochs for segmentation and 80 epochs for registration, while training loss continued to decline. All folds performed similarly, with an average final DSC plus cross-entropy training loss of 0.12.

Registration training was performed by the same principle and training was stopped after 80 epochs. A final MAE+SSIM training loss of 0.55 was calculated.

B.3.3 Deep Learning Registration

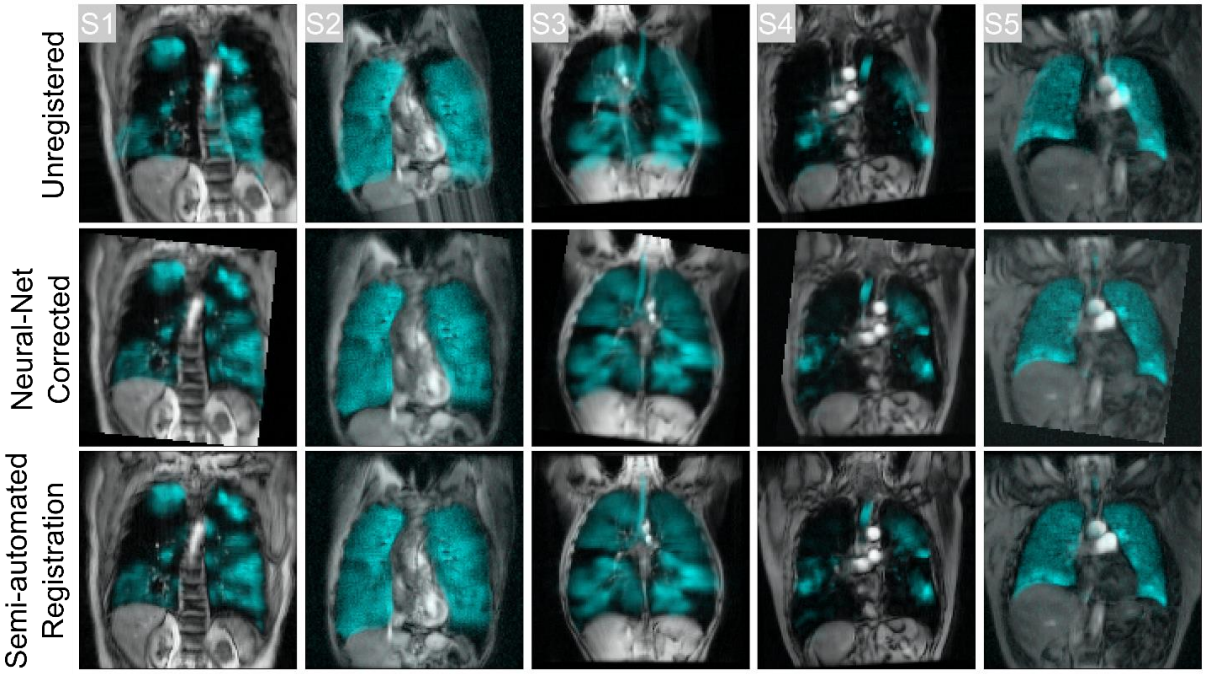

Figure B-2 Demonstration of neural-net registration compared to ground truth registration. Top row: un-registered gas images overlaid on ^{1}H images. Images underwent random translation, rotation and scaling and were further degraded with Gaussian noise. Middle row: registration performed by neural-network successfully aligned the gas images with the thoracic cavity. Bottom row: ground truth registration previously obtained through semi-automated, landmark-based registration. S1: ^{3}He image of healthy participant, S2: ^{3}He image of participant with asthma, S3: ^{129}Xe image of participant with asthma, S4: ^{129}Xe image of participant with COPD, S5: ^{129}Xe image of participant following COVID-19 recovery.

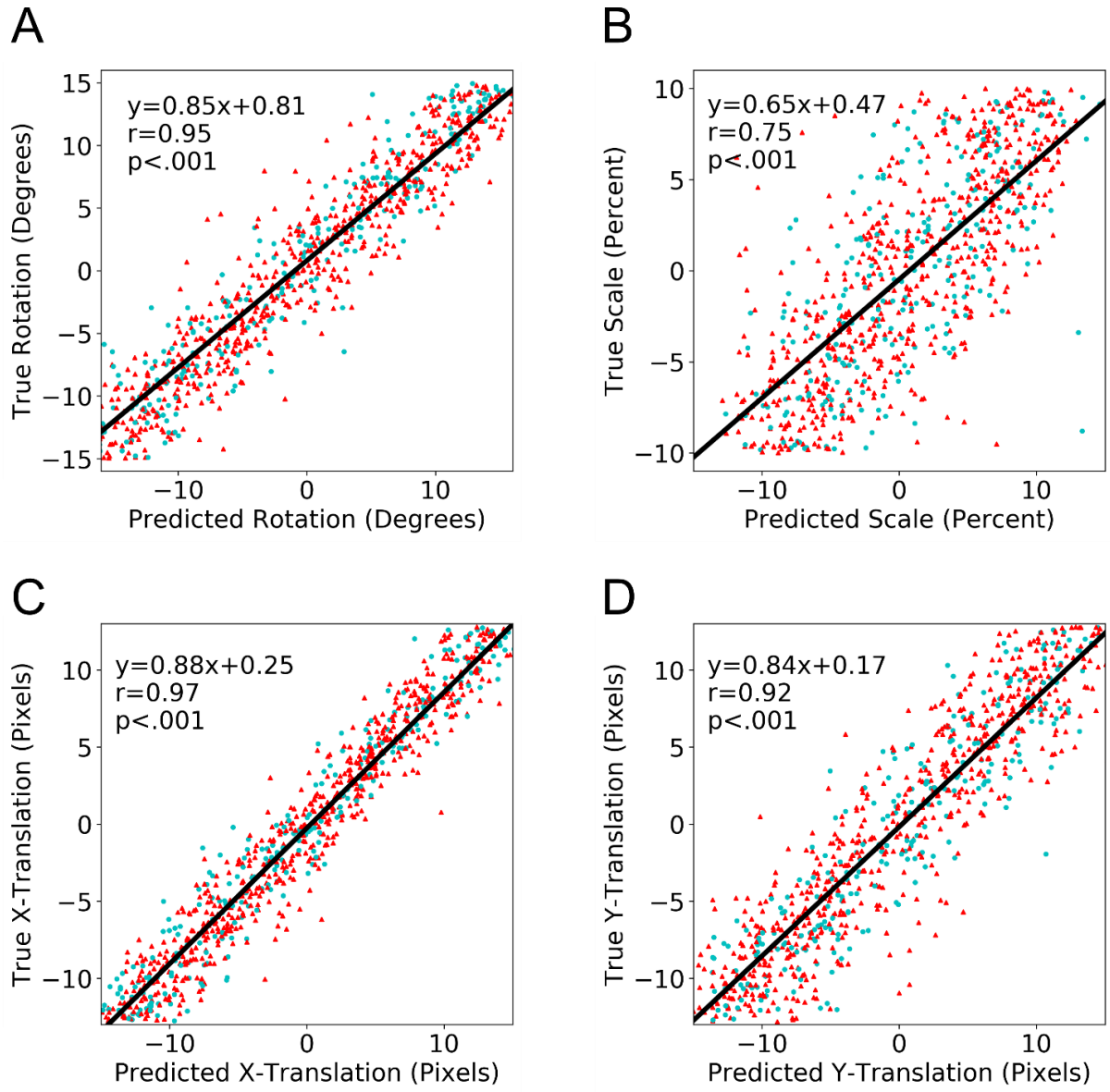

Figure B-3 Performance of registration neural network on affine degrees of freedom. Correlation metrics were calculated for each of rotation (A), scaling (B) as percent scaled (e.g. +10% corresponds to an image 10% larger than in the ground truth), x-translation (C) and y-translation (D). Red points: ^{3}He measurements, cyan points: ^{129}Xe points.

Figure B-2 shows the results of the deep learning registration network on testing data. Qualitatively, registration demonstrated good agreement with the original semi-automated registration, with the margins of the gas images aligned to the thoracic cavity. Central slices

exhibited better registration compared to anterior and posterior slices. **Table B-2** shows quantitative results of the registration. Xenon images had a significantly diminished MAE for rotation (p=.03) and x-translation (p=.003), however there were no significant differences in MAE scaling (p=.21) and y-translation (p=.42) did not perform significantly different. X-translation was the parameter most accurately predicted by the neural network. **Figure B-3** shows correlations between generated and predicted transform parameters. Rotation and translation parameters correlated strongly with the generated values (rotation R^2=.95, x-translation R^2=0.96, y-translation R^2=0.92) however scaling correlated less strongly (R^2=0.79).

Table B-2 Performance of segmentation and registration neural networks on testing data

	All (n=305)	Healthy (n=51)	Asthma (n=47)	COPD (x=179)	COVID-19 (n=28)	Helium (n=210)	Xenon (n=95)
Segmentation performance (DSC):							
Whole-lung	0.93	0.94	0.90	0.94	0.89	0.95	0.92
Left lung	0.93	0.94	0.91	0.94	0.89	0.95	0.92
Right lung	0.93	0.94	0.90	0.94	0.89	0.94	0.91
Registration mean absolute error:							
Rotation (degrees)	2.4	2.4	2.5	2.4	2.1	2.4	2.4
Scale (%)	3.4	3.3	3.1	3.3	4.6	3.3	3.6
X-Translation (px)	1.6	1.7	1.6	1.6	1.7	1.6	1.6
Y-Translation (px)	2.4	2.7	2.7	2.3	1.9	2.4	2.5

DSC=Dice similarity coefficient, px=pixels

B.3.4 Deep Learning Segmentation

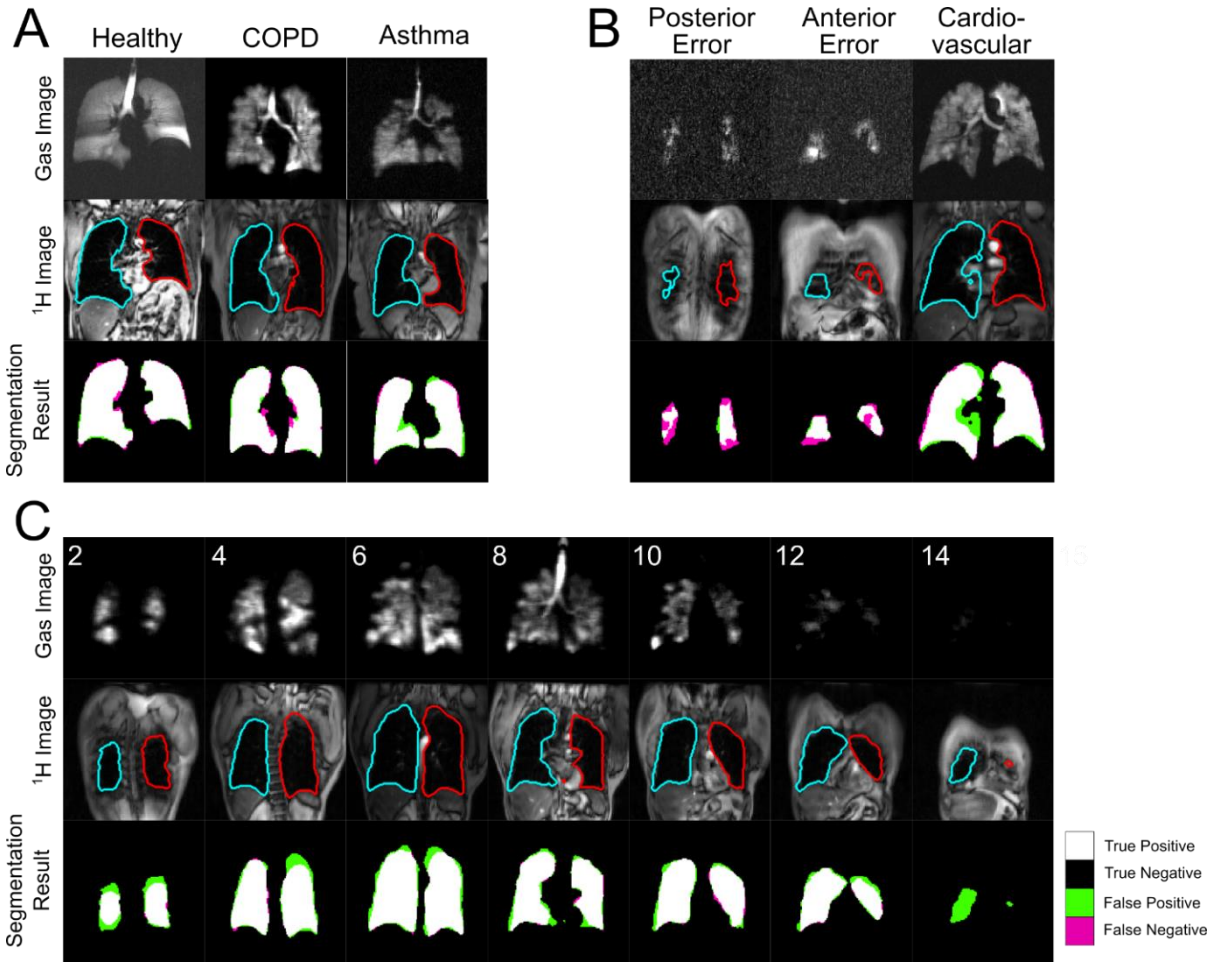

Figure B-4 Segmentation CNN output.
Top rows: acquired hyperpolarized gas image; Middle rows: acquired ^{1}H MRI with CNN prediction of left (red) and right (blue) lung overlaid; Bottom rows: comparison between predicted and ground truth segmentation depicting true positive (white), true negative (black), false positive (lime) and false negative (pink) voxels. A: representative center slices for individuals of varying health, including a healthy participant, a participant with COPD, and a participant with asthma. B: common errors produced by the segmentation CNN. Both posterior and anterior slices exhibit jagged segmentation boundaries compared to ground truth. In cases of conflict between ^{1}H and gas images, the CNN has difficulty matching ground-truth segmentations near the heart and major vessels. C: Representative participant (with asthma) imaged with ^{129}Xe MRI showing segmentation performance across posterior to anterior slices.

Figure B-4 shows the qualitative results of the segmentation network. **Table B-2** shows the quantitative results of the segmentation network across different disease states and nuclei of interest. Overall qualitative agreement was very good (whole-lung gDSC=0.93±0.03) between

ground-truth and neural-network segmentations across diseases states and for both ^{3}He and ^{129}Xe. There were no significant differences in overlap between left and right lungs (p=.096). Overlap was significantly higher in ^{3}He images (gDSC=0.95±0.02) than in ^{129}Xe images (gDSC=0.90±0.06, p=.006).

Different types of segmentation error occurred in different slices. As **Figure B-4** shows, anterior and posterior slices (slices 1-4 and slices 12-16) exhibited worse overlap than more central slices. An exception to this was for slice 17, which exactly matched predictions of no thoracic cavity present across all images. Figure 3B shows representative images of overlap problems in anterior and posterior slices. Although there was generally good agreement between central slices, occasional images demonstrated disagreement around the mediastinum, especially near the bronchi and major pulmonary vessels, also shown in 3B. Figure 3C shows segmentation performance across even-numbered slices from posterior to anterior for a representative participant with asthma, demonstrating good agreement across slices, with weaker performance at the extreme anterior and posterior slices.

B.3.5 Inter-method Correlation and Agreement

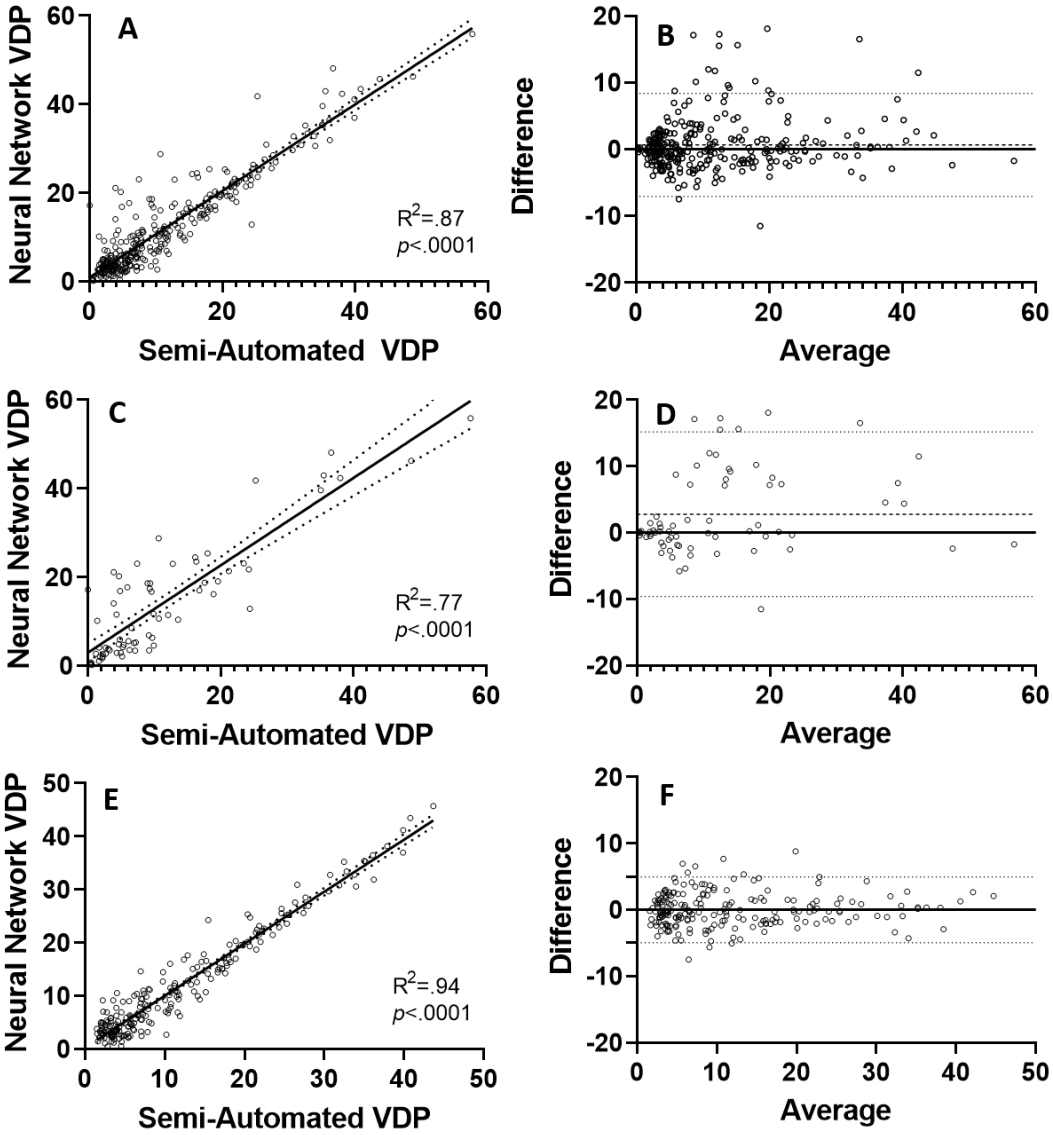

Figure B-5 Comparison between semi-automated ventilation measurements and fully-automated CNN ventilation measurements.

Data were merged from all five folds due to similar network performance. Graphs show correlation between VDP calculated by semi-automated pipeline and by neural network. A: correlation for all data points (R^2=.87, p<.0001, slope=0.98, intercept=1) C: correlation for ^{129}Xe data (R^2=.77, p<.0001, slope=0.99, intercept=3) E: correlation for ^{3}He data (R^2=0.94, p<.0001, slope=0.98, intercept=0). Bland-Altman plots show agreement between semi-automated VDP and neural network VDP. B: Bland-Altman analysis for all data points (bias=0.66, upper limit=8.4, lower limit=-7.1) D: Bland-Altman analysis for ^{129}Xe data (bias=2.8, upper limit=15.2, lower limit=-9.6) F: Bland-Altman analysis for ^{3}He data (bias=0.01, upper limit=5.0, lower limit = -4.9). Dotted lines indicate the 95% confidence intervals. Dashed lines indicate bias values.

B.3.6 External Validation

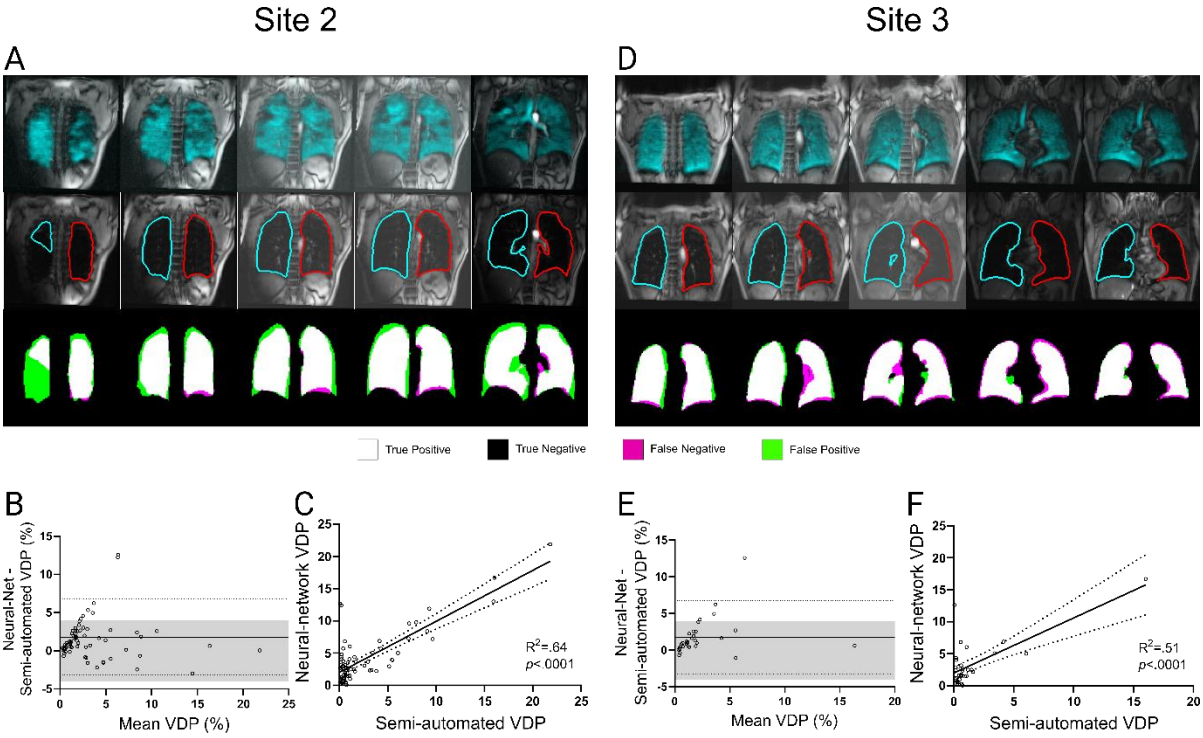

Figure B-6 Performance of neural networks in external data sets.
Data from two external sites were processed using the final epochs of fold 1 versions of neural networks. Network output demonstrated agreement with external semi-automated results. A: neural network segmentation results visualized for site 2. Top row: overlap of hyperpolarized gas and proton images following network registration, middle: network proposed segmentation, bottom: comparison between neural network and external semi-automate segmentation depicting true positive (white), true negative (black), false positive (lime) and false negative (pink) voxels. B: Bland-Altman analysis for Site 2 (bias=1.2%, upper limit=6.4, lower limit=-3.9) C: correlation between VDP calculated using neural network registration and segmentation versus semi-automated external processing for site 2 (R^2=.64, p<.001, slope=0.77, intercept=2.03) D: neural network segmentation results visualized for site 3. E: Bland-Altman analysis for site 3(bias=-0.99, upper limit=4.79, lower limit=-6.77) C and University of British Columbia (R^2=.38, p<.0002, slope=0.16, intercept=0.68).

Figure B-5 demonstrates relationships between semi-automated and neural-network based VDP measurements across participants for all five folds. A strong and significant (R^2=.87, p<.001) correlation was observed between VDP calculated by semi-automated and neural network methods. Bland-Altman plots likewise indicated good agreement between methods (bias=0.66%, 95% confidence interval=-7.1 to 8.4). Correlation was stronger between methods for ^{3}He data (R^2=.94, p<.001) than for ^{129}Xe data (R^2=.77, p<.001). ^{3}He also demonstrated

better agreement according to Bland-Altman plots (bias=0.01%, 95% confidence interval=-4.9 to 5.0) than ^{129}Xe, with ^{129}Xe over-estimating VDP (bias=2.8%, 95% confidence interval=-9.6 to 15.2).

Figure B-6 shows qualitative and quantitative evaluations of neural-network performance on external data sets. Registration was successful at aligning hyperpolarized gas and ^{1}H images. While site 2 images were nearly perfectly aligned prior to registration, site 3 images were poorly aligned prior to registration and demonstrated the rigorous performance of the network. The segmentation network successfully identified left and right lungs, although false positive islands within the trachea were more common than in site 1 segmentations. Segmentation results were incorrect in the rare cases where registration failed. Bland-Altman analysis showed good agreement between VDP calculated from neural network segmentations compared to semiautomated VDP (site 2 bias=1.2%, CI=-3.9 to 6.4; site 3 bias=1.8%, CI=-3.2 to 6.8). VDP calculated by neural nets strongly correlated with semi-automated calculations (site 2 R^2=.64, p<.001; site 3 R^2=.51 p<.001).

B.4 Discussion

To address limitations of semi-automated hyperpolarized gas image processing, we developed a neural network pipeline for hyperpolarized gas analysis. Hyperpolarized gas metrics can vary strongly depending on disease state, nuclei of interest, gas polarization, participant anatomy and acquisition hardware, therefore the development of robust analysis tools is necessary as hyperpolarized gas research centres become more common and scan volume increases. Unlike prior approaches that sought to approximate the diverse participant population through data annotation techniques,[33] here we combined ^{3}He and ^{129}Xe datasets under the assumption that similar contrast mechanisms would allow similar imaging features to power a neural network.

Here we reported differences between performance of ^{3}He and ^{129}Xe images processed by the network, however these differences were minor and likely related to the over-representation of ^{3}He in the dataset. Furthermore, we reported the novel finding that networks could be trained to register images from different nuclei of interest (hyperpolarized gas nuclei and ^{1}H) together. Here, we determined that a semi-supervised approach of randomly generating transforms was sufficient to train a registration network that performed well at real-world registration tasks. Finally, we demonstrated that while some performance loss occurred, these results were generalizable across multiple sites, including differences in MR coils and gas dose.

Transform parameters determined by the neural network were strongly correlated and in agreement with randomly generated, provided transforms. The x-transform parameter had a lower error than the y-transform parameter, possibly due to poor registration in the y-direction in cases where training participants inhaled to different lung volumes. In some training data the border of the gas region extended below the diaphragm due to different inhalation levels even when the rest of the gas was in alignment with the thoracic cavity in ^{1}H images. The scaling parameter showed a worse correlation than other transform parameters. Scaling was underestimated, whether the image was grown or shrunk, indicating a preference for the network to not drastically change the size. Additional sources of error may have been introduced in acquisition. Heart motion during acquisition may result in different lung/heart boundary shapes between hyperpolarized gas and ^{1}H acquisitions. Additionally, relatively thick slices (15mm) relative to the in-plane resolution of 3x3mm^{2} makes registration especially difficult if slices are not aligned in the anterior-posterior axis.

Segmentation performance also demonstrated strong overall agreement between neural network performance and semi-automated performance. There was no difference in

performance between left and right lungs. Performance differences were noticed, however, between different disease states. This can be attributed to the different distribution of ^{3}He and ^{129}Xe images in each of the disease subgroups. For instance, COPD segmentations exhibited closer overlap than COVID-19, however the COPD group was dominated by ^{3}He whereas COVID-19 images were acquired exclusively with ^{129}Xe. Segmentation performance was also slice-dependent, with anterior and poster slices demonstrating poor DSC. These slices are notoriously challenging even for trained observers due to partial volume effects. The network may have had similar challenges, or may have learned these challenges if anterior and posterior slices were inconsistent between readers in the training dataset. In addition, the small size of segmented regions in these slices may contribute to poor dice score, as a 25mL error in an anterior slice is a far greater share of the total segmentation than in a central slice. Previous research[48] has shown that most crucial information from hyperpolarized gas images is in the central slices, therefore these errors are of minor consequence.

Performance differences between ^{3}He and ^{129}Xe MRI registration were observed with significantly better registration performance in ^{129}Xe for rotation and translation. While it was encouraging to see improved performance in the ^{129}Xe images, the differences on average were still less than one pixel, indicating a negligible impact on overall performance. In contrast, ^{3}He exhibited better segmentation performance than ^{129}Xe. This was likely due to the increased availability of ^{3}He data in the training set. Differences in performance between different disease states are likely dominated by the proportion of ^{3}He in the data sets. Healthy and COPD data were predominantly acquired with ^{3}He, whereas asthma and COVID-19 data were entirely ^{129}Xe.

In order to determine the impact of image processing software on clinically-relevant VDP measurements, VDP was calculated for images in the testing cohort. A strong (r=.93) correlation was observed across all data. Likely due to differences in ^{3}He versus ^{129}Xe segmentation, a stronger correlation was observed in ^{3}He (r=.97) versus ^{129}Xe (r=.88). Bland-Altman plots showed negligible bias for the complete data set (0.01%) and ^{3}He data (0.66%) while ^{129}Xe neural network results overestimated VDP (bias=2.8%). Previous research[49] has identified a minimum clinically important difference (MCID) of 2-4% based on ^{3}He VDP in asthma. The observed ±5% confidence interval for ^{3}He agreement therefore nearly aligns with the ^{3}He MCID. The ^{129}Xe confidence interval of -9.6% to 15.2% is larger than the derived ^{3}He MCID. Given the reduced VDP measured by ^{3}He versus ^{129}Xe in participants,[8,50,51] a greater MCID may be expected, however to what extent this aligns with the confidence interval is uncertain.

External validation demonstrated moderate correlation and strong agreement across the two sites. Sites demonstrated different challenges to VDP calculation. Site 2 ^{1}H images demonstrated a field inhomogeneity that caused substantial darkening of the lower right image quadrant (visible in **Figure B-6**). Site 3 images were dramatically mis-aligned when compared to images from sites 1 and 2. There was a weaker correlation between neural-network and segmentation VDP in the external data, likely due to these differences. In addition, external datasets were biased to lower VDP due to having an increased ratio of healthy participants relative to site 1. Regardless, the robust performance of the network versus external data was encouraging given differences between sites that the networks were not trained to address including acquisition differences and more dramatic mis-alignment of the acquired data.

There are lingering limitations to the pipeline presented in this work. Training data included static ventilation images and FGRE proton images, as these have been standard for ventilation imaging. Recent developments in dissolved-phase imaging and UTE ^{1}H MRI will make these image types more prevalent, and the network is not optimized for their use. Some form of transfer learning may be able to overcome this once data is plentiful enough to create a stand-alone training set. The unbalanced data in this training set are a further limitation. Given that the dataset was primarily composed of COPD and asthma data, the network may have a preferential bias to these states and data in diseases such as cystic fibrosis were not available at the sites investigated. External data in this study considered a variety of polarization and RF hardware, but the effect of different vendors and field strengths was not investigated. The choice to implement 2 dimensional networks was ideal given low z-resolution, however this approach fails to leverage relevant information from neighbouring slices. This is especially pertinent for registration networks, as a 3D transformation system includes additional parameters such as axial rotation that may better describe a transform than the four degrees of freedom used here.

B.5 Conclusions

In conclusion, we developed a fully-automated neural network pipeline to perform affine registration and joint segmentation in combined ^{1}H and hyperpolarized noble gas datasets to generate clinically-relevant biomarkers of pulmonary health. These neural networks are robust to differences in disease state, hardware, and nuclei of interest and exhibited strong correlation and agreement with existing semi-automated methods. Like the preceding semi-automated tools, we anticipate that this network pipeline will enable even faster processing of data for

increasingly large ^{129}Xe MRI studies and will provide added standardization to multi-site clinical trials.

B.6 References

1. Altes TA, Powers PL, Knight-Scott J, Rakes G, Platts-Mills TA, de Lange EE, et al. Hyperpolarized ^{3}He MR Lung Ventilation Imaging in Asthmatics: Preliminary Findings. J Magn Reson Imaging. 2001;13:378-84.

2. Parraga G, Ouriadov A, Evans A, McKay S, Lam WW, Fenster A, et al. Hyperpolarized 3He Ventilation Defects and Apparent Diffusion Coefficients in Chronic Obstructive Pulmonary Disease. Investigative Radiology. 2007;42(6):384-91.

3. Donnelly LF, MacFall JR, McAdams HP, Majure JM, Smith J, Frush DP, et al. Cystic fibrosis: combined hyperpolarized 3He-enhanced and conventional proton MR imaging in the lung--preliminary observations. Radiology. 1999;212(3):885-9.

4. Kirby M, Heydarian M, Svenningsen S, Wheatley A, McCormack DG, Etemad-Rezai R, et al. Hyperpolarized 3He magnetic resonance functional imaging semiautomated segmentation. Acad Radiol. 2012;19(2):141-52.

5. Costella S, Kirby M, Maksym GN, McCormack DG, Paterson NA, Parraga G. Regional pulmonary response to a methacholine challenge using hyperpolarized (3)He magnetic resonance imaging. Respirology. 2012;17(8):1237-46.

6. de Lange EE, Altes TA, Patrie JT, Gaare JD, Knake JJ, Mugler JP, 3rd, et al. Evaluation of asthma with hyperpolarized helium-3 MRI: correlation with clinical severity and spirometry. Chest. 2006;130(4):1055-62.

7. Qing K, Mugler JP, 3rd, Altes TA, Jiang Y, Mata JF, Miller GW, et al. Assessment of lung function in asthma and COPD using hyperpolarized 129Xe chemical shift saturation recovery spectroscopy and dissolved-phase MRI. NMR Biomed. 2014;27(12):1490-501.

8. Svenningsen S, Kirby M, Starr D, Leary D, Wheatley A, Maksym GN, et al. Hyperpolarized (3) He and (129) Xe MRI: differences in asthma before bronchodilation. J Magn Reson Imaging. 2013;38(6):1521-30.

9. Svenningsen S, Eddy RL, Kjarsgaard M, Parraga G, Nair P. Effects of Anti-T2 Biologic Treatment on Lung Ventilation Evaluated by MRI in Adults With Prednisone-Dependent Asthma. Chest. 2020;158(4):1350-60.

10. Horn FC, Marshall H, Collier GJ, Kay R, Siddiqui S, Brightling CE, et al. Regional Ventilation Changes in the Lung: Treatment Response Mapping by Using Hyperpolarized Gas MR Imaging as a Quantitative Biomarker. Radiology. 2017;284(3):854-61.

11. Salerno M, de Lange EE, Altes TA, Truwit JD, Brookeman JR, Mugler JP, 3rd. Emphysema: hyperpolarized helium 3 diffusion MR imaging of the lungs compared with spirometric indexes--initial experience. Radiology. 2002;222(1):252-60.

12. Spector ZZ, Emami K, Fischer MC, Zhu J, Ishii M, Vahdat V, et al. Quantitative assessment of emphysema using hyperpolarized 3He magnetic resonance imaging. Magn Reson Med. 2005;53(6):1341-6.

13. Swift AJ, Wild JM, Fichele S, Woodhouse N, Fleming S, Waterhouse J, et al. Emphysematous changes and normal variation in smokers and COPD patients using diffusion 3He MRI. Eur J Radiol. 2005;54(3):352-8.

14. Kaushik SS, Cleveland ZI, Cofer GP, Metz G, Beaver D, Nouls J, et al. Diffusion-weighted hyperpolarized 129Xe MRI in healthy volunteers and subjects with chronic obstructive pulmonary disease. Magn Reson Med. 2011;65(4):1154-65.

15. Kirby M, Svenningsen S, Owrangi A, Wheatley A, Farag A, Ouriadov A, et al. Hyperpolarized 3He and 129Xe MR Imaging in Healthy Volunteers and Patients with Chronic Obstructive Pulmonary Disease. Radiology. 2012;265(2):600-10.

16. Kirby M, Matthew L, Wheatley A, Santyr G, McCormack DG, Parraga G. Chronic Obstructive Pulmonary Disease: Longitudinal Hyperpolarized 3He MR Imaging. Radiology. 2010;256(1):280-9.

17. Kirby M, Pike D, Sin DD, Coxson HO, McCormack DG, Parraga G. COPD: Do Imaging Measurements of Emphysema and Airway Disease Explain Symptoms and Exercise Capacity? Radiology. 2015;277(3):872-80.

18. Hodge CW, Tomé WA, Fain SB, Bentzen SM, Mehta MP. On the Use of Hyperpolarized Helium MRI for Conformal Avoidance Lung Radiotherapy. Medical Dosimetry. 2010;35(4):297-303.

19. Fox MS, Ouriadov A, Thind K, Hegarty E, Wong E, Hope A, et al. Detection of radiation induced lung injury in rats using dynamic hyperpolarized (129)Xe magnetic resonance spectroscopy. Med Phys. 2014;41(7):072302.

20. Thomen RP, Sheshadri A, Quirk JD, Kozlowski J, Ellison HD, Szczesniak RD, et al. Regional Ventilation Changes in Severe Asthma after Bronchial Thermoplasty with 3He MR Imaging and CT. Radiology. 2014;274(1):250-9.

21. McIntosh MJ, Kooner HK, Eddy RL, Jeimy S, Licskai C, Mackenzie CA, et al. Asthma control, Airway mucus and (129)Xe MRI ventilation after a single Benralizumab dose. Chest. 2022.

22. Sun Y, O'Sullivan BP, Roche JP, Walvick R, Reno A, Baker D, et al. Using hyperpolarized 3He MRI to evaluate treatment efficacy in cystic fibrosis patients. J Magn Reson Imaging. 2011;34(5):1206-11.

23. McMahon CJ, Dodd JD, Hill C, Woodhouse N, Wild JM, Fichele S, et al. Hyperpolarized 3helium magnetic resonance ventilation imaging of the lung in cystic fibrosis: comparison with high resolution CT and spirometry. Eur Radiol. 2006;16(11):2483-90.

24. Woodhouse N, Wild JM, Paley MN, Fichele S, Said Z, Swift AJ, et al. Combined helium-3/proton magnetic resonance imaging measurement of ventilated lung volumes in smokers compared to never-smokers. J Magn Reson Imaging. 2005;21(4):365-9.

25. He M, Kaushik SS, Robertson SH, Freeman MS, Virgincar RS, McAdams HP, et al. Extending semiautomatic ventilation defect analysis for hyperpolarized (129)Xe ventilation MRI. Acad Radiol. 2014;21(12):1530-41.

26. Svenningsen S, McIntosh M, Ouriadov A, Matheson AM, Konyer NB, Eddy RL, et al. Reproducibility of Hyperpolarized (129)Xe MRI Ventilation Defect Percent in Severe Asthma to Evaluate Clinical Trial Feasibility. Acad Radiol. 2020.

27. Guo F, Yuan J, Rajchl M, Svenningsen S, Pi Capaldi D, Sheikh K, et al. Globally optimal co-segmentation of three-dimensional pulmonary 1H and hyperpolarized 3He MRI with spatial consistence prior. Medical Image Analysis. 2015;23(1):43-55.

28. Sensakovic WF, Armato SG, 3rd, Starkey A, Caligiuri P. Automated lung segmentation of diseased and artifact-corrupted magnetic resonance sections. Medical physics. 2006;33(9):3085-93.

29. Ronneberger O, Fischer P, Brox T. U-Net: Convolutional Networks for Biomedical Image Segmentation. In: Navab N, Hornegger J, Wells WM, Frangi A, editors. MICCAI 2015; Munich, Germany: Springer, Cham; 2015.

30. Erickson BJ, Korfiatis P, Akkus Z, Kline TL. Machine Learning for Medical Imaging. Radiographics. 2017;37(2):505-15.

31. Zha W, Fain SB, Schiebler ML, Evans MD, Nagle SK, Liu F. Deep convolutional neural networks with multiplane consensus labeling for lung function quantification using UTE proton MRI. J Magn Reson Imaging. 2019;50(4):1169-81.

32. Winther HB, Gutberlet M, Hundt C, Kaireit TF, Alsady TM, Schmidt B, et al. Deep semantic lung segmentation for tracking potential pulmonary perfusion biomarkers in chronic obstructive pulmonary disease (COPD): The multi-ethnic study of atherosclerosis COPD study. J Magn Reson Imaging. 2020;51(2):571-9.

33. Tustison NJ, Avants BB, Lin Z, Feng X, Cullen N, Mata JF, et al. Convolutional Neural Networks with Template-Based Data Augmentation for Functional Lung Image Quantification. Acad Radiol. 2019;26(3):412-23.

34. Oliveira FP, Tavares JM. Medical image registration: a review. Comput Methods Biomech Biomed Engin. 2014;17(2):73-93.

35. Sloan J, Goatman K, Siebert J, editors. Learning Rigid Image Registration - Utilizing Convolutional Neural Networks for Medical Image Registration. BIOIMAGING; 2018.

36. Zhu N, Najafi M, Han B, Hancock S, Hristov D. Feasibility of Image Registration for Ultrasound-Guided Prostate Radiotherapy Based on Similarity Measurement by a Convolutional Neural Network. Technol Cancer Res Treat. 2019;18:1533033818821964.

37. Cheng X, Zhang L, Zheng YF. Deep similarity learning for multimodal medical images. Comp M Bio Bio E-Iv. 2018;6(3):248-52.

38. Kaushik SS, Freeman MS, Cleveland ZI, Davies J, Stiles J, Virgincar RS, et al. Probing the regional distribution of pulmonary gas exchange through single-breath gas- and dissolved-phase 129Xe MR imaging. J Appl Physiol (1985). 2013;115(6):850-60.

39. Kirby M, Svenningsen S, Kanhere N, Owrangi A, Wheatley A, Coxson HO, et al. Pulmonary ventilation visualized using hyperpolarized helium-3 and xenon-129 magnetic resonance imaging: differences in COPD and relationship to emphysema. Journal of Applied Physiology. 2013;114(6):707-15.

40. Shammi U, D'Alessandro M, Altes T, Hersman F, Ruset I, Mugler J, et al. Comparison of Hyperpolarized (He)-H-3 and (Xe)-X-129 Mr Imaging in Cystic Fibrosis Patients. Pediatr Pulm. 2020;55:S212-S.

41. Kirby M, Pike D, McCormack DG, Sin DD, Lam S, Coxson HO, et al. Longitudinal Computed Tomography and Magnetic Resonance Imaging of COPD: Thoracic Imaging Network of Canada (TINCan) Study Objectives. Journal of the COPD Foundation. 2014;1(2):200-11.

42. Miller MR, Hankinson J, Brusasco V, Burgos F, Casaburi R, Coates A, et al. Standardisation of spirometry. Eur Respir J. 2005;26(2):319-38.

43. Wanger J, Clausen JL, Coates A, Pedersen OF, Brusasco V, Burgos F, et al. Standardisation of the measurement of lung volumes. Eur Respir J. 2005;26(3):511-22.

44. Macintyre N, Crapo RO, Viegi G, Johnson DC, van der Grinten CP, Brusasco V, et al. Standardisation of the single-breath determination of carbon monoxide uptake in the lung. Eur Respir J. 2005;26(4):720-35.

45. Kingma DP, J B. Adam: A Method for Stochastic Optimization. 3rd International Conference for Learning Representations; San Diego2015.

46. Sudre CH, Li WQ, Vercauteren T, Ourselin S, Cardoso MJ. Generalised Dice Overlap as a Deep Learning Loss Function for Highly Unbalanced Segmentations. Lect Notes Comput Sc. 2017;10553:240-8.

47. Jaderberg M, Simonyan K, Zisserman A, Kavukcuoglu K. Spatial Transformer Networks. Adv Neur In. 2015;28.

48. Westcott A, Capaldi DPI, McCormack DG, Ward AD, Fenster A, Parraga G. Chronic Obstructive Pulmonary Disease: Thoracic CT Texture Analysis and Machine Learning to Predict Pulmonary Ventilation. Radiology. 2019;293(3):676-84.

49. Eddy RL, Svenningsen S, McCormack DG, Parraga G. What is the minimal clinically important difference for helium-3 magnetic resonance imaging ventilation defects? Eur Respir J. 2018;51(6).

50. Stewart NJ, Chan HF, Hughes PJC, Horn FC, Norquay G, Rao M, et al. Comparison of (3) He and (129) Xe MRI for evaluation of lung microstructure and ventilation at 1.5T. J Magn Reson Imaging. 2018.

51. Kirby M, Svenningsen S, Kanhere N, Owrangi A, Wheatley A, Coxson HO, et al. Pulmonary ventilation visualized using hyperpolarized helium-3 and xenon-129 magnetic resonance imaging: differences in COPD and relationship to emphysema. J Appl Physiol (1985). 2013;114(6):707-15.

Appendix C – Permission for Reproduction of Scientific Articles

Figure 1-4 was published under a Creative Commons 3.0 license: https://en.wikipedia.org/wiki/File:Atrial_septal_defect-tr.png

Figure 1-8 was published under PMC Open Access.

Chapter 3 was published under PMC Open Access. As author of the original article, I do not require permission beyond citing the original source.

Figure 1-10: Permission to reproduce

JOHN WILEY AND SONS LICENSE
TERMS AND CONDITIONS

Jan 23, 2023

This Agreement between Mr. Alexander Matheson ("You") and John Wiley and Sons ("John Wiley and Sons") consists of your license details and the terms and conditions provided by John Wiley and Sons and Copyright Clearance Center.

License Number	5474850807817
License date	Jan 23, 2023
Licensed Content Publisher	John Wiley and Sons
Licensed Content Publication	Journal of Magnetic Resonance Imaging
Licensed Content Title	Clinical Potential of UTE-MRI for Assessing COVID-19: Patient- and Lesion-Based Comparative Analysis
Licensed Content Author	Fei Shan, Zhiyong Zhang, Yuxin Shi, et al
Licensed Content Date	Jun 3, 2020
Licensed Content Volume	52
Licensed Content Issue	2
Licensed Content Pages	10
Type of use	Dissertation/Thesis

Requestor type	University/Academic
Format	Electronic
Portion	Figure/table
Number of figures/tables	1
Will you be translating?	No
Title	Novel 129Xe Magnetic Resonance Imaging and Spectroscopy Measurements of Pulmonary Gas-Exchange
Institution name	University of Western Ontario
Expected presentation date	Apr 2023
Portions	Figure 3
Requestor Location	Mr. Alexander Matheson 1151 Richmond St. N London, ON N6A5B7 Canada Attn: Mr. Alexander Matheson
Publisher Tax ID	EU826007151
Total	0.00 CAD

Terms and Conditions

TERMS AND CONDITIONS

This copyrighted material is owned by or exclusively licensed to John Wiley & Sons, Inc. or one of its group companies (each a"Wiley Company") or handled on behalf of a society with which a Wiley Company has exclusive publishing rights in relation to a particular work (collectively "WILEY"). By clicking "accept" in connection with completing this licensing

Figure 1-11 permission to reproduce

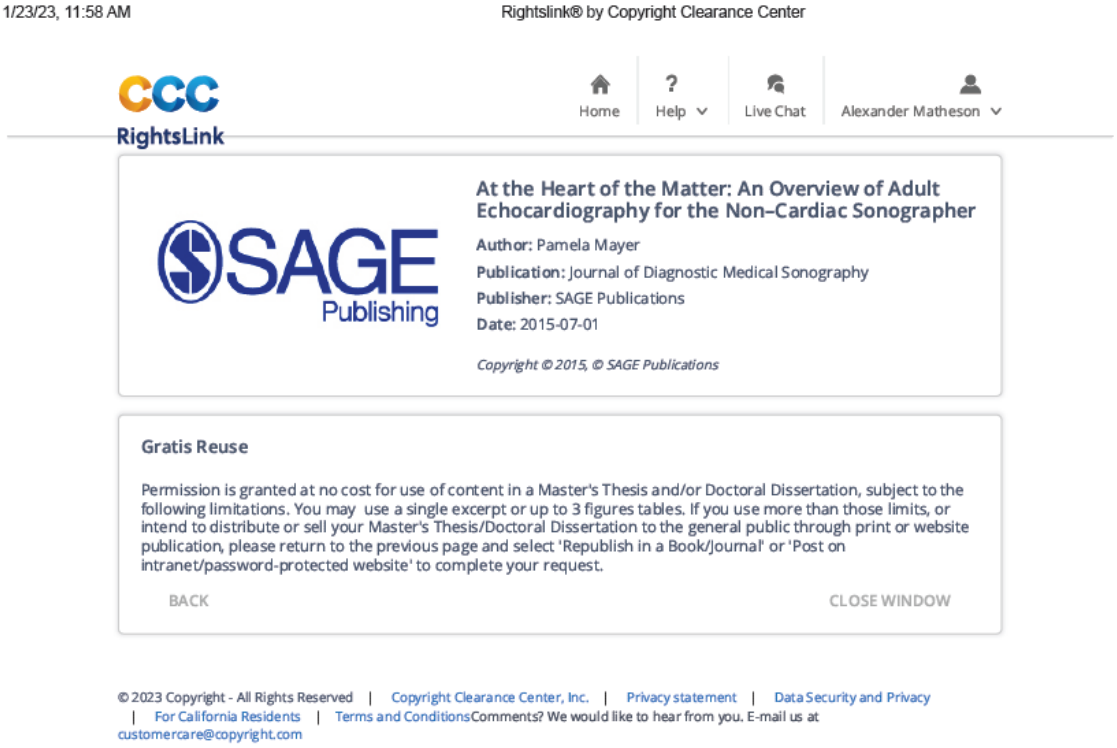

Figure 1-14 Permission to reproduce

ELSEVIER LICENSE
TERMS AND CONDITIONS

Jan 23, 2023

This Agreement between Mr. Alexander Matheson ("You") and Elsevier ("Elsevier") consists of your license details and the terms and conditions provided by Elsevier and Copyright Clearance Center.

License Number	5474860815536
License date	Jan 23, 2023
Licensed Content Publisher	Elsevier
Licensed Content Publication	Elsevier Books
Licensed Content Title	Molecular Imaging
Licensed Content Author	Alexander M. Matheson,Caleb Thompson,Grace Parraga
Licensed Content Date	Jan 1, 2021
Licensed Content Pages	19
Start Page	245
End Page	263
Type of Use	reuse in a thesis/dissertation
Portion	figures/tables/illustrations

Number of figures/tables/illustrations	1
Format	electronic
Are you the author of this Elsevier chapter?	Yes
How many pages did you author in this Elsevier book?	18
Will you be translating?	No
Title	Novel 129Xe Magnetic Resonance Imaging and Spectroscopy Measurements of Pulmonary Gas-Exchange
Institution name	University of Western Ontario
Expected presentation date	Apr 2023
Portions	Figure 14.3
Requestor Location	Mr. Alexander Matheson 1151 Richmond St. N London, ON N6A5B7 Canada Attn: Mr. Alexander Matheson
Publisher Tax ID	GB 494 6272 12
Total	0.00 CAD

Terms and Conditions

INTRODUCTION

1. The publisher for this copyrighted material is Elsevier. By clicking "accept" in connection with completing this licensing transaction, you agree that the following terms and conditions

Chapter 2 copyright was maintained by the authors, as verified below:

Alexander Malcolm Matheson

From: Karleena Burdick <karleenab@spie.org>
Sent: Friday, January 6, 2023 12:19 PM
To: Alexander Malcolm Matheson
Subject: RE: Thesis Reprint Request, Medical Imaging Proceedings

You don't often get email from karleenab@spie.org. Learn why this is important

Dear Alex Matheson,

Thank you for seeking permission from SPIE to reprint material from our publications. SPIE shares the copyright with you, so as author you retain the right to reproduce your paper in part or in whole.

Publisher's permission is hereby granted under the following conditions:
(1) the material to be used has appeared in our publication without credit or acknowledgment to another source; and
(2) you credit the original SPIE publication. Include the authors' names, title of paper, volume title, SPIE volume number, and year of publication in your credit statement.

Please let me know if I may be of any further assistance.

Best,
Karleena Burdick
Editorial Assistant, Publications
SPIE – the international society for optics and photonics
karleenab@spie.org
1 360 685 5515
SPIE.

Chapter 4 Article reproduction permission

BMJ PUBLISHING GROUP LTD. LICENSE
TERMS AND CONDITIONS

Jan 06, 2023

This Agreement between Mr. Alexander Matheson ("You") and BMJ Publishing Group Ltd. ("BMJ Publishing Group Ltd.") consists of your license details and the terms and conditions provided by BMJ Publishing Group Ltd. and Copyright Clearance Center.

License Number	5463080062104
License date	Jan 06, 2023
Licensed Content Publisher	BMJ Publishing Group Ltd.
Licensed Content Publication	Thorax
Licensed Content Title	Longitudinal follow-up of postacute COVID-19 syndrome: DL_{CO}, quality-of-life and MRI pulmonary gas-exchange abnormalities
Licensed Content Author	Alexander M Matheson,Marrissa J McIntosh,Harkiran K Kooner,Mohamed Abdelrazek,Mitchell S Albert,Inderdeep Dhaliwal,J Michael Nicholson,Alexei Ouriadov,Sarah Svenningsen,Grace Parraga
Licensed Content Date	Jan 3, 2023
Type of Use	Dissertation/Thesis
Requestor type	Author of this BMJ article
Format	Electronic
Portion	Figure/table/extract

Number of figure/table/extracts	3
Descriptionof figure/table/extracts	Full text to be used
Will you be translating?	No
Circulation/distribution	250
Title	Pulmonary Gas-exchange Evaluated Using Multi-spectral Hyperpolarized Noble Gas Magnetic Resonance Imaging
Institution name	University of Western Ontario
Expected presentation date	Apr 2023
Portions	Full text to be used
Requestor Location	Mr. Alexander Matheson 1151 Richmond St. N London, ON N6A5B7 Canada Attn: Mr. Alexander Matheson
Publisher Tax ID	GB674738491
Total	0.00 CAD
Terms and Conditions	

Chapter 5 the right to include in a thesis was retained at time of publication, as verified below:

Western Research

Date: 27 November 2020

To: Dr. Grace Parraga

Project ID: 116775

Study Title: Lung Structure-Function In SurVivors of Mild and SEvere COVID19 Infection: 129Xe MRI and CT For Rapid Evaluations and NExt-wave Healthcare Planning (LIVE COVID FREE)

Study Sponsor: Robarts Research Institute

Application Type: HSREB Initial Application

Review Type: Full Board

Meeting Date: 03/Nov/2020 13:00

Date Approval Issued: 27/Nov/2020 13:20

REB Approval Expiry Date: 27/Nov/2021

Dear Dr. Grace Parraga

The Western University Health Science Research Ethics Board (HSREB) has reviewed and approved the above mentioned study as described in the WREM application form, as of the HSREB Initial Approval Date noted above. This research study is to be conducted by the investigator noted above. All other required institutional approvals must also be obtained prior to the conduct of the study.

Documents Approved:

Document Name	Document Type	Document Date	Document Version
2.15 Other Instruments V1 Oct 14 2020	Other Data Collection Instruments	14/Oct/2020	V1
ROB0050 Borg Scale v1 June 18, 2019	Paper Survey	18/Jun/2019	V1
ROB0050 Ad with no tabs V2 November 6 2020	Recruitment Materials	06/Nov/2020	V2
ROB0050 Ad with tabs V2 November 6 2020	Recruitment Materials	06/Nov/2020	V2
ROB0050 Infographic V2 November 6 2020	Recruitment Materials	06/Nov/2020	V2
ROB0050 BDI-TDI-pdf	Paper Survey	19/Nov/1984	V1
ROB0050 CAT - English	Paper Survey	24/Jul/2009	
ROB0050 IPAQ_Elderly_English_self-admin_short (1)	Paper Survey	22/Mar/2015	V1
ROB0050 IPAQ_English_self-admin_long	Paper Survey	06/Nov/2010	V2
ROB0050 IPAQ_English_self-admin_short	Paper Survey	12/Jan/2012	V3
ROB0050 IPAQ_English_telephone_long	Paper Survey	23/Jan/2020	V1
ROB0050 IPAQ_English_telephone_short	Paper Survey	06/Nov/2010	V1
ROB0050 mMRC Dyspnea Score	Paper Survey	29/Sep/1988	
ROB0050 SGRQ 3 months	Paper Survey	03/Mar/2014	
ROB0050 Protocol V11 November 18 2020	Protocol	18/Nov/2020	V11
ROB0050 Letter of Information and Consent V3 Nov 18 2020	Written Consent/Assent	18/Nov/2020	V3

Documents Acknowledged:

Document Name	Document Type	Document Date	Document Version
Robarts IB 129Xe RRI draft revised September 21 2020	Investigator	21/Sep/2020	V8

clean	Brochure		
ROB0050 BUDGET Nov 17 2020	Study budget	17/Nov/2020	1
NOL ROB0050 Nov 27 2020	NOL/NOA/ITA	27/Nov/2020	

No deviations from, or changes to, the protocol or WREM application should be initiated without prior written approval of an appropriate amendment from Western HSREB , except when necessary to eliminate immediate hazard(s) to study participants or when the change(s) involves only administrative or logistical aspects of the trial.

REB members involved in the research project do not participate in the review, discussion or decision.

The Western University HSREB operates in compliance with, and is constituted in accordance with, the requirements of the TriCouncil Policy Statement: Ethical Conduct for Research Involving Humans (TCPS 2); the International Conference on Harmonisation Good Clinical Practice Consolidated Guideline (ICH GCP); Part C, Division 5 of the Food and Drug Regulations; Part 4 of the Natural Health Products Regulations; Part 3 of the Medical Devices Regulations and the provisions of the Ontario Personal Health Information Protection Act (PHIPA 2004) and its applicable regulations. The HSREB is registered with the U.S. Department of Health & Human Services under the IRB registration number IRB 00000940.

Please do not hesitate to contact us if you have any questions.

Sincerely,

Ms. Nicola Geoghegan-Morphet , Ethics Officer on behalf of Dr. Joseph Gilbert, HSREB Chair

Note: This correspondence includes an electronic signature (validation and approval via an online system that is compliant with all regulations).

Western Research

Date: 31 October 2022

To: Dr. Grace Parraga

Project ID: 116775

Review Reference: 2022-116775-72577

Study Title: Lung Structure-Function In SurVivors of Mild and SEvere COVID19 Infection: 129Xe MRI and CT For Rapid Evaluations and NExt-wave Healthcare Planning (LIVE COVID FREE)

Application Type: Continuing Ethics Review (CER) Form

Review Type: Delegated

REB Meeting Date: 08/Nov/2022

Date Approval Issued: 31/Oct/2022 16:07

REB Approval Expiry Date: 27/Nov/2023

Dear Dr. Grace Parraga,

The Western University Research Ethics Board has reviewed the application. This study, including all currently approved documents, has been re-approved until the expiry date noted above.

REB members involved in the research project do not participate in the review, discussion or decision.

Western University REB operates in compliance with, and is constituted in accordance with, the requirements of the Tri-Council Policy Statement: Ethical Conduct for Research Involving Humans (TCPS 2); the International Conference on Harmonisation Good Clinical Practice Consolidated Guideline (ICH GCP); Part C, Division 5 of the Food and Drug Regulations; Part 4 of the Natural Health Products Regulations; Part 3 of the Medical Devices Regulations and the provisions of the Ontario Personal Health Information Protection Act (PHIPA 2004) and its applicable regulations. The REB is registered with the U.S. Department of Health & Human Services under the IRB registration number IRB 00000940.

Please do not hesitate to contact us if you have any questions.

Electronically signed by:

Ms. Nicola Geoghegan-Morphet, Ethics Officer on behalf of Dr. P. Jones, HSREB Chair 31/Oct/2022 16:07

Reason: I am approving this document

Note: This correspondence includes an electronic signature (validation and approval via an online system that is compliant with all regulations).

Western

Office of Research Ethics

The University of Western Ontario
Room 4180 Support Services Building, London, ON, Canada N6A 5C1
Telephone: (519) 661-3036 Fax: (519) 850-2466 Email: ethics@uwo.ca
Website: www.uwo.ca/research/ethics

Use of Human Subjects - Ethics Approval Notice

Principal Investigator: Dr. G. Parraga
Review Number: 15930 **Review Level:** Full Board
Review Date: February 10, 2009

Protocol Title: Longitudinal Study of Helium-3 Magnetic Resonance Imaging of COPD
Department and Institution: Diagnostic Radiology & Nuclear Medicine, Robarts Research Institute
Sponsor: INTERNAL RESEARCH FUND-UWO
Ethics Approval Date: May 25, 2009 **Expiry Date:** November 30, 2013
Documents Reviewed and Approved: UWO Protocol, Letter of information & consent form for Patients dated March 26/09 & Letter of information & consent form for Healthy Volunteers dated March 26/09
Documents Received for Information: Protocol, January 27, 2009; IB, ed 6, 09 Sep. 05

This is to notify you that The University of Western Ontario Research Ethics Board for Health Sciences Research Involving Human Subjects (HSREB) which is organized and operates according to the Tri-Council Policy Statement: Ethical Conduct of Research Involving Humans and the Health Canada/ICH Good Clinical Practice Practices: Consolidated Guidelines; and the applicable laws and regulations of Ontario has reviewed and granted approval to the above referenced study on the approval date noted above. The membership of this REB also complies with the membership requirements for REB's as defined in Division 5 of the Food and Drug Regulations.

The ethics approval for this study shall remain valid until the expiry date noted above assuming timely and acceptable responses to the HSREB's periodic requests for surveillance and monitoring information. If you require an updated approval notice prior to that time you must request it using the UWO Updated Approval Request Form.

During the course of the research, no deviations from, or changes to, the protocol or consent form may be initiated without prior written approval from the HSREB except when necessary to eliminate immediate hazards to the subject or when the change(s) involve only logistical or administrative aspects of the study (e.g. change of monitor, telephone number). Expedited review of minor change(s) in ongoing studies will be considered. Subjects must receive a copy of the signed information/consent documentation.

Investigators must promptly also report to the HSREB:

a) changes increasing the risk to the participant(s) and/or affecting significantly the conduct of the study;
b) all adverse and unexpected experiences or events that are both serious and unexpected;
c) new information that may adversely affect the safety of the subjects or the conduct of the study.

If these changes/adverse events require a change to the information/consent documentation, and/or recruitment advertisement, the newly revised information/consent documentation, and/or advertisement, must be submitted to this office for approval.

Members of the HSREB who are named as investigators in research studies, or declare a conflict of interest, do not participate in discussion related to, nor vote on, such studies when they are presented to the HSREB.

[redacted]

Chair of HSREB: Dr. Joseph Gilbert

Ethics Officer to Contact for Further Information			
☑ Janice Sutherland [redacted]	☐ Elizabeth Wambolt [redacted]	☐ Grace Kelly [redacted]	☐ Denise Grafton [redacted]

This is an official document. Please retain the original in your files.

cc: ORE File
LHRI

Western Research

Date: 25 January 2022

To: Dr. Grace Parraga

Project ID: 6014

Study Title: Longitudinal Study of Helium-3 Magnetic Resonance Imaging of COPD

Application Type: Continuing Ethics Review (CER) Form

Review Type: Delegated

Date Approval Issued: 25/Jan/2022

REB Approval Expiry Date: 10/Feb/2023

Dear Dr. Grace Parraga,

The Western University Research Ethics Board has reviewed the application. This study, including all currently approved documents, has been re-approved until the expiry date noted above.

REB members involved in the research project do not participate in the review, discussion or decision.

Western University REB operates in compliance with, and is constituted in accordance with, the requirements of the Tri-Council Policy Statement: Ethical Conduct for Research Involving Humans (TCPS 2); the International Conference on Harmonisation Good Clinical Practice Consolidated Guideline (ICH GCP); Part C, Division 5 of the Food and Drug Regulations; Part 4 of the Natural Health Products Regulations; Part 3 of the Medical Devices Regulations and the provisions of the Ontario Personal Health Information Protection Act (PHIPA 2004) and its applicable regulations. The REB is registered with the U.S. Department of Health & Human Services under the IRB registration number IRB 00000940.

Please do not hesitate to contact us if you have any questions.

Sincerely,

The Office of Human Research Ethics

Note: This correspondence includes an electronic signature (validation and approval via an online system that is compliant with all regulations).

Research Western

Use of Human Participants - Ethics Approval Notice

Principal Investigator: Dr. Grace Parraga
Review Number: 18130
Review Level: Full Board
Approved Local Adult Participants: 100
Approved Local Minor Participants: 0
Protocol Title: A Single-center Study Evaluating Hyperpolarized 129Xenon Magnetic Resonance Imaging in Subjects with Chronic Lung Disease
Department & Institution: Imaging,Robarts Research Institute
Sponsor: Canadian Institutes of Health Research

Ethics Approval Date: August 12, 2011 **Expiry Date:** August 31, 2016

Documents Reviewed & Approved & Documents Received for Information:

Document Name	Comments	Version Date
UWO Protocol		
Letter of Information & Consent		2011/07/13
Advertisement		2011/07/13
Protocol	Received for information only	2011/06/22

This is to notify you that the University of Western Ontario Health Sciences Research Ethics Board (HSREB) which is organized and operates according to the Tri-Council Policy Statement: Ethical Conduct of Research Involving Humans and the Health Canada/ICH Good Clinical Practice Practices: Consolidated Guidelines; and the applicable laws and regulations of Ontario has reviewed and granted approval to the above referenced study on the approval date noted above. The membership of this HSREB also complies with the membership requirements for REB's as defined in Division 5 of the Food and Drug Regulations.

The ethics approval for this study shall remain valid until the expiry date noted above assuming timely and acceptable responses to the HSREB's periodic requests for surveillance and monitoring information. If you require an updated approval notice prior to that time you must request it using the UWO Updated Approval Request form.

Member of the HSREB that are named as investigators in research studies, or declare a conflict of interest, do not participate in discussions related to, nor vote on, such studies when they are presented to the HSREB.

The Chair of the HSREB is Dr. Joseph Gilbert. The UWO HSREB is registered with the U.S. Department of Health & Human Services under the IRB registration number IRB 00000940.

Signat [redacted]

Ethics Officer to Contact for Further Information

Janice Sutherland [redacted]	Grace Kelly [redacted]	Shantel Walcott [redacted]

This is an official document. Please retain the original in your files.

Western Research

Date: 10 June 2022

To: Dr. Grace Parraga

Project ID: 100974

Review Reference: 2022-100974-67240

Study Title: A Single-center Study Evaluating Hyperpolarized 129Xenon Magnetic Resonance Imaging in Subjects with Chronic Lung Disease (REB #18130)

Application Type: Continuing Ethics Review (CER) Form

Review Type: Delegated

REB Meeting Date: 28/June/2022

Date Approval Issued: 10/Jun/2022 12:51

REB Approval Expiry Date: 05/Jul/2023

Dear Dr. Grace Parraga,

The Western University Research Ethics Board has reviewed the application. This study, including all currently approved documents, has been re-approved until the expiry date noted above.

REB members involved in the research project do not participate in the review, discussion or decision.

Western University REB operates in compliance with, and is constituted in accordance with, the requirements of the Tri-Council Policy Statement: Ethical Conduct for Research Involving Humans (TCPS 2); the International Conference on Harmonisation Good Clinical Practice Consolidated Guideline (ICH GCP); Part C, Division 5 of the Food and Drug Regulations; Part 4 of the Natural Health Products Regulations; Part 3 of the Medical Devices Regulations and the provisions of the Ontario Personal Health Information Protection Act (PHIPA 2004) and its applicable regulations. The REB is registered with the U.S. Department of Health & Human Services under the IRB registration number IRB 00000940.

Please do not hesitate to contact us if you have any questions.

Electronically signed by:

Karen Gopaul, Ethics Officer on behalf of Dr. P. Jones, HSREB Chair 10/Jun/2022 12:51

Reason: I am approving this document

Note: This correspondence includes an electronic signature (validation and approval via an online system that is compliant with all regulations).

Western Research

Use of Human Participants - Ethics Approval Notice

Principal Investigator: Dr. Grace Parraga
File Number:103516
Review Level: Full Board
Approved Local Adult Participants:200
Approved Local Minor Participants:0
Protocol Title: Structure and Function MRI of Asthma
Department & Institution: Schulich School of Medicine and Dentistry\Imaging,Robarts Research Institute
Sponsor:
Ethics Approval Date: April 08, 2013
Ethics Expiry Date: March 31, 2020

Documents Reviewed & Approved & Documents Received for Information:

Document Name	Comments	Version Date
Protocol	Robarts Protocol - Received for information only	2013/02/06
Instruments	Telephone Script	2013/03/14
Letter of Information & Consent	ROB0037 ICF March 13 2013	2013/03/13
Western University Protocol	(including study instruments & questionnaires)	

This is to notify you that the University of Western Ontario Health Sciences Research Ethics Board (HSREB) which is organized and operates according to the Tri-Council Policy Statement: Ethical Conduct of Research Involving Humans and the Health Canada/ICH Good Clinical Practice Practices: Consolidated Guidelines; and the applicable laws and regulations of Ontario has reviewed and granted approval to the above referenced study on the approval date noted above. The membership of this HSREB also complies with the membership requirements for REB's as defined in Division 5 of the Food and Drug Regulations.

The ethics approval for this study shall remain valid until the expiry date noted above assuming timely and acceptable responses to the HSREB's periodic requests for surveillance and monitoring information. If you require an updated approval notice prior to that time you must request it using the University of Western Ontario Updated Approval Request form.

Member of the HSREB that are named as investigators in research studies, or declare a conflict of interest, do not participate in discussions related to, nor vote on, such studies when they are presented to the HSREB.

The Chair of the HSREB is Dr. Joseph Gilbert. The HSREB is registered with the U.S. Department of Health & Human Services under the IRB registration number IRB 00000940.

Signat[redacted]

Ethics Officer to Contact for Further Information

Janice Sutherland [redacted]	Grace Kelly [redacted]	Shantel Walcott [redacted]

This is an official document. Please retain the original in your files.

Western Research

Date: 27 January 2022

To: Dr. Grace Parraga

Project ID: 103516

Study Title: Structure and Function MRI of Asthma

Application Type: Continuing Ethics Review (CER) Form

Review Type: Delegated

Date Approval Issued: 27/Jan/2022

REB Approval Expiry Date: 19/Feb/2023

Dear Dr. Grace Parraga,

The Western University Research Ethics Board has reviewed the application. This study, including all currently approved documents, has been re-approved until the expiry date noted above.

REB members involved in the research project do not participate in the review, discussion or decision.

Western University REB operates in compliance with, and is constituted in accordance with, the requirements of the Tri-Council Policy Statement: Ethical Conduct for Research Involving Humans (TCPS 2); the International Conference on Harmonisation Good Clinical Practice Consolidated Guideline (ICH GCP); Part C, Division 5 of the Food and Drug Regulations; Part 4 of the Natural Health Products Regulations; Part 3 of the Medical Devices Regulations and the provisions of the Ontario Personal Health Information Protection Act (PHIPA 2004) and its applicable regulations. The REB is registered with the U.S. Department of Health & Human Services under the IRB registration number IRB 00000940.

Please do not hesitate to contact us if you have any questions.

Sincerely,

The Office of Human Research Ethics

Note: This correspondence includes an electronic signature (validation and approval via an online system that is compliant with all regulations).

Research Western

Use of Human Participants - Ethics Approval Notice

Principal Investigator: Dr. Grace Parraga
Review Number: 18131
Review Level: Full Board
Approved Local Adult Participants: 50
Approved Local Minor Participants: 0
Protocol Title: Xenon-129 Magnetic Resonance Imaging of Healthy Subjects: Hardware and Software Development and Reproducibility
Department & Institution: Imaging,Robarts Research Institute
Sponsor: Canadian Institutes of Health Research

Ethics Approval Date: August 12, 2011 **Expiry Date:** August 31, 2016

Documents Reviewed & Approved & Documents Received for Information:

Document Name	Comments	Version Date
UWO Protocol		
Letter of Information & Consent		2011/07/13
Protocol	Received for information only	2011/06/22
Advertisement		2011/07/13

This is to notify you that the University of Western Ontario Health Sciences Research Ethics Board (HSREB) which is organized and operates according to the Tri-Council Policy Statement: Ethical Conduct of Research Involving Humans and the Health Canada/ICH Good Clinical Practice Practices: Consolidated Guidelines; and the applicable laws and regulations of Ontario has reviewed and granted approval to the above referenced study on the approval date noted above. The membership of this HSREB also complies with the membership requirements for REB's as defined in Division 5 of the Food and Drug Regulations.

The ethics approval for this study shall remain valid until the expiry date noted above assuming timely and acceptable responses to the HSREB's periodic requests for surveillance and monitoring information. If you require an updated approval notice prior to that time you must request it using the UWO Updated Approval Request form.

Member of the HSREB that are named as investigators in research studies, or declare a conflict of interest, do not participate in discussions related to, nor vote on, such studies when they are presented to the HSREB.

The Chair of the HSREB is Dr. Joseph Gilbert. The UWO HSREB is registered with the U.S. Department of Health & Human Services under the IRB registration number IRB 00000940.

Signat[redacted]

Ethics Officer to Contact for Further Information

Janice Sutherland [redacted]	Grace Kelly [redacted]	Shantel Walcott [redacted]

This is an official document. Please retain the original in your files.

The **University** *of* **Western Ontario**
Office of Research Ethics
Support Services Building Room 5150 • London, Ontario • CANADA - N6A 3K7
PH: 519-661-3036 • F: 519-850-2466 • ethics@uwo.ca • www.uwo.ca/research/ethics

Western Research

Date: 10 June 2022

To: Dr. Grace Parraga

Project ID: 100975

Review Reference: 2022-100975-67241

Study Title: Xenon-129 Magnetic Resonance Imaging of Healthy Subjects: Hardware and Software Development and Reproducibility (REB #18131)

Application Type: Continuing Ethics Review (CER) Form

Review Type: Delegated

REB Meeting Date: 28/June/2022

Date Approval Issued: 10/Jun/2022 12:49

REB Approval Expiry Date: 05/Jul/2023

Dear Dr. Grace Parraga,

The Western University Research Ethics Board has reviewed the application. This study, including all currently approved documents, has been re-approved until the expiry date noted above.

REB members involved in the research project do not participate in the review, discussion or decision.

Western University REB operates in compliance with, and is constituted in accordance with, the requirements of the Tri-Council Policy Statement: Ethical Conduct for Research Involving Humans (TCPS 2); the International Conference on Harmonisation Good Clinical Practice Consolidated Guideline (ICH GCP); Part C, Division 5 of the Food and Drug Regulations; Part 4 of the Natural Health Products Regulations; Part 3 of the Medical Devices Regulations and the provisions of the Ontario Personal Health Information Protection Act (PHIPA 2004) and its applicable regulations. The REB is registered with the U.S. Department of Health & Human Services under the IRB registration number IRB 00000940.

Please do not hesitate to contact us if you have any questions.

Electronically signed by:

Karen Gopaul, Ethics Officer on behalf of Dr. P. Jones, HSREB Chair 10/Jun/2022 12:49

Reason: I am approving this document

Note: This correspondence includes an electronic signature (validation and approval via an online system that is compliant with all regulations).

Appendix E - Curriculum Vitae
Curriculum Vitae - Alexander M Matheson BSc

PhD Candidate, Department of Medical Biophysics

Supervisor: Dr. Grace Parraga

EDUCATION

2018-2023	**Ph.D. Medical Biophysics (*Candidate*)**
	Western University, London ON
	Supervisor: Dr. Grace Parraga
	Project: Gas-exchange abnormalities in chronic lung disease
2015-2018	**B.Sc. (Honours) Physics**
	University of Calgary, Calgary AB
	Project: Sulphate aerosols of Alberta as tracers of cloud transport
	Supervisor: Dr. Ann-Lise Norman
2008-2013	**B.Sc. Archaeology**
	University of Calgary, Calgary AB

EMPLOYMENT

2019-2022	**Western University**
	Teaching Assistant – MEDBIO 3503
	Supervisor: Dr. Corey Baron
	Description: Assisted in teaching a course on digital imaging including tutorials, developing teaching materials, marking and invigilating
2019	**Western University**
	Research Assistant - Technician
	Supervisor: Dr. Grace Parraga
	Description: Information technology support and polarizer responsibilities during laboratory manager leave of absence
2018-2023	**Western University**
	Research Assistant

Supervisor: Dr. Grace Parraga

Description: Perform ongoing research, performed human research study data collection

2015-2017 **Youthlink Calgary**

Curatorial Assistant

Supervisor: Sean Corscaden

Description: Performed collection research and lead youth educational programming in a police outreach museum.

2013-2015 **Seneca College Newnham – Campus Living Centres**

Residence Life Coordinator

Supervisor: Paul Evans

Description: Lead a campus leadership program of 22 student leaders for a community of 1000 students. Included extracurricular education, student safety, and outreach.

2012-2013 **University of Calgary Residence Services**

Residence Life Assistant

Supervisor: Zac Wiens

Description: Developed training program and provided staff support for team of 52 student leaders.

2009-2012 **University of Calgary Residence Services**

Community Advisor

Supervisor: Brianna McElroy

Description: Created and delivered educational programming and student support to communities of 36-70 undergraduate students.

HONOURS, AWARDS AND RECOGNITIONS

2023 **Post-Doctoral Fellowship**

Natural Science and Engineering Research Council of Canada (NSERC)

National ($45,000/yr)

2021 **Robert F. Wagner All Conference Best Student Paper Award**

	Finalist
	SPIE Medical Imaging 2021
	International
2020-2022	**Alexander Graham Bell Canada Graduate Scholarship - Doctoral**
	Natural Science and Engineering Research Council of Canada (NSERC)
	National ($35,000/yr)
2019-2022	**ISMRM Trainee (Educational) Award**
	International Society for Magnetic Resonance in Medicine
	International ($535/yr)
2019	**Ontario Graduate Scholarship**
	Province of Ontario
	Provincial ($15,000/yr)
	CIHR Travel Award, Institute of Respiratory Health
	Canadian Institutes of Health Research
	National ($1,000)
	London Imaging Discovery Day – Oral Presentation 3rd Place
	London Health Sciences Centre
	Local
	Oral Presentation Award, Honourable Mention
	Imaging Network Ontario Conference
	Provincial
2018-2023	**Western Graduate Research Scholarship**
	Western University
	Institutional ($5,000/yr)
2018	**Queen Elizabeth II Graduate Research Scholarship (Declined)**
	Province of Alberta
	Provincial ($10,800)
	NSERC Undergraduate Student Research Award (Declined)
	Natural Science and Engineering Research Council of Canada

National ($7,000)

2016 **University of Calgary Undergraduate Merit Award**

University of Calgary

Institutional ($1,100)

2012 **Leadership Society Award**

Residence Life Professionals Association

National

2011 **Wes Johnston Student Award in Archaeology**

Archaeological Society of Alberta

Institutional ($300)

Canadian Federation of University Women/Calgary Bursary

Canadian Federation of University Women, Calgary Branch

Institutional ($1,000)

2010 **University of Calgary Undergraduate Merit Award**

The University of Calgary

Institutional ($500)

TEACHING AND MENTORING

2022-2023 **Graduate Student Mentor**

Caleb Thompson (3rd year undergraduate student, Medical Biophysics)

Western University, London ON

Project: A software pipeline for ^{129}Xe dissolved phase spectroscopy

2021-2022 **Graduate Student Mentor**

Justin Lee (4th year undergraduate student, Physiology and Pharmacology)

Western University, London ON

Project: ^{129}Xe MRS in people with long-COVID

2021 **Curriculum Design, BIOPHYS 9709B**

Western University, London ON

Designed a course (Biomedical applications of Neural Networks) which was later delivered annually by the department. Designed course outline, lectures, online learning, assessments and exams.

2021-2022 **Graduate Student Mentor**

Yasal Rajapaska (4th year undergraduate student, Physiology and Pharmacology)

Western University, London ON

Project: Hyperpolarized Xenon MRI in Survivors of COVID Infection

2019 **Graduate Student Mentor**

Jenna Veugen (3rd year undergraduate student, Physics)

Western University, London ON

Project: UTE Proton Density in Broncho-pulmonary Dysplasia

Graduate Student Mentor

Hannah Yaremko (2nd year undergraduate student, Physiology and Pharmacology)

Western University, London ON

Project: Implementing a UTE Proton Density Image Processing Pipeline

2019-2022 **Graduate Teaching Assistant**

Western University, London ON

Taught tutorials, prepared review materials, marked assessments

2013-2015 **Residence Life Coordinator**

University of Calgary, Calgary AB

Lead a campus leadership program of 22 student leaders for a community of 1000 students. Included extracurricular education, student safety, and outreach.

2012-2013 **Residence Life Assistant**

University of Calgary, Calgary AB

Developed training program and provided staff support for team of 52 student leaders of the Residence Education Team.

2009-2012 **Community Advisor**

University of Calgary, Calgary AB

Created and delivered educational programming and student support to communities of 36-70 undergraduate students.

PUBLICATIONS AND PRESENTATIONS

A Peer-Reviewed Journal Manuscripts (9)

1. HK Kooner, MJ McIntosh, **AM Matheson**, M Abdelrazek, MS Albert, I Dhaliwal, M Kirby, A Ouriadov, G Santyr, CPV Garrido, N Radadia, S Svenningsen, M Nicholson, G Parraga. Post-Acute COVID-19 Syndrome: ^{129}Xe MRI Ventilation Defects and Respiratory Outcomes One Year Later. Radiology (In Press, RAD-22-2557.R2). 2022.
2. **AM Matheson,** MJ McIntosh, HK Kooner, M Abdelrazek, MS Albert, I Dhaliwal, JM Nicholson, A Ouriadov, S Svenningsen and G Parraga. Longitudinal follow-up of post-acute COVID-19 syndrome: Improved DL_{CO}, Quality-of-Life and MRI pulmonary gas-exchange abnormalities. Thorax (Under review manuscript ID: thorax-2022-219378.R2) 2022.
3. **AM Matheson**, MJ McIntosh, HK Kooner, J Lee, V Desaigoudar, E Bier, B Driehuys, S Svenningsen, G Santyr, M Kirby, MS Albert, Y Shepelytskyi, V Grynko, A Ouriadov, M Abdelrazek, I Dhaliwal, JM Nicholson, G Parraga. Persistent ^{129}Xe MRI Pulmonary and CT Vascular Abnormalities in Symptomatic Individuals with Post-acute COVID-19 Syndrome. Radiology 305(2):466-476, 2022.
4. HK Kooner & MJ McIntosh, **AM Matheson**, C Venegas, N Radadia, T Ho, E Haider, N Konyer, GE Santyr, MS Albert, A Ouriadov, M Abdelrazek, M Kirby, I Dhaliwal, JM Nicholson, P Nair, S Svenningsen and G Parraga. ^{129}Xe MRI ventilation defects in ever-hospitalised and never-hospitalised people with post-acute COVID-19 syndrome. BMJ Open Resp Res 2022; 9:e001235. doi:10.1136/bmjresp-2022-001235.
5. **AM Matheson,** RSP Cunningham, G Parraga, MWA Chu and S Blissett. Cardiac Surgery for Atrial Septal Defect Repair: Normalization of Hyperpolarized Xenon-129 MRI RBC-to-Barrier Ratio. CHEST 162(4):E205-E206, 2022.
6. RL Eddy, MJ McIntosh, **AM Matheson,** DG McCormack, C Licskai, G Parraga. Pulmonary Imaging Biomarkers and Cluster Analysis to Identify Novel Asthma Phenotypes: Proof-of-Concept Evaluation. JMRI 2022. doi:10.1002/jmri.28152.
7. **AM Matheson**, RSP Cunningham, E Bier, J Lu, B Driehuys, JG Pickering, P Diamantouros, A Islam, JM Nicholson and G Parraga. Hyperpolarized 129Xe Pulmonary MRI and Asymptomatic Atrial Septal Defect. CHEST 2021 161(4): e199-e202.
8. S Svenningsen, M McIntosh, A Ouriadov, **AM Matheson**, NB Konyer, RL Eddy, DG McCormack, MD Noseworthy, P Nair, G Parraga. Reproducibility of Hyperpolarized 129Xe MRI Ventilation Defect Percent in Severe Asthma to Evaluate Clinical Trial Feasibility. Acad Radiol 2021; 28(6):817-826. doi: 10.1016/j.acra.2020.04.025.
9. RL Eddy, **AM Matheson**, S Svenningsen, D Knipping, C Licskai, DG McCormack and G Parraga. Non-identical Twins with Asthma: Spatially-matched CT Airway and MRI Ventilation Abnormailities. Chest 2019 156(6).

B Journal Publications (3)

1. G Parraga and **AM Matheson**. Step on the 129Xe Gas: The MRI Race to Uncover Drivers of Post-COVID-19 Symptoms. Radiology 305(3):718-720, 2022.
2. **AM Matheson** and G Parraga. Machine Learning Predictions of COPD Mortality: Computational Hide and Seek. Chest 158(3), 2020.
3. **AM Matheson** and G Parraga. Emerging and Established Pulmonary Function Measurements of Primary Ciliary Dyskinesia: One of these things is not like the others. Annals of the American Thoracic Society. 15(12), 2018.

C Book Chapter (1)

1. **AM Matheson,** C Thompson and G Parraga. Inhaled Gas Magnetic Resonance Imaging: Advances, Applications, Limitations and New Frontiers. Chapter in Molecular Imaging, 2nd Ed. BD Ross and SS Gambhir (Eds.). Elsevier: New York.

D Peer-Reviewed Published Conference Manuscripts (3)

1. **AM Matheson,** G Parraga and IA Cunningham. A Linear Systems Description of Multi-Compartment Pulmonary 129Xe Magnetic Resonance Imaging Methods. Proceedings of SPIE Medical Imaging 2021 San Diego, FEB 14-18, 2021.
2. **AM Matheson,** DPI Capaldi, F Guo, R Eddy, S Svenningsen, D McCormack, and G Parraga. A Fourier Decomposition MRI Processing Pipeline for Mapping Ventilation/Perfusion Mismatch in Asthma Patients. Proceedings of SPIE Medical Imaging 2019. San Diego, FEB 16-21, 2019.
3. JL MacNeil, DPI Capaldi, RL Eddy, AR Westcott, **AM Matheson**, AL Barker, C Ong Ly, DG McCormack and G Parraga. Development and Evaluation of Pulmonary Imaging Multi-Parametric Response Maps for Deep Phenotyping of Chronic Obstructive Pulmonary Disease. Proceedings of SPIE Medical Imaging 2019. San Diego, FEB 16-21, 2019.

E Invited Oral Presentations (4) ***presenter***

1. **AM Matheson***, HK Kooner, E Bier, J Lu, B Driehuys, M Kirby, G Santyr, MS Albert, Y Shepelytskyi, V Grynko, S Svenningsen, A Ouriadov, I Dhaliwal, M Nicholson and G Parraga. ^{129}Xe Gas-Transfer MRI RBC-to-Barrier Ratio in Post-Acute COVID19 Syndrome. Polarization in Noble Gases Workshop. Dec 6-10, 2021.
2. **AM Matheson***. Magnetic Resonance to Understand Gas-exchange Pathophysiology: Long-COVID and Congenital Heart Disease. Cincinnati Children's Hospital and Medical Center – Center for Pulmonary Imaging Research. February 7, 2023.
3. **AM Matheson***. Magnetic Resonance to Understand Gas-exchange Pathophysiology: Long-COVID and Congenital Heart Disease. Duke University Department of Radiology Journal Club. February 21, 2023.
4. **AM Matheson***. Magnetic Resonance to Understand Gas-exchange Pathophysiology: Long-COVID and Congenital Heart Disease. SickKids Hospital Translational Medicine Seminar Series. February 27, 2023.

F Conference Abstracts – Oral Presentations (17) **presenter*

1. **AM Matheson**, MJ McIntosh, N Paul, A Bhalla, C Yamashita and G Parraga. 129Xe Gas-Exchange MRI and CT Pulmonary Vascular Abnormalities in GINA 4-5 Asthma. American Thoracic Society Annual Scientific Meeting. Washington, DC. May 19-24, 2023.
2. MJ McIntosh, **AM Matheson**, HK Kooner, RL Eddy, C Yamashita and G Parraga. Pulmonary Vascular Redistribution following 2.5-years anti-IL5-Rα treatment in Eosinophilic Asthma. American Thoracic Society Annual Scientific Meeting. Washington, DC. May 19-24, 2023.
3. JM Nicholson, **AM Matheson**, HK Kooner, MJ McIntosh, S Svenningsen and G Parraga. Unique MRI Phenotypes help explain Post-Acute COVID-19 syndrome. American Thoracic Society Annual Scientific Meeting. Washington, DC. May 19-24, 2023.
4. **AM Matheson**, MJ McIntosh, N Paul, A Bhalla, C Yamashita and G Parraga. 129Xe Gas-Exchange MRI and CT Pulmonary Vascular Abnormalities in GINA 4-5 Asthma. Imaging Network of Ontario Annual Symposium, London Ontario. March 23-24, 2023.
5. HK Kooner*, MJ McIntosh, **AM Matheson**, M Abdelrazek, I Dhaliwal, JM Nicholson and G Parraga. ^{129}Xe MRI Ventilation Improvements 15 Months Post-COVID Infection. International Workshop on Pulmonary Functional Imaging 2022, Hannover, Germany. September 15-17, 2022.
6. **AM Matheson***, MJ McIntosh, HK Kooner, J Lee, V Desaigoudar, A Ouriadov, M Abdelrazek, I Dhaliwal, JM Nicholson and G Parraga. ^{129}Xe Gas-Transfer MRI RBC-to-Barrier Ratio in Post-Acute COVID19 Syndrome: Clinically-relevant? Robarts Research Retreat. London ON. June 9, 2022.
7. MJ McIntosh*, **AM Matheson**, M Sharma, HK Kooner, RL Eddy, DG McCormack, C Yamashita and G Parraga. Pulmponary Proton MRI Lobar Classification Using Convolutional Neural Networks. Date: JUNE 22-25, 2021. Canadian Organization of Medical Physicists Annual Scientific Meeting.
8. M Sharma*, MJ McIntosh, **AM Matheson**, HK Kooner, DG McCormack, DA Palma and G Parraga. Short-term Reduction in 6MWD Characterized Using Machine Learning CT and MRI Texture Features. American Thoracic Society 2021 International Conference. Location: San Diego, USA. Date: MAY 16-21, 2021.
9. RL Eddy*, MJ McIntosh, **AM Matheson**, C Licskai, DG McCormack and G Parraga. Structure function Imaging Phenotypes of Asthma Using CT and 129Xe MRI. American Thoracic Society 2021 International Conference. Location: San Diego, USA. Date: MAY 16-21, 2021.
10. **AM Matheson***, G Parraga and IA Cunningham. A Linear Systems Description of Multi-Compartment Pulmonary ^{129}Xe Magnetic Resonance Imaging Methods. SPIE Medical Imaging Location: San Diego, CA Date: FEB 14-18, 2021.
11. **AM Matheson*,** RL Eddy, JL MacNeil, MJ McIntosh and G Parraga. Fully Automated 1H MRI Thoracic Cavity Segmentation for Hyperpolarized Gas Imaging using a Convolution Neural Network. Proceedings of ISMRM, 2020. Sydney, AUS. APRIL 19-23, 2020.

12. RL Eddy*, MJ McIntosh, **AM Matheson**, C Licskai, DG McCormack and G Parraga. 129Xe MRI Ventilation Heterogeneity Phenotypes of Asthma. American Thoracic Society 2020 International Conference Location: Philadelphia, PN. Date: MAY 17-21, 2020.
13. **AM Matheson** and G Parraga. FDMRI Perfusion Defects in COPD. Canadian Respiratory Research Network Annual Meeting. Ottawa, ON. JAN 16-17, 2020.
14. **AM Matheson** and G Parraga. FDMRI Perfusion Defects in COPD: Function Follows Form? International Workshop on Pulmonary Functional Imaging. New Orleans, LA. OCT 17-20, 2019.
15. **AM Matheson***, DPI Capaldi, F Guo, DG McCormack and G Parraga. A Comprehensive Pipeline for Pulmonary Vascular Tree Structure/Function Biomarkers. London Imaging Discovery Day, 2019. Location: London, ON. Date: JUNE 12, 2019.
16. **AM Matheson**, RL Eddy, DPI Capaldi, F Guo, DG McCormack and G Parraga. Multi-scalar Perfusion and Ventilation Defects in Asthma. Imaging Network Ontario 2019 Conference London, ON. MAR 27-28, 2019.
17. AM Matheson, DPI Capaldi, F Guo, R Eddy, S Svenningsen, D McCormack, and G Parraga. A Fourier Decomposition MRI Processing Pipeline for Mapping Ventilation/Perfusion Mismatch in Asthma Patients. SPIE Medical Imaging Location: San Diego, CA Date: FEB 16-21, 2019.

G Conference Abstracts – Poster Presentations (26) ****presenter***

1. **AM Matheson**, MJ McIntosh, N Paul, A Bhalla, C Yamashita, and G Parraga. 129Xe MRS Gas-Exchange Abnormalities in Poorly-controlled Asthma. Annual International Society of Magnetic Resonance in Medicine Scientific Meeting 2023, Toronto, Canada. June 3-8, 2023.
2. M Sharma, PV Wyszkiewicz, MJ McIntosh, HK Kooner, **AM Matheson**, DG McCormack and G Parraga. MRI and CT Measurements Uniquely Explain All-cause Mortality in Ex-smokers with and without COPD. American Thoracic Society Annual Scientific Meeting. Washington, DC. May 19-24, 2023.
3. HK Kooner, M Faran, MJ McIntosh, **AM Matheson**, PV Wyszkiewicz, I Dhaliwal, M Abdelrazek, JM Nicholson, and G Parraga. Sex Differences in CT Airway Measurements and their Relationship to Post-Acute COVID-19 Syndrome. American Thoracic Society Annual Scientific Meeting. Washington, DC. May 19-24, 2023.
4. M Sharma, PV Wyszkiewicz, MJ McIntosh, HK Kooner, **AM Matheson**, DG McCormack and G Parraga. CT and MRI Measurements Uniquely Explain All-cause Mortality in Ex-smokers. Imaging Network of Ontario Annual Symposium, London Ontario. March 23-24, 2023.
5. HK Kooner, M Faran, MJ McIntosh, **AM Matheson**, PV Wyszkiewicz, I Dhaliwal, M Abdelrazek, JM Nicholson, and G Parraga. Sex Differences in CT Airway Measurements and their Relationship to Post-Acute COVID-19 Syndrome. Imaging Network of Ontario Annual Symposium, London Ontario. March 23-24, 2023.
6. **AM Matheson***, MJ McIntosh, HK Kooner, C Yamashita, N Paul and G Parraga. 129Xe Magnetic Resonance Spectroscopy: Abnormal Cardiogenic Oscillations in Severe Asthma. International Workshop on Pulmonary Functional Imaging 2022, Hannover, DE. Sept 15-17, 2022.

7. HK Kooner*, MJ McIntosh, **AM Matheson**, M Abdelrazek, I Dhaliwal, JM Nicholson, and G Parraga. 129Xe MRI Ventilation Improvements 15 Months Post-COVID Infection. International Workshop on Pulmonary Functional Imaging 2022, Hannover, DE. September 15-17, 2022.
8. **AM Matheson***, MJ McIntosh, HK Kooner, J Lee, V Desaigoudar, A Ouriadov, M Abdelrazek, I Dhaliwal, JM Nicholson and G Parraga.29Xe Gas-Transfer MRI RBC-to-Barrier Ratio in Post-Acute COVID19 Syndrome: Clinically-relevant? Robarts Research Retreat. London ON. June 16, 2022.
9. **AM Matheson***, HK Kooner, E Bier, J Lu, B Driehuys, M Kirby, G Santyr, MS Albert, Y Shepelytskyi, V Grynko, S Svenningsen, A Ouriadov, I Dhaliwal, M Nicholson and G Parraga. 129Xe Gas-Transfer MRI RBC-to-Barrier Ratio in Post-Acute COVID19 Syndrome: Clinically-relevant? ISMRM Meeting 2022, London, UK. May 7-12, 2022.
10. MJ McIntosh*, M Sharma, **AM Matheson**, HK Kooner, RL Eddy, C Licksai, DG McCormack, M Nicholson, C Yamashita and G Parraga. Respiratory System Resistance Explained using Hyperpolarized ^{129}Xe MRI Texture Features and Machine Learning. ISMRM Meeting 2022, London, UK. May 7-12, 2022.
11. **AM Matheson***, MJ McIntosh, Y Rajapaksa, I Dhaliwal, M Nicholson and G Parraga. This is what COVID-19 Survival Looks Like: 129Xe MRI, Oscillometry and Pulmonary Function Measurements. American Thoracic Society 2021 Conference. San Diego, CA. MAY 16-21, 2021.
12. **AM Matheson*,** RL Eddy, JL MacNeil, MJ McIntosh and G Parraga. Fully-automated Multi-Spectral Pulmonary Registration in Hyperpolarized Noble Gas MRI Using Neural Networks. ISMRM meeting 2021. Vancouver, BC. MAY 15-20, 2021.
13. M Sharma*, **AM Matheson**, DG McCormack, DA Palma and G Parraga. Hyperpolarized ^{3}He MRI ADC and Ventilation Features Predict Rapidly Worsening Emphysema Using Machine-Learning. ISMRM meeting 2021. Vancouver, BC. MAY 15-20, 2021.
14. FR Salerno, T Lindenmaier, **AM Matheson**, RL Eddy, M McIntosh, J Dorie, G Parraga and CW McIntyre. Noninvasive assessment of pulmonary hypertension using quantitative imaging in hemodialysis patients. European Conference of Nephrology 2020 Location: Milan IT. Date: JUNE 6-9, 2020. Cancelled due to COVID-19.
15. MJ McIntosh, RL Eddy, JL MacNeil, AM Matheson and G Parraga. Automated quantification of spatially abnormal 129Xe MRI ventilation and perfusion: implications for lung cancer, asthma, and COPD interventions. American Association of Physicists in Medicine - Canadian Organization of Medical Physicists Joint Meeting, Vancouver, Canada. Date: JULY 12-16, 2020.
16. **AM Matheson*,** RL Eddy, AL Barker, DG McCormack and G Parraga. Perfusion Abnormalities in COPD: How do Emphysema and Airways Contribute? American Thoracic Society 2020 Conference. Philadelphia, PN. MAY 17-21, 2020.
17. **AM Matheson***, RL Eddy, JL MacNeil, M McIntosh and G Parraga. Convolution Neural Network ^{1}H Lung Segmentation For Hyperpolarized Gas Imaging. Imaging Network Ontario 2020. Location: Toronto, ON. Date: MAR 30-31, 2020.
18. **AM Matheson*** and G Parraga. FDMRI Perfusion Defects in COPD: Function Follows Form? International Workshop on Pulmonary Functional Imaging. Location: New Orleans, LA. Date: OCT 18-20, 2019.

19. FR Salerno*, RL Eddy, **AM Matheson**, J Dorie, T Tamasi, G Parraga, CW McIntyre. Lung Ventilation Abnormalities in Chronic Hemodialysis Patients with Hyperpolarized ^{129}Xenon Gas Magnetic Resonance Imaging. American Society of Nephrology Conference Location: Washington, DC. Date: NOV 5-10, 2019.
20. **AM Matheson**, RL Eddy, DPI Capaldi, F Guo, RL Eddy, DG McCormack and G Parraga. Perfusion Abnormalities and Ventilation Heterogeneity in Asthma. Robarts Research Retreat Location: London, ON. Date: JUNE 7, 2019.
21. **AM Matheson***, DPI Capaldi, F Guo, DG McCormack and G Parraga. A Comprehensive Pipeline for non-contrast enhanced Pulmonary Vascular 1H MRI. ISMRM Meeting 2019. Montreal, QC. MAY 11-16, 2019.
22. **AM Matheson***, DPI Capaldi, F Guo and G Parraga. Flow-Compensated Ventilation and Perfusion Fourier-decomposition Pulmonary MRI, ISMRM Meeting 2019. Montreal, QC. MAY 11-16, 2019.ISMRM Annual Meeting
23. **AM Matheson***, RL Eddy, DPI Capaldi, F Guo, RL Eddy, DG McCormack and G Parraga. Perfusion Abnormalities and Ventilation Heterogeneity in Asthma. London Health Research Day Location: London, ON Date: MAY 31, 2019.
24. **AM Matheson***, RL Eddy, DPI Capaldi, F Guo, RL Eddy, DG McCormack and G Parraga. Perfusion Abnormalities and Ventilation Heterogeneity in Asthma. American Thoracic Society 2019 International Conference Location: Dallas, TX. Date: MAY 15-20, 2019.
25. AL Barker*, RL Eddy, **AM Matheson**, AR Westcott, GR Washko and G Parraga. Bronchiectasis, Vascular Pruning and Ventilation Defects in COPD and Bronchiectatic Patients: Are They Related? American Thoracic Society 2019 International Conference Location: Dallas, TX. Date: MAY 15-20, 2019.
26. K Stenhouse*, **AM Matheson**, C Ge, S Beamish, B Jansens, and AL Norman. High-Volume Rainfall Events in Calgary, Alberta, Canada & Their Relationship to HYSPLIT Back Trajectories & Chemical Constituents. American Geophysical Union, Fall General Assembly 2016 San Francisco CA 12-16 December, 2016.

H Media Coverage (15)

1. Xenon 129 MRI in patients with long COVID. Radiology Podcasts. Podcast interview. https://podcasts.apple.com/ca/podcast/xenon-129-mri-in-patients-with-long-covid/id318156476?i=1000586290126 Nov 15, 2022.
2. Montreal study looks for ways to treat COVID-19 long-haulers crippled by lingering symptoms. CBC News. Print news article. https://www.cbc.ca/news/canada/montreal/long-covid-study-montreal-1.6521131. 16 July 2022
3. What is long COVID? Four explanations on how and why it occurs. The Globe and Mail. Print news article. https://www.theglobeandmail.com/canada/article-what-is-long-covid-symptoms-causesexplained/ 16 July 2022
4. Montreal study looks for ways to treat COVID-19 long-haulers crippled by lingering symptoms. CBC News. Print new article. https://www.cbc.ca/news/canada/montreal/long-covid-study-montreal-1.6521131 10 July 2022

5. Can an Ontario breakthrough help long COVID sufferers? Toronto Star, This Matters Podcast. Podcast. https://www.thestar.com/podcasts/thismatters/2022/07/06/can-an-ontario-breakthroughhelp-long-covid-sufferers.html 6 July 2022
6. It's not in your head - it's in your lungs': A researcher on her long-COVID findings. TVO. Print news interview. https://www.tvo.org/article/its-not-in-your-head-its-in-your-lungs-a-researcher-onher-long-covid-findings 5 July 2022
7. Xenon-129 MRI exams show long-term effects of COVID-19. AuntMinnie.com. Online new article. https://www.auntminnie.com/index.aspx?sec=log&URL=https%3a%2f%2fwww.auntminnie.com%2findex.aspx%30 June 2022
8. Canadian researchers reveal hope-filled discovery for long COVID patients. Burnabynow. Republished in North Shore News. Online news article. https://www.burnabynow.com/highlights/canadianresearchers-reveal-hope-filled-discovery-for-long-covid-patients-5532322 29 June 2022.
9. Western researchers use MRI to learn cause of long-COVID symptoms. London News Today. Online news article. https://blackburnnews.com/london/london-news/2022/06/29/western-researchers-usemri-learn-cause-long-covid-symptoms/ 29 June 2022.
10. Ontario researcher focus on possible clue of long COVID. Global News. National news television broadcast. https://globalnews.ca/video/8954880/ontario-researchers-focus-on-possible-clue-of-longcovid/ 28 June 2022
11. Western-led study points to possible long COVID trigger in lungs. The London Free Press. Republished in The Toronto Sun, The Ottawa Sun, The Calgary Sun, and other PostMedia regional print publications. Print news article. https://lfpress.com/news/local-news/microscopic-lung-abnormalitymay-play-role-in-long-covid-study June 28 2022.
12. Cause of long-COVID symptoms revealed by lung-imaging research at Western University. CBC News. Print news article. https://www.cbc.ca/news/canada/london/cause-of-long-covid-symptomsrevealed-by-lung-imaging-research-at-western-university-1.6504318 28 June 2022
13. Research into Long COVID and Lung Impact by Western University. Afternoon Drive with Allison Devereaux, CBC Radio. Live radio broadcast. https://www.cbc.ca/listen/live-radio/1-80-afternoondrive/ clip/15922029-research-into-long-covid-lung-impact-by-western 28 June 2022.
14. Ontario researchers say they've found what causes long-COVID symptoms. CTV News. Online news article. https://london.ctvnews.ca/lung-imaging-technology-reveals-cause-of-long-covid-symptomswestern-study-1.5966717 28 June 2022
15. Innovative lung-imaging technique shows cause of long-COVID symptoms. Western News. Online news article. https://news.westernu.ca/2022/06/innovative-lung-imaging-technique-shows-cause-oflong-covid-symptoms/ 28 June 2022.

PROFESSIONAL MEMBERSHIPS

2020-	**Biomedical Imaging Research Centre – Western University**
	Student Member
2020-	**Canadian Respiratory Research Network**
	Member
2018-	**The American Thoracic Society**
	Trainee Member
2018-	**The International Society for Magnetic Resonance in Medicine**
	Trainee Member
2018-	**Society of Photo-Optical Instrumentation Engineers**
	Trainee Member